The Dissertation Committee for Peng Zhang Certifies that this is the approved version of the following dissertation:

LOW FREQUENCY DOWNHOLE ELECTRICAL MEASUREMENTS FOR MAPPING PROPPANT DISTRIBUTION IN HYDRAULIC FRACTURES IN CASED-HOLE WELLS

Committee:

Mukul M. Sharma, Supervisor

Hugh Daigle

David DiCarlo

Kishore K. Mohanty

Mrinal K. Sen

LOW FREQUENCY DOWNHOLE ELECTRICAL MEASUREMENTS FOR MAPPING PROPPANT DISTRIBUTION IN HYDRAULIC FRACTURES IN CASED-HOLE WELLS

by

Peng Zhang

Dissertation

Presented to the Faculty of the Graduate School of

The University of Texas at Austin

in Partial Fulfillment

of the Requirements

for the Degree of

Doctor of Philosophy

The University of Texas at Austin

August 2018

Dedication

致我的父母，张永正和彭业华，感谢他们无条件的爱、理解、支持与付出。

致远在中国的家人和朋友，特别是孙月光叔叔，感谢他们的关心和帮助。

Acknowledgements

I would like to express my deepest gratitude to my advisor, Dr. Mukul M. Sharma, for his financial support and guidance throughout my study at UT. In these four and half years he has been sharing his brilliant ideas with me and helping me pass through many difficulties. The experience of Dr. Sharma as an outstanding researcher, a successful businessman and a respected supervisor made me always eager to learn from him. Dr. Mrinal K. Sen must also be acknowledged for his advice regarding the inverse modeling in this work. I would like to extend my appreciation to the other committee members: Dr. Hugh Daigle, Dr. Kishore K. Mohanty and Dr. David DiCarlo, for providing insightful comments on my research proposal and dissertation.

The life of being a graduate student can be very challenging, without the day-to-day contribution of Jin Lee, Frankie Hart, Amy Stewart, Rodney T. Russell and Glen Baum. Many of my colleges have also contributed to this dissertation in different ways. In particular I would like to thank Yaniv Brick, Javid Shiriyev, Ripudaman Manchanda, Philip Cardiff, Haotian Wang, Jongsoo Hwang, Sho Hirose, Williams Ozowe, Alex Ahn, and Shuang Zheng.

I'm also very grateful to my friends for being part of my life at UT. Their support and care made such a joyful journey for me. In particular I would like to thank Sophie Yi, Hongtao Yang, Ke Xu, Runqi Han, Wan Wei, Puneet Seth, Yifei Xu, Songyang Tong and many others whom I did not cite explicitly.

Low Frequency Downhole Electrical Measurements for Mapping Proppant Distribution in Hydraulic Fractures in Cased-Hole Wells

Peng Zhang, PhD

The University of Texas at Austin, 2018

Supervisor: Mukul M. Sharma

A tool using downhole electrical measurements for mapping electrically conductive proppant in hydraulic fractures is presented. The method relies on direct excitation of the casing, which is expected to overcome the severe limitations of induction tools in cased-hole wells. An array of insulating gaps is installed and cemented in place as a permanent part of the casing string. The electrical measurements are done by imposing a voltage across each insulating gap, one at a time, before and after hydraulic fracture operations. The voltages across other insulating gaps near the transmitter gap are recorded.

A conductive proppant, petroleum coke (PC) was tested using a resistivity core holder. Experimental results show that the electrical resistivity of PC stays low (~$6 \times 10^{-4}\ \Omega \cdot m$) under confining stress of 4000 psi when up to 50% sand is added, which makes it a good candidate proppant for the tool's application.

The tool's response to the presence of fractures was modeled by solving for the electrical potential using a finite volume method. Simulation results show that the electrically conductive proppant alters the path of the electrical current in the formation and this is recorded as differential signals by the string of insulating gaps surrounding the source gap. The simulated differential signals are highly sensitive to a fracture's

conductivity, location and length, and less sensitive to a fracture's orientation and asymmetry with the wellbore axis.

Parametric inversion of multiple fractures from synthetic data, generated by exciting various gaps in a casing string, was solved with a divide-and-conquer approach. The original problem was divided into sub-problems and each sub-problem was solved separately using a global optimization algorithm Very Fast Simulated Annealing (VFSA). The results show that VFSA can invert the data and output widths and radii of multiple fractures without requiring a large number of forward simulations. The robustness of VFSA was also tested by adding Gaussian noise to the synthetic data. Example cases show that when 5% noise is introduced, VFSA still provides very accurate inversion results with moderate uncertainties.

Table of Contents

List of Tables xi

List of Figures xiii

Chapter 1: Introduction 1

1.1 Problem statement 1

1.2 Tiltmeters 3

1.3 Tracers 4

1.4 Pressure Monitoring 5

1.5 Borehole microseismic 7

1.6 Fiber optics 8

1.7 Electromagnetic and electrical methods 9

Chapter 2: Electrical Resistivity & Hydraulic Conductivity of Petroleum Coke 13

2.1 Background 13

2.2 Electrical resistivity of petroleum coke 15

2.2.1 Experimental System 15

2.2.2 Resistivity of Bulk PC 18

2.2.3 Resistivity of PC in a Fracture 21

2.3 Hydraulic conductivity of petroleum coke 26

2.3.1 Experimental System 26

2.3.2 Hydraulic Conductivity of PC in a Fracture 28

2.4 Conclusion 30

Nomenclature 32

Chapter 3: Tool Configuration and Numerical Methods 33

3.1 Background 33

3.2 Configuration of downhole transmitter and receiver 34

3.3 Forward model formulation 36

3.4 Harmonic interpolation and non-orthogonality correction 38

3.5 Matrix equation 41

3.6 Validation of the numerical methods 44
3.6.1 Validation Case 1 44
3.6.2 Validation Case 2 46
3.7 Model simplifications 49
3.7.1 Simplification of the Well 51
3.7.2 Simplification on the Fracture 53
3.8 Summary 56
Nomenclature 58
Chapter 4: Forward Modeling – Sensitivity Study of the Tool 59
4.1 Background 59
4.2 Effect of fracture location 60
4.3 Effect of fracture conductance 63
4.4 Effect of fracture size 66
4.5 Effect of fracture angle 74
4.6 Effect of fracture asymmetry 77
4.7 Effect of fracture's aspect ratio 79
4.8 Influence of the background conductivity 83
4.9 Effect of proppant discontinuity 86
4.10 Power requirement analysis of the tool 90
4.11 Summary and conclusions 95
Nomenclature 98
Chapter 5 Forward Modeling – Simulation of Multiple Fractures 99
5.1 Background 99
5.2 multiple fractures separated by insulating gaps 100
5.3 Two fractures on one casing section 104
5.4 Simplification of multiple-fracture simulations 112
5.5 Summary 116
Chapter 6: Building a Framework for Inverse Modeling 118
6.1 Background 118

6.2 Local optimization methods....121
6.3 Global optimization methods....125
6.4 Building an inversion framework for the tool....128
6.5 Inverse solver test - the method of steepest descent....130
6.6 Inverse solver test - very fast simulated annealing....135
6.7 Summary....141
Nomenclature....142
Chapter 7: Inversion Results with Uncertainty Estimation....143
7.1 Background....143
7.2 Inversion methodology – divide and conquer....144
7.3 Inversion results from strategy 1....148
7.4 Inversion results from strategy 2....157
7.5 Realistic fractures – what to expect....164
7.5.1 Fracture deviation from the wellbore....165
7.5.2 Non-uniform fracture width....168
7.5.3 Tilted fractures....171
7.5.4 Complex fractures....173
7.6 Additional observations....174
7.7 Summary....178
Chapter 8: Conclusions....181
Bibliography....189

List of Tables

Table 2.1. Measured resistivity of a brine saturated sand pack with respect to different brine concentration.....17

Table 2.2. The measured electrical resistivity of the PC (40 – 70 mesh) -sand mixture at different confining pressure. 23

Table 2.3. The measured electrical resistivity of the PC (70 – 100 mesh) -sand mixture at different confining pressure.....26

Table 4.1 Total current and power consumption when a fracture with radius 30 m is present. 93

Table 4.2 Total current and power consumption when no fracture is present. 94

Table 6.1 The relative errors for the single-fracture case from steepest descent and VFSA. 136

Table 6.2 The relative errors for the multiple-fracture case from steepest descent and VFSA. 139

Table 7.1 The true model and inverted model when 2% Gaussian noise is added to the synthetic data. The values for the inverted model are the average from 15 inversion runs.....149

Table 7.2 Covariance matrix for the inverted model. Each element on the diagonal is the variance of the corresponding model parameter. 153

Table 7.3 Correlation matrix for the inverted model. 154

Table 7.4 The true model and inverted model for the fiver fractures marked in Fig. 7.2(a), when 5% Gaussian noise is added to the synthetic data.....155

Table 7.5 The true model and inverted model when 2% Gaussian noise is added to the synthetic data. The values for the inverted model are the average from 15 inversion runs. 157
Table 7.6 The true model and inverted model for the fiver fractures marked in Fig. 7.2(b), when 5% Gaussian noise is added to the synthetic data. 160
Table 7.7 Covariance matrix for the inverted model. Each element on the diagonal is the variance of the corresponding model parameter. 163
Table 7.8 Correlation matrix for the inverted model. 164
Table 7.9 Comparison between actual and estimated proppant volume. 170
Table 7.10 Error and uncertainty of the estimated fracture parameters corresponding to different noise levels in the synthetic data. 175

List of Figures

Figure 1.1 Multiple fracture stages along the well axis for shale stimulation. (From Dusseault and McLennan, 2011) 1

Figure 1.2 Principle of tiltmeter fracture mapping. (From Cipolla and Wright, 2000) 3

Figure 1.3 Water hammer signature properties: amplitude, period, decay rate and duration. (From Iriarte et al., 2017) 6

Figure 1.4 Borehole microseicmic for fracture detection. (From Fisher et al., 2002) 7

Figure 1.5 DAS and DTS results showing the lack of fluid and proppant entering the toe-side clusters (quite zone). (From Haustveit et al., 2017).....8

Figure 1.6 A schematic of the low-frequency induction tool for fracture mapping in an open-hole wellbore. (From Yang et al., 2015).....10

Figure 2.1. Configuration of the resistivity core holder. The yellow bars identify the electrodes, while the black cylinder and the red arrows represent the core and the confining pressure, respectively. 15

Figure 2.2. The measured resistivity of the sand pack Ro versus the resistivity of brine Rw. A linear relationship is observed.....18

Figure 2.3. Electrical resistivity of the PC pack with respect to confining pressure. No brine is present in these two sets of measurements.....19

Figure 2.4. Electrical resistivity of the PC pack with respect to confining pressure. Sea water was injected to the pack for both Test 1 and Test 2. 19

Figure 2.5. (a) A schematic of proppant in a fracture of width wf. (b) A fractured sandstone core propped by PC. The core length and diameter are 2' and 1.5', respectively. 21
Figure 2.6. Measured resistivity of PC (40 – 70 mesh) at various confining pressures. The green, blue and red curves represent the PC mixed with 0%, 25% and 50% sand, respectively. 22
Figure 2.7. Measured resistivity of PC (40 – 70 mesh) mixed with 75% sand at various confining pressures.....23
Figure 2.8. Measured resistivity of PC (70 – 100 mesh) at various confining pressures. The green, blue and red curves represent the PC mixed with 0%, 25% and 50% sand, respectively. 25
Figure 2.9. Measured resistivity of PC (70 – 100 mesh) mixed with 75% sand at various confining pressures.....25
Figure 2.10. Experimental method for fracture conductivity measurements. Fluid is injected from the accumulator into the core. The back pressure regulators (BPR's) are used to adjust the flow rates. A confining stress is applied on the core. 27
Figure 2.11. (a) The measured fracture conductivities for different proppants (40 – 70 mesh) at various confining stresses. (b) Fracture conductivities normalized by the ones under 2000 psi confining stress. 28
Figure 2.12. (a) The measured fracture conductivities for different proppants (70 – 100 mesh) at various confining stresses. (b) Fracture conductivities normalized by the ones under 2000 psi confining stress. 29

Figure 2.13. Stimulation ratio versus dimensionless fracture conductivity from two models. 'Current model' and 'Prats' represents Friehauf's and Prats's model, respectively. 30

Figure 3.1. A schematic of the tool. Inside the well are the coiled tubing and BHA. The numbered blocks indicate insulating gaps. The transmitter gap is denoted #0 and the remaining gaps (receivers) are numbered accordingly. The curved lines 'a' and 'b' depict hydraulic fractures with different geometries. 35

Figure 3.2. (a) The computation domain containing the well, fracture and the surrounding formation is discretized using an unstructured mesh. (b) An enlarged view of the mesh around the well and the fracture. (c) A volumetric cell (right) and its cross-section (left). c indicates the cell center, on which the unknown potential Φ is defined, and $f(i)$ is the center of the ith face of the cell. 37

Figure 3.3. Harmonic interpolation of electric conductivity on the interface ensures the continuity of electric potential and normal current. 39

Figure 3.4 Non-orthogonality correction when calculating the normal current on the cell face. 41

Figure 3.5. Discretization for internal and boundary cells.....42

Figure 3.6. A 2D orthogonal mesh with the boundary value defined. The edge length for the grids is d. 43

Figure 3.7. The matrix equation for the system in Fig. 3.6.....43

Figure 3.8. (a) The tetrahedral mesh around the source and the conductive spheres (the mesh size increases gradually away from the source). The color plot denotes the electrical conductivity. Samples of the calculated results are taken along the white line, which is corresponding to the dashed line in (b). (b) The results from our FVM (blue triangles) match well with the analytical and FEM solutions (Weiss et al., 2016). 45

Figure 3.9. (a) Side view illustration of the test-case problem. (b) Map view of the source, wellbore and the mesh surrounding them. The computation domain is 10 km, 10 km and 5 km along X, Y and Z directions, respectively. The left and right boxes mark the location of the well and source, respectively.....47

Figure 3.10. (a) Average potentials along the well as a function of its radius for various near-source mesh sizes in a 20 m x 20 m x 10 m box. (b) Average error relative to the analytical solution as a function of mesh size. 49

Figure 3.11. Illustration of an electrode array configuration. Gap #0 is used for excitation.....51

Figure3.12. (a) Equivalent conductivity model for casing/insulator sections. A and σ represent the area and conductivity of a specific region, respectively. (b) The electric potentials along the well computed using the solid volume well model and the mud-filled casing/gap well model. 52

Figure 3.13. The realistic thin hydraulic fracture (yellow) is replaced by a thicker fracture (green) with lower electrical conductivity.....54

Figure 3.14. (a) Illustration of an electrode array configuration. Gap #0 is used for excitation. The fracture is placed 5 m away from gap #0. (b) The electric potentials along the well are plotted for two cases (the position of zero is set at the center of gap #0). 55
Figure 4.1 Illustration of the tool configuration with three possible fracture locations. 61
Figure 4.2 Potentials along the wellbore for three different fracture locations and the no-fracture case. 62
Figure 4.3 (a) Voltages at the various gaps corresponding to three fracture locations and the no-fracture case. (b) Voltage differences from the no-fracture case corresponding to the voltages in (a). 63
Figure 4.4 Illustration of the tool configuration that is used to investigate the effect of fracture conductance. 64
Figure 4.5 Voltages at the various gaps corresponding to different fracture conductance and the no-fracture case. (b) Voltage differences from the no-fracture case corresponding to the voltages in (a). (c) Differential voltages in (b) relative to the *differential* ones obtained for the least conductive fracture ($G = 6$ S).....65
Figure 4.6 Potentials along the wellbore for fractures with different radii and the no-fracture case. 67
Figure 4.7 The electrical potential on the fractures along the radial direction. The legend marks the fracture radii. 68
Figure 4.8 Voltage differences from the no-fracture case at various gaps as a function of the fracture area. 69

Figure 4.9 Differential voltages measured at various gaps in Fig. 4.8 normalized by the corresponding voltages without fractures. 70
Figure 4.10 Differential voltages in Fig. 4.8 relative to the *differential* ones obtained for the largest fracture ($r = 120\ m$). Dashed lines mark a threshold of $\pm$2%. 71
Figure 4.11 (a) Saturation limit for the various gaps assuming a $\pm$2% differentiation threshold. (b) Illustration of the saturation limit for gaps #1 ($r = \sim 65\ m$) and #2 ($r = \sim 49\ m$). 72
Figure 4.12 Relative signal strength using a low frequency (100 Hz) induction tool with respect to the fracture area (Yang et al., 2015). The green dashed lines mark a 2% threshold from the saturation level. The green circle marks the largest fracture size that can be differentiated.....73
Figure 4.13 Illustration of the tool configuration with a tilted fracture of angle α.74
Figure 4.14 Voltage differences from the no-fracture case at various gaps as a function of fracture angle. The integers denote the number of the receiver gaps. 75
Figure 4.15 Differential voltages in Fig. 4.14 relative to the *differential* voltages obtained for an orthogonal fracture. Dashed lines mark a threshold of $\pm$2%. 76
Figure 4.16 Illustration of the tool configuration with a circular fracture whose axis is displaced from the well axis by a distance d. 77
Figure 4.17 Voltage differences from the no-fracture case at various gaps as a function of the fracture deviation from the well axis.....78

Figure 4.18 Differential voltages in Fig. 4.17 relative to the *differential* voltages obtained for the centered fracture (d = 0). Dashed lines mark a threshold of $\pm$2%. 79
Figure 4.19 Illustration of the tool configuration with a fracture of aspect ratio a/b. 80
Figure 4.20 Voltage differences from the no-fracture case at various gaps as a function of the aspect ratio. 81
Figure 4.21 Differential voltages in Fig. 4.17 relative to the *differential* voltages obtained for the square fracture (aspect ratio = 1). Dashed lines mark a threshold of $\pm$2%. 82
Figure 4.22 Typical ranges of electrical resistivity for selected earth materials (Ley-Cooper et al., 2015). 83
Figure 4.23 Potential along the well corresponding to difference shale resistivity. 84
Figure 4.24 (a) Voltages at the various gaps corresponding to different shale resistivity. (b) Voltage differences from the no-fracture case corresponding to the voltages in (a). 85
Figure 4.25 Possible proppant distribution profiles in the fracture. (a) The proppant is continuous. (b) A ring cuts the fracture into two separate parts. (c) The proppant branches out at the fracture tip. 86
Figure 4.26 (a) Illustration of the tool configuration that is used to investigate the effect of proppant discontinuity. (b). Proppant discontinuity happens in the radial direction at radius r in a fracture of radius 30 m. (c) Voltages at the various gaps corresponding to different scenarios. (d) Voltage differences from the no-fracture case corresponding to the voltages in (c). 88

Figure 4.27 (a). Proppant discontinuity happens in the tangential direction from radius r to the tip in a fracture of radius 30 m. (b) Voltages at the various gaps corresponding to different scenarios. (c) Voltage differences from the no-fracture case corresponding to the voltages in (b). (d) An enlarged view of the area marked by the black square in (c). 89
Figure 4.28 Current flow pattern around the fracture and the transmitter gap. The triangles represent the contact points between the tool and the casing, where a voltage source is applied. 91
Figure 4.29 The calculated electrical potential along the excited casing on the positive side of the transmitter gap when a fracture with radius 30 m is present. Different shale resistivity is used for the simulations. 92
Figure 4.30 The calculated electrical potential along the excited casing on the positive side of the transmitter gap when no fracture is present. Different shale resistivity is used for the simulations. 94
Figure 5.1 Illustration of the tool configuration with three fractures touching different casing sections. 101
Figure 5.2 Computed potentials along the wellbore for different cases. 102
Figure 5.3 Voltages at the various receivers calculated based on the results in Fig. 5.2. 102
Figure 5.4 Voltage differences from the no-fracture case corresponding to the voltages in Fig. 5.3. 103
Figure 5.5 (a) Illustration of the tool configuration with two fractures touching the same excited casing section. (b) The complex fracture is simplified to two planar fractures in parallel with the same total thickness. 105
Figure 5.6 Voltages at the various gaps with respect to different scenarios. 106

Figure 5.7 Voltage differences from the no-fracture case corresponding to the voltages in Fig. 5.6. 106
Figure 5.8 Illustration of the tool configuration with two fractures touching a passive casing section. This casing section is isolated from the excited one by an insulating gap. 107
Figure 5.9 Voltages at the various gaps with respect to different scenarios when the fractures are not touching the excited casing section..... 108
Figure 5.10 Voltage differences from the no-fracture case corresponding to the voltages in Fig. 5.6. 109
Figure 5.11 Relative signal strength for planar and complex fracture geometries. (a) The complex fracture was simplified to either two or three planar elliptical fractures in parallel with the same total thickness. (b) Relative signal strength for short-spacing coaxial configuration corresponding to planar (red) and simplified complex fracture (blue and green). 111
Figure 5.12 A schematic depicting a well with multiple fractures. The transmitter (#0) and receiver gaps are marked separately. The solid lines are the 10 fractures right next to the 8 receiver gaps close to the transmitter. 113
Figure 5.13 Voltages at the various gaps with respect to different scenarios. The blue dotted ellipses mark the voltages measured at the 8 receiver gaps, 4 on each side of the transmitter. 114
Figure 5.14 A schematic depicting a well with multiple fractures. The solid lines are the 8 fractures right next to the 6 receiver gaps close to the transmitter. 115

Figure 5.15 Voltages at the various gaps with respect to different scenarios. The blue dotted ellipses mark the voltages measured at the 6 receiver gaps, 3 on each side of the transmitter. 115
Figure 6.1 A typical workflow for model-based inversion in geophysical applications (From Arora et al., 2011). 119
Figure 6.2 A hypothetical objective function that shows several minima. Gradient based methods will find the global minimum only when starting at position 1. Others will be trapped at secondary minima. (From Arora et al., 2011; Sen and Stoffa, 2013).....120
Figure 6.3 A model-based inversion algorithm using local optimization methods. (From Sen and Stoffa, 2013).....122
Figure 6.4 A 1D example illustrating Newton's method. It uses the slope and curvature (corresponding to the gradient and Hessian for multidimensional problems) to calculate the search direction. (From Sen and Stoffa, 2013).....123
Figure 6.5 A 2D example demonstrating the method of steepest descent. The search direction at iteration $k+1$ is orthogonal to the one at iteration k. (From Shewchuk, 1994).....124
Figure 6.6 A 2D example demonstrating the conjugate gradient method. The search direction at iteration $k+1$ is conjugate to the one at iteration k. (From Shewchuk, 1994).....125
Figure 6.7—A flow chart for VFSA. 127
Figure 6.8 A detailed framework for inversion. 129

Figure 6.9 Backtracking line search for a parabolic function $\mathcal{L}(\xi)$. The search starts from $\xi(1)$ and moves along the opposite direction of the local gradient to the next point $\xi(2)$. The step length is decreased by a factor of 0.8 if $\mathcal{L}\xi 1 \leq \mathcal{L}\xi 2$ (a) or increased by a factor of 1.2 (b) if $\mathcal{L}\xi 1 > \mathcal{L}\xi 2$, until the optimal step length is found. (From Jung and Taciroglu, 2014)130

Figure 6.10 Illustration of the tool configuration that is used to invert for the radius and width of a single fracture.....131

Figure 6.11 The change of the cost function with respect to the fracture width. The red circle and the green square mark the starting and end point in this iteration, respectively. 132

Figure 6.12 The change of the cost function with respect to the fracture radius. 132

Figure 6.13 Illustration of the logging process for inversion analysis. Three fracture are present, each separated by an insulating gap. 133

Figure 6.14 The change of the cost function with respect to the width of the first fracture (located 5 m from the transmitter gap). The red circle and the green square mark the starting and end point in this iteration, respectively. 134

Figure 6.15 The change of the cost function with respect to the radius of the first fracture. 135

Figure 6.16 (a) Cost function in each iteration. (b) The temperature scheme used for the study. (c) Comparison between true radii and inverted radii of the three fractures. (d) Comparison between true widths and inverted widths of the three fractures. 137

Figure 6.17—Comparison between true data and inverted data for three excitation locations. (a), (b) and (c) correspond to the data when gap #0, #1 and #2 (Fig. 6.13) are excited, respectively. 138
Figure 6.18—(a) Cost function in each iteration when inverting the noisy data. (b) 2% of random noise is added to the clean synthetic data. (c) Comparison between true radii and inverted radii of the three fractures. (d) Comparison between true widths and inverted widths of the three fractures.....140
Figure 7.1 A schematic depicting a horizontal well with multiple fractures. 145
Figure 7.2 (a) 13 fractures are involved in a four-excitation (at gap 0, 1, 2 and 3) sub-problem, if voltages at 8 receivers from each excitation are used for inversion. (b) 11 fractures are involved in a four-excitation (0, 1, 2 and 3) sub-problem, if voltages at 6 receivers from each excitation are considered. The red dashed rectangles mark the fractures directly in contact with the casing sections that have been excited when the tool moves from gap 0 to 4. 147
Figure 7.3 Cost function and temperature at each iteration during an inversion process.....150
Figure 7.4 Comparison between the true and inverted model for the five fractures highlighted in Table 7.1. 2% Gaussian noise is added to the data. The error bars indicate the uncertainties associated with each parameter.152
Figure 7.5 Comparison between the true and inverted model for the five fractures highlighted in Table 7.1. 5% Gaussian noise is added to the data. The error bars indicate the uncertainties associated with each parameter.156

Figure 7.6 Comparison between the true and inverted model for the five fractures highlighted in Table 7.5. 2% Gaussian noise is added to the data. The error bars indicate the uncertainties associated with each parameter.158

Figure 7.7 Comparison between the true and inverted model for the five fractures highlighted in Table 7.6. 5% Gaussian noise is added to the data. The error bars indicate the uncertainties associated with each parameter.161

Figure 7.8 Comparison between true data and estimated data for four excitation locations. (a), (b), (c) and (d) correspond to the data when gap #0, #1, #2 and #3 are excited, respectively. 162

Figure 7.9 Illustration of the tool configuration that is used to invert for the radius and width of a single fracture. 165

Figure 7.10 A circular fracture that deviates from the wellbore by distance d. .166

Figure 7.11 The estimated fracture width (a) and radius (b) as a function of the fracture's deviation from the wellbore. The error bars mark the uncertainties associated with the model parameters. 167

Figure 7.12 A simplified model for fractures with non-uniform width. The fracture has five layers and the width of each layer gets thinner towards the edge. 168

Figure 7.13 (a) Different width profiles used in the simulations. (b) The estimated fracture width corresponding to different scenarios. (c) The estimated fracture radius corresponding to different scenarios. The error bars mark the uncertainties associated with the model parameters. 169

Figure 7.14 A tilted fracture of angle α is placed 5 m away from the transmitter gap. 171

Figure 7.15 (a) The estimated fracture width corresponding to different scenarios. (b) The estimated fracture radius corresponding to different scenarios. The error bars mark the uncertainties associated with the model parameters. 172
Figure 7.16 A complex fracture with a few fracture branches. 173
Figure 7.17 The estimated fracture width (a) and radius (b) corresponding to a planar and complex fracture.....174
Figure 7.18 (a) The data are synthesized using three excitation locations (#0, #1 and #2). (b), (c). Comparison between the true and inverted model for three fractures with a wide variation in the radius. 5% Gaussian noise is added to the data. 176
Figure 7.19 Comparison between true data and estimated data for three excitation locations. (a), (b) and (c) correspond to the data when gap #0, #1 and #2 (Fig. 7.18 (a)) are excited, respectively. 177
Figure 7.20 Cost function VS iteration during the inversion process. In case A the search intervals for fracture width and radius are [2 mm, 8 mm] and [10 m, 50 m], respectively. The search intervals for case B are set as [3 mm, 6 mm] and [15 m, 40 m]. 178

Chapter 1: Introduction

1.1 PROBLEM STATEMENT

With more than thirty years of development, hydraulic fracturing is playing an essential role in unlocking oil and gas production from low permeability reservoirs. Some key technologies for hydraulic fracturing have been widely used to achieve high initial production rates and improve recovery of hydrocarbons. Horizontal wells, for example, with lateral lengths of 5000 ft to over 10,000 ft are drilled and then fractured in multiple stages (Fig. 1.1). Multi-stage fracturing increases the fracture contact area with the formation and, therefore, greatly improves the productivity of the well (King, 2010; Casero et al., 2008; Castaneda et al., 2010; Durst et al., 2008; Grieser et al., 2009; Seale et al., 2006).

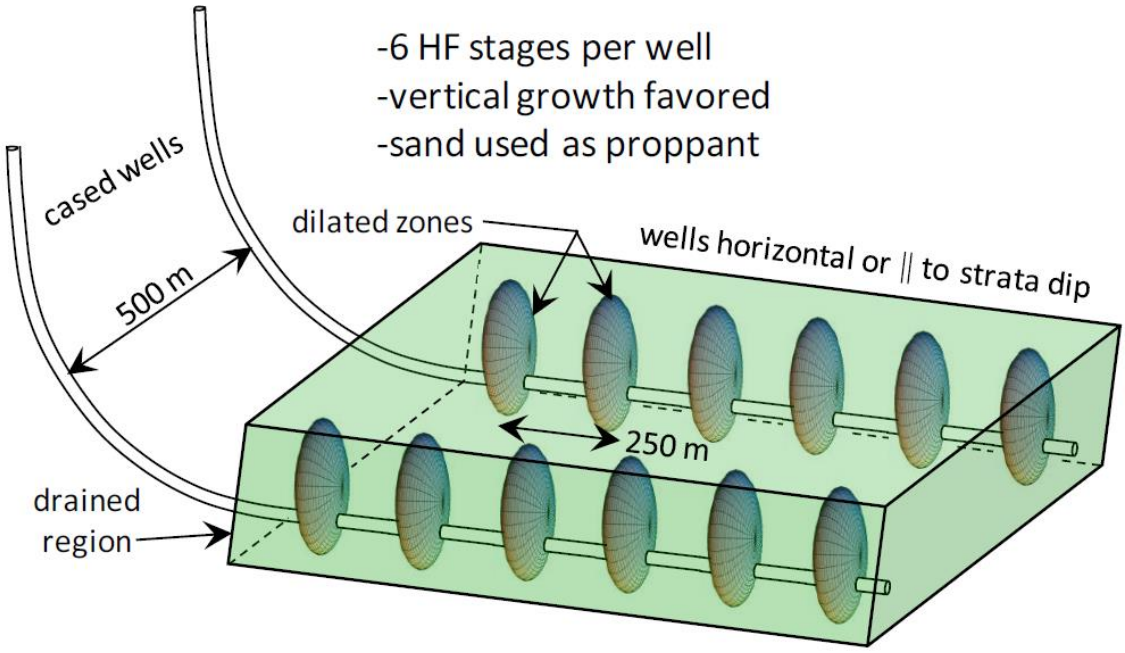

Figure 1.1 Multiple fracture stages along the well axis for shale stimulation. (From Dusseault and McLennan, 2011)

In order to know what events are happening in the reservoir during a fracturing job, people have developed several models to predict how fluid-driven cracks propagate in reservoir rocks. These models, including pure geomechanical models and fully coupled porous flow and geomechanical ones, are being widely used in the oil and gas industry (Adachi et al., 2007; Ouchi et al., 2015; Settari and Mourits, 1998; Bryant et al., 2015). Models were also established to simulate the growth of fractures at multiple clusters of perforations (Roussel and Sharma, 2011; Manchanda et al., 2014; Manchanda et al., 2016; Dahi-Taleghani and Olson, 2011; Yamamoto et al., 2004). Parameters such as stage spacing and reservoir permeability were studied to optimize production by generating more sophisticated fracture networks (Bunger et al., 2012; Manchanda et al., 2016).

Predicting the geometry of induced fractures, however, is not sufficient for forecasting or history matching a well's productivity. This is because only the propped fractures will remain open after the fracturing fluids leak off. The induced unpropped fractures, some natural fractures and micro-fractures created during the hydraulic operation, will close soon after completion, therefore will not contribute to the well's productivity (Sharma and Manchanda, 2015). A few attempts have been made to understand proppant transport and settling in fracture networks. Both experimental and simulation results show that proppants reach only a portion of the induced fractures, depending on numerous factors, e.g., injection rate or fluid rheology (Blyton et al., 2015; Blyton, 2016; Shrivastava and Sharma, 2018; Sahai et al., 2014; Tong and Mohanty, 2016). These studies improve our understanding of proppant distribution in the induced fractures, to better interpret and predict production in fractured wells.

While all the previous models and methods focus on prediction of induced and propped fractures, validation of these models requires independent diagnostic methods to

measure the actual fracture dimensions in the post-fracturing stage. Most importantly, direct evidence of the stimulated reservoir volume and the proppant distribution provided by fracture diagnostic techniques can greatly benefit reservoir characterization, which is critical for improving the fracture treatment design in the life cycle of a reservoir. There are a few categories of fracture diagnostic methods applied or currently being explored in the industry. They are summarized in the following sections of this chapter.

1.2 TILTMETERS

Tiltmeter is one of the earlier diagnostic methods that have been used for fracture mapping. It is based on a simple principle: a created fracture induces deformation in the rock surrounding, which can be detected either on the surface or downhole (Fig. 1.2).

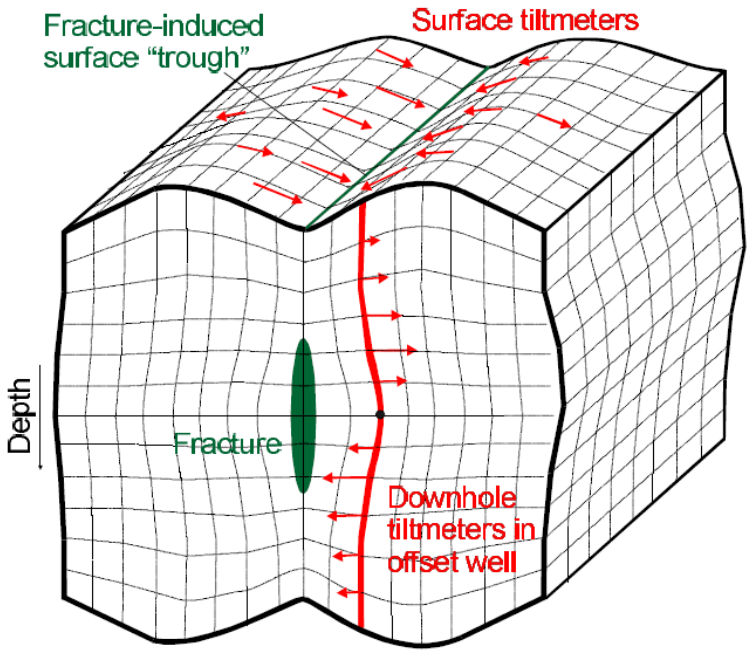

Figure 1.2 Principle of tiltmeter fracture mapping. (From Cipolla and Wright, 2000)

An array of surface tiltmeters measure the tilt of the earth at several locations, from which the fracture azimuth can be obtained. However, surface tiltmeters can barely

detect fracture length and height, because they are typically very far from the created fractures deep under the ground (Cipolla and Wright, 2000; Warpinski, 1996). Downhole tiltmeters are placed in one or a few monitor wells next to the treatment well. They are at the depth of the fracture so the deformation in the proximity to the fracture can be captured. Although downhole tiltmeters are significantly more sensitive to fracture dimensions than surface tiltmeters (Wright et al, 1998 a; Wright et al, 1998 b), they provide no direct information about proppant distribution. Hence, they are seldom the primary choice to infer propped fracture geometries.

1.3 TRACERS

Another category of diagnostic methods in the petroleum industry relies on proppant tracers or fluid tracers that can be dissolved in water or hydrocarbons. They are typically pumped into the well with the fracturing fluids, and then detected based on various mechanisms depending on the unique properties of the tracer.

Radioactive tracers, which are coated either on the proppant or dissolved in the fracturing fluids, emit gammy rays that can be detected by radiation sensors. However, this method fails to provide fracture information at distances more than a few inches from the wellbore (Gore and Terry, 1956; Scott et al., 2010; Warpinski 1996). These radioactive tracers also involve environmental and safety concerns for operators. An alternate non-radioactive ceramic proppant that contains a high thermal neutron capture compound has proven effective in evaluating fracture height (Grae et al., 2012; Saldungaray et al., 2012; Duenckel et al., 2011). Unfortunately, this method also focuses on near-wellbore proppant detection, due to the small depth of investigation of neutron logs.

Chemical tracers carried by the fracturing fluids can potentially overcome the limitation of radioactive tracers and allow far-field fracture detection. These chemical tracers travel deep into the reservoir with the fluids at the pumping stage. The recorded tracer concentrations during flowback and historical production data can reveal important information about fracture properties, such as the fracture length, height and hydraulic connectivity. However, the complexity in the fracture and reservoir, coupled with data limitations, complicates the estimation of these properties (Elahi and Jafarpour, 2018). Due to the non-uniqueness of the results, they offer more qualitative than quantitative characterization of the proppant distribution. Nonetheless, analysis of tracer returns provides a clear indication of which fracture stages hydrocarbon is being produced from. This technology can also be used to determine hydrocarbon cross flow between wells due to hydraulic communication (Catlett et al., 2013; Mayerhofer et al., 2011).

1.4 PRESSURE MONITORING

Pressure data from surface or downhole gauges are often available in a hydraulic fracture treatment. Pressure monitoring is recognized as a low-cost fracture diagnostic method without particular requirements for the fracturing fluid or proppant properties and downhole instrumentation.

There are different ways of utilizing the pressure data to diagnose fractures. For example, due to the poroelastic effects, a large pressure increase is often observed in fractures next to a stimulated well. These pressure signals acquired in one or multiple monitor wells on the same pad can be used to determine the geometry of induced fractures as well as their orientation (Kampfer and Dawson, 2016). This method requires that the horizontal wells are in reasonable proximity both in the vertical and lateral

directions. Limited natural fractures and faults are also desired for the successful implementation of this approach (Dawson and Kampfer, 2016).

Pump shutdown or valve closure at the conclusion of a hydraulic fracture treatment generates a series of pressure pulses, known as a water hammer. The different water hammer signature properties (Fig. 1.3) can be used to describe the fracture connection to the wellbore (Iriarte et al., 2017). History matching of field data with simulations reveals that the water hammer signature can be correlated to fracture spacing, length and stimulated reservoir volume (Carey et al., 2015; Carey et al., 2016).

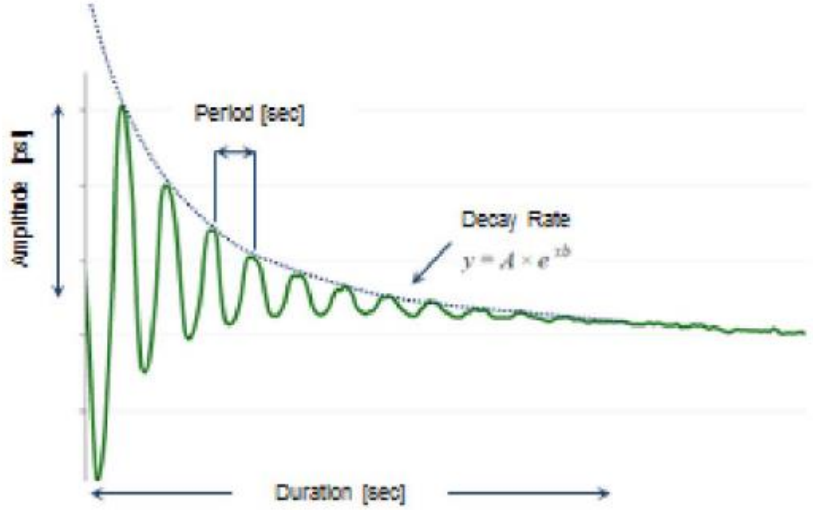

Figure 1.3 Water hammer signature properties: amplitude, period, decay rate and duration. (From Iriarte et al., 2017)

Pressure monitoring does not impact completion efficiency, which makes it advantageous in terms of costs. However, these methods rely on limited surface or downhole pressure measurements, which makes the extraction of fracture geometry very challenging. The solutions are often non-unique and they provide very limited insights into the proppant distribution in the fracture.

1.5 BOREHOLE MICROSEISMIC

Fracture propagation results in micro-earthquakes or microseisms, which can be detected by receivers in an adjacent monitor well (Fig. 1.4). The locations of the microseisms are obtained from inversion by using an appropriate velocity model. With more than twenty years of development, borehole microseismic monitoring can efficiently provide extensive information on induced fracture geometry. Sophisticated data processing techniques can even provide real-time microseismic monitoring of hydraulic fracture treatments (Le Calvez et al., 2007). This method has been the primary SRV identification technique and has been proved to be an effective tool for improving completion and reservoir management (Mayerhofer et al., 2010).

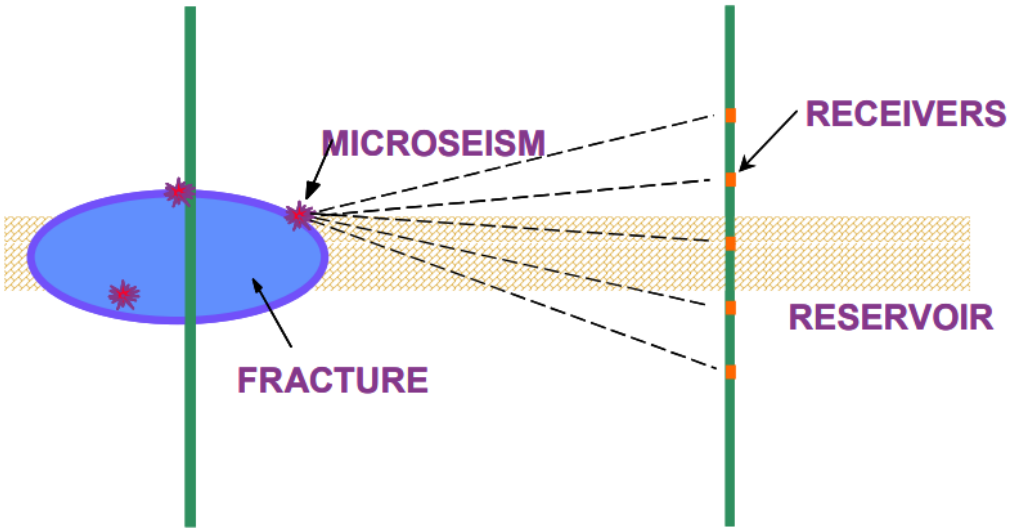

Figure 1.4 Borehole microseicmic for fracture detection. (From Fisher et al., 2002)

Even so, microseismic measurements only capture a portion of the rock failure events and the results can be easily biased by adopting inaccurate velocity models. Moreover, this technique only focuses on seismic events associated with shear failure (Eisner et al., 2006; Warpinski and Du, 2010), without accounting for fluid and proppant

transport. Therefore, this technique provides very limited insight into the propped fracture geometry, which is the main factor controlling the effectiveness of a hydraulic fracturing job.

1.6 FIBER OPTICS

Fiber optic monitoring, including distributed temperature sensing (DTS) and distributed acoustic sensing (DAS), has been shown to be an effective technology to quantify fluid and proppant taken by each cluster in a fracture stage (Sierra et al., 2008; Bhatnagar, 2016; Zhang and Zhu, 2017; Sookprasong et al., 2014). Specifically, DTS measures the temperature change, while DAS monitors acoustic perturbations at the perforations generated by fluid and proppant injection (Fig. 1.5). They are frequently integrated with borehole microseismic monitoring to determine the fracture geometry (Webster et al., 2013; Haustveit et al., 2017).

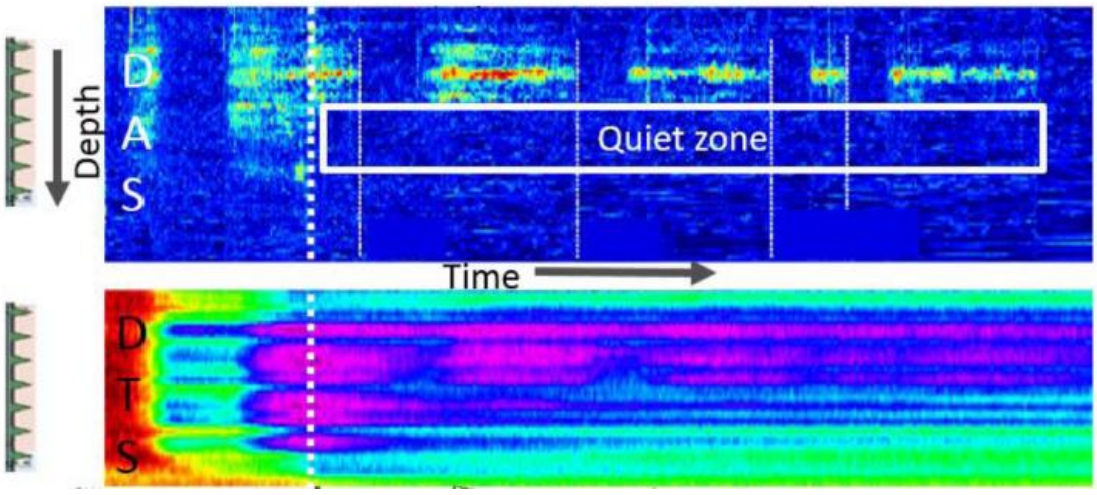

Figure 1.5 DAS and DTS results showing the lack of fluid and proppant entering the toe-side clusters (quite zone). (From Haustveit et al., 2017)

The mechanism behind this technique makes it very effective for assessing the fracturing fluid taken by each cluster, but its ability to evaluate proppant distribution is

still under debate. Indeed, fluid transport is not equivalent to proppant transport. It has been shown that proppants reach only a portion of the induced fractures, depending on numerous factors such as the injection rate and fluid rheology (Blyton et al., 2015). Simulations also show a strong heel bias in the proppant distribution in a majority of the stages (Wu, et al., 2017). Moreover, DTS and DAS are not capable of tracking the lateral extension of the proppant. Hence fiber optic monitoring is not a solution for direct far-field mapping of the proppant distribution.

1.7 ELECTROMAGNETIC AND ELECTRICAL METHODS

So far we have reviewed a few categories of fracture diagnostic methods, mainly based on the physics behind them. Unfortunately, none of these methods can track proppant distribution or map propped fracture geometry directly. Electromagnetic (EM) borehole measurement methods have been proposed to directly map proppants with distinct physical properties (electrical conductivity, magnetic permeability, etc.). Previous research involved open-hole and through-casing multi-component induction measurements (Basu and Sharma, 2014; Fang et al., 2017; Wang et al., 2005; Yang et al., 2015; Yu et al., 2017; Palisch et al., 2016), cross-well tomography (Heagy et al., 2014) and borehole-to-surface resistivity logging (Hoversten et al., 2015; LaBrecque et al., 2016). Out of these methods, low frequency induction tools are the most promising in terms of the depth of investigation, due to the fast decay of EM waves in a conductive rock. Typically the tool is composed of one transmitter and two receiver coils (Fig. 1.6). The transmitter coil transmit EM fields that induce eddy currents in the fracture. This current emits secondary EM fields, which carries the information of the propped fracture geometry and is captured by the receivers. While working well for open-hole completions, these methods are still expected to fail when operated from within a highly

conductive steel casing. This shortcoming significantly limits its applications in the oil and gas industry, since open-hole completions are becoming less common in recent years.

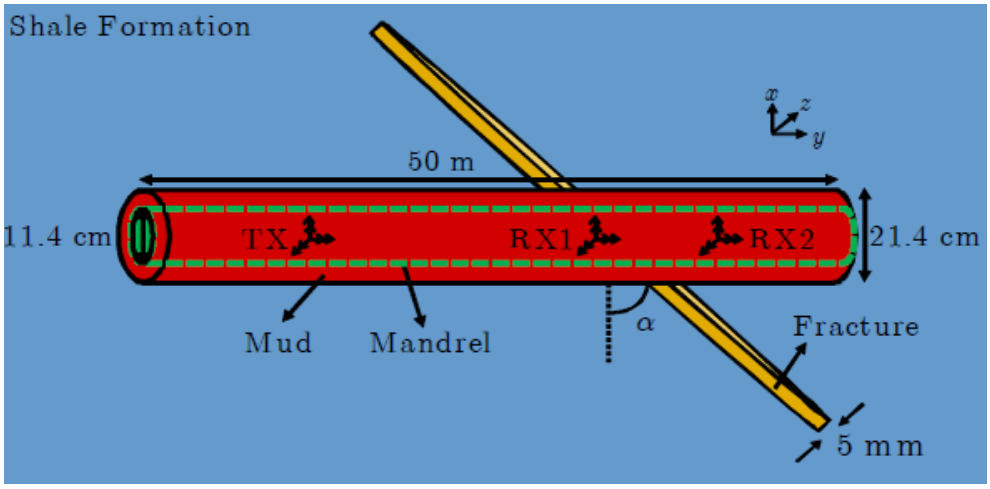

Figure 1.6 A schematic of the low-frequency induction tool for fracture mapping in an open-hole wellbore. (From Yang et al., 2015)

Direct excitation of the casing itself can enable resistivity measurements, while avoiding the through-casing signal attenuation and allowing for characterization of subsurface fractures with elevated conductivity in cased-hole wellbores (Cannan et al., 2015; Weiss et al., 2016). Using this idea, a novel concept of an electrode-based resistivity tool was proposed. It makes use of standard steel casing sections, separated by insulating gaps, and makes measurements in the same well (Gabelmann et al., 2017). Each pair of casing sections, connected by a thin gap section, can be excited independently by a bottom-hole assembly, such that the casing pair acts as a transmitter. When not excited, a casing pair separated by the gap serves as a receiver, recording information on the fractures in contact with the casing. By performing the measurement near the fractures, i.e., downhole rather than on the surface or in an adjacent wellbore, the

concept is expected to mitigate the problem of signal attenuation, leading to much higher signal levels.

This work aims towards developing models and clearly defining the tool concept proposed by Gabelmann et al., 2017, into a field deployable tool. While the tool is being designed and manufactured separately, this work mainly focuses on modeling of borehole resistivity measurements for mapping proppant distribution using the tool. A candidate conductive proppant is also tested in the lab. The following chapters are organized in this manner:

- Chapter 2 introduces a lab setup for measuring electrical resistivity of proppants. A candidate proppant, petroleum coke, is tested to evaluate both its electrical and hydraulic conductivity.
- Chapter 3 discusses the tool geometry and configuration of downhole transmitters and receivers. Then the formulation of the model is presented, followed by verification of these methods.
- Chapter 4 presents forward simulation results that show the tool's sensitivity to fracture's location, conductivity, size, angle, etc.
- Chapter 5 demonstrates the tool's response to multiple fractures, which provides useful information and guidance for inversion analysis.
- Chapter 6 proposes a framework for inverse modeling. A few local and global optimization algorithms, e.g., Very Fast Simulated Annealing, can possibly be the inversion kernel for inverting the measured data.
- Chapter 7 presents a couple of inversion strategies that can effectively extract the propped fracture geometry. Inversion results are shown and the associated uncertainties are evaluated.

- Chapter 8 presents the conclusions of this work and proposes possible directions for future research.

Chapter 2: Electrical Resistivity & Hydraulic Conductivity of Petroleum Coke

2.1 BACKGROUND

As discussed in the last chapter, electromagnetic (EM) methods rely on proppants that demonstrate unique EM properties in high contrast with those of the formation. These properties can be electrical conductivity, electric permittivity, magnetic permeability, etc.

Prior to the developments of field applicable proppants, people have studied 'proppant analogs', which are materials that display unique EM properties but may not be acceptable for injection into deep reservoirs (LaBrecque et al., 2016). For example, steel shots (Symington, et al., 2010) exhibits a high relative permittivity of 10^7 at 100 Hz frequency. Small-scale field experiments at shallow depth indicate that this material shows a significant increase in the intrinsic phase response over that of the background. Coke breeze, as a conductive proppant analog, has been tested as a contrast agent as well. Mixing coke breeze with sand can reduce its consumption while keeping a reasonably high electrical conductivity (LaBrecque et al., 2016). However, the main problem for these materials is the lack of mechanical strength for withstanding high confining stress.

Recent advancements in proppant detection brought up a few new candidates that can potentially be applied in deep wells. Coke-breeze-coated sand slurry was expected to have an effective resistivity as low as $5 \times 10^{-4}\ \Omega \cdot \mathrm{m}$ when the volume of proppant in the slurry is above 70% (Hoversten et al., 2015). A ceramic proppant with an electrically conductive coating possesses the high mechanical strength of ceramic and was tested in a horizontal well 8000 ft deep (Palisch et al., 2016).

Effective Medium Theory was used to estimate the proppants' electrical resistivity (Berryman and Hoversten 2013). A better evaluation of proppant electrical

resistivity requires a general and robust experimental method. Measurements on one or several types of conductive proppants in the lab can provide valuable information for numerical simulations, as well as help in selecting the desired proppant for field applications.

The effective electrical resistivity of the propped fracture is dictated by the proppant conductivity, distribution, as well as by factors such as in-situ stress in the reservoir. To better simulate a realistic situation, an experimental system (or method) for resistivity measurements on proppants should be able to:

- Conduct consistent and accurate measurements on different proppants;
- Apply a high enough confining pressure to simulate downhole conditions;
- Saturate the proppant with different fluids.
- Measure electrical resistivity as well as hydraulic conductivity of the proppant pack.

Although a few candidate proppants have been reported in the literature, the cost of applying these materials in large quantities remains questionable. So another important goal of our work is to find a material that is cheap while exhibiting contrasting EM properties relative to the formation rock. Proppants with high intrinsic conductivity are natural candidates for our application. Petroleum coke (PC), for example, is one such cheap possibility which is easily accessible in the market. It is a byproduct from oil refining with a density of 2.03 $\mathrm{g/cm^3}$ and a particle size of 150 - 400 μm. More than 96% of its composition is carbon, which makes it a good electrical conductor. PC has been used to make anodes for the aluminum, steel and titanium smelting industry. The main scope of this chapter is building a general and effective experimental method, measuring the electrical resistivity of PC and exploring the possibility of mixing it with sand for fracture diagnostics using EM methods.

For field applications, it is also very important to verify that PC (mixed with sand) shows reasonable hydraulic conductivity, especially under high confining stress, in order to be used as a proppant. Some results on PC's hydraulic conductivity under confining stress will also be presented.

2.2 ELECTRICAL RESISTIVITY OF PETROLEUM COKE

2.2.1 Experimental System

People have been using a resistivity core holder (Fig. 2.1) to conduct electrical resistivity/conductivity measurements on well-consolidated cores. The measurements are conducted using a four-point probe method, which minimizes the error introduced by contact resistance.

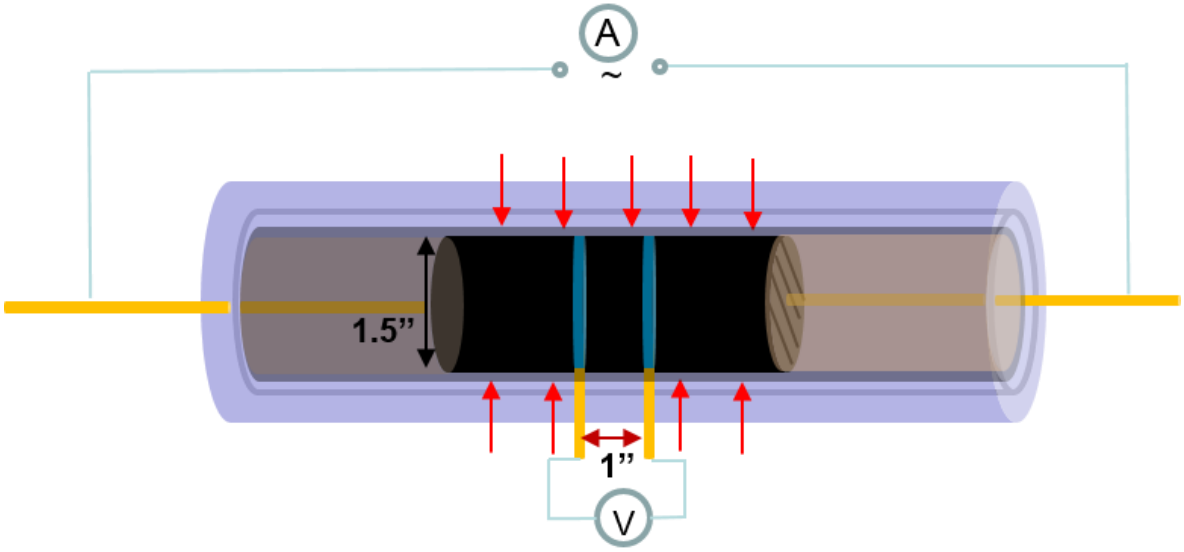

Figure 2.1. Configuration of the resistivity core holder. The yellow bars identify the electrodes, while the black cylinder and the red arrows represent the core and the confining pressure, respectively.

A core with a length of 5.08 cm (2 inches) and a diameter of 3.81 cm (1.5 inches), which is represented by the black cylinder in Fig. 2.1 is wrapped with a rubber sleeve and

constrained by the end pieces of the core holder at both ends. Fluids can be injected through one of the current-carrying electrodes into the core. Confining pressure around the rubber sleeve is applied using a hydraulic pump, in order to prevent the fluid bypassing the core through the gap between the core and the robber sleeve. An alternating current I is applied via the current-carrying electrodes at the two ends. These current-carrying electrodes are isolated from the outer shell of the core holder such that current is forced to flow through the core. A voltage U is measured on the voltage-sensing electrodes in the center (Fig. 2.1). These electrodes are connected to two ring electrodes which are directly in contact with the core. The spacing between the two voltage sensing electrodes is 2.54 cm (1 inch). The measured resistance can be obtained from Ohm's law:

$$R = U/I. \tag{2.1}$$

Assuming that the core with resistance R has cross sectional area A and length L, the resistivity of the core is

$$\rho = R \cdot A/L. \tag{2.2}$$

We proposed to adopt this setup for resistivity measurements on conductive proppants (Zhang et al., 2016). For this purpose, the core in the setup will be replaced by a proppant pack or a fractured core propped by proppant. Due to the fact that the resistivity core holder was initially designed for well consolidated cores, it's necessary to verify that it works properly for unconsolidated grains (e.g., sand or proppant). We used a sand pack which has a porosity of 25.2% for this verification. Brine of different concentrations was injected to saturate the sand pack (S_w=100%) and resistivity measurements were conducted using this resistivity core holder. The brine concentration c, resistivity R_w and measured resistivity of the sand pack R_o are listed in Table 2.1.

c (g/L)	36	70	100	150
$R_w\ (\Omega \cdot m)$	0.18	0.10	0.08	0.06
$R_o\ (\Omega \cdot m)$	0.86	0.54	0.44	0.29

Table 2.1. Measured resistivity of a brine saturated sand pack with respect to different brine concentration.

A plot of R_o VS R_w shows the measured resistivity of the sand pack R_o is proportional to the resistivity of brine that saturates the sand pack (Fig. 2.2). This is consistent with Archie's Law, which demonstrates the relationship between the core resistivity and resistivity of the saturation fluid:

$$R_o = F \cdot R_w. \tag{2.3}$$

The formation factor F for this unconsolidated sand pack is about 4.55. The agreement with Archie's equation (Eq. 2.3) verifies the applicability of this core holder for resistivity measurements of unconsolidated grains.

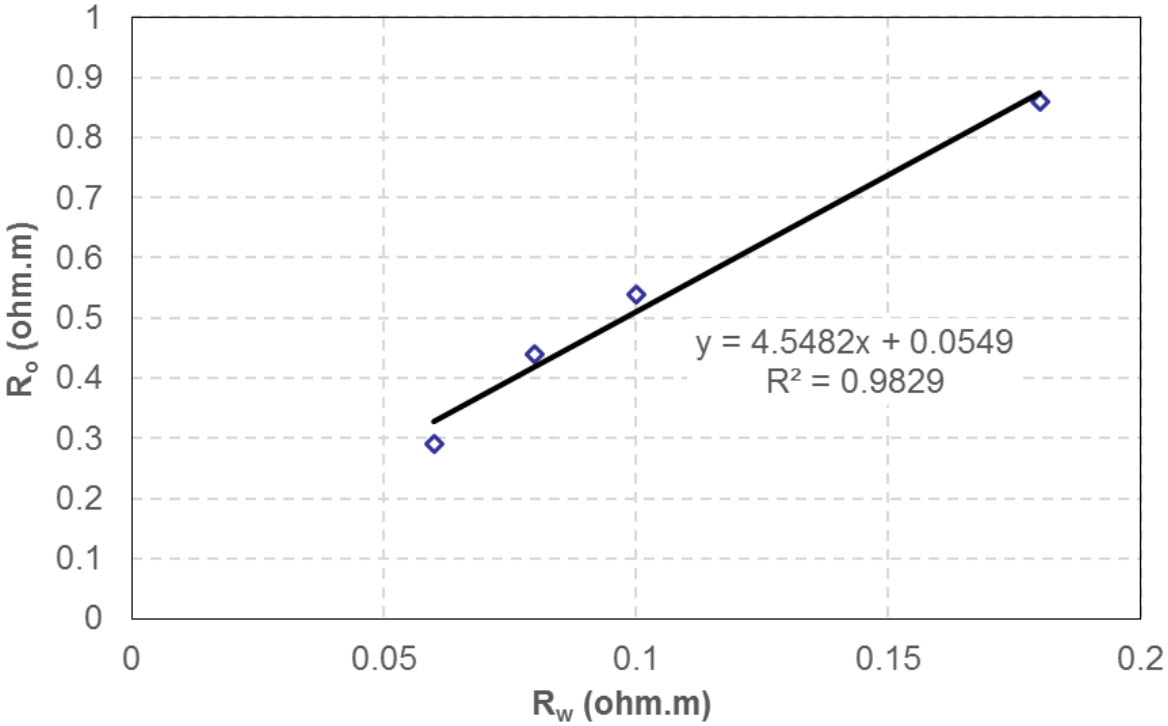

Figure 2.2. The measured resistivity of the sand pack R_o versus the resistivity of brine R_w. A linear relationship is observed.

Next we used the experimental system to conduct resistivity measurements on PC. Our lab measurements mainly focused on this material and all the measurements were performed at room temperature. Although under reservoir conditions fluid temperature will be higher, room temperature experiments are expected to be very predictive, because the effective conductivity is dominated by that of the proppant instead of the fracturing fluid. The proppant resistivity was measured for both a cylindrical pack and a planar thin layer in a simulated fracture created in the core.

2.2.2 Resistivity of Bulk PC

The PC was packed in the rubber sleeve of the core holder with and without brine occupying the void space between the particles (Fig.2.1). In this case, the cross sectional area A equals $\pi D^2/4$, where D is the diameter of the cylinder (1.5 inch) and the length L is 1 inch. The particle size of the PC is 70 – 100 mesh (150 – 210 μm). Eq. 2.2 is used to calculate the electrical resistivity. Fig. 2.3 shows the measured resistivity when no brine is present.

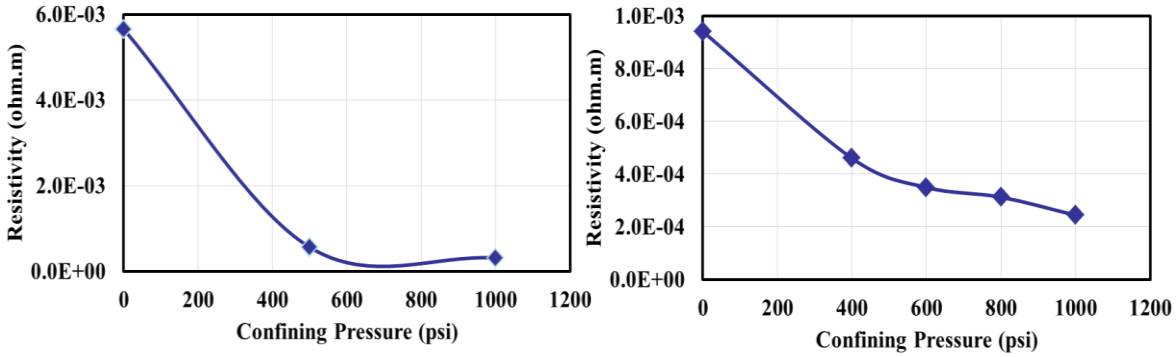

Figure 2.3. Electrical resistivity of the PC pack with respect to confining pressure. No brine is present in these two sets of measurements.

The initial packing condition affects the proppant's resistivity significantly when no extra confining pressure is applied. As shown in Fig. 2.3(a), the measured resistivity is about $6.0 \times 10^{-3}\ \Omega \cdot \mathrm{m}$ when the initial bulk density of PC is 1.14 $\mathrm{g/cm^3}$, which corresponds to a porosity of 43.9%. However, when the initial bulk density is increased to 1.27 $\mathrm{g/cm^3}$ (37.6% porosity), the resistivity decreases to about $1.0 \times 10^{-3}\ \Omega \cdot \mathrm{m}$ (Fig. 2.3(b)). When a confining pressure is applied, the resistivity quickly decreases and reaches a plateau. End point values for Fig. 2.3(a) and Fig. 2.3(b) are $3.2 \times 10^{-4}\ \Omega \cdot \mathrm{m}$ and $2.4 \times 10^{-4}\ \Omega \cdot \mathrm{m}$ at 1000 psi. Even though the two curves have very different starting values, they eventually approach a similar number (Zhang et al., 2016).

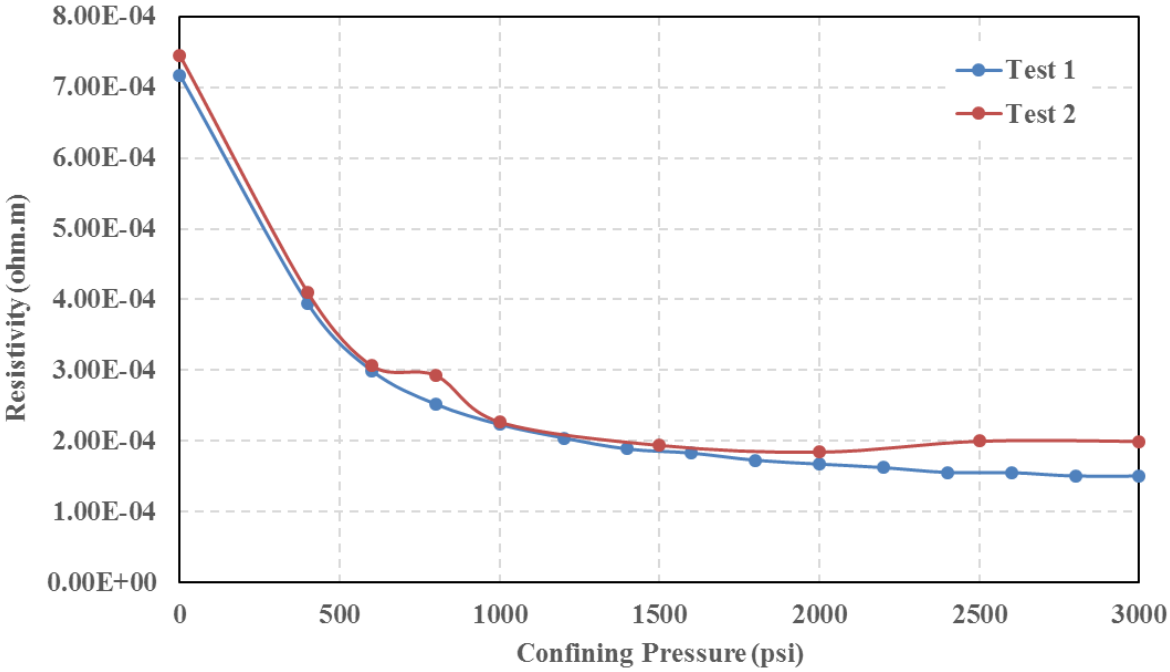

Figure 2.4. Electrical resistivity of the PC pack with respect to confining pressure. Sea water was injected to the pack for both Test 1 and Test 2.

Fig. 2.4 shows two sets of measurements (blue and red curves) with the same initial PC bulk density of 1.27 g/cm^3. As opposed to the measurements shown in Fig. 2.3, here, sea water (35 g/L. NaCl solution) was injected into the proppant pack. Sea water has a resistivity of 0.2 $\Omega \cdot m$ at room temperature, which is several orders of magnitude greater than the resistivity of PC. Hence similar results are expected when sea water fills the void space between the particles. The measured resistivity starts from about $7.0 \times 10^{-4}\ \Omega \cdot m$ when no confining pressure is applied. End point values for Test 1 and Test 2 are 1.5×10^{-4} and $1.9 \times 10^{-4}\ \Omega \cdot m$, as the confining pressure reaches 3000 psi (Fig. 2.4). Note that, unlike the smooth decrease of the blue curve, some humps can be observed in the red curve. We interpret this as the result of the simplification in our calculations: the rubber sleeve shrinks under pressure, which gives us an apparent higher resistivity because the change of the cross sectional area is not accounted for in the calculations (Zhang et al., 2016). Shrinking of the rubber sleeve also leads to the break of the seals on the core holder and therefore leaking occurs as the confining pressure increases. Higher confining pressures could be achieved with sea water (Fig. 2.4 compared to Fig. 2.3).

Apart from the intrinsic conductivity, the contact between the PC particles is the most important factor that controls the pack's resistivity. This justifies the role that initial bulk density plays. As the confining pressure increases, the contact improves, which leads to a lower resistivity. However, as the confining pressure rises to ~1000 psi this effect reaches the saturation point, thereby explaining why all the results converge at high confining pressure to the same value of ~$2 \times 10^{-4}\ \Omega \cdot m$.

2.2.3 Resistivity of PC in a Fracture

A second set of measurements was conducted on the proppant in a fractured sandstone core, mimicking proppant in a hydraulic fracture. The core has the same dimensions as that of the proppant pack in Subsection 2.2.1 and the initial fracture width w_f is set to be 3 mm (Fig. 2.5). Confining pressure was applied as well. PC of particle size 40 – 70 and 70 – 100 mesh, corresponding to 210 – 420 and 150 -210 μm were used. In order to explore the possibility of using a mixture of PC and sand in the field, a few combinations of these two materials (0 wt% sand, 25 wt%, 50 wt% and 75 wt% sand) were tested. Again Eq. 2.2 is used to calculate the electrical resistivity. The cross sectional area A in this case is $D \cdot w_f$.

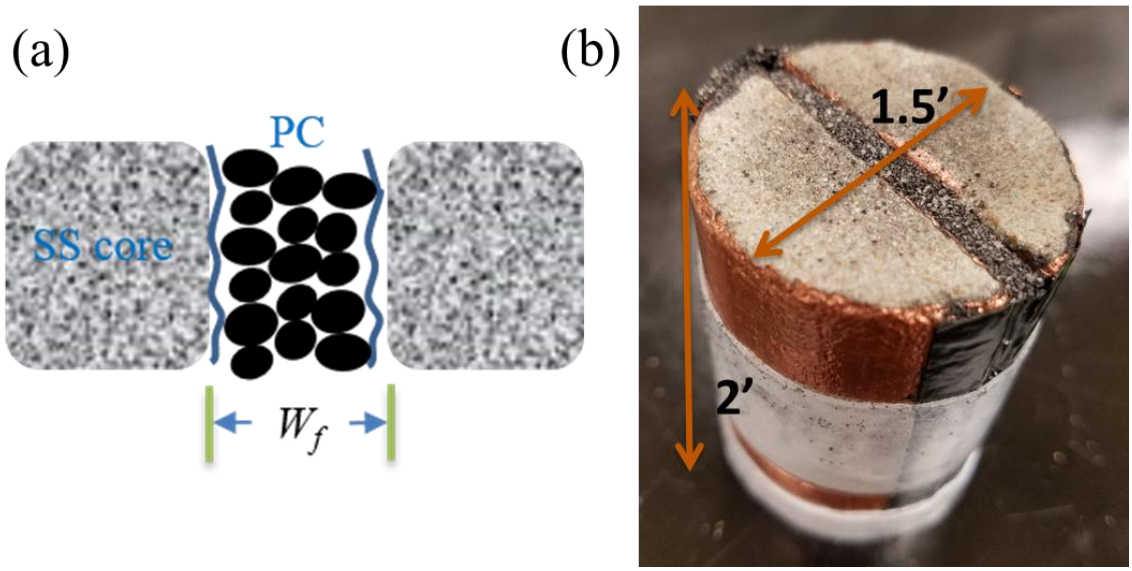

Figure 2.5. (a) A schematic of proppant in a fracture of width w_f. (b) A fractured sandstone core propped by PC. The core length and diameter are 2' and 1.5', respectively.

For the PC with particle size of 210 – 420 μm (40 – 70 mesh), no sea water was injected in the test. The measured electrical resistivity at various confining pressure is shown in Fig. 2.6 and 2.7. Different curves represent the resistivity of PC mixed with

different proportions of sand. The O-ring seal at the voltage sensing electrodes of the core holder is not very consistent, due to the deformation of the rubber sleeve at elevated pressures. The end point pressure on different curves denote the highest confining pressure achieved before leak happens. The end point values of the measured resistivity are listed in Table 2.2.

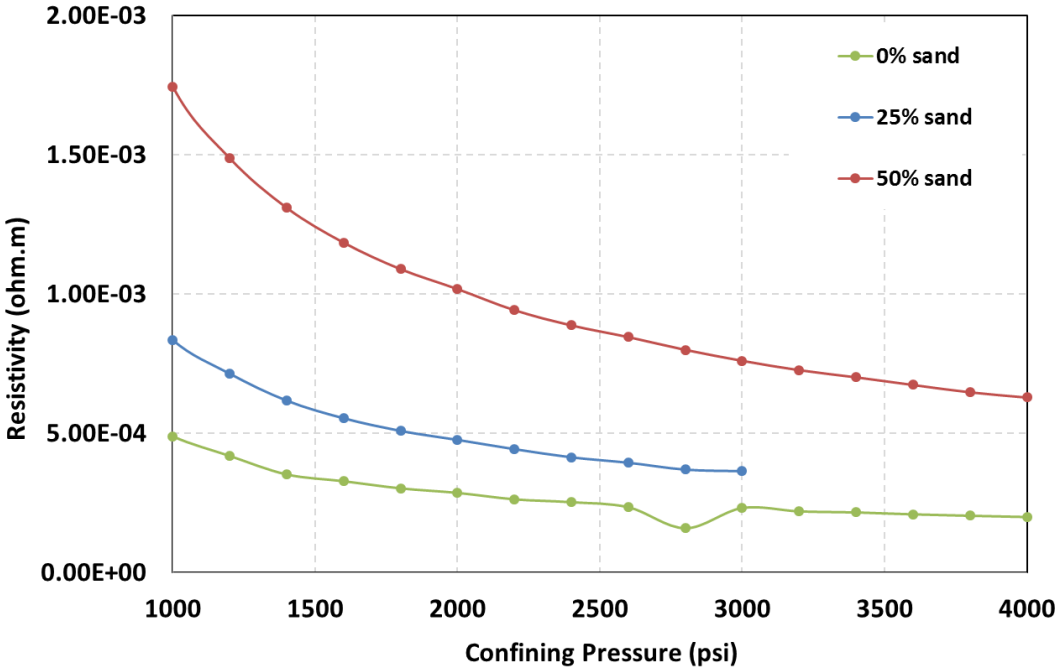

Figure 2.6. Measured resistivity of PC (40 – 70 mesh) at various confining pressures. The green, blue and red curves represent the PC mixed with 0%, 25% and 50% sand, respectively.

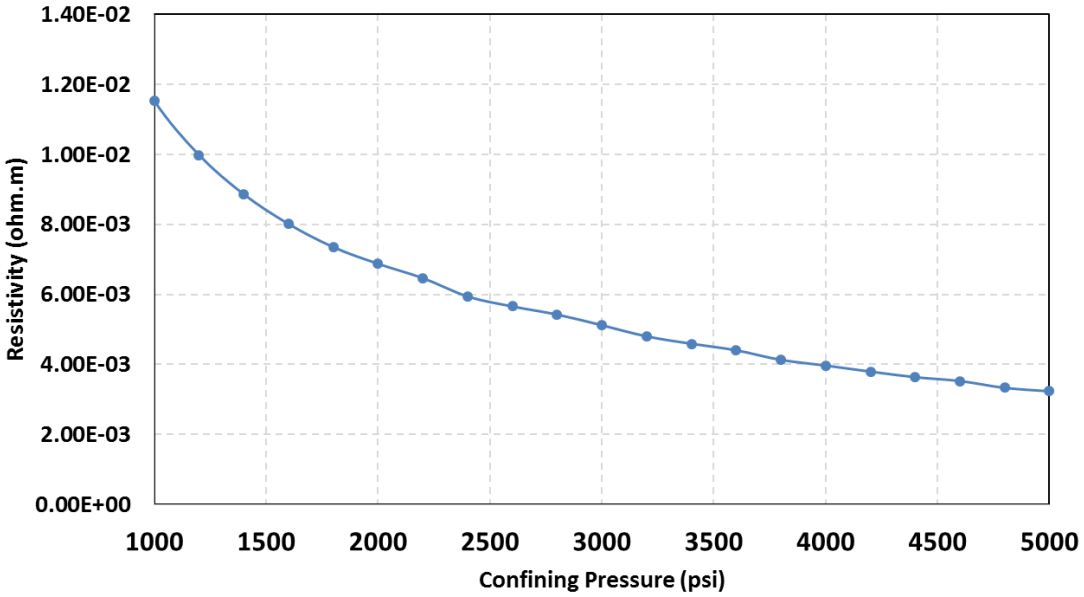

Figure 2.7. Measured resistivity of PC (40 – 70 mesh) mixed with 75% sand at various confining pressures.

0% sand	$1.99 \times 10^{-4}\ \Omega \cdot m$ @4000 psi
25% sand	$3.64 \times 10^{-4}\ \Omega \cdot m$ @3000 psi
50% sand	$6.28 \times 10^{-4}\ \Omega \cdot m$ @4000 psi
75% sand	$3.24 \times 10^{-3}\ \Omega \cdot m$ @5000 psi

Table 2.2. The measured electrical resistivity of the PC (40 – 70 mesh) -sand mixture at different confining pressure.

Similar to the results of the proppant pack, for a given composition of PC-sand mixture, the electrical resistivity decreases with an increasing confining pressure, due to a better contact between the PC particles. The electrical resistivity of pure PC is $1.99 \times$

$10^{-4}\ \Omega \cdot m$ under a confining pressure of 4000 psi, which is close to that of a PC pack (Fig. 2.6). This resistivity is about four orders of magnitude lower than the typical resistivity of shale, which makes it a suitable candidate that can be tracked using EM methods.

As the weight percentage of sand increases, the effective resistivity of the mixture increases. This is because sand, as a very resistive material, fills the gap between the PC particles and prevents the direct contact between them. The effective resistivity of the mixture is quite low till 50% sand is mixed with PC (Fig. 2.6). However, when the weight percentage of sand reaches 75%, the measured resistivity is substantially higher ($3.24 \times 10^{-3}\ \Omega \cdot m$ at a confining pressure of 5000 psi), which will impact its effectiveness in field applications (Fig. 2.7).

The PC with a smaller particle size of 150 -210 μm (70 -100 mesh) was also tested (Fig. 2.8 and 2.9). Sea water was injected to saturate the proppant, in order to achieve a higher confining pressure. Since the minor effect of sea water on the effective resistivity of the proppant has been verified in 2.2.1, the difference in the measured resistivity (if there's any) will be attributed to the smaller particle size in this set of measurements.

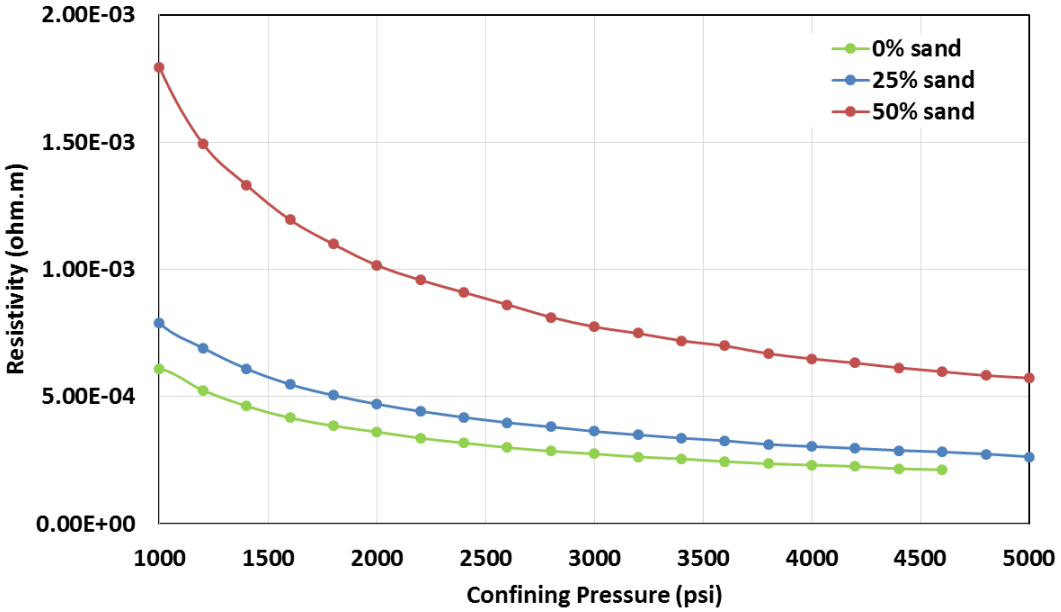

Figure 2.8. Measured resistivity of PC (70 – 100 mesh) at various confining pressures. The green, blue and red curves represent the PC mixed with 0%, 25% and 50% sand, respectively.

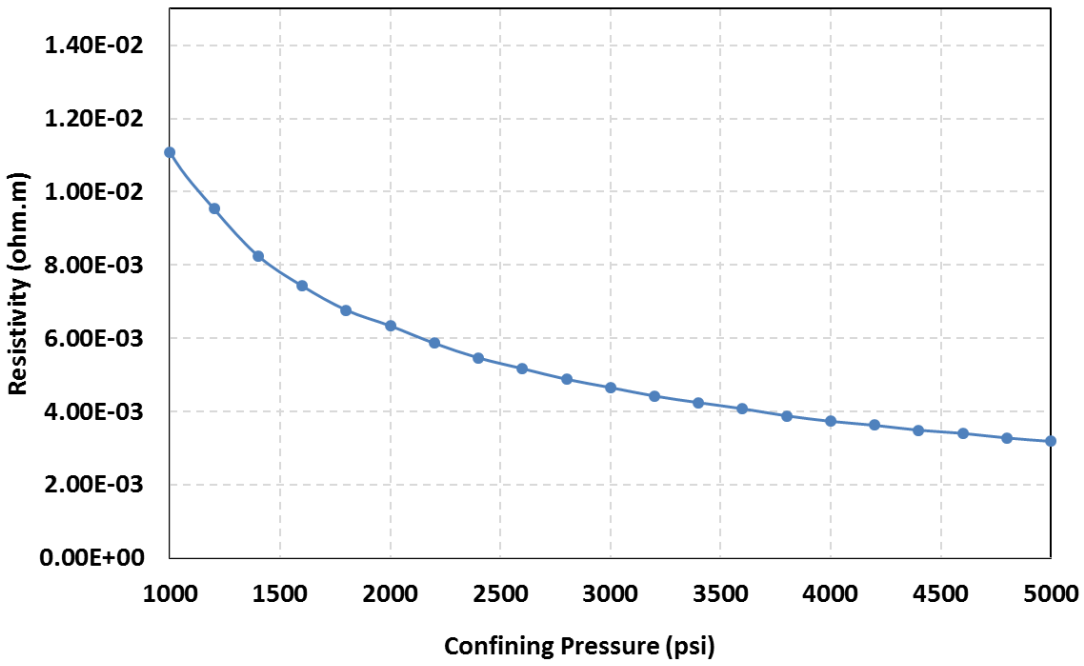

Figure 2.9. Measured resistivity of PC (70 – 100 mesh) mixed with 75% sand at various confining pressures.

The results show a few similarities to the ones obtained on the PC with a larger particle size. The end point values of the measured resistivity are listed in Table 2.3. The measured resistivity of different PC-sand mixture at high pressure remains close to the previous results, which means the particle size doesn't affect the effective resistivity much. Again, the mixture stays highly conductive when up to 50 wt% sand is added. However, when 75 wt% sand is added, the electrical resistivity is one order of magnitude higher, which makes it questionable for field applications.

0% sand	$2.12 \times 10^{-4}\ \Omega \cdot m$ @4600 psi
25% sand	$2.64 \times 10^{-4}\ \Omega \cdot m$ @5000 psi
50% sand	$5.73 \times 10^{-4}\ \Omega \cdot m$ @5000 psi
75% sand	$3.18 \times 10^{-3}\ \Omega \cdot m$ @5000 psi

Table 2.3. The measured electrical resistivity of the PC (70 – 100 mesh) -sand mixture at different confining pressure.

2.3 HYDRAULIC CONDUCTIVITY OF PETROLEUM COKE

2.3.1 Experimental System

We measured the conductivity of fractures propped by PC (or PC – sand mixture) using an experimental method described in Fig. 2.10. The application of this system for fracture conductivity measurements has been reported earlier (Wu, et al., 2017). A Berea sandstone core of 1'' diameter by 8'' length was prepared with a fracture width of 1mm. The fracture was filled with proppant and then the core was placed inside a Hassler

sleeve core holder and evacuated to remove trapped air. Confining closure stress was applied for 24 hours. After that a 3% brine solution was pumped from the accumulator through the core at a range of constant flow rates Q. For each closure stress applied, the pressure drop ΔP across the core was measured and used to calculate the fracture conductivity using Darcy's Law

$$Q = \frac{k_f \cdot w_f \cdot D}{\mu} \cdot \frac{\Delta P}{L}, \tag{2.4}$$

where w_f, D and L represent the fracture width, core diameter and length, respectively, and k_f and μ stands for the fracture permeability and fluid viscosity.

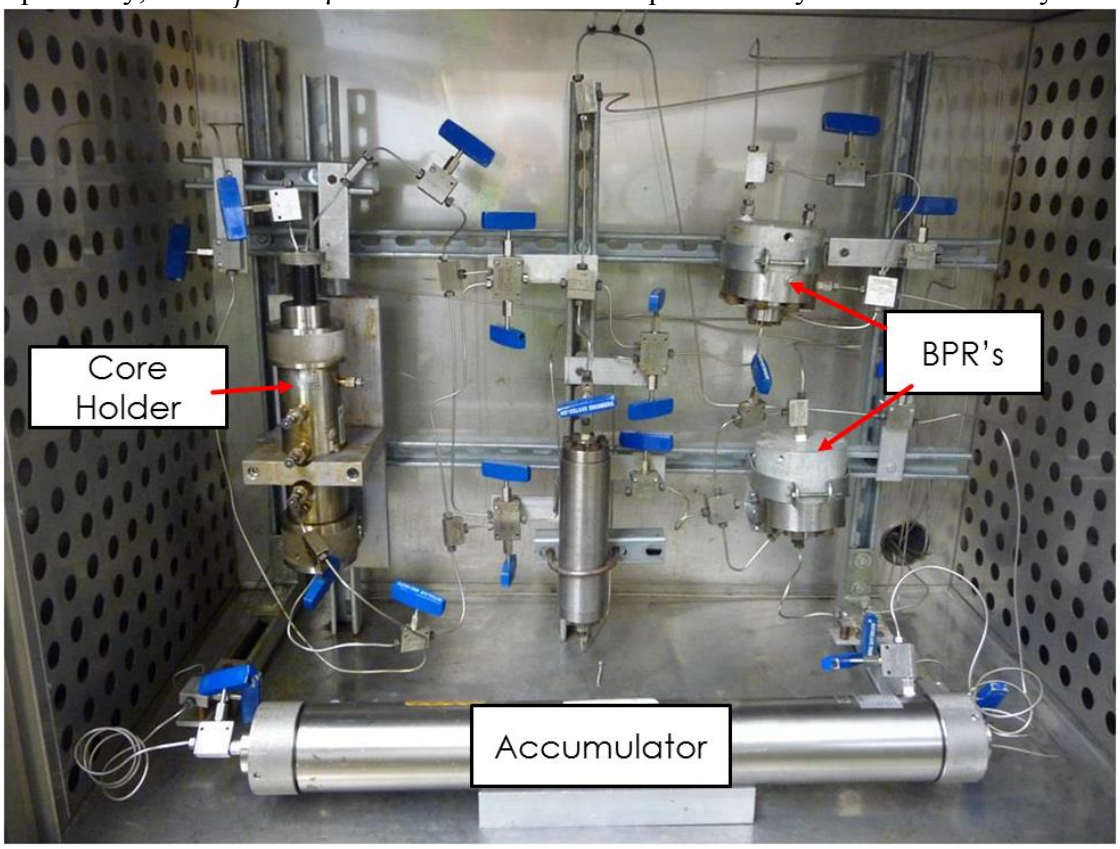

Figure 2.10. Experimental method for fracture conductivity measurements. Fluid is injected from the accumulator into the core. The back pressure regulators (BPR's) are used to adjust the flow rates. A confining stress is applied on the core.

2.3.2 Hydraulic Conductivity of PC in a Fracture

Pure PC, pure sand with the same particle size and PC – sand mixtures are tested for comparison. The measured fracture conductivity $k_f \cdot w_f$ for 40 – 70 mesh and 70 – 100 mesh proppants are shown in Fig 2.11 and 2.12. Fig. 2.11 (b) and Fig. 2.12 (b) are the normalized fracture conductivities with respect to the ones under 2000 psi closure stress. For both cases, as the weight percentage of sand increases, the measured fracture conductivity under a given confining stress increases. This indicates sand has a higher mechanical strength or lower compressibility than PC does. The actual mechanism for this phenomenon should be explored in the future by conducting mechanical tests on the sand and PC particles. Comparison between Fig. 2.11 and 2.12 indicates the fracture propped by 40 – 70 mesh grains has an overall higher conductivity.

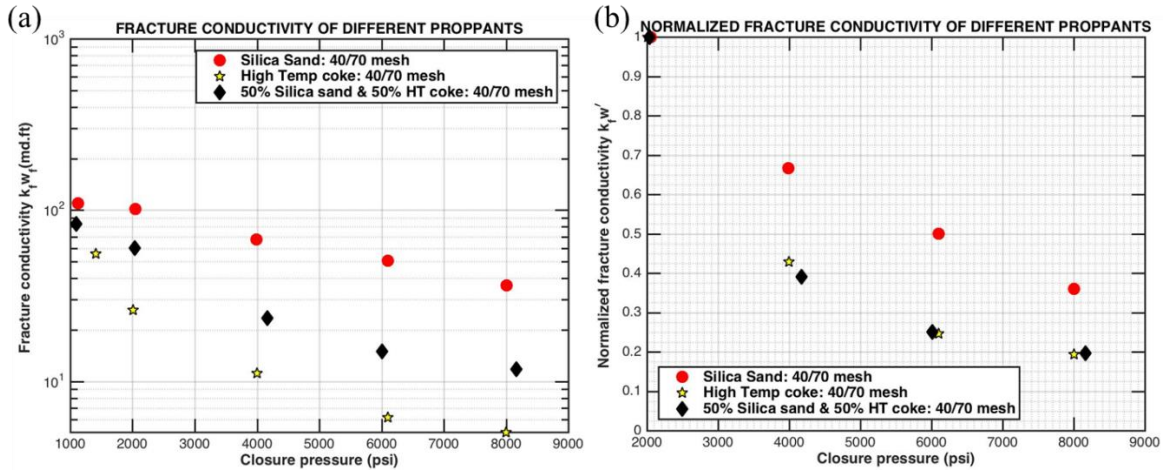

Figure 2.11. (a) The measured fracture conductivities for different proppants (40 – 70 mesh) at various confining stresses. (b) Fracture conductivities normalized by the ones under 2000 psi confining stress.

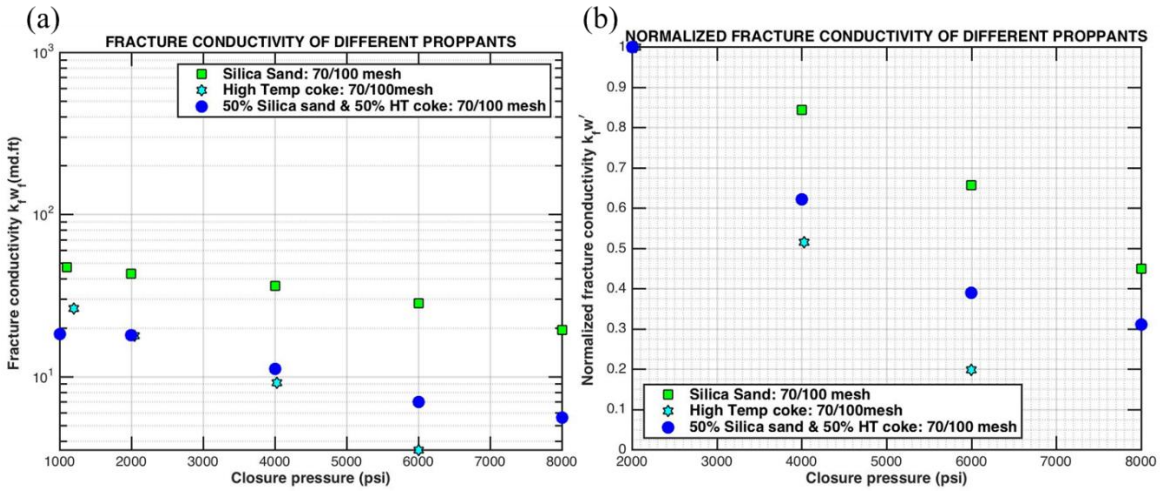

Figure 2.12. (a) The measured fracture conductivities for different proppants (70 – 100 mesh) at various confining stresses. (b) Fracture conductivities normalized by the ones under 2000 psi confining stress.

To better interpret the results, we calculate the dimensionless fracture conductivity by assuming a matrix permeability of 10^{-4} md and a fracture half-length of 250 ft. For the worst case observed, when pure PC (70 – 100 mesh) is under a confining stress of 6000 psi, the measured fracture conductivity is about 4 $\text{md} \cdot \text{ft}$. The corresponding dimensionless fracture conductivity is $F_{CD} = (k_f \cdot w_f)/(L_f \cdot k_{matrix}) = 160$. Using this value in a few fracture productivity models (e.g., Friehauf and Sharma (2009) and Prats (1961)), it can be concluded that the stimulation ratio J/J_0 reaches a maximum, which means the fracture is already infinitely conductive (Fig.2.13). Therefore, application of PC (or PC – sand mixture) for fracture diagnostics using EM methods will also assure the productivity of the fractured well.

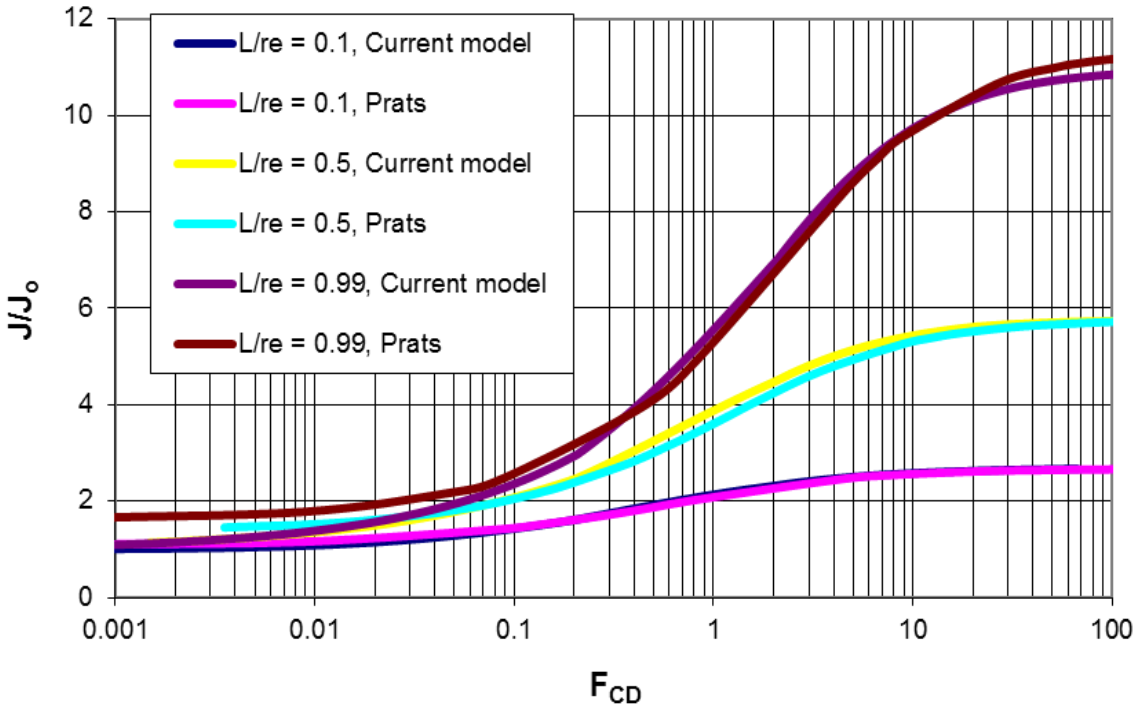

Figure 2.13. Stimulation ratio versus dimensionless fracture conductivity from two models. 'Current model' and 'Prats' represents Friehauf's and Prats's model, respectively.

2.4 CONCLUSION

A resistivity core holder was used to measure the electrical resistivity of a candidate proppant (PC) with different particle size. The results show that the effective resistivity of the proppant decreases as the confining stress increases, due to the better contact between the PC particles under higher stress. Pure PC shows an electrical resistivity of around $2 \times 10^{-4}\,\Omega \cdot m$ when the confining stress is above 3000 psi. Particle size does not play a noticeable role in the measured results. When sand is mixed with PC, the effective resistivity increases with an increasing weight percentage of sand. This is because sand, as a non-conductive material, prevents the direct contact between PC particles and changes the current path. The electrical resistivity stays reasonably low

(~$6 \times 10^{-4}\ \Omega \cdot m$) when up to 50% sand is added. This is of great significance because in field applications, when a huge quantity of proppant is pumped, adding sand can reduce the consumption of PC and therefore, the cost of hydraulic fracture operations.

Fracture conductivity measurements on PC show that when sand is added, the measured fracture conductivity increases, probably because the higher mechanical strength of sand. Even using pure PC, the measured fracture conductivity is above 4 md · ft under confining stress of 6000 psi, which means the fracture is infinitely conductive for a general field-scale fracture. Therefore, PC is a good candidate for fracture diagnostics not only due to its low electrical resistivity, but also due to its high conductivity to fluid flow.

Notice that when more sand is mixed with the PC, it leads to a trade-off between a higher electrical resistivity and a higher fracture conductivity. When applying this proppant in the field, the ratio of PC to sand should be tailored according to the field conditions (e.g., reservoir depth and in situ stresses) to assure the fractures propped by this proppant is conductive enough to both current and fluid flow.

NOMENCLATURE

R = resistance, Ω

U = voltage, V

I = current, A

ρ = electrical resistivity, $\Omega \cdot \mathrm{m}$

A = area, m^2

L = length, m

R_o = resistivity of a core saturated by brine, $\Omega \cdot \mathrm{m}$

R_w = resistivity of brine, $\Omega \cdot \mathrm{m}$

F = formation factor

Q = flow rate, cc/s

k_f = permeability, darcy

w_f = fracture width, cm

D = core diameter, cm

μ = fluid viscosity, cp

ΔP = pressure drop, atm

F_{CD} = dimensionless fracture conductivity

Chapter 3: Tool Configuration and Numerical Methods

3.1 BACKGROUND

Electromagnetic (EM) borehole measurement methods have been proposed to directly map proppants with distinct physical properties (electrical conductivity, magnetic permeability, etc.). However, they are severely limited in cased wellbores, due to the fast decay of EM waves in conductive media. Direct excitation of the casing itself can enable resistivity measurements, while avoiding through-casing signal attenuation and allowing for characterization of subsurface fractures with elevated conductivity in cased wellbores.

Borehole-to-surface experiments by exciting the entire casing string have been simulated to demonstrate the capability for fracture detection and reservoir monitoring (Weiss et al., 2016; Everett and Schultz, 1996; Mackie et al., 1993; Newman and Alumbaugh, 1995). The novel concept of an electrode-based resistivity tool that makes use of standard steel casing sections, separated by insulating gaps, and makes downhole measurements in the same well was first introduced by our research group (Gabelmann et al., 2017). Each pair of casing sections connected by a thin gap section can be excited independently by a bottom-hole assembly (BHA), such that a pair of casing sections acts as a transmitter. When not excited, the same gap can serve as a receiver, recording information while other pairs of casing sections act as transmitters. By performing the measurement near the fractures, i.e., downhole rather than on the surface or in an adjacent wellbore (Cannan et al., 2015; Weiss et al., 2016), this concept also mitigates the problem of signal attenuation, leading to much higher signal levels (0.01 mV to 100 mV) than those observed ($0.1 - 20\ \mu V$) in surface measurements (Weiss et al., 2016).

To simulate the tool's response from downhole EM surveys the governing electromagnetic equations need to be solved fast and accurately. The underlying equations for the general 3-D problem need to be solved using numerical methods, such

as finite differences (Haber et al., 2000; Jin, 2011), finite element methods (Um et al., 2015; Weiss et al., 2016; Lou and Jin, 2006; Jin, 2015) and the method of moments (Gibson 2014; Yang et al., 2015). The problem involves different spatial resolutions in different parts of the domain and multiple regions of highly varying electrical conductivity. Therefore, special care needs to be taken to assure stability of the solutions and to enforce the continuity of electric potential and normal current across the interfaces. We propose a finite difference method, which can discretize the computation domain on a structured or unstructured mesh, to solve the governing equation iteratively. The continuity of electric potential and normal current across the interfaces are enforced by harmonic interpolation of the electrical conductivity on all the cell faces.

3.2 CONFIGURATION OF DOWNHOLE TRANSMITTER AND RECEIVER

An array of specialized insulating gap sub sections (subs, 2 cm long) is placed between standard casing sections (9 m long) and cemented in place as a permanent part of the casing string (Fig.3.1). These gap subs are designed with inner and outer diameters identical to those of the steel casing collars that are commonly used in any string of casing. Each gap (together with its two neighboring casing sections) can function both as a transmitter and as a receiver. The wellbore is assumed to be filled with resistive drilling mud. Before and after hydraulic fracturing operations are completed, a bottom-hole assembly (BHA) is run inside the casing in the fractured zone, on coiled tubing. The BHA is referred to as an EDRIVE. When passing by an insulating gap, the BHA imposes a low frequency or static (DC) voltage U_0 across it by straddling the inner wall of the gap's two neighboring casing sections, effectively forming a transmitter composed of a positive and a negative electrode (Fig. 3.1). The formation draws electric current directly from these two conductive casing sections. If one or more fractures propped by highly

conductive proppant are connected to the casing, they effectively extend the electrodes, which drives more current into the formation. While a voltage is imposed across the transmitter gap, the voltages across the other insulating gaps, e.g., U_{-1}, U_{-2}, U_1, are recorded by the electronics embedded in the gap subs, and stored (Fig. 3.1). These data sets are later retrieved by the BHA, after all the voltage excitations have been applied across each of the gap subs. When the BHA returns to the surface, the data are downloaded and processed.

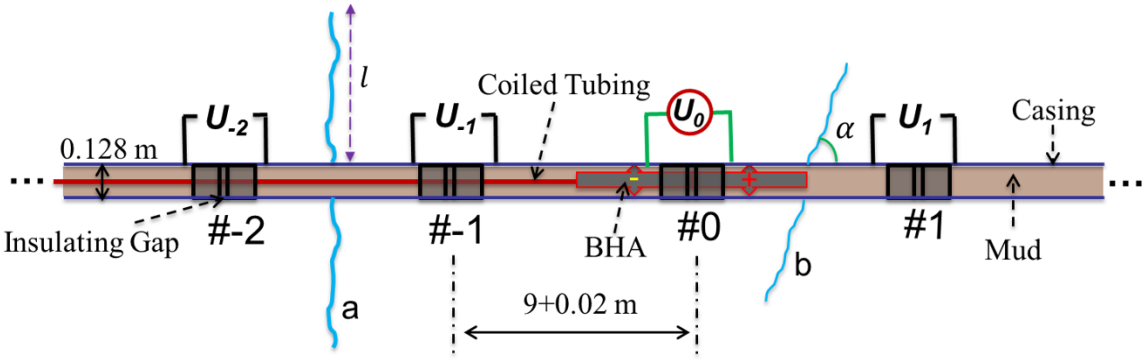

Figure 3.1. A schematic of the tool. Inside the well are the coiled tubing and BHA. The numbered blocks indicate insulating gaps. The transmitter gap is denoted #0 and the remaining gaps (receivers) are numbered accordingly. The curved lines 'a' and 'b' depict hydraulic fractures with different geometries.

With the installation of insulating gap subs, current flow directly through the highly conductive steel casing is prevented. Instead, the presence of the gaps "forces" the current into the formation. Conductive fractures that are directly in contact with the casing offer a path for the current into the formation. Due to the fractures' large surface area, they modify the current distribution and result in different measured voltages across the receiver gaps, compared to the case when fractures are absent. The deviation from the no-fracture case depends on the fracture geometry, and this enables us to invert the

measurements to infer the fracture geometry using deterministic or stochastic inversion techniques.

3.3 FORWARD MODEL FORMULATION

The governing equation for modeling the resistivity problem at zero (or low) frequency is,

$$\nabla \cdot \left(\sigma(\boldsymbol{X})\nabla\Phi(\boldsymbol{X})\right) = \nabla \cdot \boldsymbol{J_s}, \tag{3.1}$$

where $\Phi(\boldsymbol{X})$ and $\sigma(\boldsymbol{X})$ are the scalar electric potential and conductivity as a function of the position vector $\boldsymbol{X}$, respectively. Note that the electrically conductive materials in this work are assumed isotropic. Also in Eq. 3.1, J_s stands for the impressed excitation current density. In this work, a current source is imposed in the following validation cases and the current source is represented by a Neumann boundary condition (fixed gradient) at the source location. However, for describing the electrode-based tool, a voltage source excitation is applied by imposing a Dirichlet boundary condition. For both cases, the equation to be solved simplifies to the Laplace equation $\nabla \cdot \left(\sigma(\boldsymbol{X})\nabla\Phi(\boldsymbol{X})\right) = 0$. The boundary and initial conditions for the different cases will be specifically explained when they appear later.

This forward model equation is solved for the unknown electric potential $\Phi(\boldsymbol{X})$, , by using FVM (Versteeg and Malalasekera, 2007) in a finite computation domain containing the well, fractures, and the surrounding formation. The measured voltage across each receiver gap is the computed potential difference on the casing sections across the receiver gap. The electrical conductivities $\sigma(\boldsymbol{X})$ of the well, fractures, and the formation are defined accordingly, to appropriately represent the different materials in the computation domain. The Laplace equation $\nabla \cdot \left(\sigma(\boldsymbol{X})\nabla\Phi(\boldsymbol{X})\right) = 0$ can be discretized on a structured or unstructured mesh (Fig. 3.2(a), (b)), with the discrete sets of unknown

electric potential Φ and known electrical conductivity, σ values, defined at the centers of volumetric cells (c), and discrete values of the gradient of the potential $\nabla\Phi$ defined on the centers of each cell's P faces (f(1), f(2)…) (Fig. 3.2(c)). Over each cell, the FVM constructs a discretized form of the local integral equation

$$\iiint_V \nabla \cdot (\sigma_c \nabla \Phi_c) dv = 0. \tag{3.2}$$

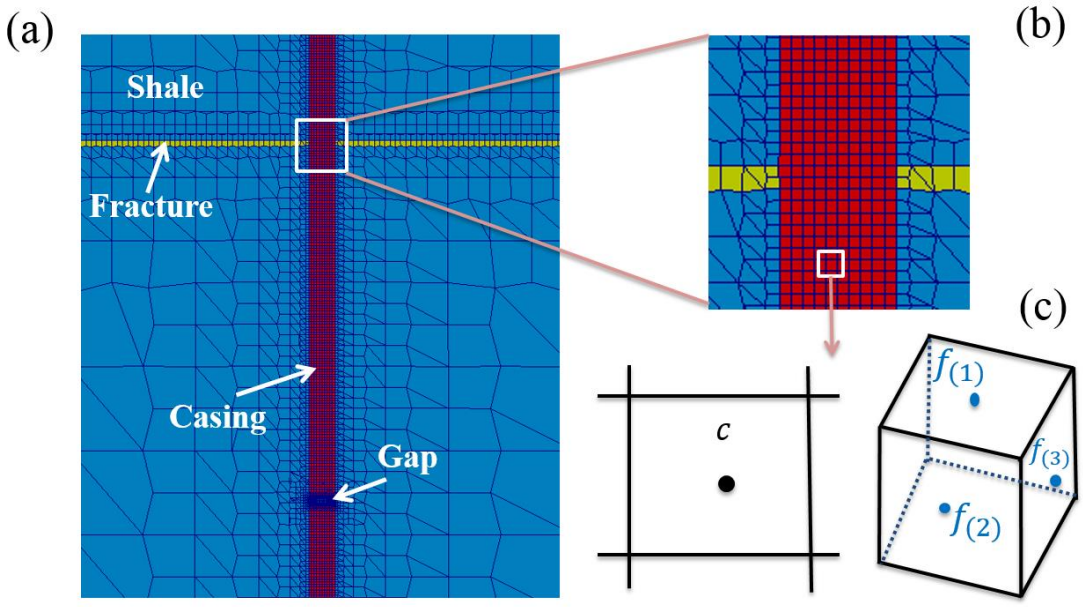

Figure 3.2. (a) The computation domain containing the well, fracture and the surrounding formation is discretized using an unstructured mesh. (b) An enlarged view of the mesh around the well and the fracture. (c) A volumetric cell (right) and its cross-section (left). c indicates the cell center, on which the unknown potential Φ is defined, and $f_{(i)}$ is the center of the ith face of the cell.

The volume integral in Eq. 3.2 can be converted to a surface integral by applying Gauss' divergence theorem, such that

$$\iint_S (\sigma \nabla \Phi) \cdot \boldsymbol{ds} = \sum_{p=1}^{P} \boldsymbol{S}_{f(p)} \cdot (\sigma_{f(p)} \nabla \Phi_{f(p)}) = 0, \tag{3.3}$$

where $\nabla\Phi_{f(p)}$, defined on a face center, is approximated by central differencing from the two unknown potentials defined at two neighboring cell centers. The conductivity value $\sigma_{f(p)}$ assigned to each face center is calculated by taking the harmonic average of electrical conductivities defined at the centers of two neighboring cells.

3.4 HARMONIC INTERPOLATION AND NON-ORTHOGONALITY CORRECTION

The interface condition, which is the continuity of electrical potential and normal current is the most important multi-material boundary condition to satisfy in our problem. Haber et al. (2000) has shown that taking a harmonic average of the electrical conductivity can automatically guarantee the continuity of the electric potential and normal current across the interfaces (e.g., the interface between fracture and shale background) when solving an EM problem using the finite volume method (FVM). We demonstrate this by the following example, in which we assume a 2D structured mesh.

Suppose there's an interface i, across which the electrical conductivities σ_{ia} and σ_{ib} defined at two cell centers P and N are different. The distances from P and N to the interface are δ_{an} and δ_{bn}, respectively (Fig. 3.3). On the {left, right} side of the interface the electric potential and normal current are denoted by subscripts $\{ia,\ ib\}$. The continuity conditions can be written in the following form:

$$\Phi_{ia}=\Phi_{ib} = \Phi_i, \tag{3.4}$$

$$(\sigma \cdot \nabla\Phi_n)_{ia}= \ (\sigma \cdot \nabla\Phi_n)_{ib} = J_{ni}. \tag{3.5}$$

The normal currents on both sides can be approximated using a finite difference method

$$(\sigma \cdot \nabla\Phi_n)_{ia} = \frac{\sigma_{ia}(\Phi_{ia}-\Phi_P)}{\delta_{an}}, \tag{3.6}$$

$$(\sigma \cdot \nabla\Phi_n)_{ib} = \frac{\sigma_{ib}(\Phi_N-\Phi_{ib})}{\delta_{bn}}. \tag{3.7}$$

The electric potential on both sides next to the interface can be solved by combing Eq. 3.4 – 3.7 and it can be expressed in the following

$$\Phi_i = \frac{\sigma_{ib}\delta_{an}\Phi_N + \sigma_{ia}\delta_{bn}\Phi_P}{\sigma_{ia}\delta_{bn} + \sigma_{ib}\delta_{an}}. \tag{3.8}$$

Substituting this solution back into Eq. 3.6 or 3.7, we can solve for the normal current across the interface:

$$J_{ni} = \frac{\sigma_{ia}\sigma_{ib}(\delta_{an}+\delta_{bn})}{\sigma_{ia}\delta_{bn}+\sigma_{ib}\delta_{an}} \cdot \frac{\Phi_N - \Phi_P}{(\delta_{an}+\delta_{bn})} = \sigma_f \cdot \frac{\Phi_N - \Phi_P}{(\delta_{an}+\delta_{bn})}, \tag{3.9}$$

where $\sigma_f = \frac{\sigma_{ia}\sigma_{ib}(\delta_{an}+\delta_{bn})}{\sigma_{ia}\delta_{bn}+\sigma_{ib}\delta_{an}}$ is the harmonic average of the electrical conductivities defined at the centers of two neighboring cells.

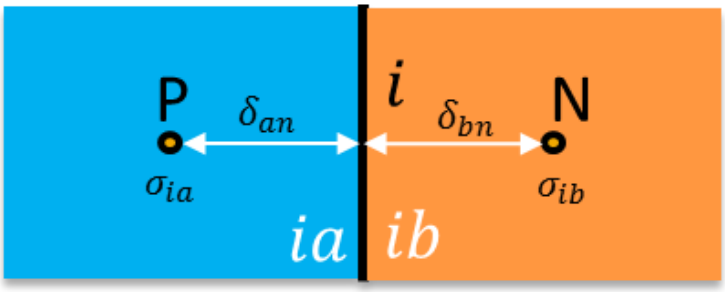

Figure 3.3. Harmonic interpolation of electric conductivity on the interface ensures the continuity of electric potential and normal current.

There are two main sources of numerical errors when solving a problem using finite volume methods. The first type is a consequence of estimating derivatives using numerical schemes that are lower than second-order accurate. The second type is caused by the finite size of the discrete elements in the computation domain (directly related to

the mesh size and quality). The numerical schemes for the finite volume method used in this work are second-order accurate. This still creates higher-order errors. However, numerical errors from the non-orthogonality of the mesh in this work are more pronounced and they have to be corrected for to obtain more accurate solutions.

To simulate the tool's response we have to solve the governing Eq. 3.1 in a computation domain containing the well, fracture, formation, etc. Some small objects such as the thin fracture and the casing require an unstructured and non-orthogonal mesh to capture these fine features. This practice, however, introduces numerical errors when calculating the gradient in Eq. 3.3 (Jasak, 1996). Take cell 6 and 7 on a non-orthogonal mesh as an example (Fig. 3.4). In this case the line joining the two cell centers is no longer perpendicular to the face f. Therefore, calculating the normal current $\boldsymbol{S} \cdot (\nabla\Phi_{\boldsymbol{f}})$ on face f simply by using $|\boldsymbol{S}| \cdot (\Phi_7 - \Phi_6)/|d|$ introduces an error. In fact, the surface normal vector $\boldsymbol{S}$ can be decomposed to an orthogonal component $\boldsymbol{\Delta}$, which is parallel to d, and a non-orthogonal component $\boldsymbol{k}$ (Fig. 3.4). This splits the normal current on face f into two parts:

$$\boldsymbol{S} \cdot (\nabla\Phi)_f = \boldsymbol{\Delta} \cdot (\nabla\Phi)_f + \boldsymbol{k} \cdot (\nabla\Phi)_f. \tag{3.10}$$

This allows us to use the same numerical scheme as for orthogonal mesh to calculate the orthogonal contribution, with the necessary non-orthogonality correction. So the normal current can be approximate by

$$\boldsymbol{S} \cdot (\nabla\Phi)_f = |\boldsymbol{\Delta}| \frac{\Phi_7 - \Phi_6}{|\boldsymbol{d}|} + \boldsymbol{k} \cdot (\nabla\Phi)_f. \tag{3.11}$$

The gradient term in Eq. 3.11 can be evaluated explicitly by the following equations (Jasak, 1996):

$$(\nabla\Phi)_f = f_x(\nabla\Phi)_6 + (1 - f_x)(\nabla\Phi)_7 \tag{3.12}$$

$$(\nabla\Phi)_{6,7} = \frac{1}{V_{6,7}} \sum_f \boldsymbol{S}\, \Phi_f. \tag{3.13}$$

f_x and V stand for the weight and cell volume, respectively. As the non-orthogonality increases, the contribution from Φ_6 and Φ_7 decreases.

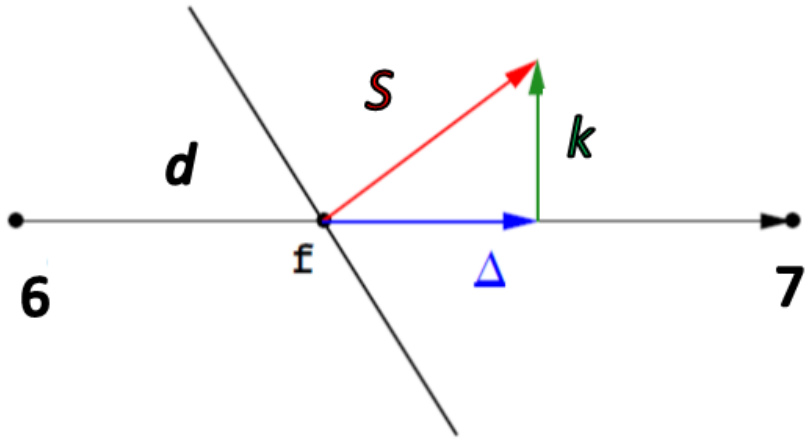

Figure 3.4 Non-orthogonality correction when calculating the normal current on the cell face.

3.5 MATRIX EQUATION

With the equation discretized on each cell, the next step is to assemble all these discretized equations and solve for the unknowns in a matrix equation. This part demonstrates a detailed procedure for formulating the matrix equation using a simple 2D example.

Starting from the simplest case, when the mesh is orthogonal or when the mesh is non-orthogonal but no correction is required, the discretized equation for an internal cell (Fig. 3.5) is

$$\sum_{i=1}^{n} \sigma_{f(i)} \left|S_{f(i)}\right| \cdot (\nabla\Phi)_{f(i)} = \sum_{i=1}^{n} \sigma_{f(i)} \left|S_{f(i)}\right| \cdot \frac{\Phi_{\mathrm{N}(i)} - \Phi_{\mathrm{P}}}{d(i)} = 0. \tag{3.12}$$

For a boundary cell (Fig 3.5), the discretized equation is

$$\sum_{internal} \sigma_{f(i)} \left|S_{f(i)}\right| \cdot \frac{\Phi_{N(i)} - \Phi_P}{d(i)} + \sigma_{f,b} \left|S_{f,b}\right| \cdot \frac{\Phi_b - \Phi_P}{d'} = 0. \quad (3.13)$$

i is the index for the neighbor cells (excluding boundary cells) of cell P and f denotes the values on the corresponding faces.

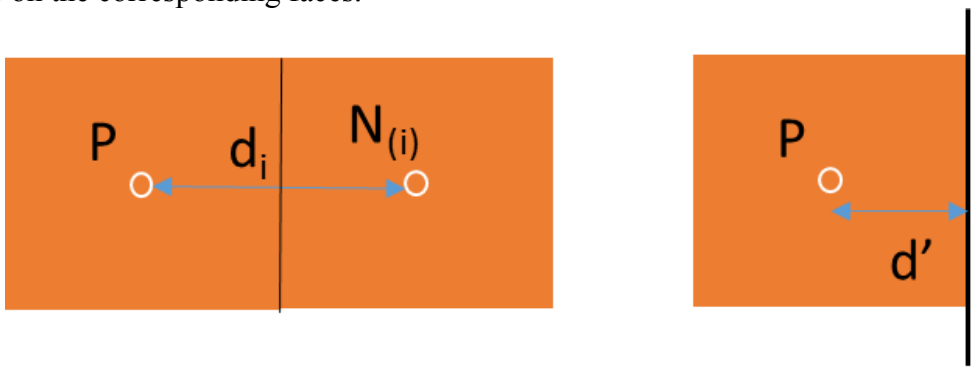

Figure 3.5. Discretization for internal and boundary cells

Assembly of these equations leads to a linear system $\boldsymbol{A} \cdot \boldsymbol{x} = \boldsymbol{b}$, where $\boldsymbol{A}$ is a sparse coefficient matrix, $\boldsymbol{x}$ is a column vector formed by the unknowns that need to be solved, and $\boldsymbol{b}$ is a column vector which represents the excitation and some known boundary conditions. For a realistic case the matrix equation may contain millions of unknowns, depending on the size of the problem. Here we use a 2D orthogonal mesh (Fig. 3.6) in a homogeneous medium. The grids are squares with an edge length of d. The values of the potential on the boundaries (red lines) are known as Φ_b. The potentials Φ_i at each cell center are the unknowns that need to be solved. For each cell a discretized equation (Eq. 3.12 or 3.13) is formulated and assembling of these equations forms a matrix equation (Fig. 3.7).

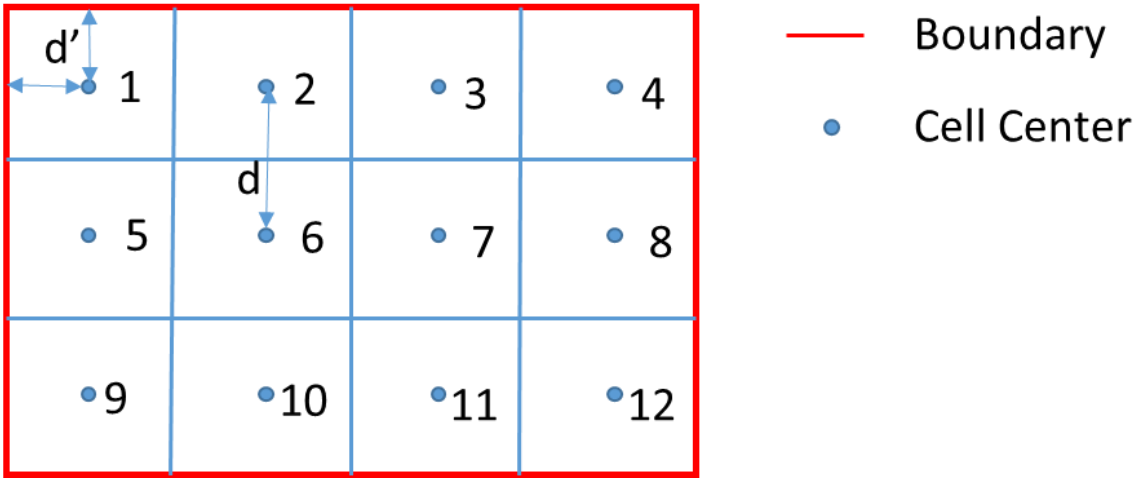

Figure 3.6. A 2D orthogonal mesh with the boundary value defined. The edge length for the grids is d.

$$\begin{bmatrix}
-\frac{2}{d}-\frac{2}{d'} & \frac{1}{d} & 0 & 0 & \frac{1}{d} & 0 & 0 & 0 & 0 & 0 & 0 & 0 \\
1/d & -\frac{3}{d}-\frac{1}{d'} & \frac{1}{d} & 0 & 0 & \frac{1}{d} & 0 & 0 & 0 & 0 & 0 & 0 \\
0 & \frac{1}{d} & -\frac{3}{d}-\frac{1}{d'} & \frac{1}{d} & 0 & 0 & \frac{1}{d} & 0 & 0 & 0 & 0 & 0 \\
0 & 0 & \frac{1}{d} & -\frac{2}{d}-\frac{2}{d'} & 0 & 0 & 0 & \frac{1}{d} & 0 & 0 & 0 & 0 \\
\frac{1}{d} & 0 & 0 & 0 & -\frac{3}{d}-\frac{1}{d'} & \frac{1}{d} & 0 & 0 & \frac{1}{d} & 0 & 0 & 0 \\
0 & \frac{1}{d} & 0 & 0 & \frac{1}{d} & -\frac{4}{d} & \frac{1}{d} & 0 & 0 & \frac{1}{d} & 0 & 0 \\
0 & 0 & \frac{1}{d} & 0 & 0 & \frac{1}{d} & -4/d & \frac{1}{d} & 0 & 0 & \frac{1}{d} & 0 \\
0 & 0 & 0 & \frac{1}{d} & 0 & 0 & \frac{1}{d} & -\frac{3}{d}-\frac{1}{d'} & 0 & 0 & 0 & \frac{1}{d} \\
0 & 0 & 0 & 0 & \frac{1}{d} & 0 & 0 & 0 & -\frac{2}{d}-\frac{2}{d'} & \frac{1}{d} & 0 & 0 \\
0 & 0 & 0 & 0 & 0 & \frac{1}{d} & 0 & 0 & \frac{1}{d} & -\frac{3}{d}-\frac{1}{d'} & \frac{1}{d} & 0 \\
0 & 0 & 0 & 0 & 0 & 0 & \frac{1}{d} & 0 & 0 & \frac{1}{d} & -\frac{3}{d}-\frac{1}{d'} & \frac{1}{d} \\
0 & 0 & 0 & 0 & 0 & 0 & 0 & \frac{1}{d} & 0 & 0 & \frac{1}{d} & -\frac{2}{d}-\frac{2}{d'}
\end{bmatrix} \cdot \begin{bmatrix} \Phi_1 \\ \Phi_2 \\ \Phi_3 \\ \Phi_4 \\ \Phi_5 \\ \Phi_6 \\ \Phi_7 \\ \Phi_8 \\ \Phi_9 \\ \Phi_{10} \\ \Phi_{11} \\ \Phi_{12} \end{bmatrix} = \begin{bmatrix} -\frac{2\Phi_b}{d'} \\ -\frac{\Phi_b}{d'} \\ -\frac{\Phi_b}{d'} \\ -\frac{2\Phi_b}{d'} \\ -\frac{\Phi_b}{d'} \\ 0 \\ 0 \\ -\frac{\Phi_b}{d'} \\ -\frac{2\Phi_b}{d'} \\ -\frac{\Phi_b}{d'} \\ -\frac{\Phi_b}{d'} \\ -\frac{2\Phi_b}{d'} \end{bmatrix}$$

Figure 3.7. The matrix equation for the system in Fig. 3.6.

The matrix equation similar to the above example, but in 3-D geometry, is solved using iterative methods. Specifically, a pre-conditioned conjugant gradient method is used in our work. Notice that when a non-orthogonal mesh is encountered, the correction

terms in Eq. 3.11 - 13 are calculated explicitly. During the iteration process, each new set of solutions will be used to update the non-orthogonal correction terms.

3.6 VALIDATION OF THE NUMERICAL METHODS

Before simulating the proposed tool's response to highly conductive hydraulic fractures, it is necessary to validate the modeling approach described above for problems that include a large conductivity contrast. For this purpose, we examined two test-case problems for which analytical solutions exist and can be compared with our FVM solution.

3.6.1 Validation Case 1

Consider two spheres embedded in a homogeneous resistivity background (Fig. 3.8). The spheres (0.1 S/m) are 100 times more conductive than the background (0.001 S/m). The radii of the spheres are 10 m and they are separated by a distance of 60 m. A current source of 1A is placed 20 m from the center of the spheres. Assume the potential is zero infinitely far from the current source and the analytical solution of the potential in the whole domain can be derived from series expansion of spherical harmonics in a bispherical coordinate system (Aldridge and Oldenburg, 1989; Weiss, et al., 2016).

Using our numerical method we simulate this scenario in a 2000 x 2000 x 2000 m box, with the two identical spheres centered inside. The current source is represented by a sphere with radius of 0.02 m, which is meshed using tetrahedral elements with a typical edge length of 0.005 m. A total DC current of 1 A is uniformly emitted out of the source, which is applied by enforcing a Neumann boundary condition (fixed gradient of electrical potential). A Dirichlet boundary condition (zero potential) is applied on the outer boundary of the box. The edge length of largest elements on the outer boundary is about 200 m and the tetrahedral grids are gradually refined to match the edge length around the

conductive spheres and the current source to capture the rapid change of electric potential in the vicinity of the current source (Fig. 3.8 (a)).

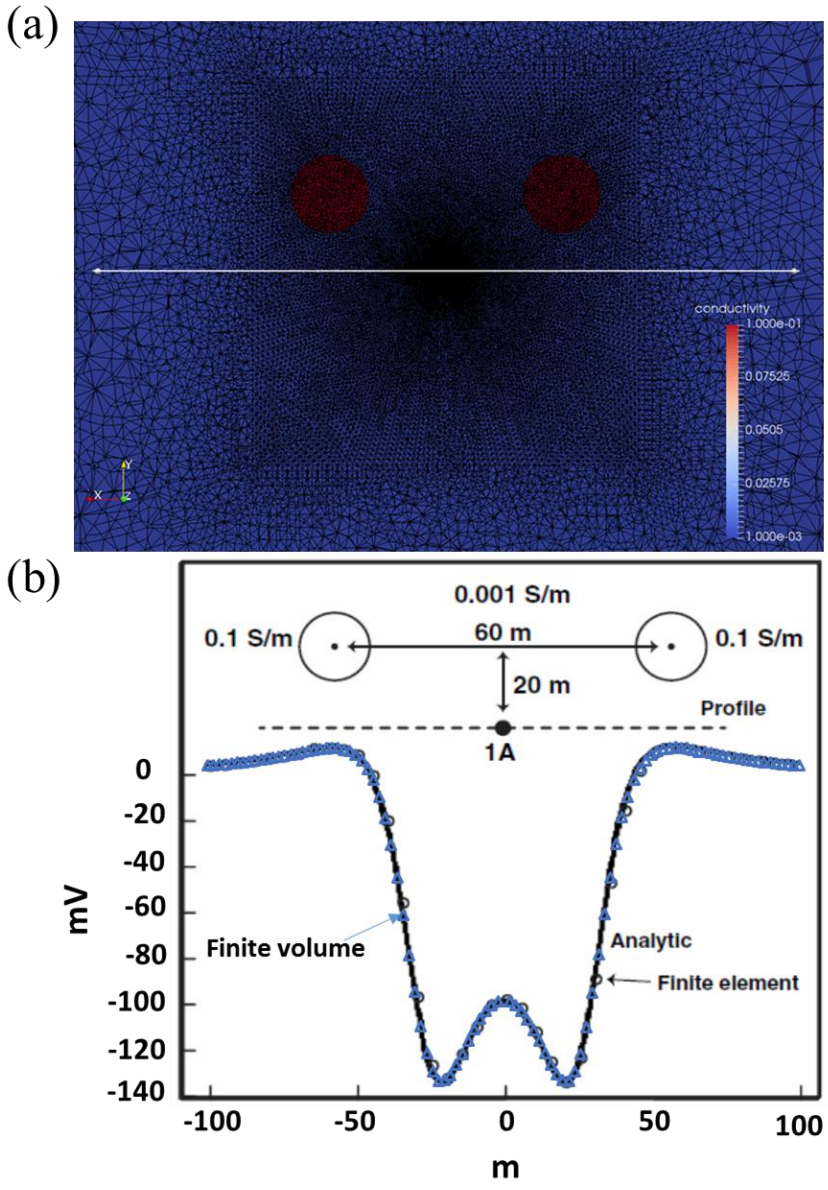

Figure 3.8. (a) The tetrahedral mesh around the source and the conductive spheres (the mesh size increases gradually away from the source). The color plot denotes the electrical conductivity. Samples of the calculated results are taken along the white line, which is corresponding to the dashed line in (b). (b) The results from our FVM (blue triangles) match well with the analytical and FEM solutions (Weiss et al., 2016).

To compare the calculated results from our FVM model with other solutions, samples are taken along a straight line across the current source (the white line in Fig. 3.8(a) and the dashed line in Fig. 3.8(b)). With the mesh size introduced earlier, the FVM solution (blue triangles) agrees well with the analytical solution and the FEM solution. Hence our numerical method is verified to work well for solving the governing equation of the resistivity problem (Eq. 3.1).

3.6.2 Validation Case 2

A big challenge of simulating the electrode-based resistivity tool is the high conductivity contrast in the computation domain. Validating the numerical method using a case with high conductivity contrast is important to assure the accuracy of the simulated results. Consider a solid cylindrical conductor ("well") of electrical conductivity 10^5 S/m and length of 100 m that is buried close to the interface between air and earth of conductivity 10^{-3} S/m (Fig. 3.9(a)). The difference in the electrical conductivity is eight orders of magnitude, which is close to that in the real problem we are solving. A point current source (I_s) out of which a total DC current of 1 A is uniformly emitted, is placed at a distance of 100 m from the cylinder on the earth – air interface. The electric potentials along the well Φ_{w} with respect to various wellbore radii r_{w} were calculated analytically by Johnston et al. (1987) and these results are used for our benchmarking purposes.

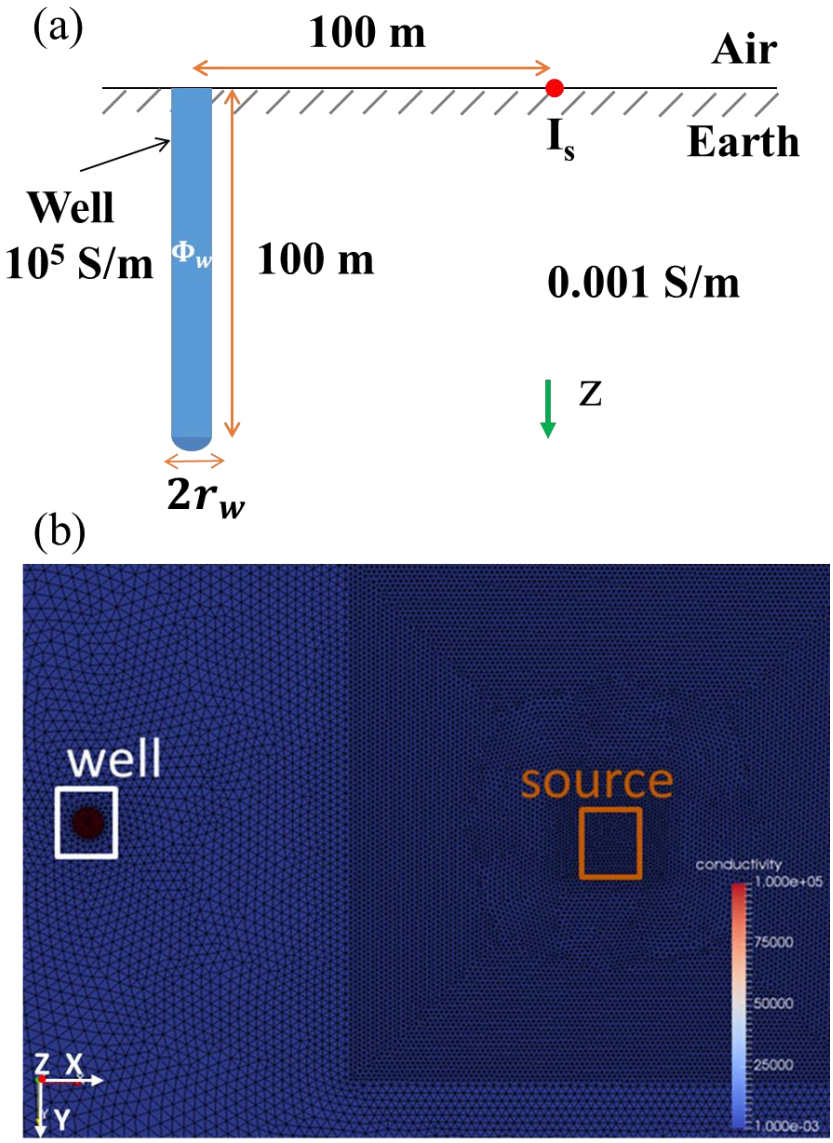

Figure 3.9. (a) Side view illustration of the test-case problem. (b) Map view of the source, wellbore and the mesh surrounding them. The computation domain is 10 km, 10 km and 5 km along X, Y and Z directions, respectively. The left and right boxes mark the location of the well and source, respectively.

In the numerical model, the current source is modeled as a 1 cm radius sphere on one face center (air-earth interface) of a 10 x 10 x 5 km box. On the air-earth interface, a Neumann boundary condition (zero normal current) is imposed. A Dirichlet boundary

condition (zero potential) is imposed on the other faces of the box, far from the well and source. The wellbore and source are meshed using tetrahedral elements with typical edge lengths of 0.5 m and 0.005 m, respectively. The outer surface boundaries of the computation domain are meshed with a typical edge length of 500 m. In the vicinity of the well, the mesh is gradually refined to match the fine mesh on the cylinder (Fig. 3.9(b)). Enclosing the source, a box of size 20 x 20 x 10 m is defined, inside which the mesh is even further refined to accommodate the $1/r$ singularity of the potential (Weiss et al., 2016).

The potential on the cylinder surface for various cylinder radii are calculated numerically using the FVM. Due to the high conductivity the cylinder is roughly equipotential. The results calculated, using different grid sizes in the 20 x 20 x 10 m box enclosing the source, are plotted as a function of the cylinder radius and compared to an analytical solution. It can be seen that, for all three cylinder radii investigated, convergence to the analytical solution is obtained as the mesh density in the box enclosing the source increases (Fig. 3.10(a)). The error relative to the analytical solution varied between 0.5% and 0.03%, as the grid size is refined from 1 m to 0.2 m, thus validating the FVM solver (Fig. 3.10 (b)). Refining the mesh only in a small region around the source can dramatically improve the accuracy of the numerical results, without increasing the number of unknowns too much, due to the $1/r$ singularity of the electric potential around the source. These results set a standard for choosing a suitable grid size when simulating the real problem in the following chapters.

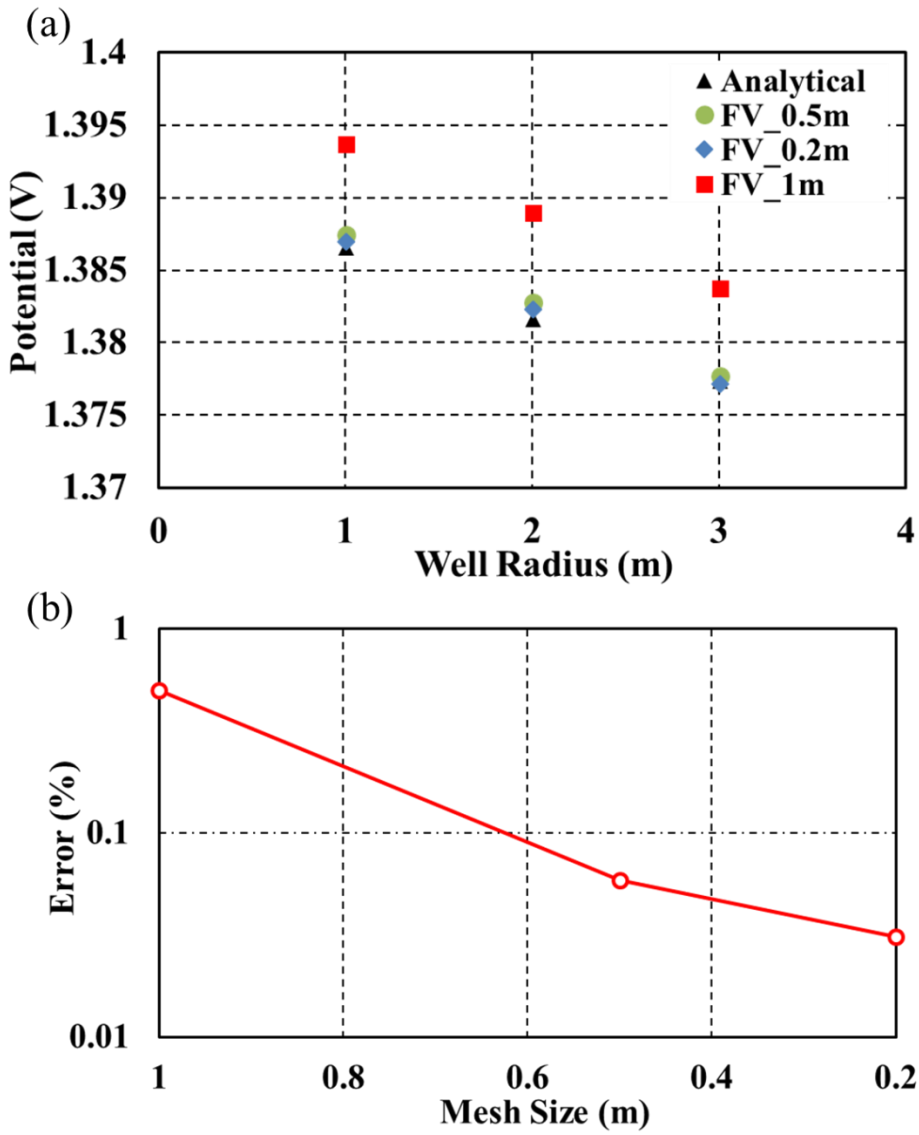

Figure 3.10. (a) Average potentials along the well as a function of its radius for various near-source mesh sizes in a 20 m x 20 m x 10 m box. (b) Average error relative to the analytical solution as a function of mesh size.

3.7 Model Simplifications

When simulating the electrode-based resistivity tool, the FVM is applied to a geometrical model representing the casing string in the surrounding medium. This model must be translated to representative model conductivities for all the materials involved.

While the exact geometry of the casing and gaps can include complex structures and fine details, certain simplifications are made for the proof-of-concept tool used in this work. Even when the casing and gaps are modeled as cylindrical pipes, the modeling of thin casing/gap walls and hydraulic fractures dictates meshing them using extremely fine grids, which can lead to a very large number of unknowns and, consequently, large storage and computation time. This can be mitigated by the following approximations to simplify the model without sacrificing the accuracy of the simulations.

For the well (comprising of the casing and resistive mud), a common approach to avoid excessive mesh refinement is to replace the casing and mud system by a single solid volume with an equivalent volume-averaged conductivity. The equivalent well model only need to be moderately refined or perhaps not refined at all (Haber et al., 2016; Um et al., 2015; Weiss et al., 2016; Yang, et al, 2016; Yang and Oldenburg, 2017). This material averaging method works well for DC and AC modeling at low frequency (<1 Hz) and it breaks down at higher frequency when the impact of the skin effect cannot be neglected. Since our resistivity tool is excited by a static or low-frequency voltage source, the casing and mud system can be replaced by a solid rod with a conductivity calculated as the equivalent conductivity of parallel resistors. An identical treatment is given to the insulating gap (filled with mud) sections. This approach is proved by a validation case in 3.7.1.

Hydraulic fractures are usually a few millimeters thick and hence require very fine mesh to capture their features. In many simulations, these thin fractures are replaced by thicker fractures with lower conductivity, maintaining the product of their conductivity σ and thickness δ, i.e., $\sigma \cdot \delta$, constant. The validity and advantage of adopting this practice is demonstrated in 3.7.2.

3.7.1 Simplification of the Well

To validate the solid volume well model with equivalent conductivity proposed earlier, we simulated a short well composed of 6 casing sections and 5 gaps, without a fracture. The casing sections and gaps are each 0.5 m and 0.1 m long, respectively. The well is embedded in a homogeneous shale formation. The inner and outer diameter of the original casing sections are 0.128 m and 0.14 m, respectively. A mud column of 0.128 m diameter is assumed. The electrical conductivities of the casing sections, insulating gaps, mud, and formation are set to 10^5 S/m, 10^{-12} S/m, 0.05 S/m, and 0.33 S/m, respectively (Fig. 3.11).

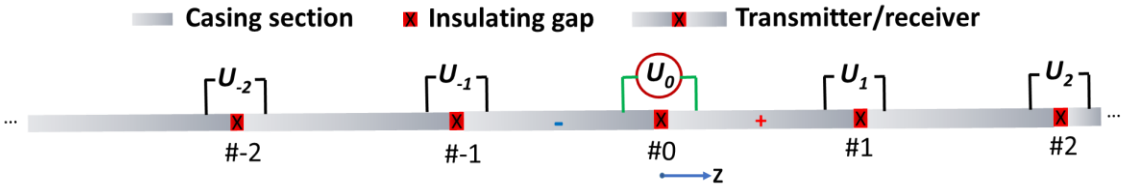

Figure 3.11. Illustration of an electrode array configuration. Gap #0 is used for excitation.

Across the central gap (denoted #0), a voltage 20 V is imposed by setting the potentials to ± 10 V at two contact points on the casing sections forming the gap. We set the origin (z=0) at the center of gap #0. The gaps on the positive z –axis are numbered as #1, #2 etc., whereas the ones on the negative z –axis are denoted as #-1, #-2, etc. (Fig. 3.11). The computation domain is truncated by a Dirichlet boundary condition ($\Phi = 0$) on a bounding box of 1 x 1 x 1.2 km, with the well oriented in the direction of the box's larger dimension. The typical mesh edge length is set to 60 m on the faces of the box.

Using our numerical method, we calculated the electric potentials obtained with finely meshed (2 mm) mud-filled casing/gap well model and those obtained using a more coarsely meshed (2 cm) solid well model with equivalent volume-averaged conductivity.

This equivalent conductivity is calculated as the conductivity of parallel resistors. Suppose the cross sectional area and electrical conductivity of the {mud, casing (insulator)} are $\{A_1,\ \sigma_1;\ A_2,\ \sigma_2\}$ (Fig. 3.12(a)). The solid volume well model proposed has a cross sectional area and a conductivity

$$A = A_1 + A_2, \tag{3.14}$$

$$\sigma = \frac{\frac{1}{A_1 \cdot \sigma_1} + \frac{1}{A_2 \cdot \sigma_2}}{\frac{1}{A_1 \cdot \sigma_1} \cdot \frac{1}{A_2 \cdot \sigma_2} \cdot (A_1 + A_2)}. \tag{3.15}$$

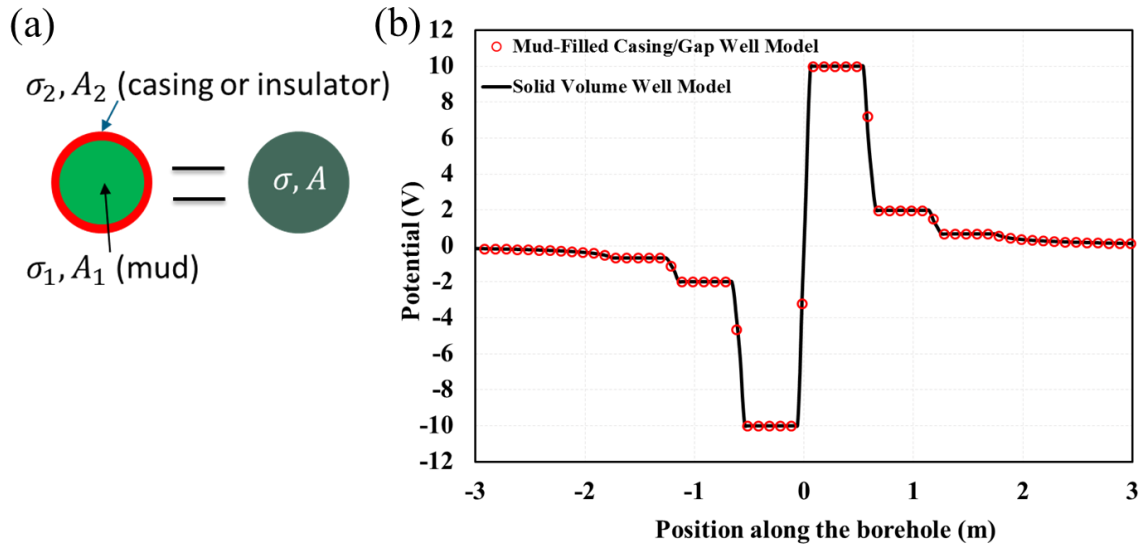

Figure3.12. (a) Equivalent conductivity model for casing/insulator sections. A and σ represent the area and conductivity of a specific region, respectively. (b) The electric potentials along the well computed using the solid volume well model and the mud-filled casing/gap well model.

Using the conductivities and sizes proposed earlier in this section, the equivalent conductivities for the solid volume well model at the casing/mud and gap/mud section are 16408 S/m and 0.0418 S/m, respectively. Samples of the calculated electric potentials are taken along center of the well and the results from the solid volume well model and the mud-filled casing/gap well model are plotted in Fig. 3.12(b). The relative difference

between these two cases is 0.3%, thus validating the equivalent conductivity approximation for the wellbore. This simplification not only eases the mesh generation, but also reduces the ratio between the casing conductivity and the gap conductivity from 17 orders of magnitude to 6 orders of magnitude, which improves the system's conditioning and accelerates the numerical solver's convergence. For this simple validation case, the computation time is reduced from ~36 min to ~ 3 min, due to the dramatic decrease of the number of unknowns.

3.7.2 Simplification on the Fracture

The other important simplification we made in the numerical model is to replace the thin hydraulic fracture by a thicker one with lower conductivity, maintaining the product of their conductivity σ and thickness δ (conductance), i.e., $\sigma \cdot \delta$, constant (Fig. 3.13). In our case the mesh size around the fracture is dictated by the fracture width or thickness, which is very fine compared to the large size of the computation domain (a few thousand meters). Moreover, if the fracture that needs to be simulated is large (e.g., 100 m long), only the fracture itself will require a very large number of unknowns. In fact, due to the high electrical conductivity of the fracture (propped by conductive proppant), the electric potential doesn't change very much along the fracture, which makes the use of fine grids unnecessary.

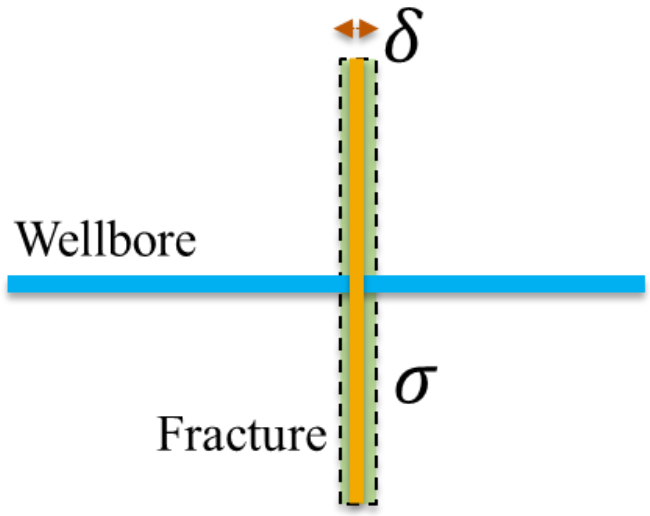

Figure 3.13. The realistic thin hydraulic fracture (yellow) is replaced by a thicker fracture (green) with lower electrical conductivity.

To prove the validity of this approach, we simulated two fractures with the same conductance ($\sigma \cdot \delta$). The thinner one has a thickness of 3 cm and a conductivity of 200 S/m, whereas the thicker one has a thickness of 6 cm and a conductivity of 100 S/m. Both fractures are 30 m in radius and placed perpendicular to the well 5 m away from the excited electrode (Fig. 3.14(a)). In this case the solid volume well model with equivalent conductivity is used. The inner and outer diameter of the original casing sections are 0.128 m and 0.14 m, respectively. The length for the insulator is set to 0.02 m, and the length for each casing section is still 9 m. The conductivities for different materials are kept the same as those in Section 3.7.1.

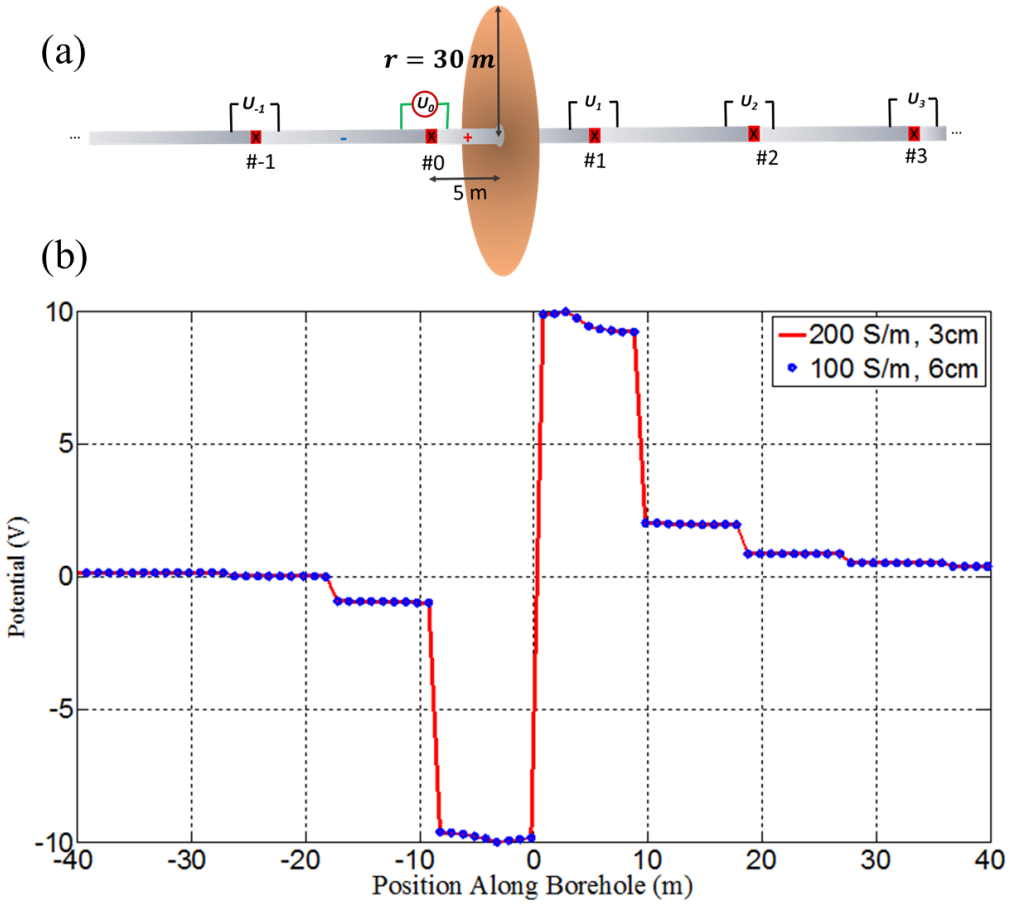

Figure 3.14. (a) Illustration of an electrode array configuration. Gap #0 is used for excitation. The fracture is placed 5 m away from gap #0. (b) The electric potentials along the well are plotted for two cases (the position of zero is set at the center of gap #0).

The calculated potentials along the well from these two cases match well with a relative difference around 0.1% (Fig. 3.14(b)). Therefore, simplification on the fracture allows us to get accurate results with a negligible difference in results. The computation time, however, is reduced by over 20 times (from ~180 min to ~8 min), which greatly speeds up the simulation.

3.8 SUMMARY

We propose a new method for fracture diagnostics in steel-cased wellbores. In this method, an array of specialized gap subs with electrically insulated internal connections is installed as a permanent part of the casing string. Before and after perforating and fracturing operations, using highly conductive proppants, a coiled-tubing conveyed BHA is run into the fracture zone to straddle and impose a voltage across each insulating gap, one at a time. The voltages across many of the other insulating gaps in the casing string are measured, stored in memory, and uploaded to the BHA. The tool concept overcomes the problem of through-casing signal attenuation typical for induction tools, by direct excitation of the casing sections. It also mitigates the problem of signal attenuation in the rock which is a big issue in borehole-to-surface and borehole-to-borehole measurements.

To simulate the tool's response to hydraulic fractures, a numerical model based on FVM has been built and benchmarked by two validation cases with analytical solutions. The computational domain is discretized on an unstructured mesh. The resulting equations form a matrix equation that is solved using iterative methods. Mesh non-orthogonality is also corrected for to obtain more accurate solutions, especially around the fine features, such as the wellbore and fractures. The model assures the continuity of electric potential and normal current on the interface by harmonically interpolating the electrical conductivity.

When the casing and gaps are modeled as cylindrical pipes, the modeling of thin casing/gap walls and hydraulic fractures dictates meshing them using extremely fine grids, which can lead to a very large number of unknowns and, consequently, large storage and computation time. This is alleviated mainly by making two simplifications in the model: (i) replacing the casing and mud system by a single solid volume with an

equivalent volume-averaged conductivity; (ii) replacing the thin hydraulic fracture by a thicker one with lower conductivity, maintaining the product of their conductivity σ and thickness δ (conductance), i.e., $\sigma \cdot \delta$, constant. Both practices have been proved to significantly reduce the computation time, without sacrificing the accuracy of the solutions.

NOMENCLATURE

$\boldsymbol{X}$ = position vector, m

$\boldsymbol{\Phi}$ = electric potential, V

$\boldsymbol{\sigma}$ = electrical conductivity, S/m

$\boldsymbol{J_s}$ = imposed current source, A/m^2

$\boldsymbol{S}$, s = area, m^2

V, v = volume, m^3

A = area, m^2

I_s = current source, A

$\boldsymbol{\delta}$ = thickness, m

$\boldsymbol{U}$ = voltage, V

Chapter 4: Forward Modeling – Sensitivity Study of the Tool

4.1 BACKGROUND

The propagation of hydraulic fractures is controlled by many factors, such as the in-situ stress condition, stress shadowing and fracture interference, the presence of a natural fracture network, etc. (Bryant et al., 2015; Wu and Olson, 2013; Potluri et al., 2005; Zhou and Xue, 2011; Olson and Taleghani, 2009). The proppant distribution in the induced fractures also depends on numerous factors, such as injection rate and fluid rheology (Blyton et al., 2015). The combined effect of all these factors can lead to fractures with different length, height, angle etc. in different clusters of a fracturing stage. Hence, a fracture diagnostics technique that is capable of evaluating many fracture parameters is beneficial for precisely describing the fracture geometry and predicting or history matching the productivity of a fractured well. The sensitivity of a specific method to different fracture parameters can be investigated using a sensitivity study. The results are critical for optimizing the method, or seeking a complementary technique to remedy the shortcomings of the method.

In this chapter we use our FVM-based forward model to simulate the electrode-based resistivity tool. We demonstrate, using various examples, the sensitivity of the tool to various geometrical parameters of a fracture. This is done by using different excitation configurations for the tool. For all the examples, we consider a horizontal well embedded in a resistive shale reservoir. For the sake of illustrating the fundamental properties of the proposed tool, we also assume that the shale background is homogenous (the solver is capable of accounting for formation inhomogeneity). The horizontal well under investigation is about 200 m long, and is composed of 22 standard 9 m long casing sections and 21 0.02 m long insulating gaps. The model is sufficiently long to incorporate all the gaps at which detectable signal levels are observed. The inner and outer diameters

of the casing and gaps parts are 0.128 m and 0.14 m, respectively. The typical mesh edge lengths on the casing and insulating gaps are set to 2 cm and 5 mm, respectively. The electrical conductivities of the casing, insulating gaps, mud, and formation are set to 10^5 S/m, 10^{-12} S/m, 0.05 S/m, and 0.33 S/m, respectively. Using the previous parameters, the equivalent conductivities for the solid volume well model at the casing/mud and gap/mud section are 16408 S/m and 0.0418 S/m, respectively. The casing sections forming the central gap #0 are excited at two contact points located ± 3 m from gap #0, with DC potentials of ± 10 V. When not specified otherwise, the fracture's width δ and conductivity σ are set to 3 cm and 500 S/m, respectively, equivalent to that of hydraulic fractures with practical width (3 mm) and a measured conductivity of 5000 S/m (Zhang et al., 2016). The remainder of this chapter summarizes the proposed tool's response as a function of various fracture parameters (e.g., location, size, angle, deviation from the well and aspect ratio). The tool's sensitivity to these fracture parameters was studied using the simplest configuration, when only one fracture is present. The influence of the shale's conductivity was also investigated.

4.2 EFFECT OF FRACTURE LOCATION

By varying the distance between the fracture and the excitation gap, we investigated the tool's response to fracture locations. Figure 4.1 illustrates the simulations for three different cases (we set z=0 along the well to be at the center of gap #0): (i) the fracture is in contact with one of the excited casing sections (fracture is at z=5 m), (ii) the fracture is in contact with the casing section that is next to the excited section (fracture is at z=14 m), and (iii) the fracture is in contact with the casing section that is two sections away from the excitation gap (fracture is at z=23 m). For all cases, a circular fracture of 30 m radius was used and the fracture is perpendicular to the borehole axis.

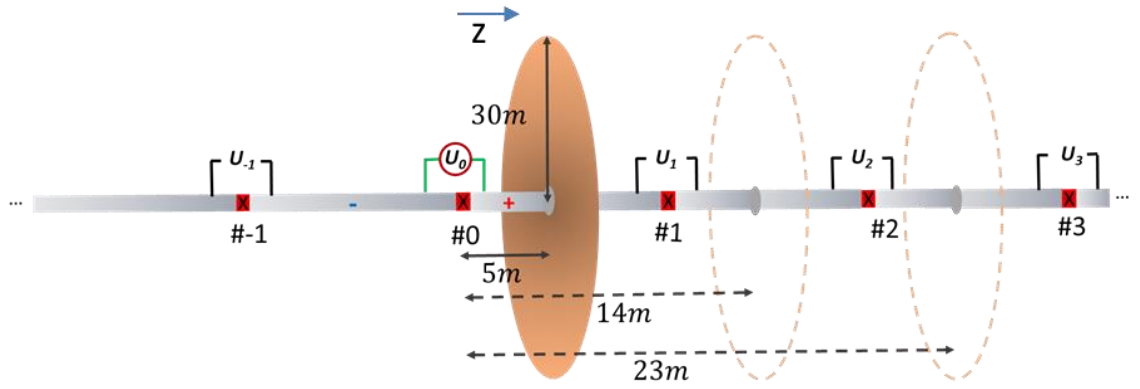

Figure 4.1 Illustration of the tool configuration with three possible fracture locations.

The electrical potential along the well and voltages across all the receiver gaps, for three cases (i, ii and iii) and the no-fracture case, were computed and plotted for comparison. It can be clearly seen that, along the positive z-axis, potential drops occur across each of the gaps (Fig. 4.2). Note that the potential decays along the well faster than expected from a short electric dipole in free space (which is sometimes used to model a small voltage source) due to the insulating gaps. When the fracture is in contact with the excitation electrode (fracture is at z=5 m), the potentials almost everywhere along the casing are higher than those without a fracture, except for on the excitation electrode. On that section, the presence of the fracture creates a preferred path for current into the formation via the fracture. As a result, the total current drawn from the source increases and the voltage drop on the part of the casing section that is between the voltage excitation point (at z=3 m) and the fracture-casing contact (at z=5 m). Thus, the potential on the remainder of the section is lower. A similar effect (although due to a slightly different mechanism) is observed in cases (ii)-(iii), for casing sections that are in contact with the fracture away from the excitation gap. The difference from the no-fracture case is the most pronounced for case (i), i.e., when the fracture is in contact with one of the excited casing sections (Fig. 4.2).

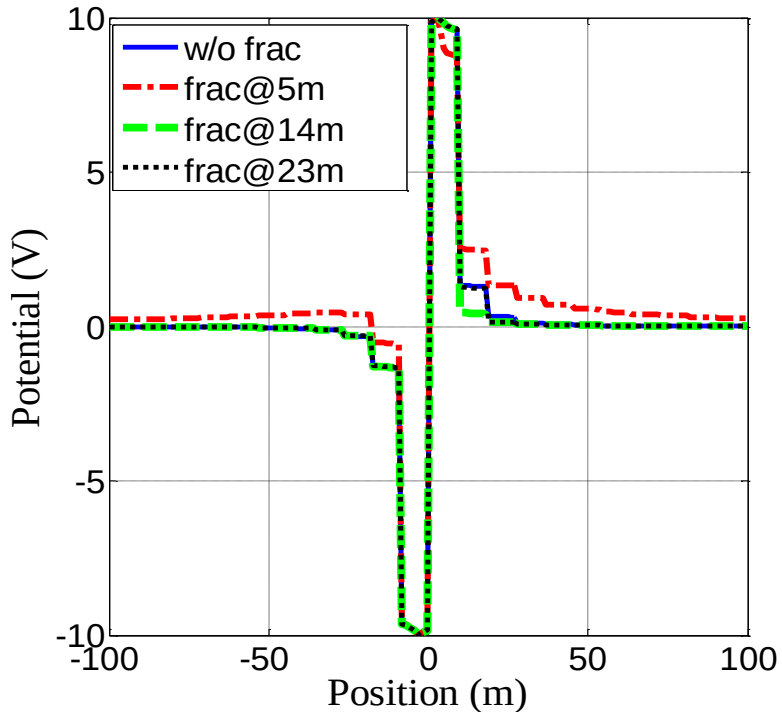

Figure 4.2 Potentials along the wellbore for three different fracture locations and the no-fracture case.

The same holds for the voltages across the various gaps and the differential voltage with respect to the no-fracture case. In case (i), the voltages detected at the receivers are about 10 times stronger compared to the ones when the fracture is not in direct contact with the electrode (Fig. 4.3(a), (b)). This is due to the dominant physical mechanism in case (i) – the strong leakage of current from the excited casing section into the fracture and then into the formation. This is as opposed to leakage directly from the casing sections into the formation and then to the fracture, which is a secondary effect. In the former, the fracture serves effectively as an extension of the casing section it touches. When there is no direct contact between the excited section and the fracture, the only mechanism for exciting the fracture is through the formation and the signal levels decrease. Note that the latter effect's influence in an actual well will greatly depend on

the conductivities of the formation surrounding the casing, which will be reported in a later section.

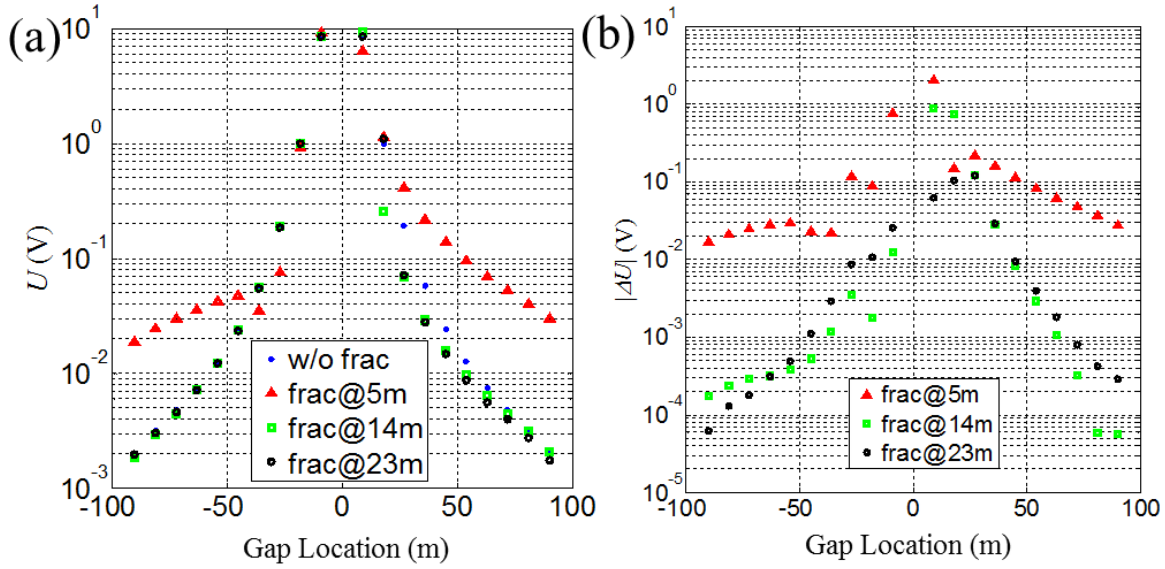

Figure 4.3 (a) Voltages at the various gaps corresponding to three fracture locations and the no-fracture case. (b) Voltage differences from the no-fracture case corresponding to the voltages in (a).

4.3 EFFECT OF FRACTURE CONDUCTANCE

As mentioned in Chapter 3, our method for fracture diagnostics relies on conductive proppant that can change the current distribution around it. The benefits of using highly conductive proppant can be demonstrated by simulating the tool's response to a fracture with different conductivity. A circular fracture with radius 30 m and width of 3 cm is placed on the positive electrode (5 m from the transmitter gap), and the fracture conductivity was varied from 200 S/m to 600 S/m (Fig. 4.4). We have already shown that maintaining the product of a fracture's conductivity σ and width δ (conductance), i.e., conductance G, constant will lead to the same measured voltages at the receiver gaps (3.7.2). Therefore, the results are equivalent to those for a fracture with more realistic width 3 mm and conductivity from 2000 S/m to 6000 S/m.

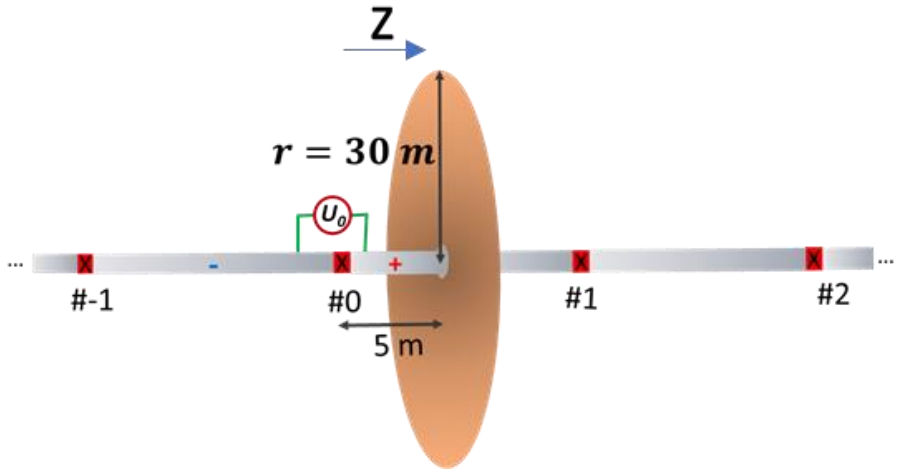

Figure 4.4 Illustration of the tool configuration that is used to investigate the effect of fracture conductance.

The voltages across the various gaps and the differential voltage from the no-fracture case are plotted in Fig. 4.5 (a) and (b). Fracture conductance, instead of conductivity, is shown in the plots, since the fracture's conductance is the dominant factor. Clearly as the fracture conductance (the conductivity or width) increases, both the voltages and the differential voltages increase (shown by the red arrows). This is because more current is pulled from the electrode as the fracture becomes more conductive. Consequently, more current gets distributed over the fracture's surface and reaches the receiver gaps. The voltages across these gaps increase according to Ohm's law. We can conclude that more conductive proppant will lead to higher signal to noise ratio if the noise floor is constant, which justifies the necessity of using highly conductive proppant for the deployment of this electrode-based resistivity tool.

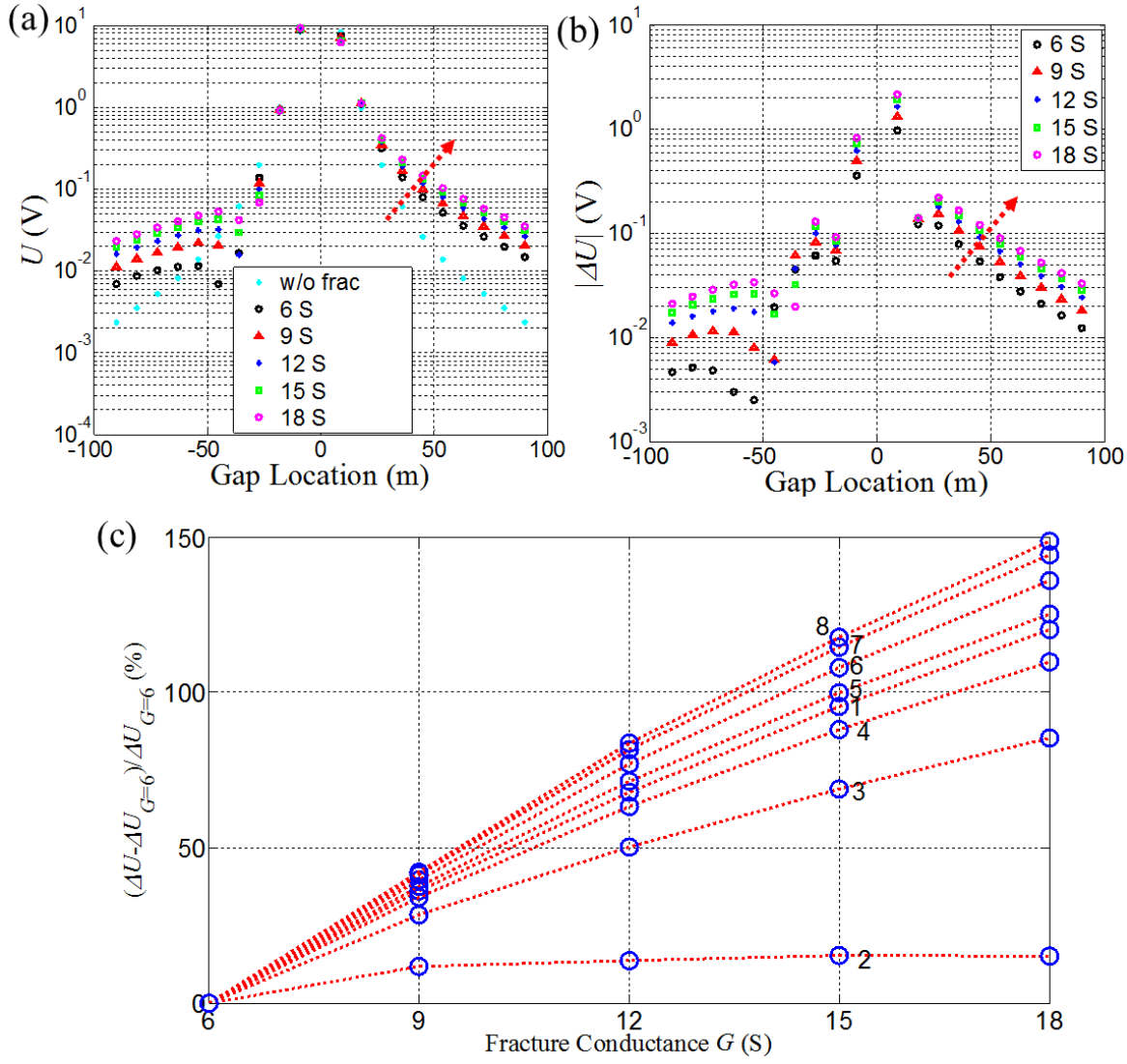

Figure 4.5 Voltages at the various gaps corresponding to different fracture conductance and the no-fracture case. (b) Voltage differences from the no-fracture case corresponding to the voltages in (a). (c) Differential voltages in (b) relative to the *differential* ones obtained for the least conductive fracture ($G = 6$ S).

The tool's sensitivity to fracture conductance can be analyzed by calculating the differential voltages relative to the differential ones obtained for the least conductive fracture $\frac{(\Delta U_i - \Delta U_{i,G=6S})}{\Delta U_{i,G=6S}} \times 100\%$ (Fig 4.5 (c)). High sensitivity to fracture conductance is

shown by the nearly linear increase of the differential voltages at most of the receivers. Only at receiver #2 the differential voltage gradually reaches a saturation level. The tool's high sensitivity to fracture conductance leads to the possibility of extracting it by inverting the measured data. Since the conductance is defined as the product of the fracture conductivity and width, if a proppant's conductivity under a given confining pressure is known, the fracture width can be extracted by inverting the measured voltages collected in a logging sequence, which will be demonstrated later in this work.

4.4 EFFECT OF FRACTURE SIZE

The most important information for predicting and history matching a fractured well's productivity is the propped fracture height and length. To study the tool's capability to differentiate fractures of various sizes, the numerical experiment was repeated with multiple fracture sizes. Let us define the tool's saturation limit as the fracture radius, beyond which larger fractures create a residual voltage response at the receiver gaps that is not sufficient for differentiating them. For investigating the saturation limit, only circular fractures are considered. In his study, three formats are used for the results at each receiver gap i: the voltage difference from the no-fracture case ($\Delta U_i = U_{frac,i} - U_{no-frac,i}$), the differential voltages normalized by the voltages without fractures $\frac{(U_{frac,i} - U_{no-frac,i})}{U_{no-frac,i}} \times 100\%$, and the differential voltages relative to the differential ones obtained for the largest fracture $\frac{(\Delta U_i - \Delta U_{i,r=120m})}{\Delta U_{i,r=120m}} \times 100\%$. In this set of examples, the fractures are placed on the positive electrode (z=5 m), orthogonal to the borehole axis (Fig. 4.4) and a range of realistic hydraulic fracture radii from 2 m to 120 m is examined. The fracture's width δ and conductivity σ are set to 50 cm and 30 S/m, respectively, to enable simulation of the fractures of large radii. Note that the product $\sigma \cdot$

δ (conductance) of the fractures remains the same for all the cases, and these fractures are equivalent to the ones with realistic width (3 mm) and conductivity (5000 S/m).

Fig. 4.6 plots the electrical potential calculated along the well for different fracture sizes. We take the part on the positive side of the transmitter gap (#0) as an example to interpret the physics. The presence of the conductive fracture creates a preferred path for current into the formation via the fracture. As the fracture size increases, the total current drawn from the source increases. This leads to a larger potential drop on the part of the casing section that is between the voltage excitation point (at z=3 m) and the fracture-casing contact (at z=5 m). This is the reason why the electrical potential on that section is higher for smaller fractures and lower for larger fractures (Fig. 4.6).

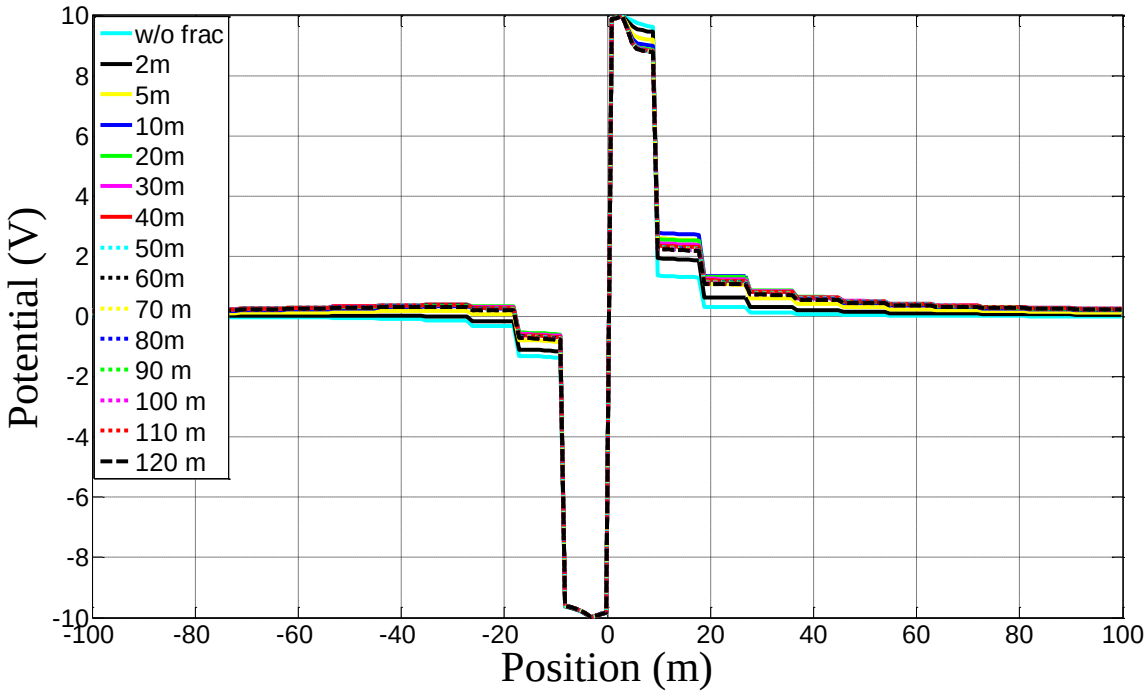

Figure 4.6 Potentials along the wellbore for fractures with different radii and the no-fracture case.

Fig. 4.6 can be further explained by plotting the potential along the radial direction of the fractures (Fig. 4.7). Clearly, the overall potential on smaller fractures is higher, due to the smaller potential drop between the voltage excitation point (at z=3 m) and the fracture-casing contact (at z=5 m). However, the higher potential dies out faster for smaller fractures in the radial direction, because once the current flows beyond the fracture tip, it hits the shale, which is much less conductive. Due to this reason, as the distance from the fractures increases, the electrical potential curves in Fig. 4.6 flip at some point, when the potential along the well becomes higher for larger fractures. In other words, the impact of a larger fracture is weaker near the fracture, but stronger far away from the fracture.

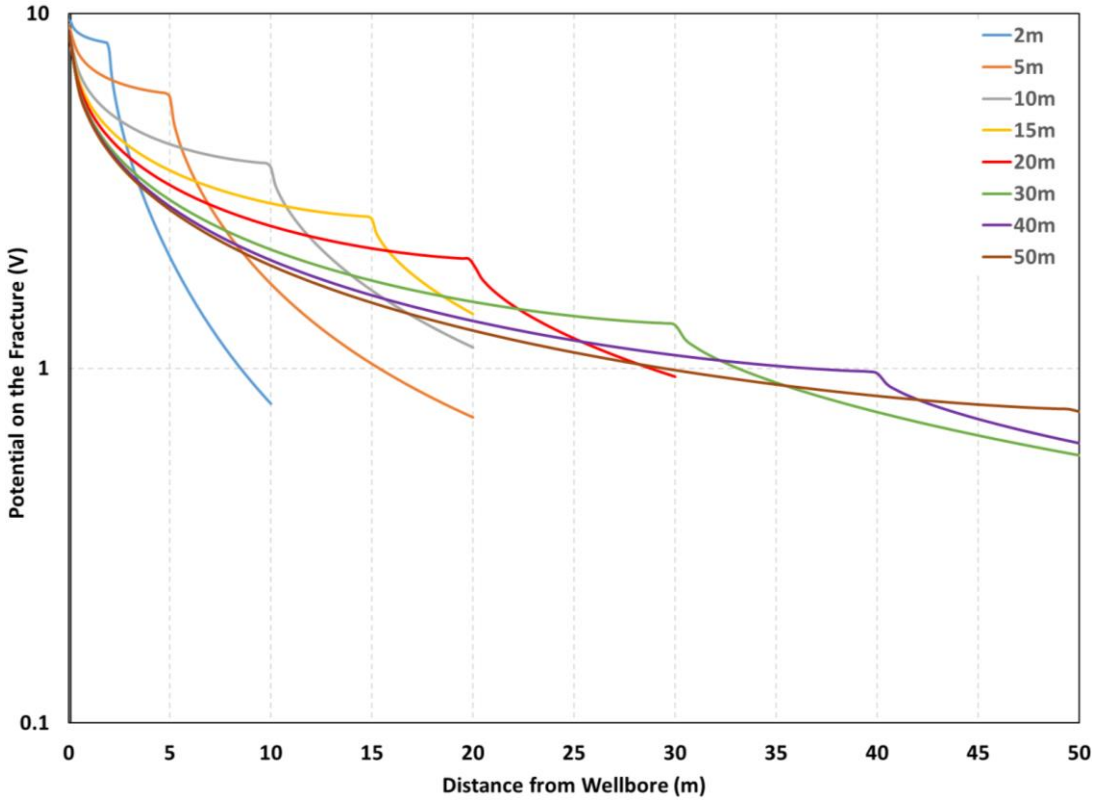

Figure 4.7 The electrical potential on the fractures along the radial direction. The legend marks the fracture radii.

To study the sensitivity of different receiver gaps to fracture size, we plot the differential voltages measured at each gap ($\Delta U_i = U_{frac,i} - U_{no-frac,i}$) as a function of fracture area (Fig. 4.8). The receiver gaps are denoted by an integer i, which is consistent with the gap number in Fig 4.4. It can be seen that the gaps further away from the fracture experience lower differential voltages, due to the decay of the signal level away from the source. Yet, all the differential voltages are above the level of 10 mV – higher levels than those observed ($0.1 - 20\ \mu V$, obtained with a current source of 1A/m^2) in surface measurements (Weiss et al., 2016). This guarantees a higher signal to noise ratio, assuming the noise level is the same for both surface and downhole measurements.

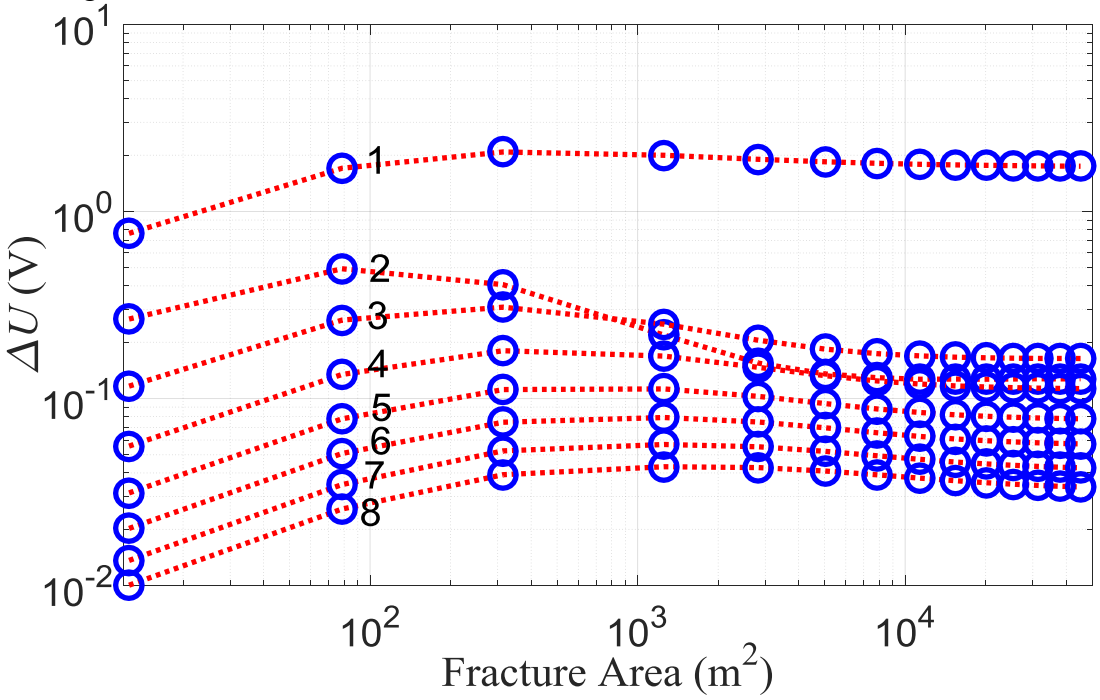

Figure 4.8 Voltage differences from the no-fracture case at various gaps as a function of the fracture area.

The normalized differential voltages with respect to the no-fracture case $\frac{(U_{frac,i} - U_{no-frac,i})}{U_{no-frac,i}} \times 100\%$ are plotted in Fig. 4.9. The sensitivity to the presence of a

fracture is gap-dependent. For all the fractures with radius from 2 m to 120 m, a relative signal strength larger than 10% is obtained. Therefore, it can be concluded that the tool can easily sense the presence of fractures of radii as small as 2 m.

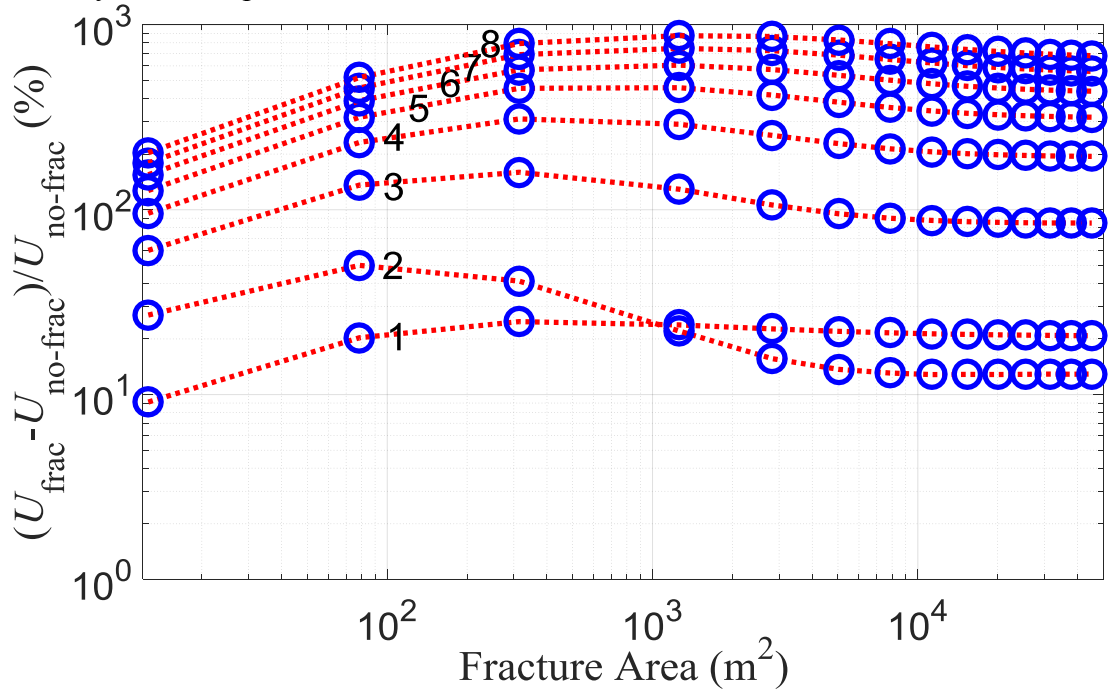

Figure 4.9 Differential voltages measured at various gaps in Fig. 4.8 normalized by the corresponding voltages without fractures.

It can also be seen that for all gaps the differential voltages ΔU_i stagnate when the fracture radius is ~120 m (Fig. 4.8). The saturation limit defined earlier can be more specifically determined from the normalized differential voltages with respect to those induced by the largest fracture ($\frac{(\Delta U_i - \Delta U_{i,r=120m})}{\Delta U_{i,r=120m}} \times 100\%$) (Fig. 4.10). Assuming that at least 2% relative difference between two voltage levels is required for the tool to tell them apart, we can examine the saturation limit for each of the receiver gaps. In Fig. 4.10 the circles that fall into the 2% threshold, marked by the green dashed lines, represent fractures that cannot be differentiated from fractures of radius 120 m or larger. The

intersection points between the red and the green dashed lines on the right side of the figure represent the saturation limit for each of the receiver gaps.

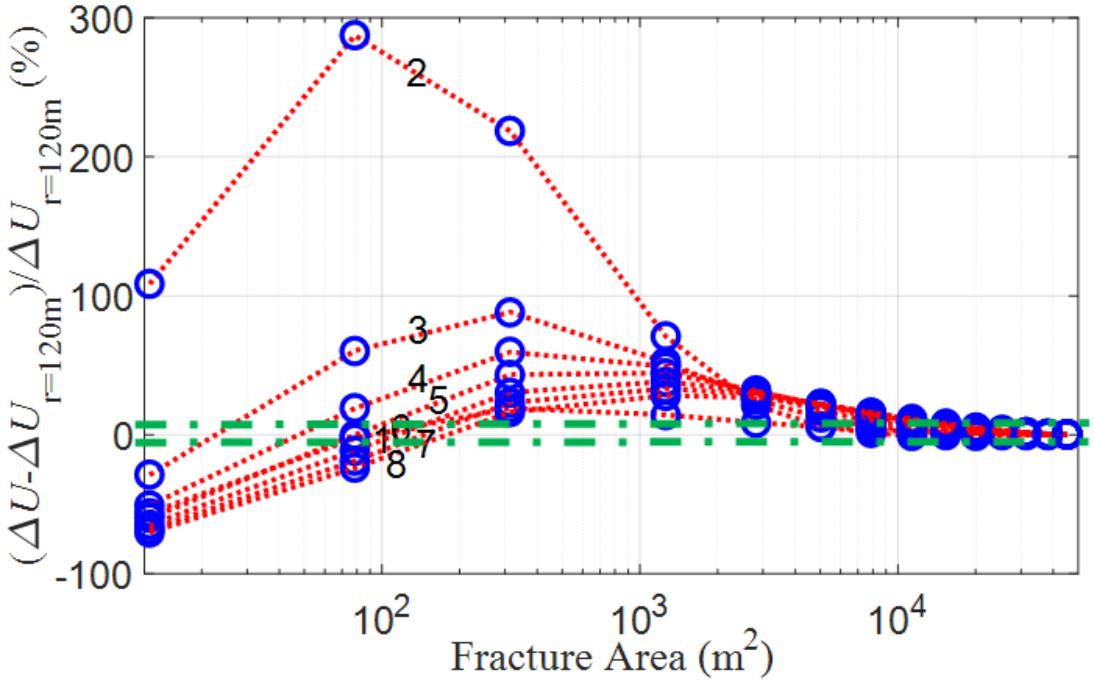

Figure 4.10 Differential voltages in Fig. 4.8 relative to the *differential* ones obtained for the largest fracture ($r = 120\ m$). Dashed lines mark a threshold of $\pm 2\%$.

The saturation limit as a function of the gap index is plotted in Fig. 4.11(a), and illustrated in Fig. 4.11 (b). Generally, the sensitivity to the fracture size increases with distance away from the fracture. Gap #9 and #10 are the most sensitive in the sense that they can sufficiently differentiate between fractures of up to 100 m radius. Notice that the signal levels at these remote gaps are substantially lower. Nevertheless, the envisioned parametric inversion techniques will use data from all the observation gaps to identify fracture size, to increase resolution compared to that achievable using a single gap.

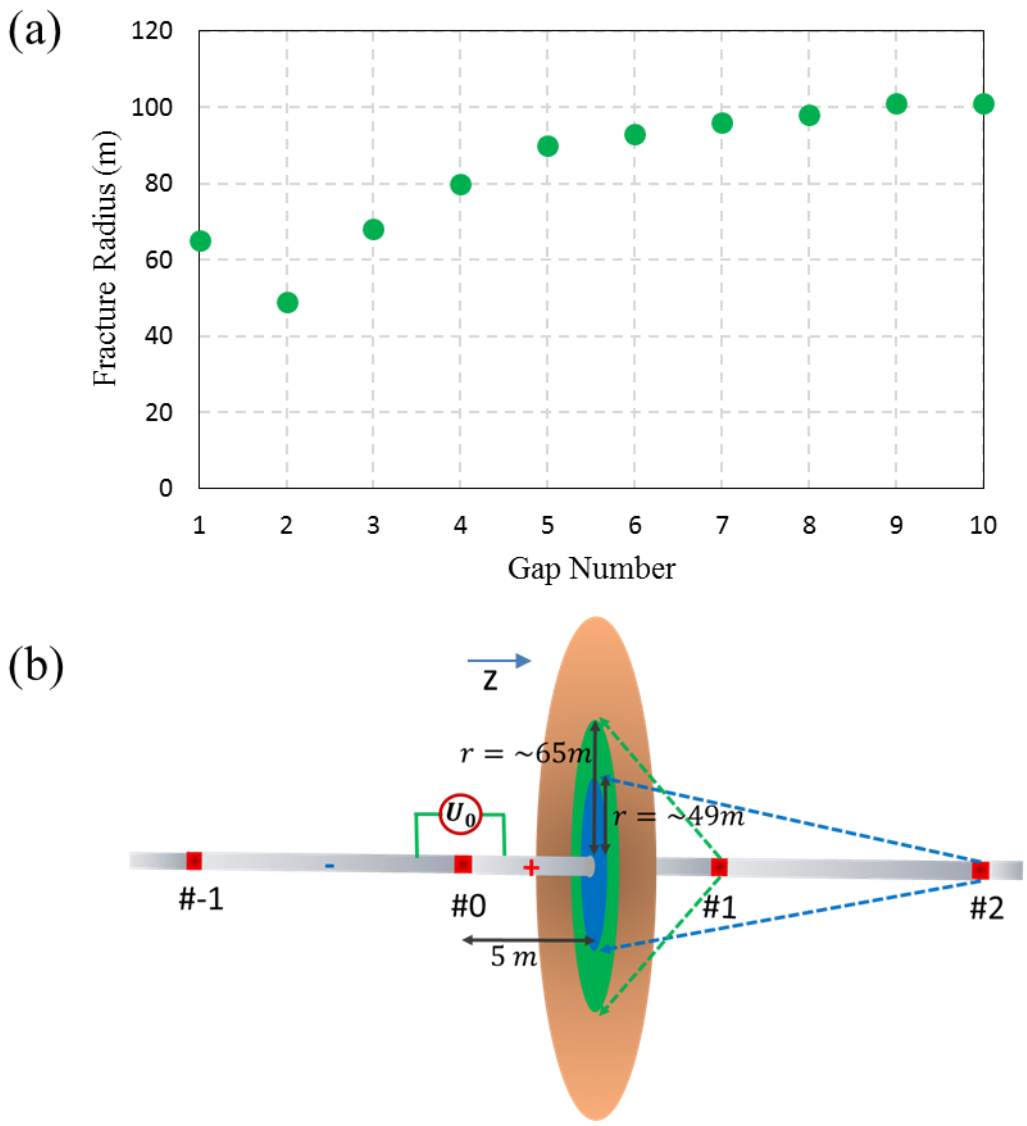

Figure 4.11 (a) Saturation limit for the various gaps assuming a $\pm 2\%$ differentiation threshold. (b) Illustration of the saturation limit for gaps #1 ($r = \sim 65\ m$) and #2 ($r = \sim 49\ m$).

The investigation depth of the proposed tool (>100 m) is much higher than what can be achieved by most of the direct proppant mapping methods. For example, radiation sensors or neutron tools can only detect radioactive or neutron capture proppant tracers in the near wellbore region, typically a few inches from the wellbore (Grae et al., 2012;

Gadeken et al., 1986). Low frequency induction methods can detect larger fractures propped by conductive proppant in open-hole wells (Yang et al., 2013; Yang et al., 2015). However, an induction tool even with long transmitter-receiver spacing (18 m) cannot differentiate between fractures with radii larger than 20 m, when the tool is operated at 100 Hz and the proppant conductivity is 100 S/m (Fig. 4.12). Using more conductive proppant and operating the tool at lower frequencies may help to increase the investigation depth. But lower frequency leads to a decreased power at the transmitter. In addition, it is impractical to use induction tools in cased wellbores. The feasibility will greatly depend on the actual signal strength under those conditions and the resolution of the receivers.

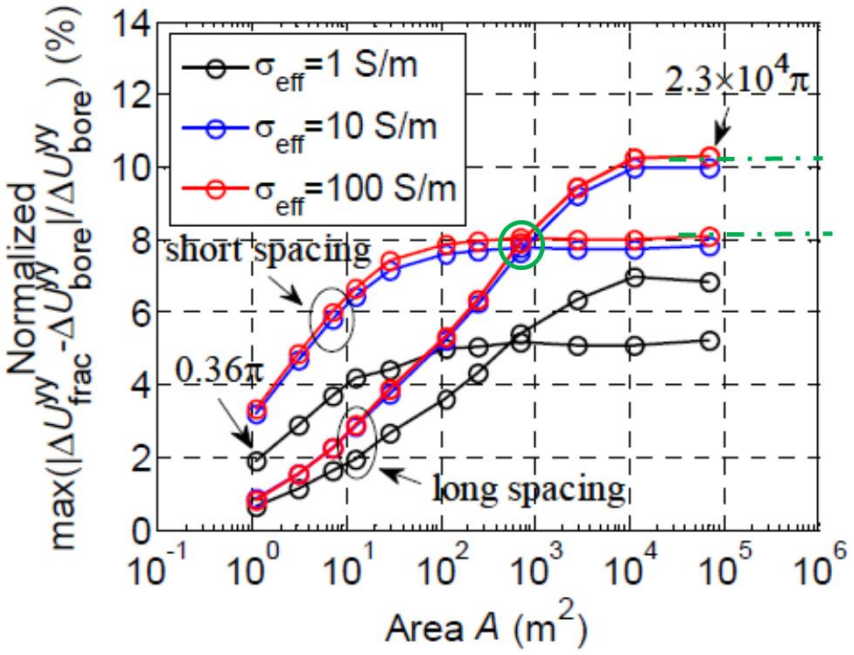

Figure 4.12 Relative signal strength using a low frequency (100 Hz) induction tool with respect to the fracture area (Yang et al., 2015). The green dashed lines mark a 2% threshold from the saturation level. The green circle marks the largest fracture size that can be differentiated.

4.5 EFFECT OF FRACTURE ANGLE

Horizontal wells are usually drilled along the direction of the minimum horizontal stress, which allows the fractures to grown perpendicular to the borehole axis. Due to the complexity and variation of the stress conditions in the reservoir, it is not uncommon to induce fractures that deviate from this orientation. Therefore, the tool's ability to detect the orientation of the fracture angle with respect to the wellbore will be very useful. To study the effect of fracture angle, we examine the tool's response to circular fractures of 30 m radius in contact with the positive electrode (5 m from gap #0), for fracture angles α in the range of 0° - 45° (Fig. 4.13).

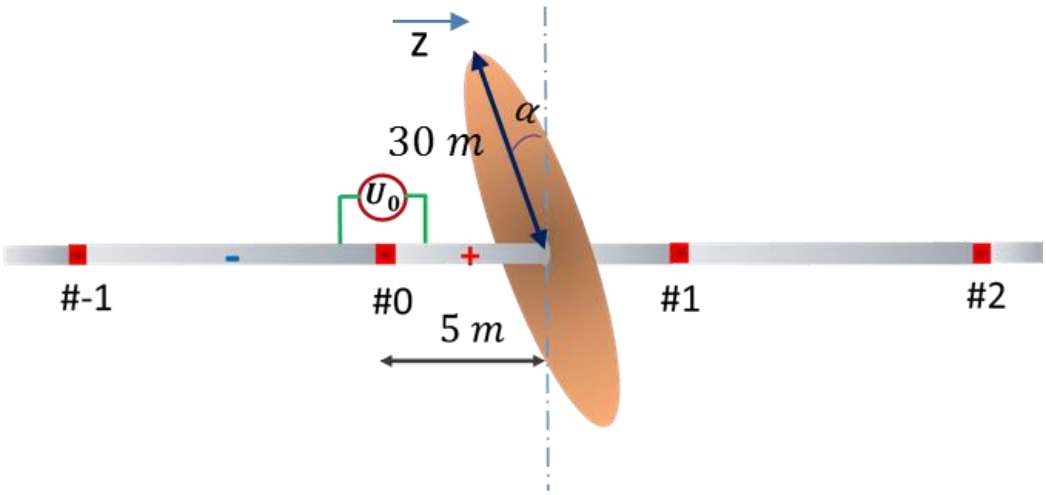

Figure 4.13 Illustration of the tool configuration with a tilted fracture of angle α.

The voltage differences from the no-fracture case for various receiver gaps ΔU_i and the normalized ones by the differential voltages obtained for the 0°-angle fracture ($\frac{(\Delta U_i - \Delta U_{i,0^\circ})}{\Delta U_{i,0^\circ}} \times 100\%$) are plotted in Fig. 4.14 and Fig. 4.15. As we have seen in the last section, the differential voltages from the no-fracture case decay as the distance between the transmitter and receiver gap increases, which is dictated by the energy dissipation in the resistive formation (Fig. 4.14). Once again, for sensitivity study purposes, a

differentiation threshold of 2% difference from the 0º case $\Delta U_{i,0^\circ}$ is assumed (Fig. 4.15). Any circles that fall into this window cannot be differentiated from the 0º case. It can be seen that most gaps are sensitive to fracture angles greater than 30º. Gap #2, unlike the rest of the gaps, appears to be sensitive to even smaller angles for a fracture of this size. If necessary, a more detailed study should be conducted to determine this gap's sensitivity to angles in the range of 0º to 15º. We expect the data from this gap to complement that from other gaps, for coverage of a broader range of angles.

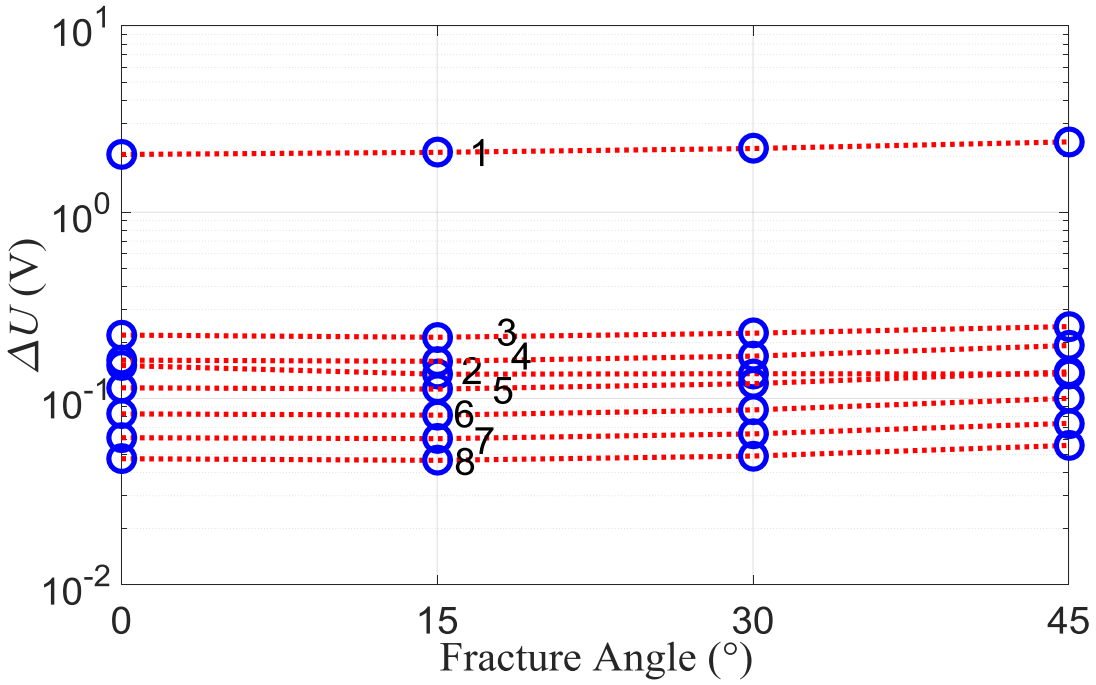

Figure 4.14 Voltage differences from the no-fracture case at various gaps as a function of fracture angle. The integers denote the number of the receiver gaps.

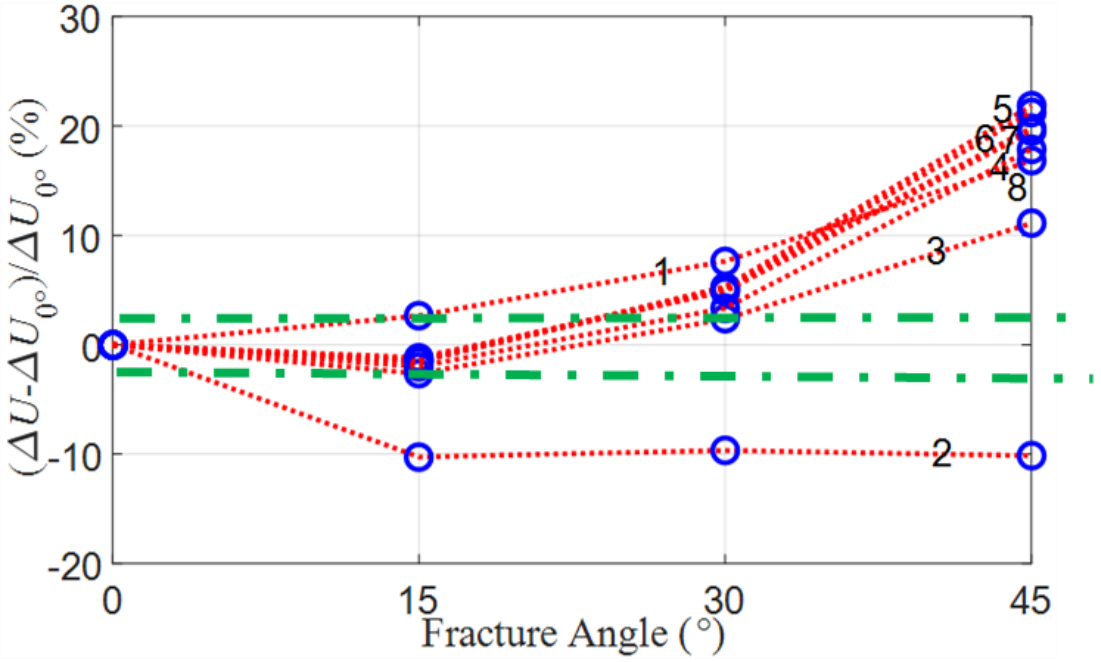

Figure 4.15 Differential voltages in Fig. 4.14 relative to the *differential* voltages obtained for an orthogonal fracture. Dashed lines mark a threshold of ±2%.

Note that the sensitivity to the angle is less than the sensitivity to fracture size. This agrees well with the observation that the dominant effect governing the signal level is the fracture's contact with the electrode, and its capability to pull current from the electrode into the formation – an effect which depends on its size more strongly than it does on its angle. The effect of the fracture orientation is likely due to (i) changes in the current distribution from the fracture into the formation and the receiver gaps and (ii) changes in the excitation of the fracture through the formation (not directly through the contact). It should be noted that these results only represent data recorded using a single transmitting gap. When multiple gaps are excited it is expected that, due to the effect of fracture location with respect to the transmitter gap demonstrated earlier, the recorded data for the various excitation gaps will contain more diagnostic information on the

fracture. Therefore, in this case, data recorded from multiple measurements will be more sensitive to the fracture angle.

4.6 EFFECT OF FRACTURE ASYMMETRY

As mentioned in the background section, proppant transport can be affected by a lot of factors, such as gravity settling and proppant retardation. Proppant tends to settle in the lower part of an induced fracture. To investigate whether the electrical measurements are sensitive to the fracture's asymmetry from the well axis, we simulated a few cases with a circular fracture (r=30 m), whose axis is displaced from the well axis by a distance of d (Fig. 4.16). The fracture is placed on the positive electrode, 5 m away from the transmitter gap. d ranges from 0 to 20 m, with an interval of 5 m.

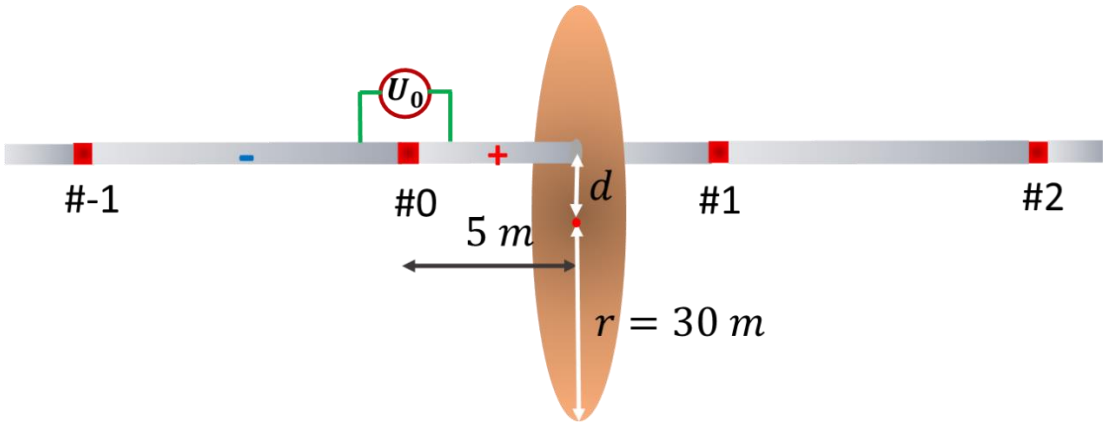

Figure 4.16 Illustration of the tool configuration with a circular fracture whose axis is displaced from the well axis by a distance d.

The voltage differences from the no-fracture case at various receiver gaps ΔU_i as a function of the deviation distance d is plotted in Fig. 4.17. Most of the curves are relatively flat, compared to the ones in the previous sections. This means the fracture's

deviation from the well axis doesn't induce significant changes at the receiver gaps, if the fracture area remains constant.

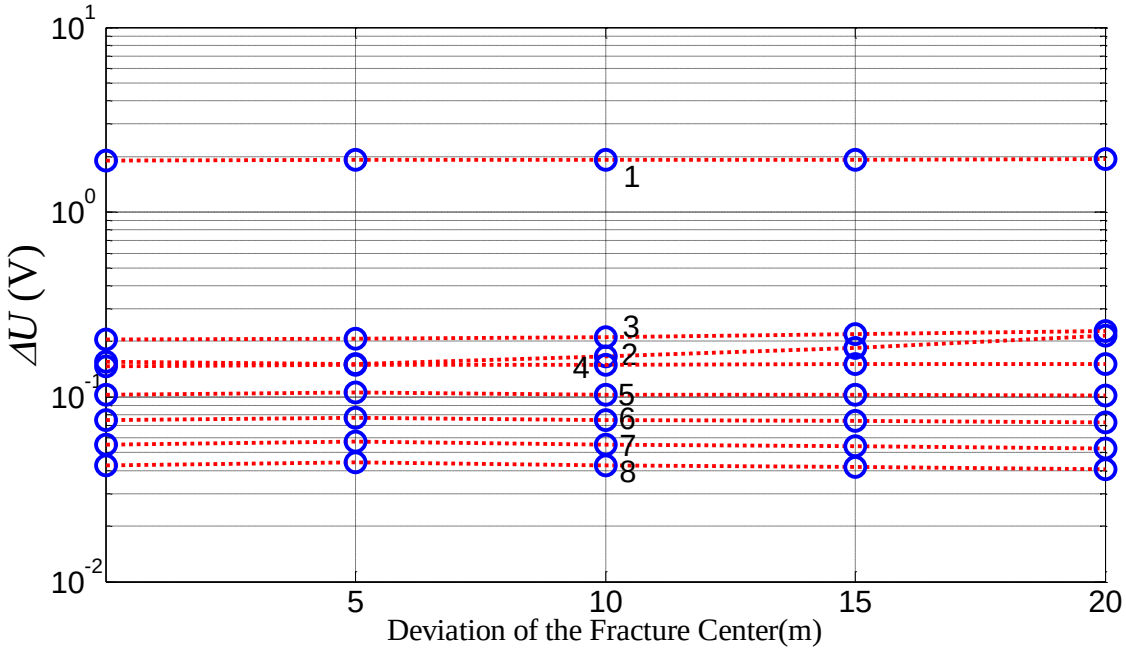

Figure 4.17 Voltage differences from the no-fracture case at various gaps as a function of the fracture deviation from the well axis.

The differential voltages relative to the ones obtained for a centered fracture ($\frac{(\Delta U_i - \Delta U_{i,\text{centered}})}{\Delta U_{i,\text{centered}}} \times 100\%$) are plotted in Fig. 4.18, for the purpose of evaluating the tool's sensitivity. Assuming a difference larger than $\pm 2\%$ is required for differentiation from the centered fracture, we can conclude that gap #2 and #3 are sensitive to a circular fracture (with radius 30 m) that is displaced from the well axis by a distance larger than 10 m. The other receiver gaps, however, are not sensitive enough to detect the difference. This limitation is expected because the tool makes measurements only in one dimension and has no azimuthal resolution.

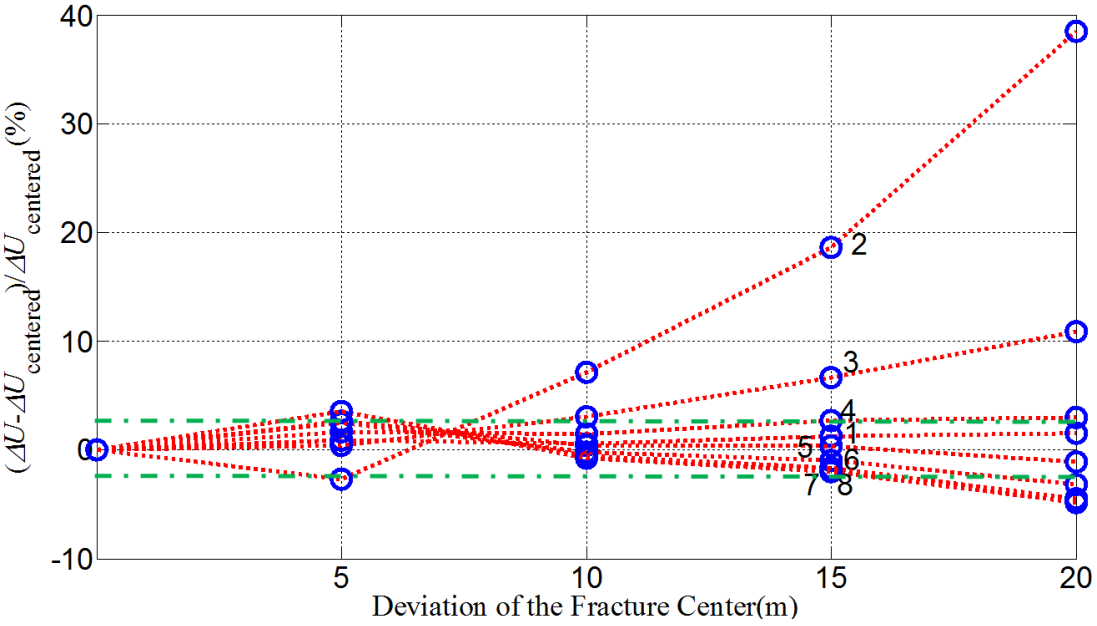

Figure 4.18 Differential voltages in Fig. 4.17 relative to the *differential* voltages obtained for the centered fracture ($d = 0$). Dashed lines mark a threshold of $\pm 2\%$.

4.7 EFFECT OF FRACTURE'S ASPECT RATIO

Thus far, we have focused on circular fractures to study the tool's sensitivity to fracture location, conductance, size, angle and deviation from the well. To study the sensitivity to the fracture's aspect ratio (or shape), we compute the tool's response to rectangular fractures of the same area ($\pi \cdot 30^2$ m^2) with varying aspect ratios. Specifically, three rectangular fractures with different aspect ratios (a/b) from 1 to 3 are placed on the positive electrode and examined separately (Fig. 4.19).

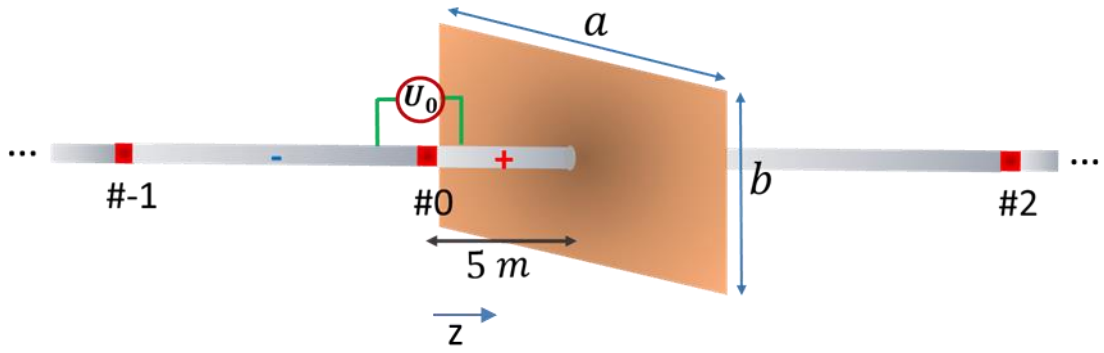

Figure 4.19 Illustration of the tool configuration with a fracture of aspect ratio a/b.

The computed potentials along the well indicate that reducing the aspect ratio results in an effect (although much less dramatic) that is similar to increasing the fracture size. This is due to the fact that when the aspect ratio is lower a greater portion of the fracture is in the vicinity of the well and contributes more to the current (and voltage) simulated at the receiver gaps.

The voltage difference from the no-fracture case ΔU_i for various receiver gaps and the differential voltages relative to the ones obtained for a square fracture ($\frac{(\Delta U_i - \Delta U_{i,AR=1})}{\Delta U_{i,AR=1}} \times 100\%$) are plotted in Fig. 4.20 and Fig. 4.21. Gap #2 and #3 can distinguish a rectangular fracture (aspect ratio > 2) from a square one, assuming, as before, that a threshold of 2% is required for differentiation. The remaining gaps are rather insensitive to the change in aspect ratio (Fig. 4.21).

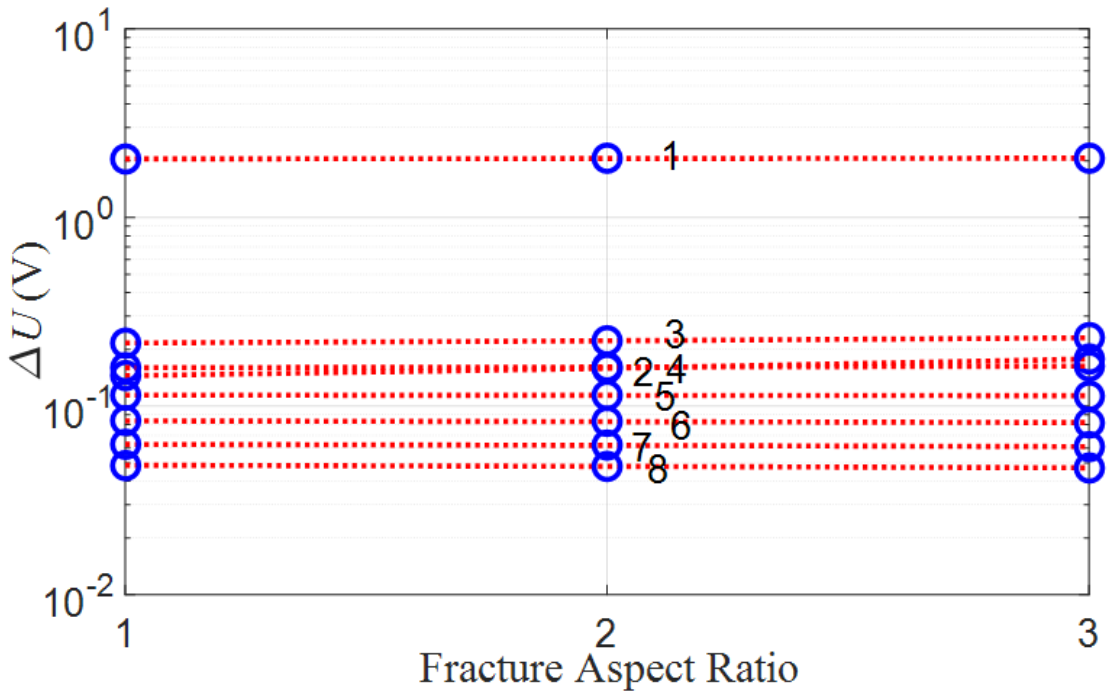

Figure 4.20 Voltage differences from the no-fracture case at various gaps as a function of the aspect ratio.

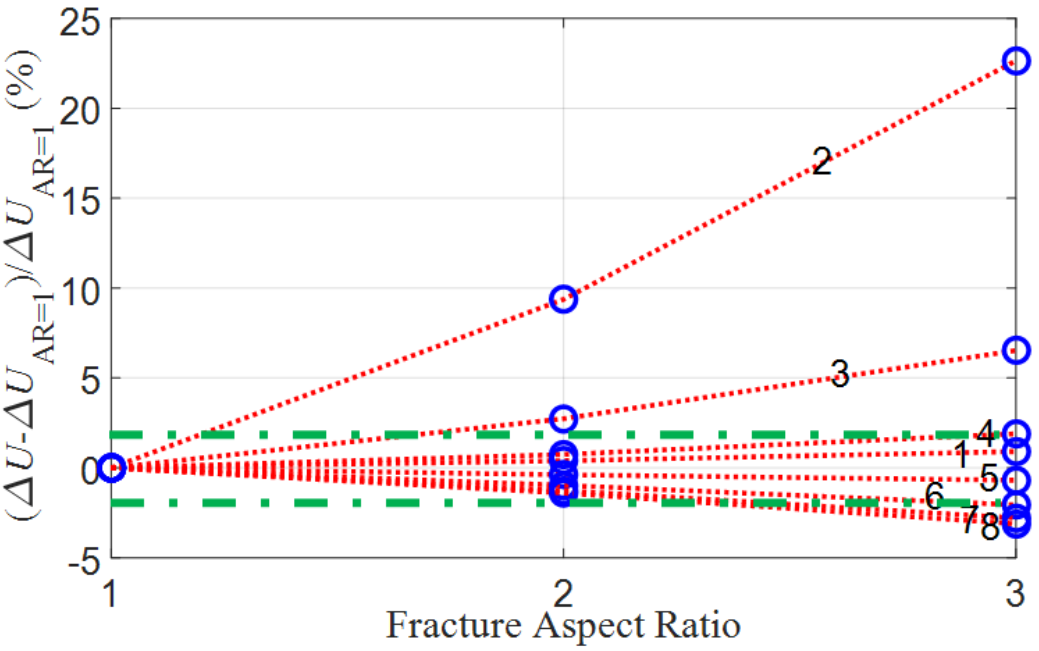

Figure 4.21 Differential voltages in Fig. 4.17 relative to the *differential* voltages obtained for the square fracture (aspect ratio = 1). Dashed lines mark a threshold of ±2%.

Similar to the previous case, where the fracture's location relative to the well has a reduced influence on the amount of current pulled from the source into the fracture, the aspect ratio does not significantly influence the current delivered from the fracture into the formation. This is the main reason why the tool's sensitivity to fracture's aspect ratio is relatively low. Moreover, our electrode-based tool only makes 1D measurements along the wellbore direction, which makes it challenging to recognize the change in fracture shape. To remedy this shortcoming, multi-dimensional measurements, such as measurements in one or more offset monitor wells, would be useful to improve the resolution in fracture shape.

4.8 INFLUENCE OF THE BACKGROUND CONDUCTIVITY

The tool's sensitivity to various fracture parameters have been investigated, assuming a homogeneous shale background with an electrical conductivity of 0.33 S/m. The actual electrical resistivity of a shale reservoir varies in a typical range of 3 – 30 $\Omega \cdot$ m (Ley-Cooper et al., 2015). Therefore, it's helpful to look at the influence of the shale resistivity for a more complete understanding of the tool's characteristics.

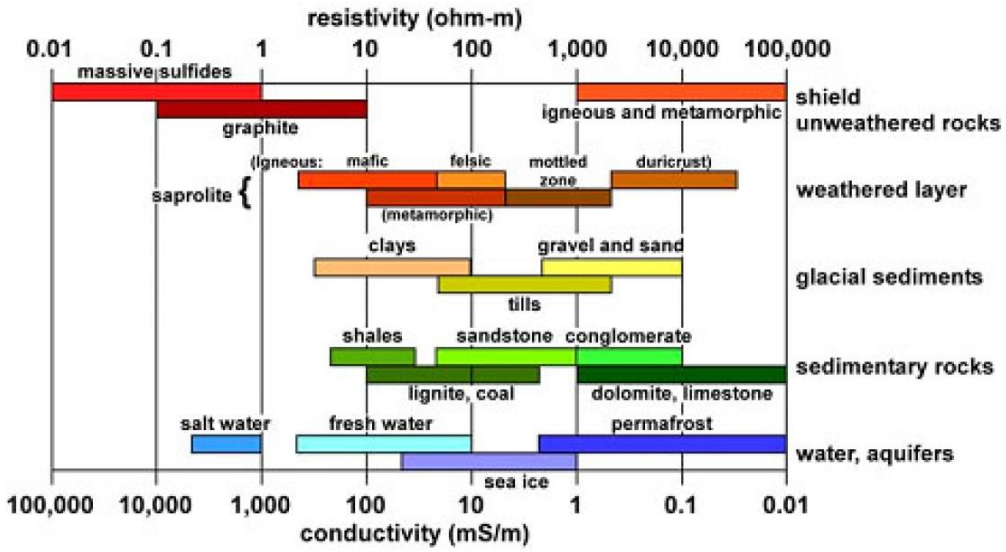

Figure 4.22 Typical ranges of electrical resistivity for selected earth materials (Ley-Cooper et al., 2015).

We selected a few values of shale resistivity within the typical range and simulated the tool's response to a circular fracture with radius 30 m. The fracture is located 5 m away from the transmitter gap (Fig. 4.4), with width of 3 cm and conductivity of 500 S/m. The calculated electrical potential along the well are plotted in Fig. 4.23. Clearly with an increasing shale resistivity (decreasing conductivity) the overall potential increases. This is because when the formation becomes more resistive,

the current density out of the source becomes weaker, which leads to a lower potential drop across every receiver gap.

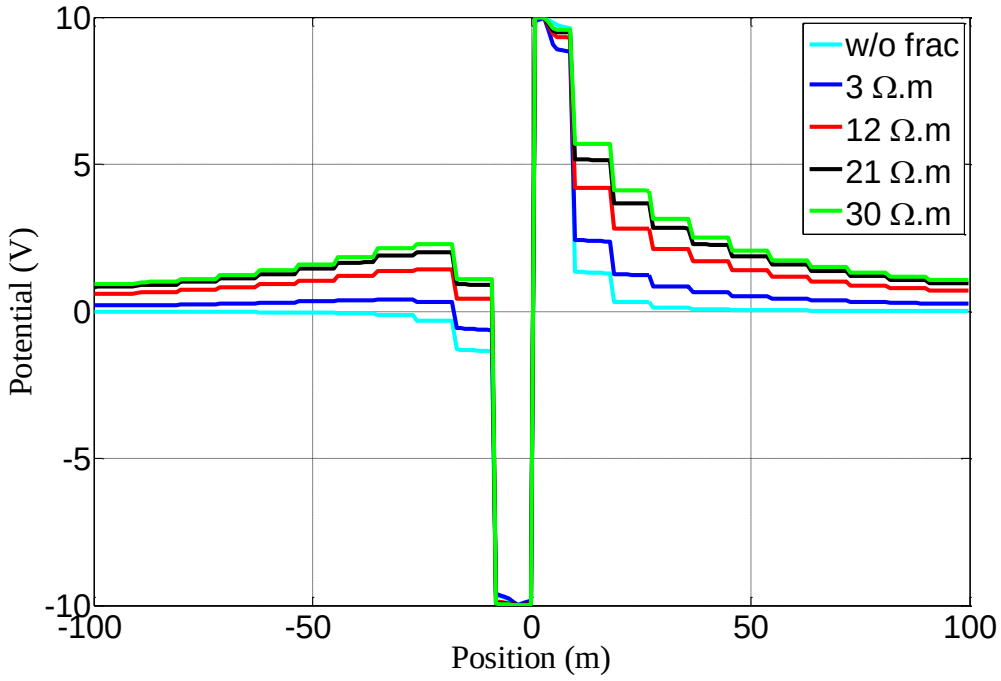

Figure 4.23 Potential along the well corresponding to difference shale resistivity.

As a result, higher voltages and differential voltages with respect to the non-fracture case are observed as the shale formation becomes less conductive (Fig. 4.24). This is similar to what's observed with increasing fracture conductance. Combing the results in 4.3 it can be concluded that the conductivity contrast between the fracture and the formation is what really matters. Not only is a more conductive proppant beneficial for a higher signal-to-noise ratio, a more resistive environment is also advantageous.

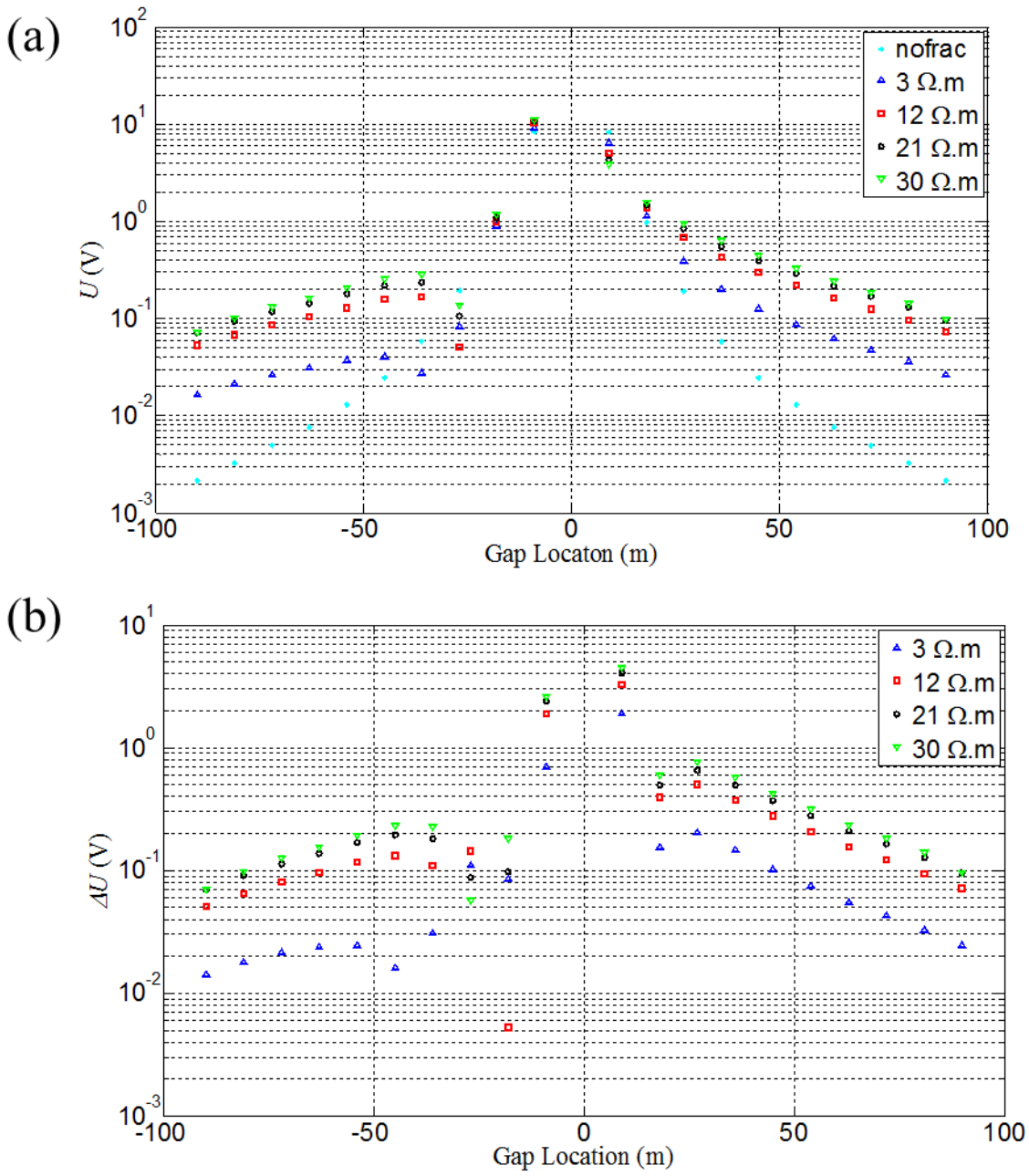

Figure 4.24 (a) Voltages at the various gaps corresponding to different shale resistivity. (b) Voltage differences from the no-fracture case corresponding to the voltages in (a).

4.9 EFFECT OF PROPPANT DISCONTINUITY

All the previous cases assume a continuous distribution of the proppant in the fracture, although the fracture's shape can be different. In reality, a lot of factors, such as the fluid rheology, injection rate and the reservoir condition, can lead to variations in proppant pack continuity. Proppant islands, or pillars may be generated. Fig. 4.25 (b) and (c) illustrate two simplified cases when proppant islands are present in different geometries. 4.25 (b) shows a case where the proppant discontinuity (white ring) happens in the radial direction, which leads to ring-shaped proppant islands. Whereas Fig. 25 (c) shows a case where the proppant discontinuity (white notches) occur in the tangential direction, which leads to fan-shaped proppant islands. We simulated these different scenarios to see how they affect the measured signals at the receivers, compared to the case when the proppant is continuous throughout the fracture (Fig. 4.25(a)).

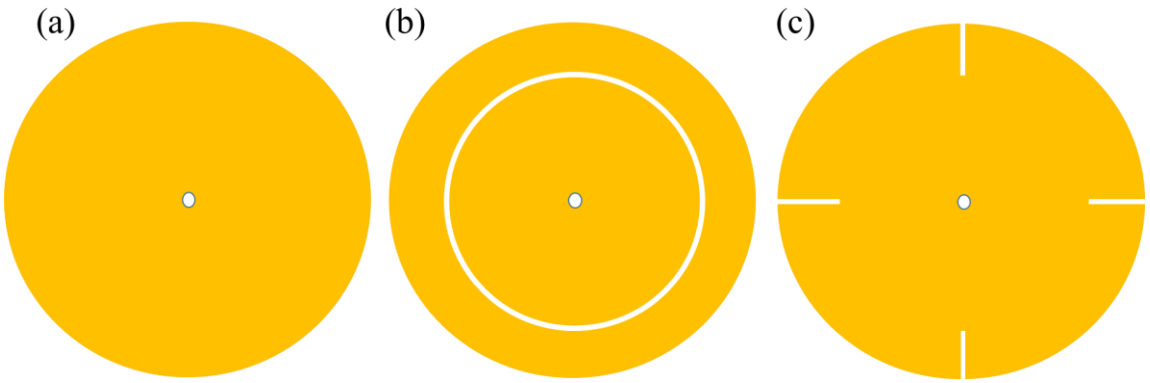

Figure 4.25 Possible proppant distribution profiles in the fracture. (a) The proppant is continuous. (b) A ring cuts the fracture into two separate parts. (c) The proppant branches out at the fracture tip.

For all the cases, the fracture is placed on the positive electrode, 5 m from the transmitter gap (Fig. 4.26(a)). For the fracture with ring-shaped proppant islands, the discontinuity is represented by a ring with inner radius r (m) and outer radius r+1 m, with the conductivity of shale (Fig. 4.26(b)). The fracture's radius is set to R=30 m. Fig.

4.26 (c) and (d) plot the voltage U and differential voltage from the no-fracture case ΔU for a fracture with continuity at r=10 m and r=20 m. Two other cases with a continuous fracture of radius 10 m and 30 m are also plotted for comparison.

Clearly the presence of proppant discontinuity in a fracture (R=30 m) affects the signals at the receiver gaps. As the discontinuity moves towards the wellbore, both the voltages and differential voltages move away from the ones for the continuous fracture of radius 30 m (blue circles). This indicates that the influence of proppant discontinuity in the radial direction becomes stronger when the continuity happens closer to the wellbore. If we take the signals when the discontinuity happens at r=10 m (black stars) and compare them to the ones for a continuous fracture of radius 10 m (red circles) and a continuous fracture of radius 30 m (blue circles), we find that the signals will suggest a continuous fracture of radius larger than 10 m, but smaller than 30 m.

To demonstrate the influence of proppant discontinuity in the tangential direction (Fig. 4.27 (a)), we also simulated a few cases for comparison: (i, ii) the discontinuity starts from (r=10 m, r=20 m) and extends to the tip; (iii, iv) a continuous fracture of radius (10 m, 30 m). The proppant discontinuity is represented by four notches of width 1 m. From the plotted voltages and differential voltages (Fig. 4.27 (b), (c)), we can conclude that the influence of proppant discontinuity in the tangential direction is much weaker than that of the discontinuity in the radial direction. Both fractures with discontinuity induce very similar signals to those induced by a continuous fracture of the same size (R=30 m). A closer look at these three cases (Fig. 4.27 (d)) tells us that if the discontinuity forms tangentially, the fracture also looks like a smaller fracture. But the tangential discontinuity does not affect the measurements or the inferred fracture dimensions as much as the radial discontinuity.

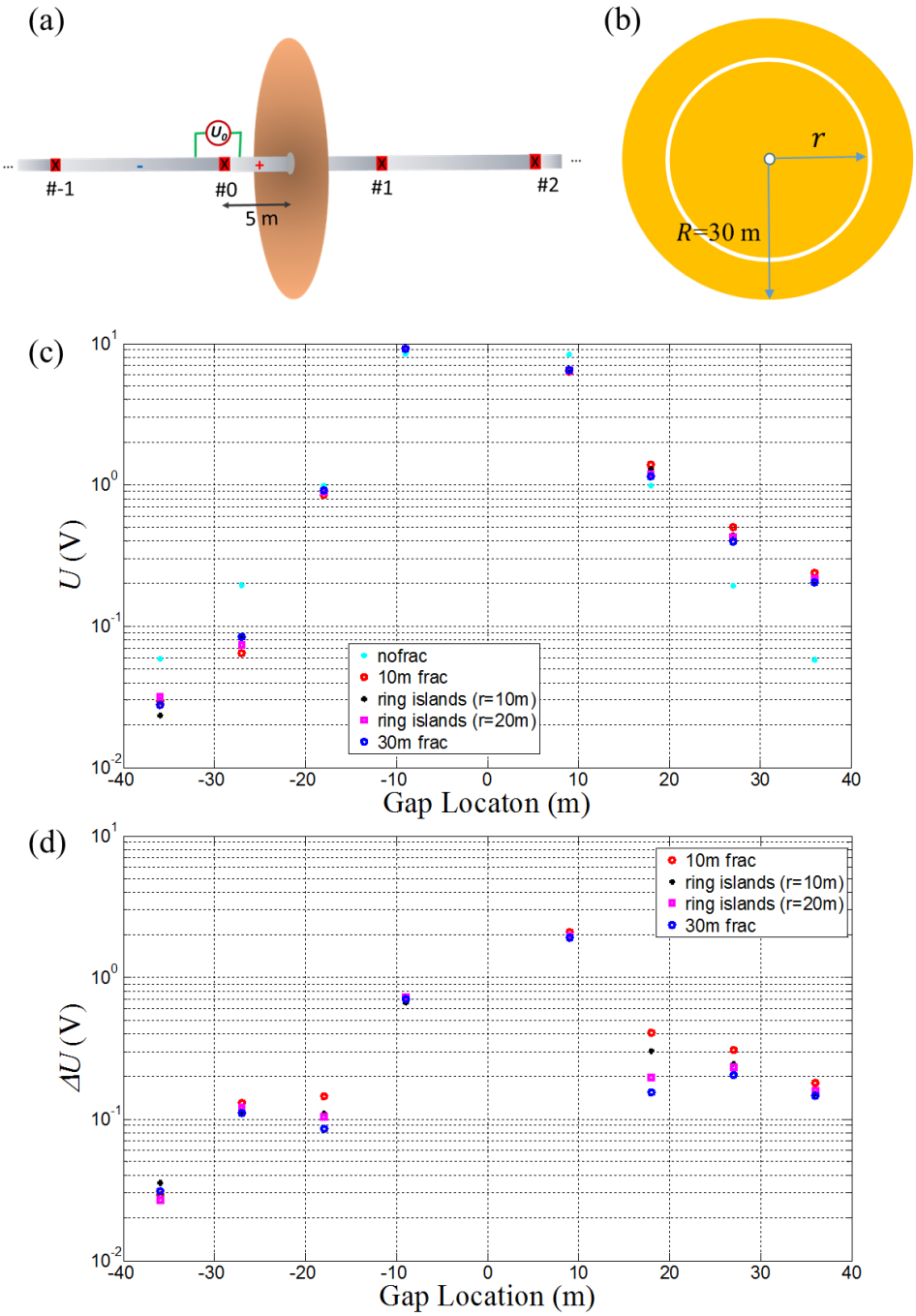

Figure 4.26 (a) Illustration of the tool configuration that is used to investigate the effect of proppant discontinuity. (b). Proppant discontinuity happens in the radial direction at radius r in a fracture of radius 30 m. (c) Voltages at the various gaps corresponding to different scenarios. (d) Voltage differences from the no-fracture case corresponding to the voltages in (c).

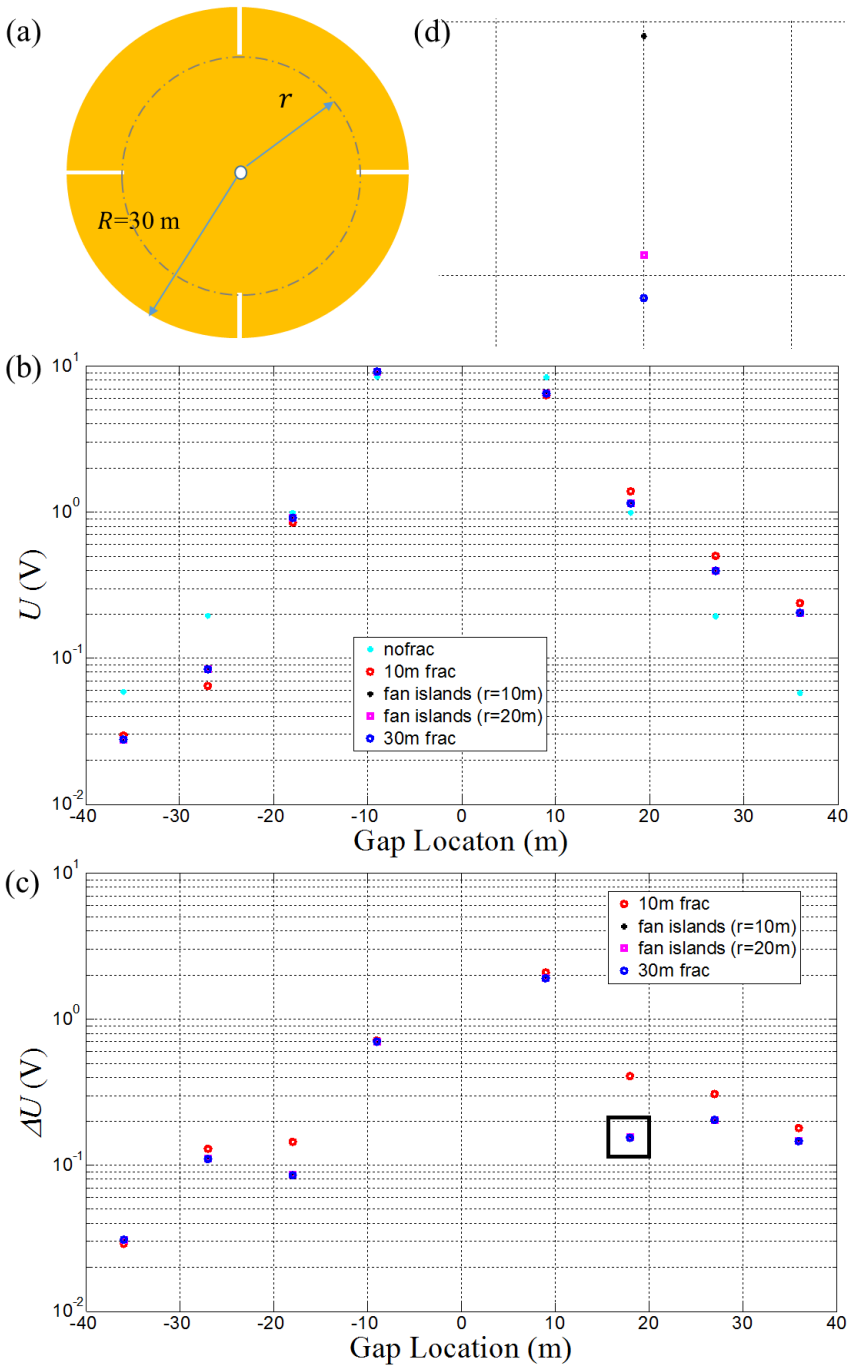

Figure 4.27 (a). Proppant discontinuity happens in the tangential direction from radius r to the tip in a fracture of radius 30 m. (b) Voltages at the various gaps corresponding to different scenarios. (c) Voltage differences from the no-fracture case corresponding to the voltages in (b). (d) An enlarged view of the area marked by the black square in (c).

In reality proppant discontinuity in the tangential direction, rather than in the radial direction, is much more likely to happen. Since our results show that the influence of proppant discontinuity in the tangential direction is insignificant, the propped fracture size can still be well captured by the tool under these circumstances.

4.10 POWER REQUIREMENT ANALYSIS OF THE TOOL

With the simulation model, we can conduct a simple power requirement analysis of the tool. This offers very useful guidance for the design and manufacture of a field-deployable tool. A case when only one fracture is in direct contact with the excited casing section and a case when no fractures are present are studied. When the conductive fracture touches the excited casing (electrode), it pulls current directly from the source, which requires more power compared to the cases when the fractures are located on the passive casing sections. When the tool takes measurements in a pre-fractured reservoir, a much weaker current out of the source is expected due to the higher resistivity of the shale background. Therefore, these two cases roughly define the upper and lower limit of the tool's power consumption.

When one fracture directly touches the excited casing section, the current flow pattern near the excited casing sections and the hydraulic fracture is depicted by Fig. 4.28. The current out of the contact point on the positive electrode (3 m from the transmitter gap) flows along the casing and gets distributed over the surface of the fracture. Meanwhile some current leaks into the formation around the casing, but it is a minor part of the total current due to the much lower conductivity of the shale background. The total current out of the source can, therefore, be approximated by the current flowing along the casing (shown by the thick green arrow in Fig. 4.28) between

the source and the fracture. The actual applied voltage on this part of the casing and its resistance, hence the current and power can be easily calculated.

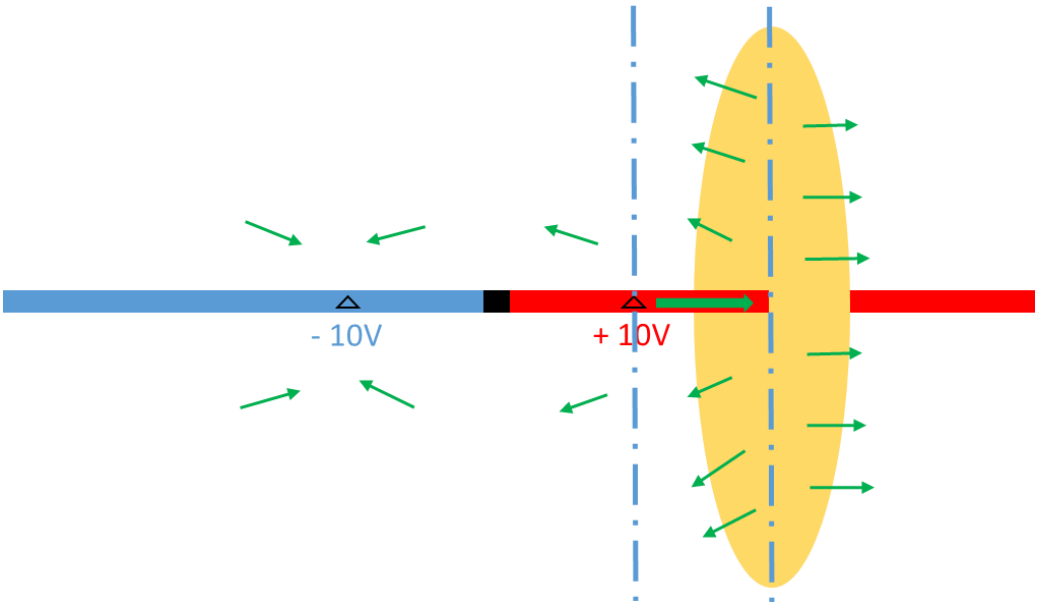

Figure 4.28 Current flow pattern around the fracture and the transmitter gap. The triangles represent the contact points between the tool and the casing, where a voltage source is applied.

Using a voltage source of $U_0 = 20$ V applied at $\pm$ 3 m from the transmitter gap (Fig. 4.28), the calculated electrical potentials along the positive electrode are plotted in Fig. 4.29. Different shale resistivity from 3 $\Omega \cdot$m to 30 $\Omega \cdot$m are used in the simulations. The fracture's radius is set to 30 m. The fractures have a width of 3 cm and a conductivity of 500 S/m, equivalent to a fracture with a width of 3 mm and a conductivity of 5000 S/m (Zhang et al., 2016). The center of the fracture is placed at 5 m on the positive side of the transmitter gap.

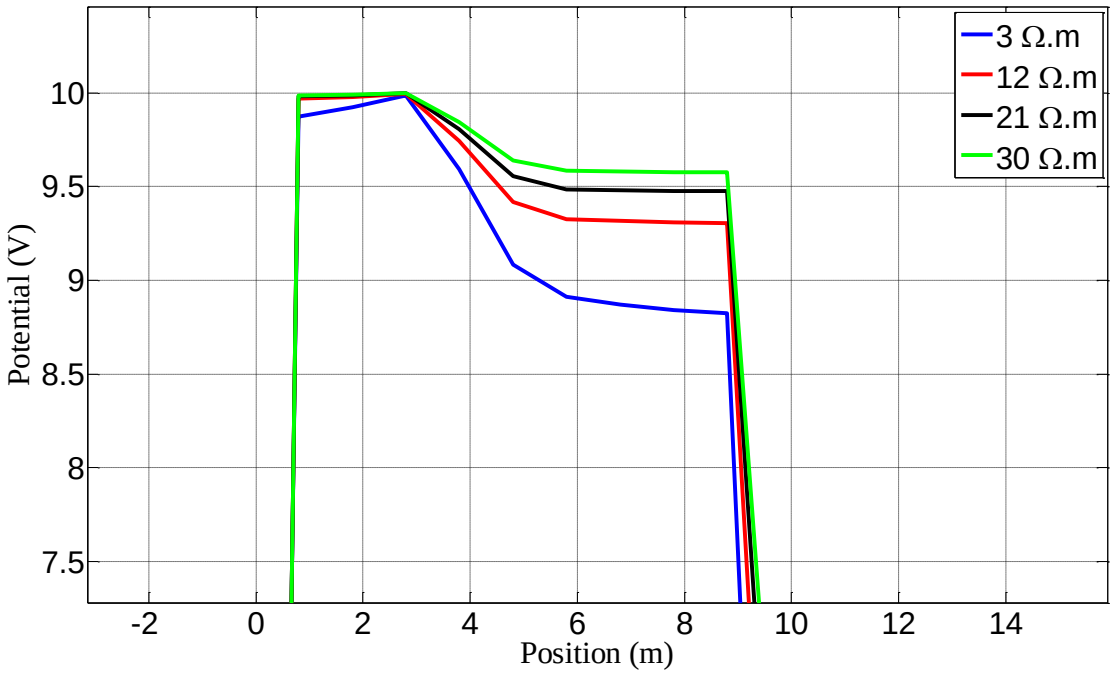

Figure 4.29 The calculated electrical potential along the excited casing on the positive side of the transmitter gap when a fracture with radius 30 m is present. Different shale resistivity is used for the simulations.

Take the case when the shale resistivity is 3 $\Omega \cdot \mathrm{m}$ as an example. The potential drop (voltage) on the casing between the source and the fracture center is about $U' =$ 1 V. Dividing U' by the resistance of this piece of casing R, we can calculate the current I, which is distributed by the fracture into the formation. The resistance of the casing is

$$R = \frac{\rho \cdot L}{A} = \frac{L}{\sigma \cdot A} = \frac{5-3}{16480 \cdot 1/4 \cdot \pi \cdot 0.14^2}\ \Omega = 0.008\ \Omega, \tag{4.1}$$

where σ and A represent the equivalent conductivity and cross sectional area of the well, which are consistent with the values used in all the cases through this chapter. Hence, the current flowing along the casing is

$$I = \frac{U'}{R} = \frac{1}{0.008}\ \mathrm{A} = 125\ \mathrm{A}. \tag{4.2}$$

Since the current flowing towards the transmitter gap is much smaller, we can approximate the total power consumption by multiplying the voltage and the current above:

$$P = U_0 \cdot I = 20\ \text{V} \cdot 125\ \text{A} = 2500\ \text{W}. \quad (4.3)$$

The current and power for the other cases are calculated in a same way and summarized in Table 2.1.

Shale Resistivity (Ω · m)	Current (A)	Power (W)
3	125	2500
12	75	1500
21	62	1240
30	50	1000

Table 4.1 Total current and power consumption when a fracture with radius 30 m is present.

If the tool makes measurements in a pre-fractured reservoir, the electrical potentials along the positive electrode are calculated, using different shale resistivity as well (Fig. 4.30). Different from the previous case, the current flowing towards and away from the transmitter gap are comparable, since no conductive fracture is present. The total current can be calculated in the following way:

$$I = J \cdot A = E \cdot \sigma \cdot A, \quad (4.4)$$

where E is the electric field, which can be calculated by taking the gradient of potential at the contact point (3 m). The results for different shale resistivity are summarized in Table 2.2. Apparently both the current and power consumption in a pre-fractured reservoir are lower, due to the lack of a highly conductive conduit, i.e., fracture.

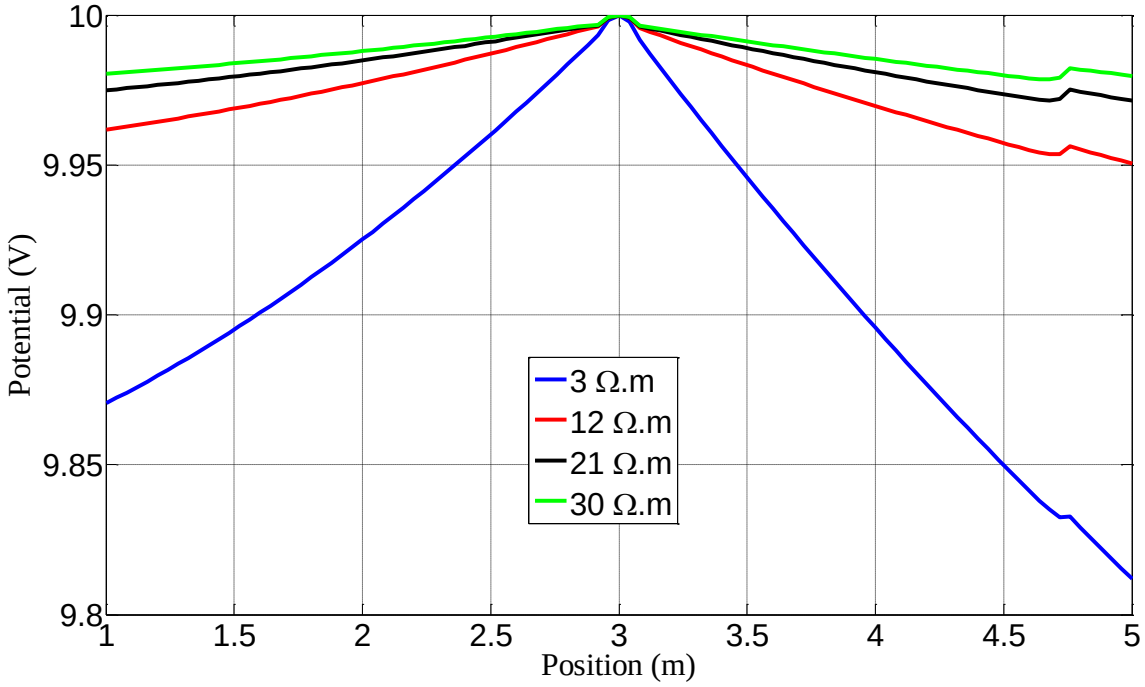

Figure 4.30 The calculated electrical potential along the excited casing on the positive side of the transmitter gap when no fracture is present. Different shale resistivity is used for the simulations.

Shale Resistivity (Ω · m)	Current (A)	Power (W)
3	40	800
12	13	260
21	9	180
30	7	140

Table 4.2 Total current and power consumption when no fracture is present.

If a downhole battery is used to apply the voltage source across the transmitter gap, both the output current and power above would be too high to achieve. Since the governing equation 3.1 is linear, the electrical potential scales with the voltage that is applied. Depending on the capacity of the battery, we can choose the strength of the

voltage source accordingly. For example, if the maximum power that a battery set can provide is 50 W, the maximum voltage that can be applied will be $U_0 = 2.8$ V, when a fracture with radius 30 m is present and the shale resistivity is 3 $\Omega \cdot$ m.

4.11 SUMMARY AND CONCLUSIONS

A numerical model based on FVM has been used to simulate the tool's sensitivity to multiple variables of a single fracture including location, conductance, size, angle, deviation from the well and aspect ratio. The fracture's presence modifies the path for current from the source (casing) into the formation and hence modifies the potential distribution along the insulator-separated casing string, compared to the no-fracture case. The tool's sensitivity to different fracture parameters is summarized below:

- The tool is highly sensitive to fracture location relative to the source electrodes (sections of casing where the voltage is applied). When the fracture is in direct contact with the transmitter electrode, two physical mechanisms were observed to govern the change in the simulated voltages: i) strong leakage of current from the excited casing section into the fracture and then into the formation; ii) weaker leakage directly from the casing sections into the formation and then to the fracture. When there is no direct contact between a transmitter electrode and the fracture, the only mechanism for exciting the fracture is through the formation and the signal levels decrease. That is why the measured voltages at the receiver gaps are much stronger when the fracture touches the excited casing section.
- The tool is also very sensitive to fracture conductance. More current is pulled from the electrode as the fracture becomes more conductive. Consequently, more current gets distributed over the fracture's surface and reaches the receiver gaps. The voltages across these gaps increase according to Ohm's law. The increase in

formation resistivity leads to similar results. What really matters is the contrast between the fracture conductivity and the shale conductivity, if all the other fracture parameters remain unchanged.

- In terms of fracture size, depending on their distance from the fracture, the gaps show varying saturation limits to fracture radii that are in the range of 50 m – 100 m, if a threshold detection limit of $\pm$2% is assumed. This depth of investigation is far larger than what an induction tool can achieve, even in an open-hole environment. The presence of a small fracture with radius 2 m can be easily detected by the tool.
- The simulations also show that the tool is sensitive to the orientation of the fracture from the wellbore axis. Most of the single receiver gaps can easily detect fracture angles greater than 30^{o} from orthogonal if a threshold detection limit of $\pm$2% is assumed. Data from all the receiver gaps can potentially be integrated to cover fracture angles lower than 15^{o}.
- The simulated signals are shown to be less sensitive to the fracture's asymmetry, as well as the fracture's aspect ratio. This is because the dominant effect governing the signal level is the fracture's influence on the current pulled from the electrode into the formation – an effect which depends on the fracture's location with respect to the source, the conductance and the size, more strongly than it does on its shape and position with respect to the well.
- Proppant discontinuity affects the simulated signals at the receiver gaps. The fracture looks like a smaller fracture if discontinuities exist. A discontinuity in the radial direction shows a stronger influence than a discontinuity in the tangential direction.

Integration of data from multiple receiver gaps, corresponding to each transmitter location, needs to be considered as a part of inversion algorithm for identifying fracture location, conductance, size, etc. This should provide a higher sensitivity to fracture geometry and reduce non-uniqueness than that obtained using a single gap. The inversion method and results will be presented in a later chapter.

A simple analysis was conducted using the simulation results to estimate the power requirements for a downhole tool. The total current output from the source was approximated by calculating the potential gradient (electrical field) at the source location. Depending on the current and power restrictions of the power source being used, the applied voltage can be scaled down linearly.

NOMENCLATURE

$\boldsymbol{\delta}$ = width, mm

$\boldsymbol{\sigma}$ = electrical conductivity, S/m

$\boldsymbol{U_i}$ = measured voltage at receiver gap $\boldsymbol{i}$, V

$\Delta\boldsymbol{U_i}$= differential voltage with respect to the no-fracture case, V

$\boldsymbol{r}$=fracture radius, m

$\boldsymbol{U_{frac,i}}$= measured voltage at receiver gap $\boldsymbol{i}$ when a fracture is present

$\boldsymbol{U_{no-frac,i}}$= measured voltage at receiver gap $\boldsymbol{i}$ when no fractures are present

α=fracture angle, degree

$\boldsymbol{d}$=fracture deviation from the well, m

a=fracture length, m

b=fracture height, m

$\boldsymbol{U_0}$=voltage applied on the transmitter gap, V

I=electric current, A

R=resistance, Ω

P=power, w

L=length, m

Chapter 5 Forward Modeling – Simulation of Multiple Fractures

5.1 BACKGROUND

As mentioned in the introduction, some key technologies for hydraulic fracturing have been widely used to achieve high initial production rates and improve recovery of hydrocarbons. Horizontal wells with toe-up lengths of 2500 ft to over 5000 ft are drilled and then fractured in multiple stages (King, 2010). Multi-stage fracturing increases the contact with the formation and, therefore, greatly improves the productivity of the well (Casero et al., 2008; Castaneda et al., 2010; Durst et al., 2008; Grieser et al., 2009; Seale et al., 2006). A detailed sensitivity study has been conducted in Chapter 4 to investigate the ability of our tool to estimate various geometrical parameters of a single fracture. However, in most wells multiple fractures will be present along one or more wells. In this chapter we present simulation results for multiple fractures and propose inversion approaches (since this is the ultimate goal of this research).

The presence of multiple fractures poses new questions, because they may interact with each other when conducting electrical measurements. This interaction cannot be simply addressed by superposition of solutions for single fractures. The interactions of fractures and their combined effect on the measured signals at the receivers have to be investigated by including them in one single simulation. Interpretation of the simulation results can provide insights into the tool's capability and possible limitations when detecting multiple fractures, as well as offer guidance for the inversion analysis.

We use the same numerical method introduced earlier to conduct forward simulations on multiple fractures. For all the examples, we consider a horizontal well embedded in a homogeneous shale reservoir. The horizontal well under investigation is about 200 m long, and is composed of 22 standard 9 m (~ 30') long casing sections and 21 0.02 m long insulating gaps. The model is sufficiently long to incorporate all the gaps

with detectable signal levels. Again, the inner and outer diameters of the casing and gaps parts are 0.128 m (5'') and 0.14 m (5.5''), respectively. The electrical conductivities of the casing, insulating gaps, and shale background are set to 10^5 S/m, 10^{-12} S/m, and 0.33 S/m, respectively. Resistive mud is required to prevent a short circuit across the transmitter gap and its conductivity is set to 0.05 S/m. The fractures are assumed to be circular disks with uniform thickness. When not specified otherwise, the fractures' width δ and conductivity σ are set to 3 mm and 5000 S/m (Zhang et al., 2016), respectively. In the actual simulations, the thin fractures are replaced by thicker ones (δ = 3 cm) with lower conductivity (σ = 500 S/m), maintaining the product of their conductivity σ and width δ constant, to ease the mesh generation and speed up the simulations without sacrificing the accuracy of the results. This approach for simplifying fractures has been validated and used in Chapter 3 and 4.

5.2 MULTIPLE FRACTURES SEPARATED BY INSULATING GAPS

A base case is simulated to demonstrate the multi-fracture problem, and to study their combined influence on the measured voltages at the receivers. Three conductive fractures 1, 2 and 3 with the same size (r=20 m) are in contact with three neighboring casing sections. The casing sections forming the central gap #0 are excited at two contact points located $\pm$3 m from gap #0, with DC potentials of $\pm$10 V. The fractures are 5 m, 14 m and 23 m away from the excited gap. We set z = 0 along the well to be at the center of gap #0 (Fig. 5.1). To investigate the role of each fracture, four other cases are also simulated: (i) two fractures (2 and 3) are present, (ii - iv) only one of the three fractures is present, with the same voltage source applied. Figure 5.2 – 5.4 show the comparison between the computed results for the base case and the other ones.

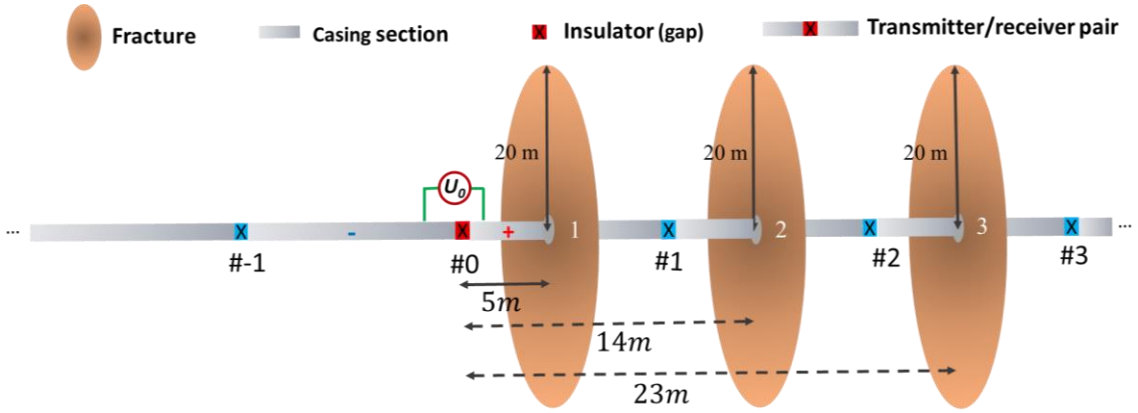

Figure 5.1 Illustration of the tool configuration with three fractures touching different casing sections.

The computed electrical potential along the well for all the cases are plotted in Fig. 5.2. Based on these results, we also calculated the measured voltages U and differential voltages $\Delta U = U_{frac} - U_{no-frac}$ at various receiver gaps (Fig. 5.3 and 5.4). The results indicate that when all the three fractures are present, the one that is in contact with the excitation electrode (fracture 1) dominates the signals received at the receiver gaps. When only fracture 1 is present, both the voltages and the differential voltages at various gaps are close to the ones in the three-fracture case, except for some local differences near fracture 2 and fracture 3. However, when one or two fractures among 2 and 3 are present, only the voltages measured at the receiver gaps right next to the fractures (marked by the red circles in Fig. 5.4) are strong. The voltage level at other receiver gaps is much lower compared to that when fracture 1 or all three fractures are present (Fig. 5.3 and 5.4).

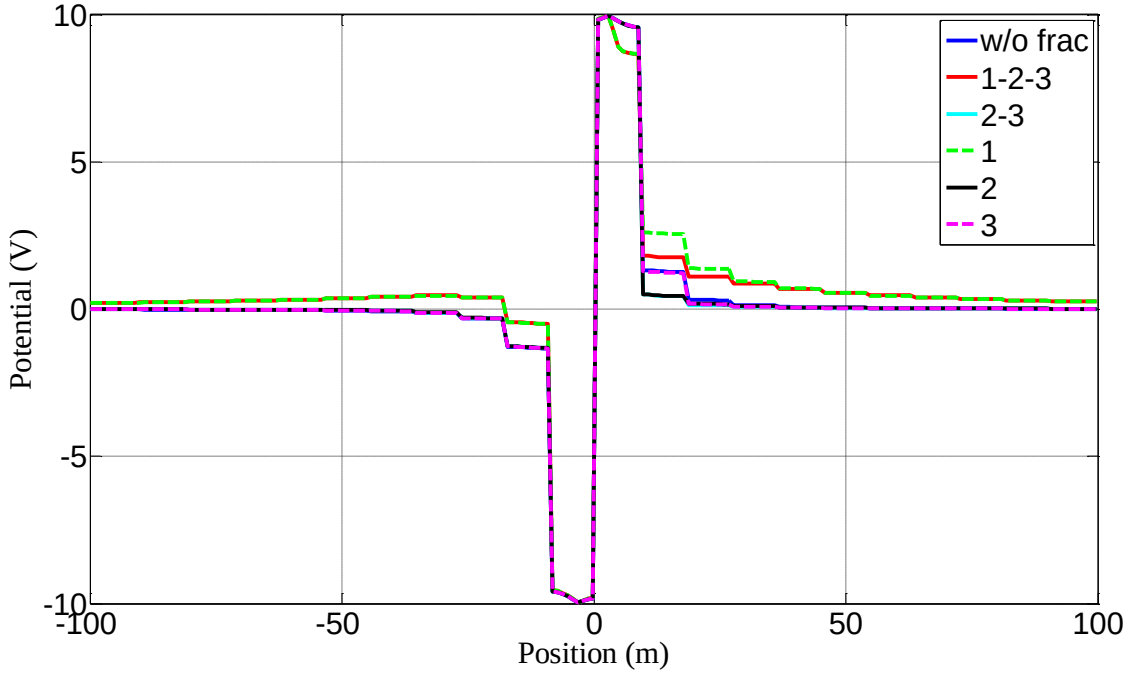

Figure 5.2 Computed potentials along the wellbore for different cases.

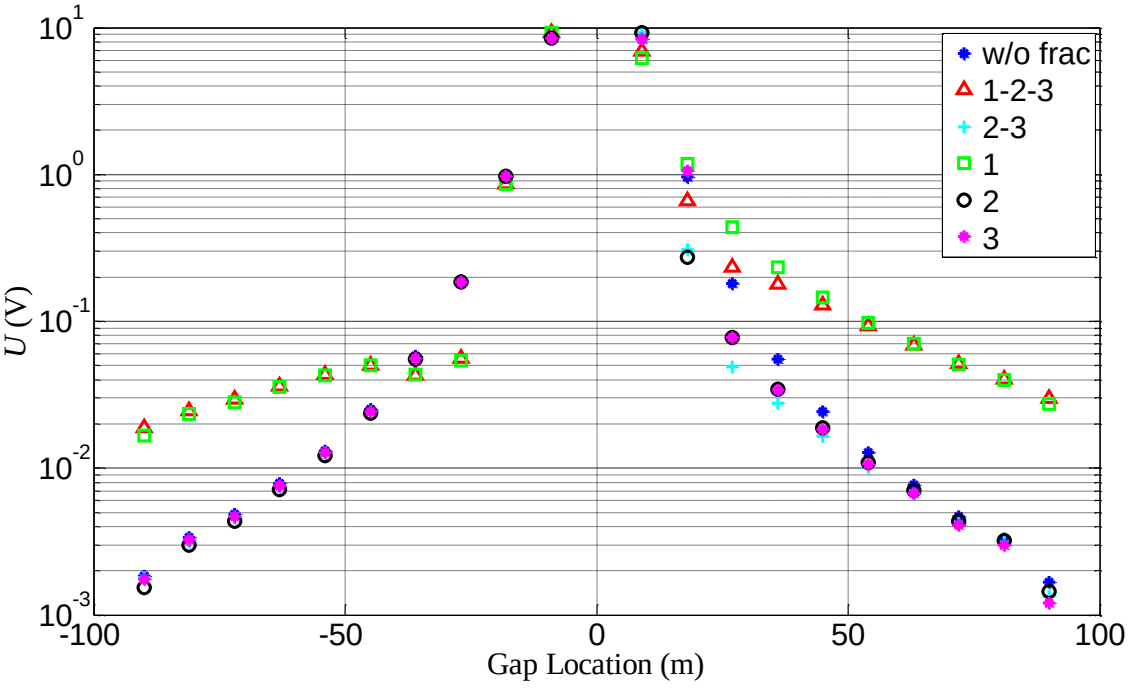

Figure 5.3 Voltages at the various receivers calculated based on the results in Fig. 5.2.

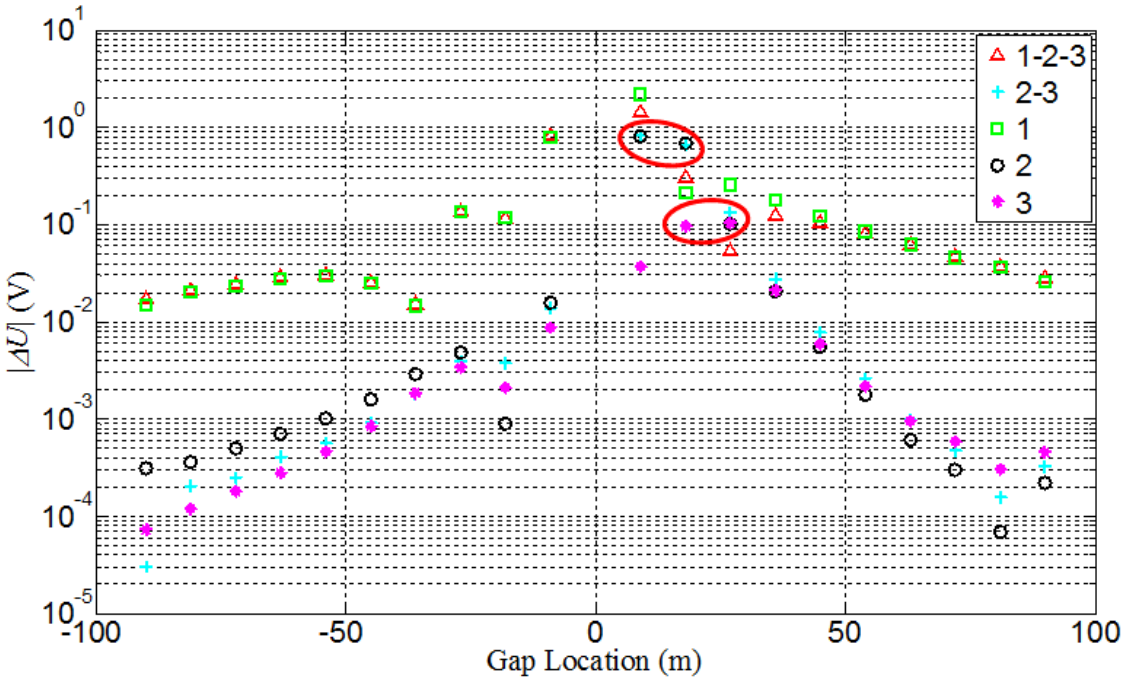

Figure 5.4 Voltage differences from the no-fracture case corresponding to the voltages in Fig. 5.3.

We observed a strong current leaking from the excited casing section into the fracture and then into the formation, when a fracture (e.g., fracture 1) touches the excitation electrode (Zhang et al., 2018 a). When a fracture (e.g., fracture 2 or 3) is not in direct contact with the excited casing, current leaks directly from the casing sections into the more resistive formation and then to the fracture (e.g., fracture 2 or 3), which is a second order effect. In the former case, the fracture serves effectively as an extension of the casing section it touches. Whereas in the latter case, the only mechanism for exciting the fracture is through the formation and the signal levels decrease.

This phenomenon confirms the necessity of exciting multiple gaps in a logging sequence, for extracting the geometries of multiple fractures. Moreover, it can be significant for choosing an appropriate inversion strategy, according to the requirements of accuracy and efficiency.

Suppose in a logging sequence N insulating gaps are excited one by one, as the tool moves in the wellbore. N sets of data will be collected when the logging sequence is finished. If speed is the primary concern, the local influence of fractures that are not in direct contact with the excited casing sections can be neglected. We can use each of the data set only for characterizing fractures that are on the excited casing. This can greatly accelerate the inversion process since only a few fractures are involved in the forward model. By adjusting parameters for these fractures we can quickly match each of the data set. On the other hand, if accuracy is the primary concern, the local effect of fractures that do not directly touch the excited casing sections has to be considered. The inversion process will be dramatically slowed down because all the fractures have to be included in the forward model. Due to the trade-off between speed and accuracy for the inversion analysis, one should determine the most suitable inversion scheme depending on the needs (Zhang et al., 2018 b). The comparison of speed and accuracy of the inversion results will be exhibited in the next chapter.

5.3 TWO FRACTURES ON ONE CASING SECTION

When the fracturing fluid is being pumped into the reservoir, some more complicated situations might be encountered. For instance, more than one fracture may be generated on the same casing section (Fig. 5.5(a)). Complex nonplanar fracture geometries are not uncommon in reservoirs with low differential stress. If we simplify a complex fracture to two planar fractures with the same total volume next to each other, we can simulate it using our forward model (Fig. 5.5(b)).

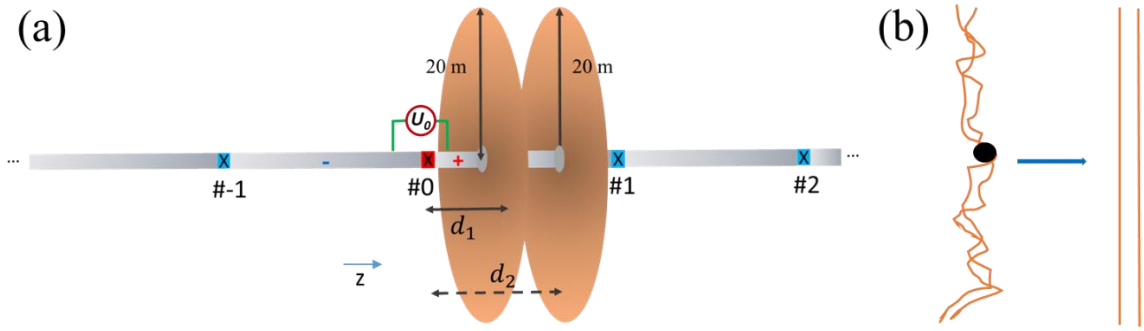

Figure 5.5 (a) Illustration of the tool configuration with two fractures touching the same excited casing section. (b) The complex fracture is simplified to two planar fractures in parallel with the same total thickness.

Three different scenarios are simulated using the forward model to investigate the tool's response: (i) two conductive fractures with a width of 3 cm on the same casing section are far apart ($d_1 = 2\ m, d_2 = 7\ m$), (ii) two fractures of the same geometries are 0.5 m away ($d_1 = 4.5\ m, d_2 = 5\ m$), which represent the complex fracture in Fig. 5.5(b), and (iii) one fracture of the same size and conductivity, but with double width (6 cm) is placed at 5 m from gap #0. Again a voltage source of 20 V is applied on gap #0 and we set z = 0 along the well to be at the center of this gap. For all three cases, the fractures are on the same excited casing section (positive electrode). The voltages U and the differential voltages ΔU from the non-fracture case are compared (Fig. 5.6 and 5.7).

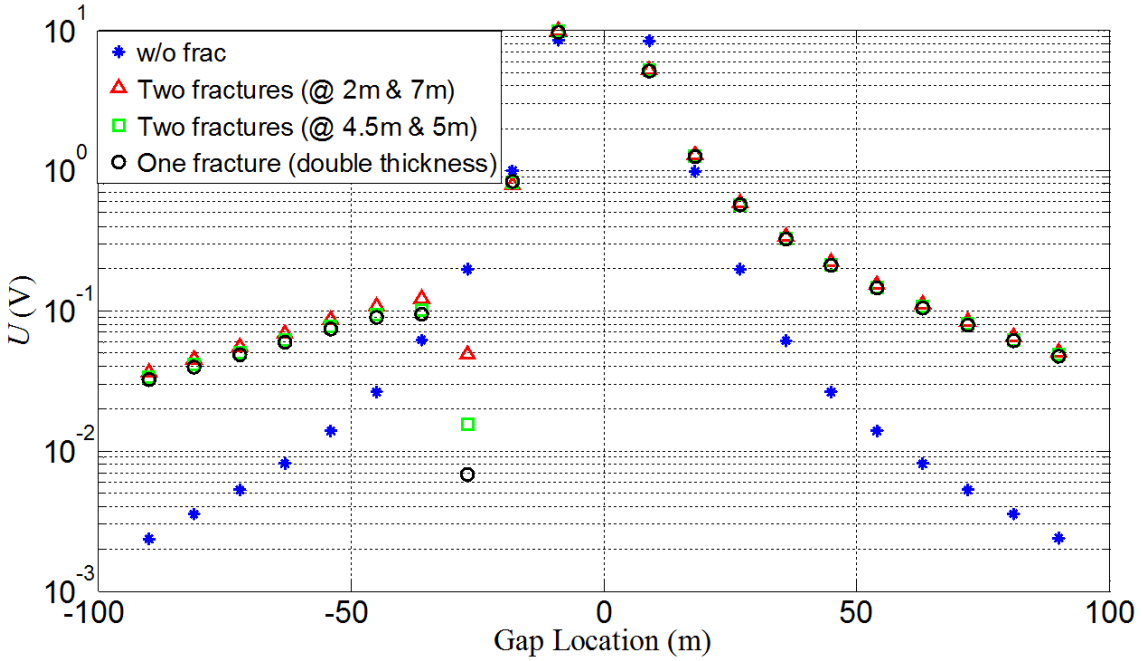

Figure 5.6 Voltages at the various gaps with respect to different scenarios.

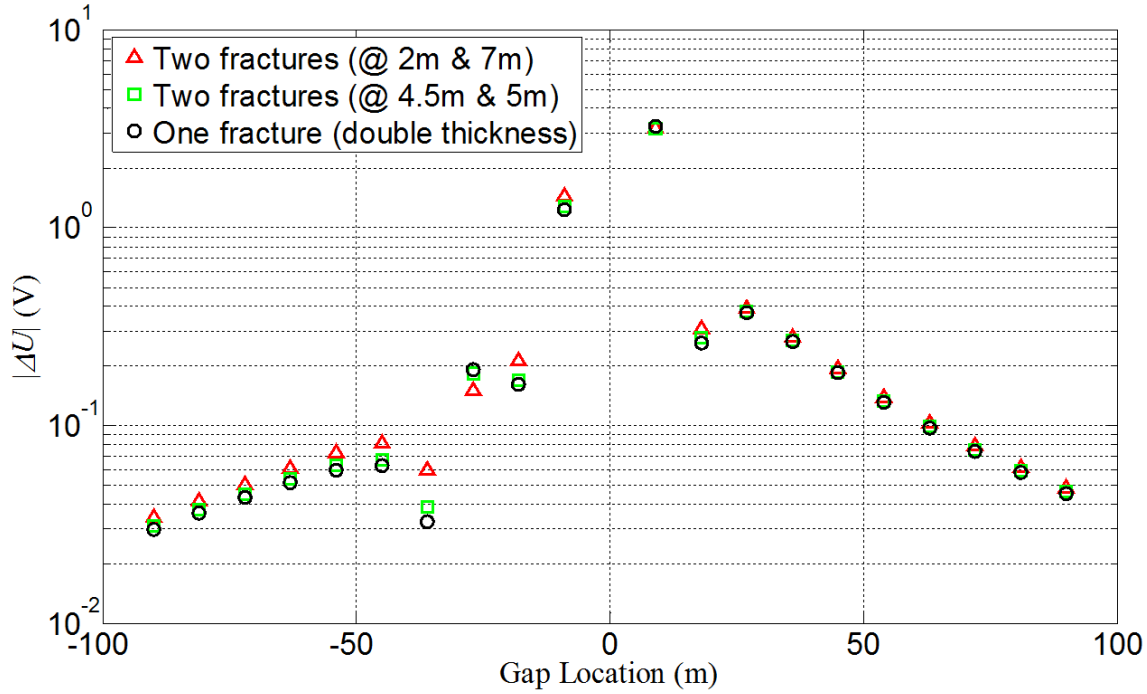

Figure 5.7 Voltage differences from the no-fracture case corresponding to the voltages in Fig. 5.6.

Clearly the single fracture with double width induces very similar signals at the receiver gaps to those from two thinner fractures with the same conductivity and total volume. And as the two fractures get closer, the results converge to the single-fracture case. Comparison of case (ii) and (iii) indicates that the tool's response depends mainly on the fracture's volume instead of its complexity, for fractures of up to the studied propped area, perpendicular to the wellbore. Comparison of case (i) and (iii) suggests that two fractures touching the same casing section are not easily recognized from a single but thicker fracture, merely by inverting the voltages at various receiver gaps. Due to this limitation, some prior knowledge of the fractures' initiation locations, that can possibly help to extract decent fracture geometries from the inverse analysis, is also important (Zhang et al., 2018 b).

We also studied similar cases when the fractures are not in direct contact with the excited casing section, to verify the universality of the previous conclusions. Fig. 5.8 shows two fractures on the same casing section that is isolated from the excited one by an insulating gap.

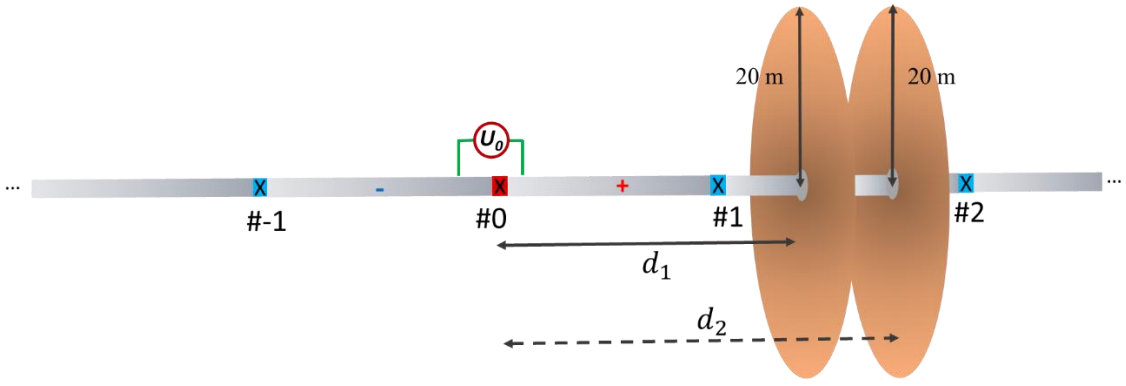

Figure 5.8 Illustration of the tool configuration with two fractures touching a passive casing section. This casing section is isolated from the excited one by an insulating gap.

Similarly, we simulated three different scenarios using the forward model to investigate the tool's response: (i) two conductive fractures with width of 3 cm on the same casing section are far apart ($d_1 = 11\ m, d_2 = 16\ m$), (ii) two fractures of the same geometries are 0.5 m away ($d_1 = 13.5\ m, d_2 = 14\ m$), which also represent a tangled fracture shown by Fig. 5.5(b), and (iii) one fracture of the same size and conductivity, but with double width (6 cm) is placed at 14 m from gap #0. Likewise, the voltages U and the differential voltages ΔU from the non-fracture case are compared (Fig. 5.9 and 5.10).

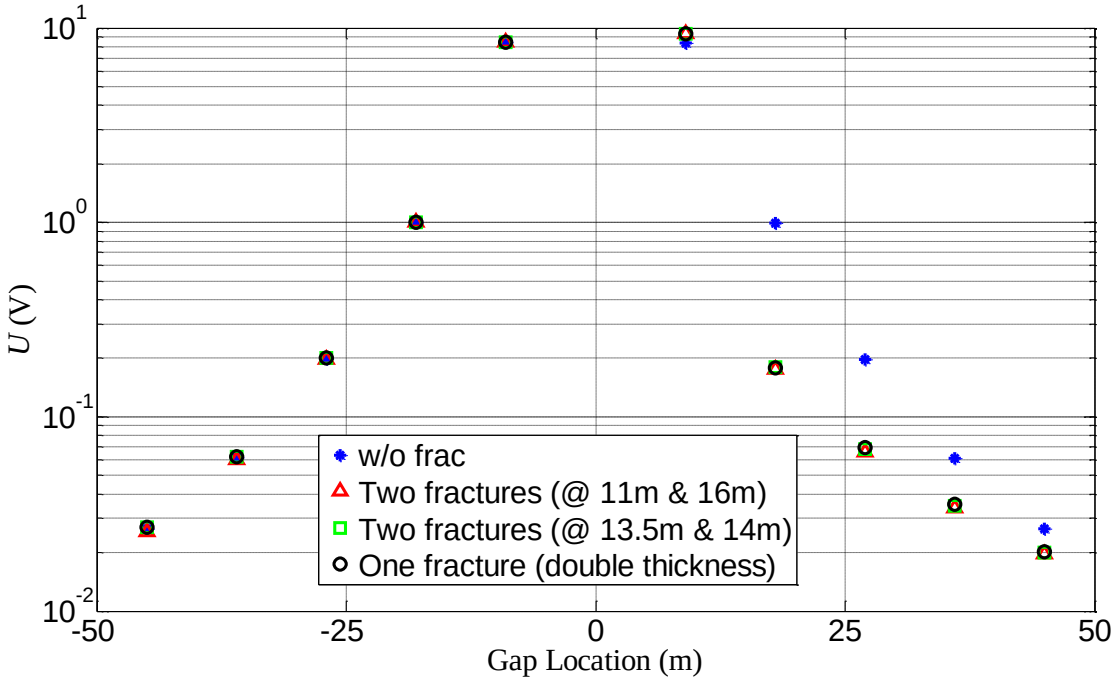

Figure 5.9 Voltages at the various gaps with respect to different scenarios when the fractures are not touching the excited casing section.

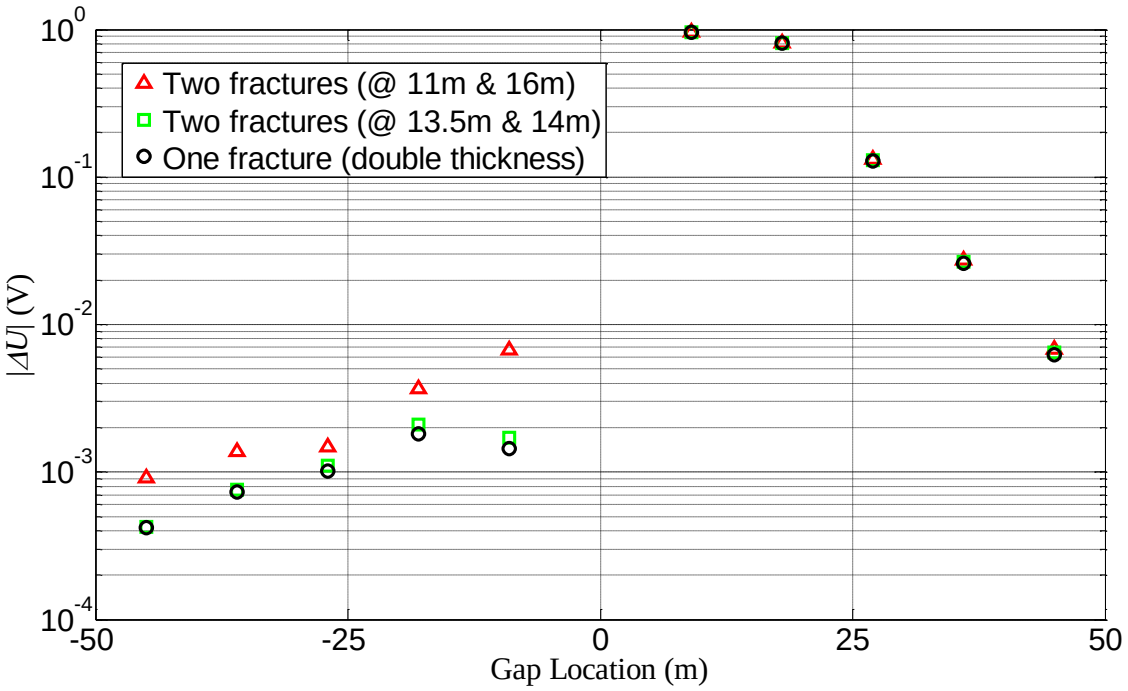

Figure 5.10 Voltage differences from the no-fracture case corresponding to the voltages in Fig. 5.6.

Because the fractures are not direct in contact with the excited casing section, the overall voltage level is lower. Besides this difference from the previously set of simulations, our conclusions still hold: a) when a complex fracture is present, the tool's response depends mainly on the fracture's volume instead of its complexity; b) two fractures on the same casing section cannot be easily recognized from a single, thicker fracture, and this is even harder when the fractures are not touching the excited casing section due to the lower measured voltage level.

The fractures' influence on the measured voltages at the receivers depends on their ability to change the current distribution in the formation. Current is drawn from the casing by the conductive fractures, flows along the radial direction of the fractures and gets distributed over the fracture surface. Therefore, the apparent resistance of the

fractures, i.e. the currents' pathway from the casing to the formation, is the primary factor that dominates the measured voltages. Specifically, it is the fractures' conductance (product of conductivity σ and width δ) in the radial direction that really matters. Since we assumed the same conductivity of the proppant, a single fracture or two fractures with the same total width (volume) have the same radial conductance. This explains the results we saw when two fractures touch the same casing section, whether it is excited or not.

Prior to this study, we also checked the possibility of using a low-frequency (100 Hz) induction tool to differentiate complicated fractures from planar ones (Zhang et al., 2016). Likewise, we use multiple planar elliptical fractures (two or three) of 5 mm total width and 1 cm separation to approximate the complex fracture (5.11(a)). The planar fractures are assumed elliptical with major radius of 150 feet (45.7 m) and minor radius of 25 feet (7.62 m). The conductivity is assumed to be 1000 S/m. A single planar fracture with width of 5 mm and the same shape is also simulated and it takes the same amount of proppant as the complex one.

Fig. 5.11(b) compares the single planar fracture and two simplified complex fractures, comprising 2 and 3 sub-fractures, for a short-spacing transmitter-receiver configuration (Zhang et al., 2016). The signals plotted on the y axis are the normalized differential voltages from the no-fracture case, when both the transmitter and the receivers are aligned with the borehole axis. The x axis shows the location of the center of the two receivers and for all three cases, the fractures are placed symmetrical to location 0 m (Fig. 5.11(b)). No significant difference is observed between the various cases, indicating that, for fractures of up to the studied propped area, with uniform effective conductivity, the induction tool's response depends only on the propped fracture's volume, and not on its complexity. This can be explained in a similar way: the current induced in the fractures is determined by the fractures' conductance in the

tangential direction, and this conductance is still linearly proportional to fractures' conductivity and thickness.

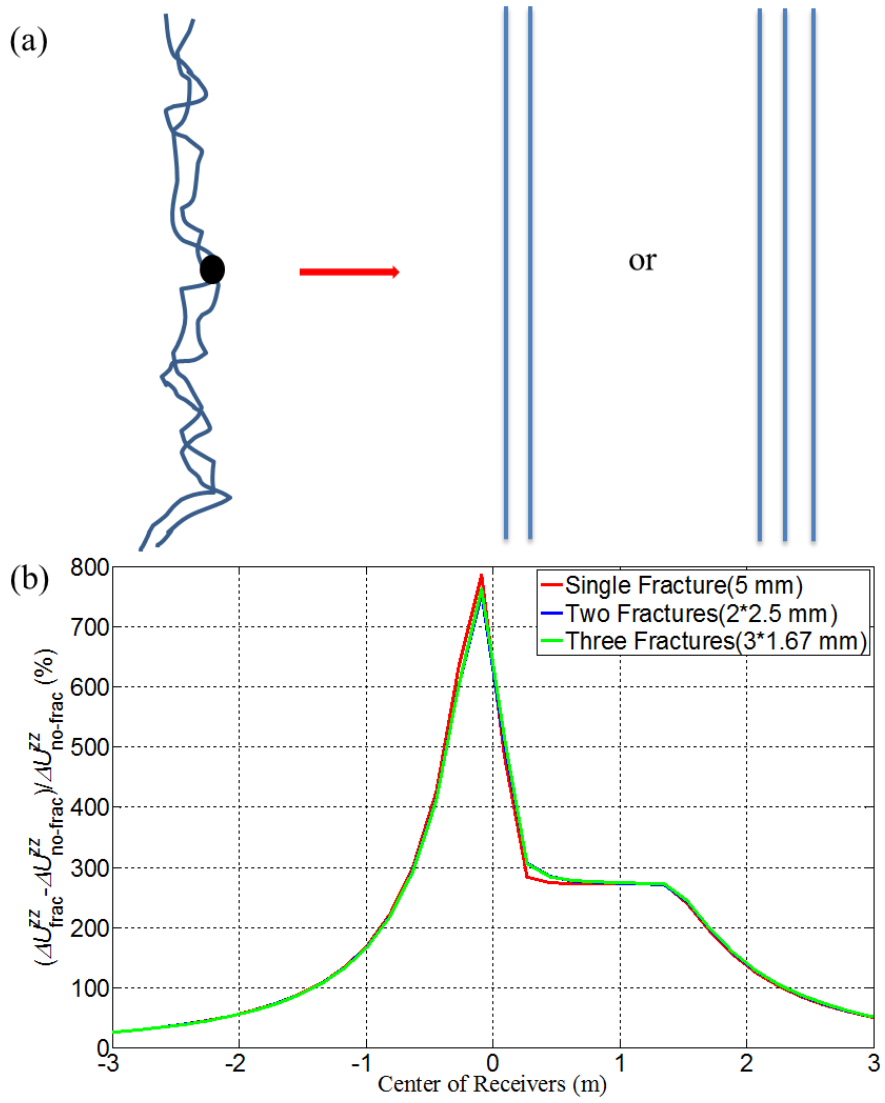

Figure 5.11 Relative signal strength for planar and complex fracture geometries. (a) The complex fracture was simplified to either two or three planar elliptical fractures in parallel with the same total thickness. (b) Relative signal strength for short-spacing coaxial configuration corresponding to planar (red) and simplified complex fracture (blue and green).

5.4 SIMPLIFICATION OF MULTIPLE-FRACTURE SIMULATIONS

As the tool takes measurements by exciting the insulating gaps, each at a time, we need incorporate all the fractures along the well, for the proper and complete simulation of a real scenario. For a multi-stage fractured well, the number of fractures generated can be very large. It is computationally expensive to simulate such a large number of fractures, due to the requirement of mesh refinement around the fractures. Hence we need a strategy to decrease the size of the problem, without sacrificing the integrity of the original geometry.

Fig. 5.4 shows that when one or two fractures that are not in direct contact with the excited casing section are present, only the voltages measured at the receiver gaps right next to these passive fractures are strong. Another fact is that the voltage level at various receivers is almost proportional to $\frac{1}{d^2}$, where d is the distance between the transmitter gap and the corresponding receiver gap. For each excitation location in the logging sequence, if the measurements only at the receivers in close proximity to the transmitter are used for inversion purpose, we might be able to truncate or simplify the geometry by including less fractures, without affecting the measured voltages at these receivers.

For each excitation location, two possible strategies for simplification are examined: (i) only the voltages at 8 receivers, 4 on each side of the transmitter, are considered; (ii) only the voltages at 6 receivers, 3 on each side of the transmitter, are considered. All the measured voltages at other receiver gaps are computed but abandoned because they are relatively weak. A base case with 16 fractures, 8 on each side of the transmitter, is simulated (Fig. 5.12 and 5.14). The fractures' radius and widths are set randomly in an interval of [15, 40] m and [2, 4] mm, respectively. The fracture's conductivity is kept to be 5000 S/m.

If the measurements from only 8 receiver gaps in close proximity to the transmitter are considered, three scenarios are compared: a) all the 16 fractures are present; b) only 10 fractures right next to the 8 receiver gaps are present (marked by the solid lines in Fig. 5.12), which means three fracture on each side are removed (dotted lines); c) only 8 fractures, 4 on each side of the transmitter are present. The voltages at all the receiver gaps are computed.

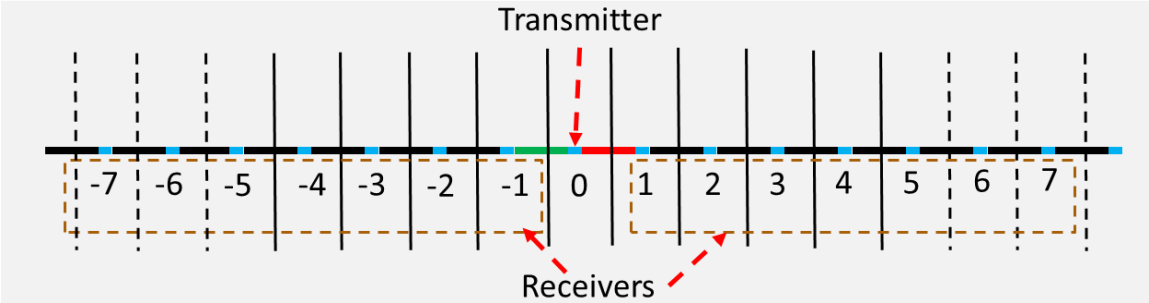

Figure 5.12 A schematic depicting a well with multiple fractures. The transmitter (#0) and receiver gaps are marked separately. The solid lines are the 10 fractures right next to the 8 receiver gaps close to the transmitter.

For the voltages measured at the 8 receivers close to the transmitter (#-4, -3…4), marked by the blue dotted ellipses in Fig. 5.13, the 16-fracture case and the 10-fracture case overlap with less than 0.5% relative error. Further simplification with 6 fractures present, 3 on each side of the transmitter, leads to apparent deviation of the voltages at the 4th receivers on both sides (marked by the green dotted square in Fig. 5.13). Therefore, when the tool excites a gap (e.g., gap #0) as a part of a set of sequential measurements in a well with multiple fractures, we can simplify or truncate the geometry to only include 10 fractures, 5 on each side of the transmitter, to simulate the voltages measured at the 8 receiver gaps in close proximity to the transmitter. This will greatly

speed up the simulations associated with different transmitter locations, without sacrificing accuracy, especially when tens of fractures are present in a well.

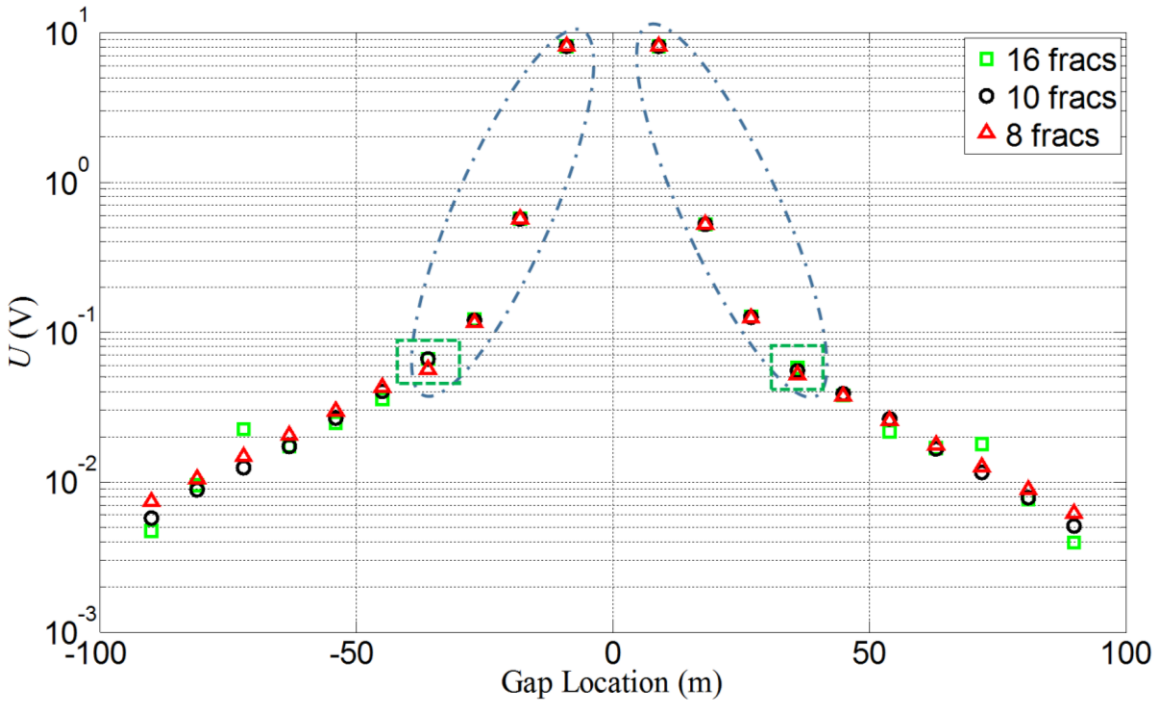

Figure 5.13 Voltages at the various gaps with respect to different scenarios. The blue dotted ellipses mark the voltages measured at the 8 receiver gaps, 4 on each side of the transmitter.

Similarly, we examined the case when the measurements from only 6 receiver gaps in close proximity to the transmitter (#-3, -2…3 in Fig 5.14) are considered. In this situation the geometry can be further simplified by including only 8 fractures marked by the solid lines in Fig. 5.14. The 8-fracture and the 16-fracture geometries induce almost identical voltages at the 6 receivers (marked by the blue dotted ellipses in Fig. 5.15). Further simplification with 6 fractures causes deviation at the two receivers on both ends (marked by the green dotted squares in Fig. 5.15).

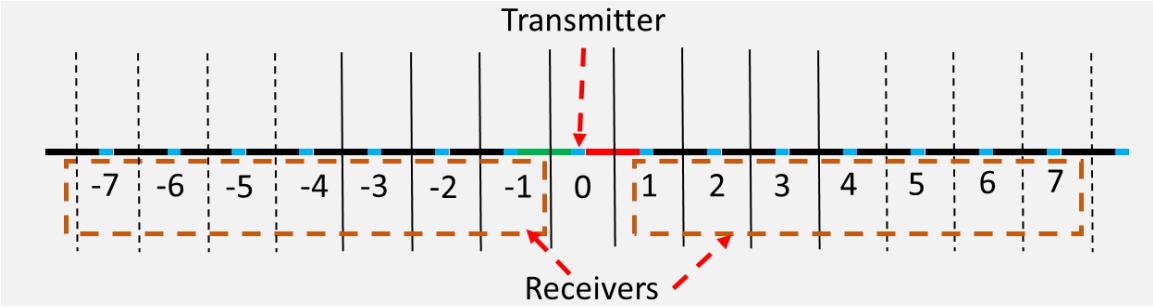

Figure 5.14 A schematic depicting a well with multiple fractures. The solid lines are the 8 fractures right next to the 6 receiver gaps close to the transmitter.

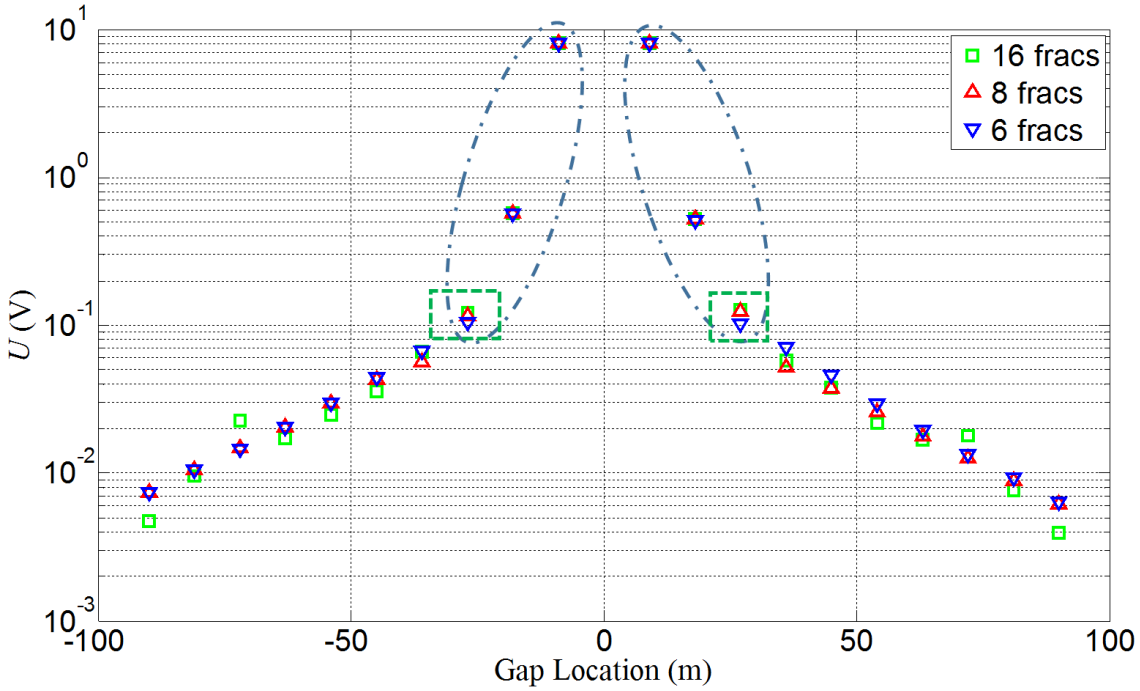

Figure 5.15 Voltages at the various gaps with respect to different scenarios. The blue dotted ellipses mark the voltages measured at the 6 receiver gaps, 3 on each side of the transmitter.

By combining the results from the two example above, we can conclude that the influence from passive fractures (not in contact with the excited casing sections) is limited in a very short distance. Only the fractures right next to the receiver gaps being

considered need to be incorporated in the simulations, for a given excitation location. This provides an important strategy for model simplification when simulating the tool's response with the presence of a large number of fractures. The geometry can be divided into several patches and solved separately, without sacrificing the integrity of the original geometry.

5.5 SUMMARY

This chapter focuses on the forward simulation of multiple fractures, which takes us one step closer to the real problem we face towards the application of the tool in the field. Most importantly, the results and conclusions provide very important information and guidance for our inversion process. These findings will be used in the following chapters for developing suitable inversion strategies.

Multiple fractures separated by insulating gaps were simulated. The results indicate that when multiple fractures are present, the one that is in contact with the excitation electrode dominates the signals received at the receiver gaps. This phenomenon confirms the necessity of exciting multiple gaps in a logging sequence, for extracting the geometries of multiple fractures.

A special scenario, when two fractures touch the same piece of casing, is also simulated using the forward model. In this case the two fractures induce very similar signals at the receiver gaps to that obtained from one single fracture with double the width. This means that if two hydraulic fractures are expected on a casing section, the tool will be unable to differentiate these fractures from a thicker one with an equivalent volume. One should seek extra information or have prior knowledge of the fracture locations to identify these fractures. This will help to get better estimates of the number, geometry and location of these propped fractures when inverting the measured data.

It was also found that the influence from passive fractures is limited to a very short distance from the active electrodes. Only the fractures right next to the receiver gaps being considered need to be incorporated in the simulations. This means when simulating the tool's response with the presence of a large number of fractures, the geometry can be divided into several groups of fractures and solved separately, without sacrificing the integrity of the original geometry.

Chapter 6: Building a Framework for Inverse Modeling

6.1 BACKGROUND

So far we have been focused on forward modeling of downhole electrical measurements using the casing electrode-based tool. With the tool's sensitivity to various fracture parameters studied, and the tool's response to multiple fractures investigated, the next step is to explore a suitable strategy to extract fracture parameters by inverting the measured data from the tool.

In a typical model-based inversion approach, an iterative forward modeling procedure is involved to find the best match between observed and synthetic data. If the match between observed and synthetic data is considered good enough, the model is accepted as the solution. Otherwise, the model has to be updated based on an optimization algorithm, until an acceptable match is obtained between data and synthetics (Fig. 6.1).

To measure the goodness of the model, an objective or cost function has to be defined, which quantifies the mismatch between the observed and synthetic data. The data mismatch norm can be written as

$$\|\Delta \boldsymbol{d}\|_p = (\sum_{i=1}^{N} |\Delta d_i|^p)^{1/p}, \tag{6.1}$$

where the integer p is the order of the norm. The L_2 norm ($p = 2$) is commonly used for the reason that it maximize the posterior probability density function of the model, assuming the error distribution is Gaussian. Therefore, the goal for an inversion procedure is to minimize the objective function, which is directly the L_2 norm defined in Eq. 6.1 or the L_2 norm with some constraints, through an optimization process.

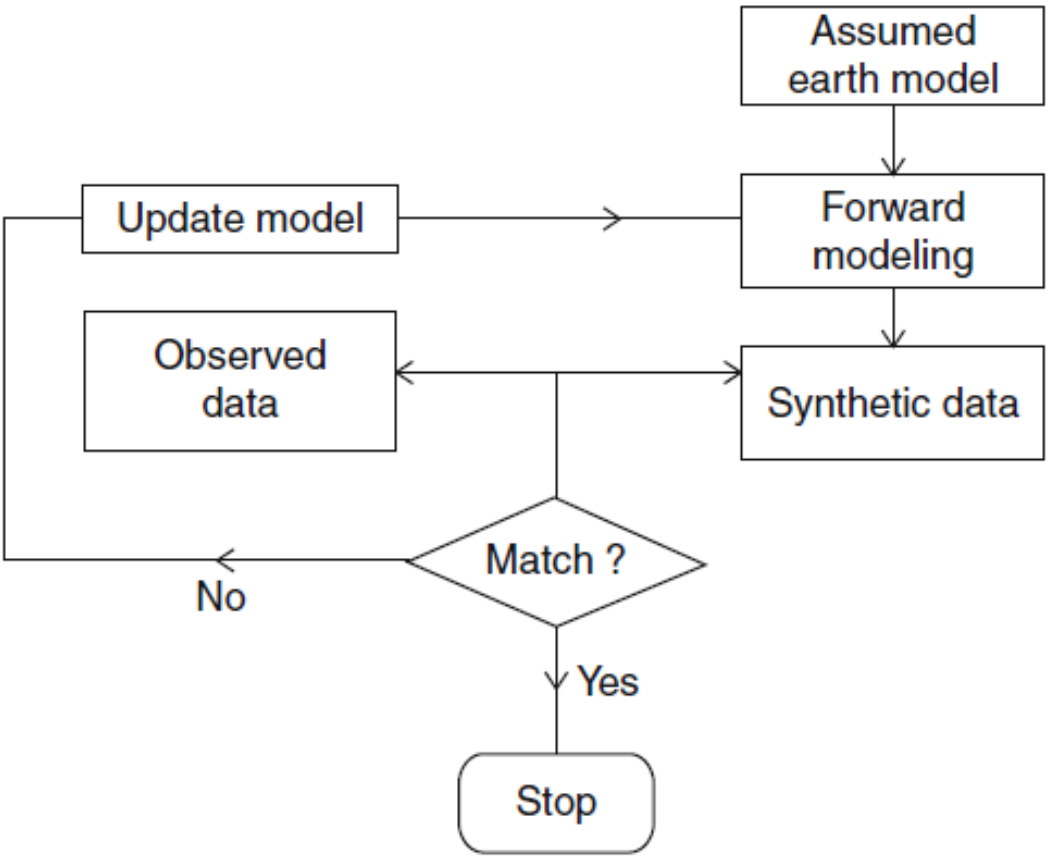

Figure 6.1 A typical workflow for model-based inversion in geophysical applications (From Arora et al., 2011).

Generally, there are two categories of optimization methods: local optimization methods and global optimization methods. Most of the local optimization methods are deterministic, which make use of local gradients to determine the updated model parameters. Because these methods only accept better models they are often called greedy algorithms. They can converge fast but unfortunately, the success of these methods is usually dictated by the choice of the starting model or initial guess. This is because they can easily be trapped in a local minimum (Fig. 6.2). Global optimization methods, such as simulated annealing, genetic algorithm, and neighborhood algorithm are

less greedy. By applying stochastic techniques they sometimes accept bad moves, which allow them to jump out the local minima and finally converge to the global minimum. The drawback is that these methods are often less directed and, therefore, take much longer to converge.

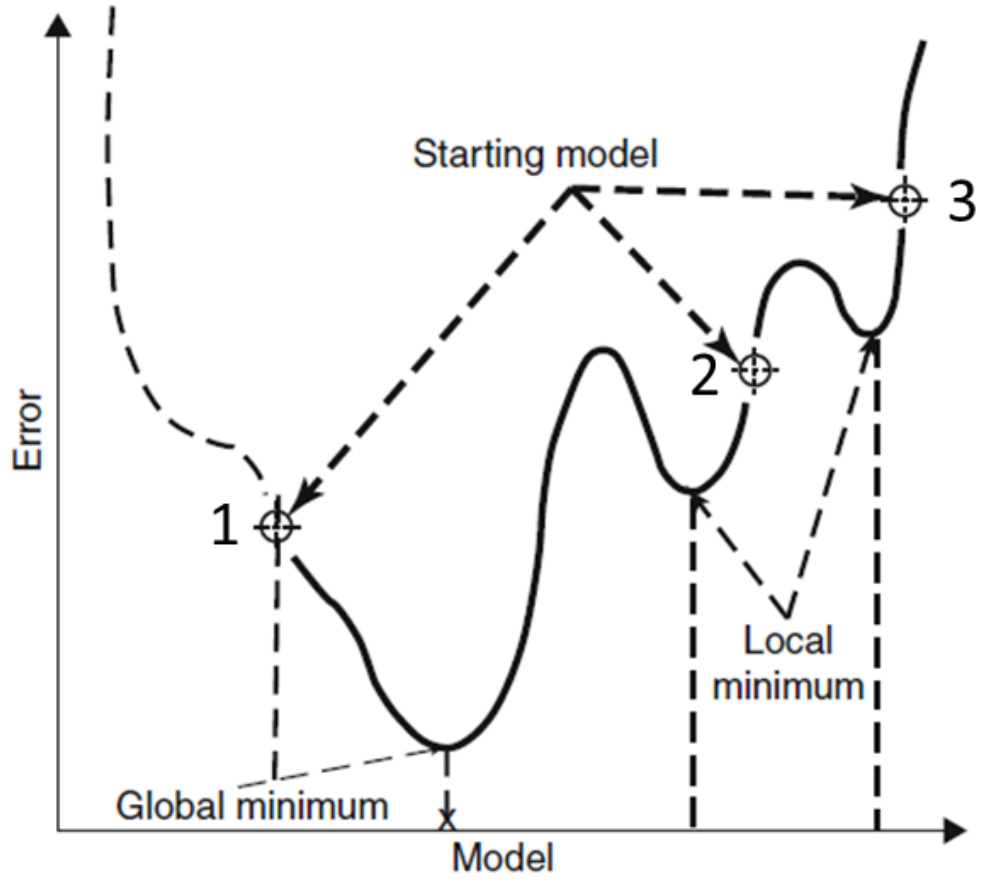

Figure 6.2 A hypothetical objective function that shows several minima. Gradient based methods will find the global minimum only when starting at position 1. Others will be trapped at secondary minima. (From Arora et al., 2011; Sen and Stoffa, 2013)

The remainder of this chapter is organized as follows: First, a few commonly used local and global optimization methods are reviewed. The advantages and drawbacks associated with each method are discussed. Next, a model-based inversion framework is

built. The framework incorporate the forward modeling methods introduced in Chapter 3 and an inversion kernel, which is able to extract the fracture parameters from the measured data in a fully automated process. Using this framework, the performance of a steepest descent method and a very fast simulated annealing are evaluated and compared. The conclusions will eventually help to develop an optimal methodology for inverse modeling of the tool data.

6.2 LOCAL OPTIMIZATION METHODS

Most of the local optimization methods follow a standard procedure, described in Fig. 6.3. Starting from a given model $\boldsymbol{m}_0$, which can be determined by using some prior knowledge about the model parameters, the local gradient at this starting point is calculated. The search direction $\Delta\boldsymbol{m}_k$ and step length α_k is determined and a new model is generated and evaluated. The process is repeated until the cost function reaches an acceptable value or there is no change in the model. There are a few commonly used local optimization methods, such as Newton's method, steepest descent and conjugate gradient. They mainly differ in the way they compute the search direction (Sen and Stoffa, 2013).

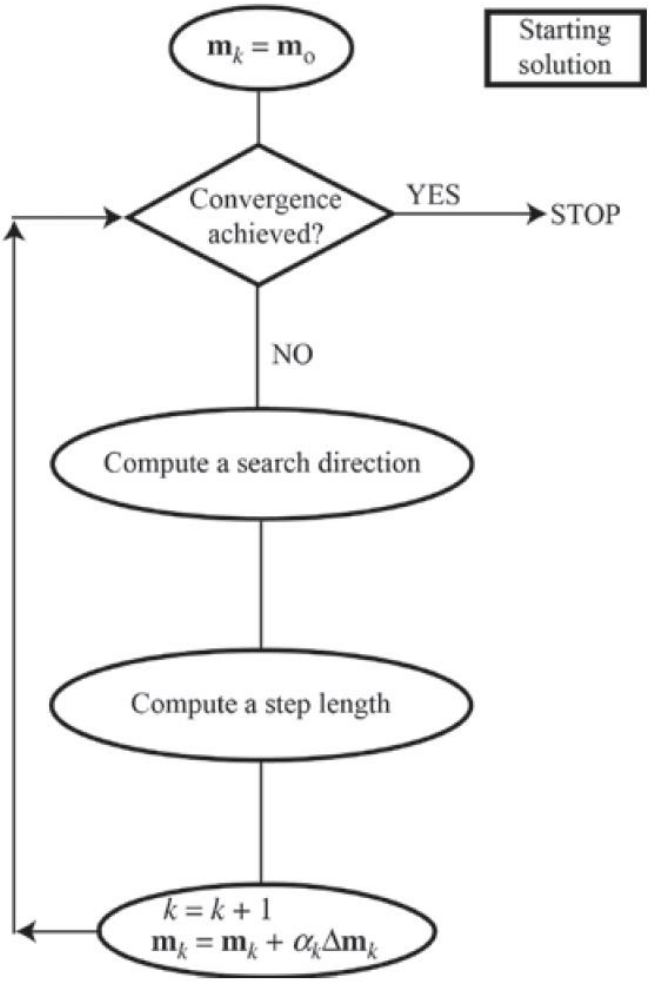

Figure 6.3 A model-based inversion algorithm using local optimization methods. (From Sen and Stoffa, 2013)

The search direction in Newton's method is computed by a product of the inverse Hessian $\boldsymbol{H}^{-1}(\boldsymbol{m}_k)$ and the gradient vector $\nabla E(\boldsymbol{m}_k)$ (Sen and Stoffa, 2013; Aster et al., 2011):

$$\boldsymbol{m}_{k+1} = \boldsymbol{m}_k - \alpha_k \boldsymbol{H}^{-1}(\boldsymbol{m}_k) \nabla E(\boldsymbol{m}_k). \tag{6.2}$$

The step length α_k can be determined using some line search technique, e.g., backtracking line search (Nocedal, 2006; Press, 1989). This method guarantees quick

convergence to the local minimum, especially for a parabolic cost function (Fig. 6.4), but the computation of the gradient and the Hessian is usually expensive.

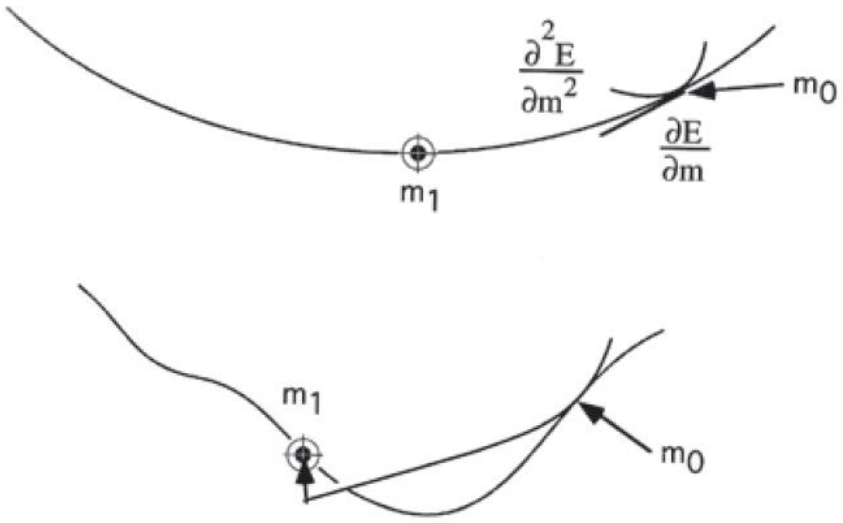

Figure 6.4 A 1D example illustrating Newton's method. It uses the slope and curvature (corresponding to the gradient and Hessian for multidimensional problems) to calculate the search direction. (From Sen and Stoffa, 2013)

The method of steepest descent searches along the direction in which the error changes most rapidly, i.e., the opposite direction of the local gradient:

$$\boldsymbol{m}_{k+1} = \boldsymbol{m}_k - \alpha_k \nabla E(\boldsymbol{m}_k). \tag{6.3}$$

The optimal step length α_k for this method makes the search direction at iteration $k+1$ orthogonal to the previous search direction at iteration k (Fig. 6.5). Due to this nature, this algorithm takes very small steps for error functions with elongated valleys. Hence it converges very slowly in those cases.

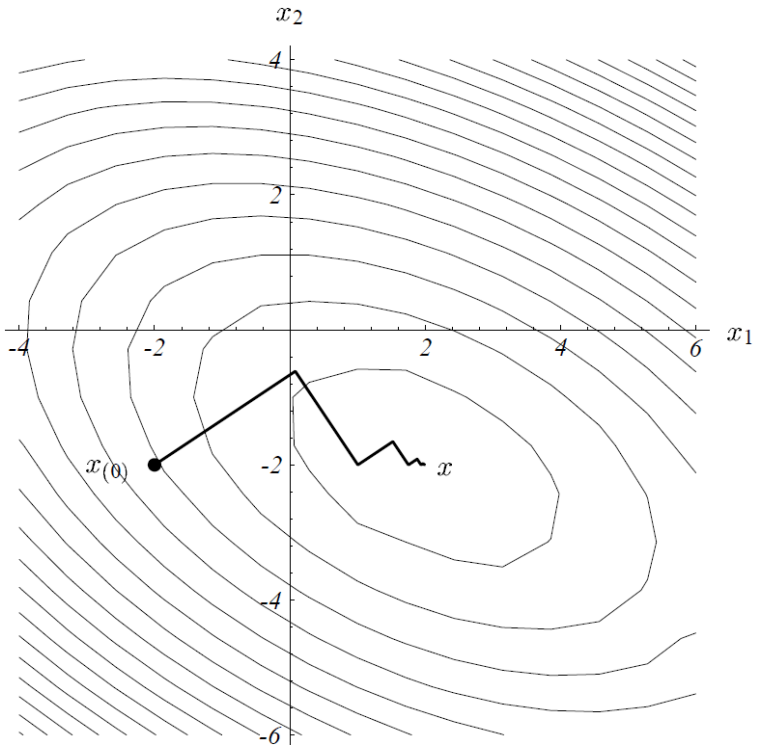

Figure 6.5 A 2D example demonstrating the method of steepest descent. The search direction at iteration $k+1$ is orthogonal to the one at iteration k. (From Shewchuk, 1994)

Conjugate gradient method can avoid the previous problem seen for the steepest descent method. It searches along a new direction $\boldsymbol{p}_k$ at each iteration, which is conjugate to the search direction at the previous iteration $\boldsymbol{p}_{k-1}$:

$$\boldsymbol{m}_{k+1} = \boldsymbol{m}_k + \alpha_k \boldsymbol{p}_k. \tag{6.4}$$

This leads to convergence to the optimal solution after n iterations for a n-dimensional problem (Fig. 6.6).

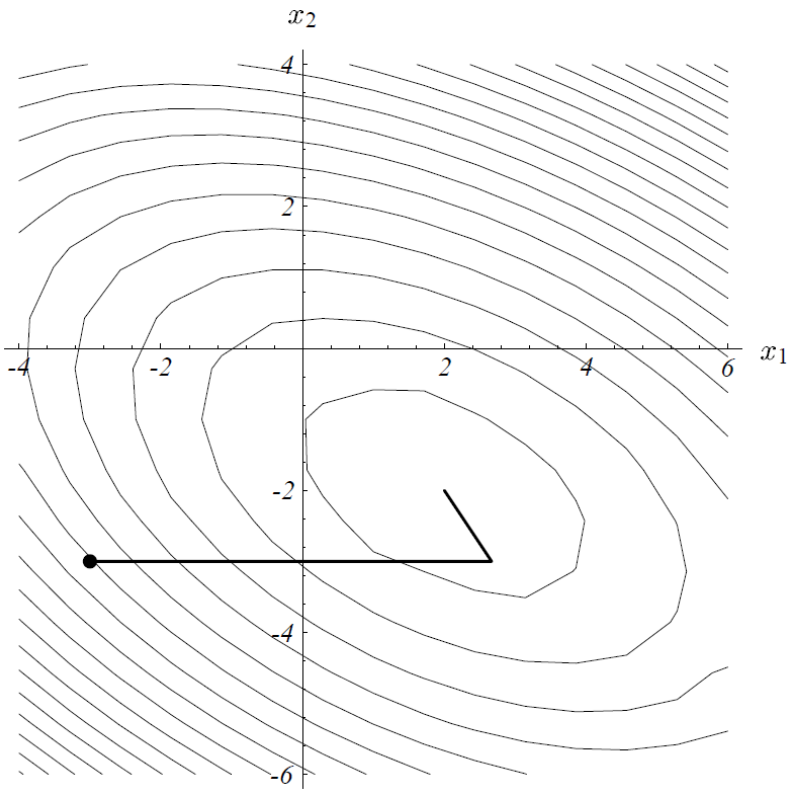

Figure 6.6 A 2D example demonstrating the conjugate gradient method. The search direction at iteration $k+1$ is conjugate to the one at iteration k. (From Shewchuk, 1994)

6.3 GLOBAL OPTIMIZATION METHODS

While the local optimization methods are well directed search algorithms, usually by calculating the gradient or Hessian, there are different kinds of global optimization methods, which are either completely undirected or partially directed.

Monte Carlo inversion, for example, is a purely random searching technique. Models are drawn randomly in a predefined search interval [$\boldsymbol{m}^{min}$, $\boldsymbol{m}^{max}$] and evaluated against the data (Sen and Stoffa, 2013). The model generation-acceptance/rejection is repeated until the stopping criterion is satisfied. The process is open ended, and can be continued as long as desired. Therefore, it does not get trapped in local minima, but may

require too much computation time to converge to the optimal solution. Moreover, the resulting model may be very different every time, depending on the starting model.

For that reason, some other global optimization methods, based on partially directed searching processes, are more commonly used in geophysical applications. These directed methods such as simulated annealing (Ingber, 1989; Kirkpatrick et al., 1983) and genetic algorithms are able to jump out of the local minima by sometimes allowing the acceptance of 'bad' solutions. They can converge in a reasonable speed without requiring the calculation of gradient terms.

In this work we focus on one special kind of simulated annealing algorithm – very fast simulated annealing (VFSA). The VFSA technique starts with an initial guess of model parameters $\boldsymbol{m}_0$ within the predefined limits $[\boldsymbol{m}_{min}, \boldsymbol{m}_{max}]$ and calculates the initial objective function or energy $E(\boldsymbol{m}_0)$, by running the forward model. Then it draws a new set of model parameters $\boldsymbol{m}_{new}$ from a Cauchy-like distribution centered on the current model, which depends on the temperature T (Sen and Stoffa, 2013). The energy associated with the new model parameters $E(\boldsymbol{m}_{new})$is compared against the initial objective function $E(\boldsymbol{m}_0)$. The new model is always accepted and replaces the initial model if the energy of the new state is lower than that of the initial state. If the energy of the new state is higher, $\boldsymbol{m}_{new}$ can still be accepted with a probability of $\exp(-(E(\boldsymbol{m}_{\text{new}}) - E(\boldsymbol{m}_0))/T)$. The possibility of accepting "bad" models in VFSA allows it to jump out of the local minima (Grieve et al., 2011; Sen and Stoffa, 2013).

The process of drawing samples is repeated many times at the initial annealing temperature. Then the annealing temperature gradually decreases, according to a specified cooling schedule. At each temperature T_j, the same model-generation and acceptance criterion is used, until the annealing temperature or energy is sufficiently low (Fig. 6.7). As the temperature decreases, the newly drawn samples from the Cauchy-like

distribution prefer to be in the close neighborhood of the current model, and the probability of accepting 'bad' models also decreases. Convergence of this algorithm is guaranteed if the cooling process is sufficiently slow.

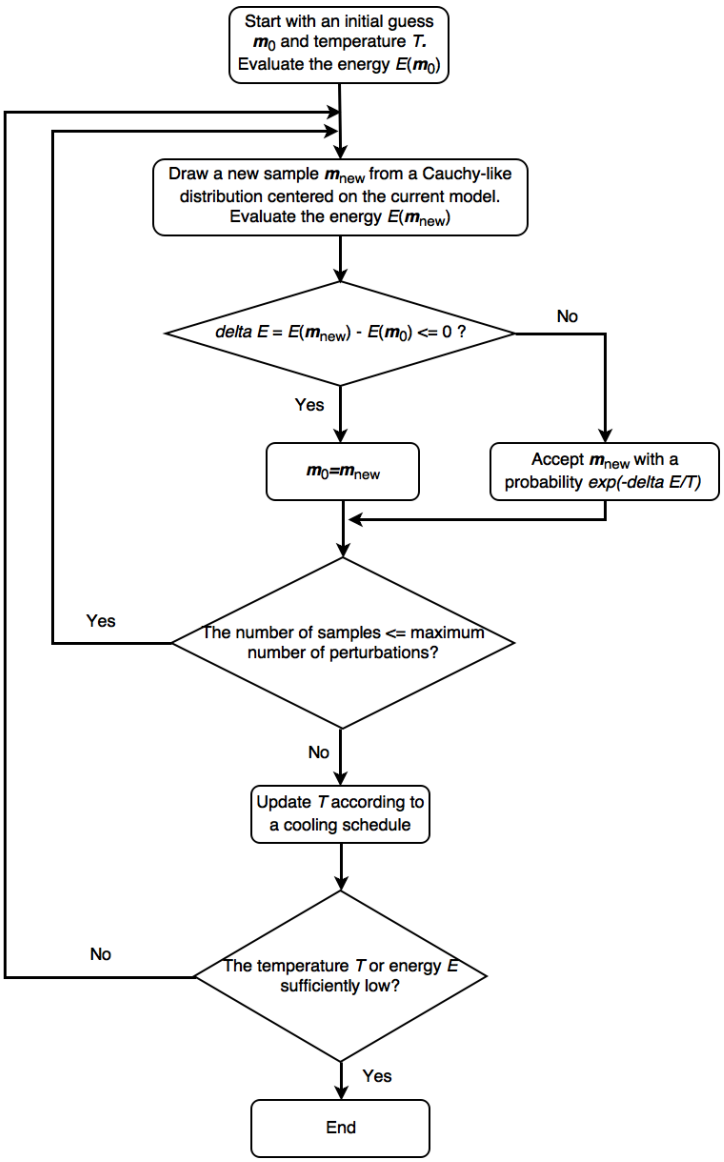

Figure 6.7—A flow chart for VFSA.

6.4 BUILDING AN INVERSION FRAMEWORK FOR THE TOOL

Thus far we have reviewed a few local and global optimization methods that can be potentially adopted for inversion of data acquired by our tool. To explore the suitability of some algorithms for our specific application, a model-based inversion framework has to be built. The framework should be able to incorporate both our forward model and an inversion kernel, which can extract the fracture parameters from the measured voltages in a fully automated process.

Fig. 6.1 demonstrates a general workflow for geophysical inversion. The forward modeling part, as introduced in Chapter 3, includes generating the mesh, setting the fracture parameters (radii, conductance, etc.), running the forward simulations and sampling the data. Model updating is from the inversion kernel, which should be able to search for the optimal fracture parameters that can best fit the data from the tool. A detailed framework is illustrated by Fig. 6.8. A deterministic method (steepest descent) and a stochastic method (VFSA) were tested and their performance for extracting the fracture parameters was evaluated using example cases.

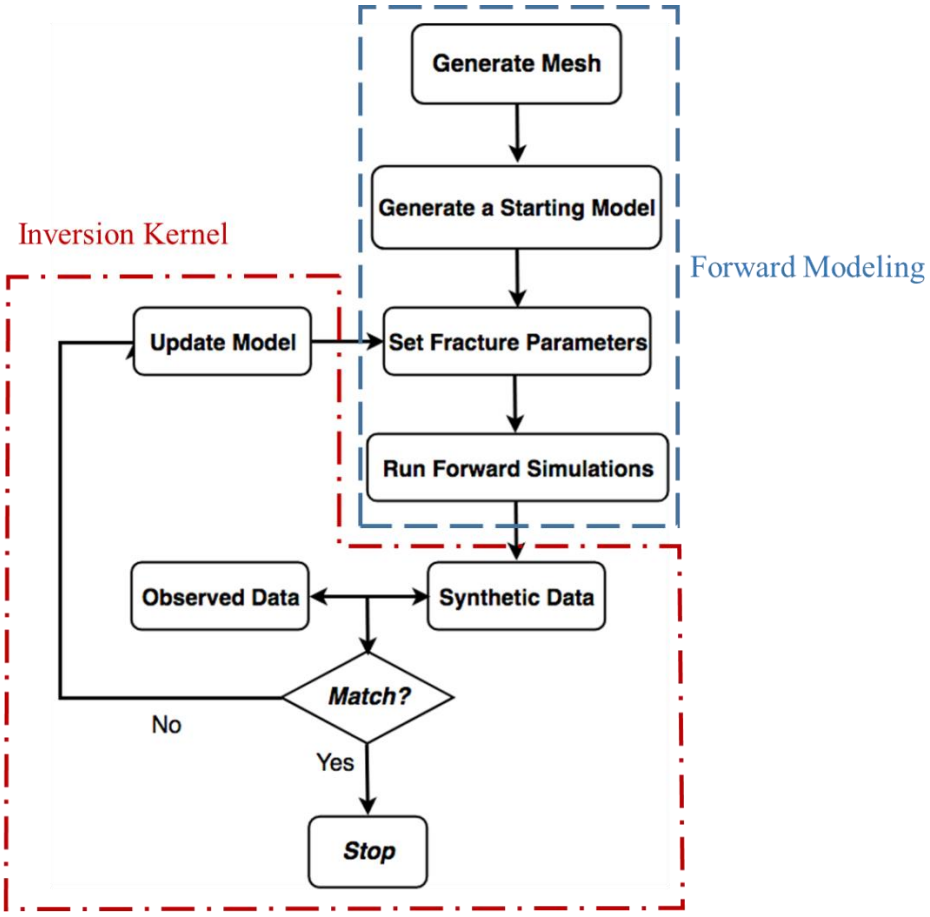

Figure 6.8 A detailed framework for inversion.

For all the cases presented, the objective function is defined as follows:

$$E(\boldsymbol{m}_{inv}) = \sum_{i=1}^{n} w_i \cdot [\Delta U_i(\boldsymbol{m}_{inv}) - \Delta U_i(\boldsymbol{m}_{true})]^2. \quad (6.5)$$

Here, $\{\boldsymbol{m}_{inv}, \boldsymbol{m}_{true}\}$ is the vector representing the {inverted, true} fracture geometries. $\{\Delta U_i(\boldsymbol{m}_{inv}), \Delta U_i(\boldsymbol{m}_{true})\}$ is the differential voltage at receiver gap i for the {inverted, true} fractures, which is the difference between the voltage computed when the fracture is present and the voltage computed when the fracture is absent. w_i is the weight put on receiver i to balance the influence from different receiver gaps. n is the total number of data that are used as inversion input.

6.5 INVERSE SOLVER TEST - THE METHOD OF STEEPEST DESCENT

The method of steepest decent, combining a backtracking line search, is the first method being tested. Quick convergence is a big advantage of this algorithm, but it may get trapped easily at local minima. The algorithm is explained by a single-parameter parabolic function in Fig. 6.9. It starts from an initial guess $\xi_{(1)}$ and the local gradient $\nabla\mathcal{L}(\xi)$ is calculated at this point. The search direction is therefore determined to be the opposite direction of the gradient $g = -\nabla\mathcal{L}(\xi)$. The original step length $\Theta_{(1)}$ is decreased by a factor of 0.8 (Fig. 6.9 (a)) or increased by a factor of 1.2 (Fig. 6.9 (b)), until the optimal step length $\Theta^*_{(1)}$ is found (Jung and Taciroglu, 2014).

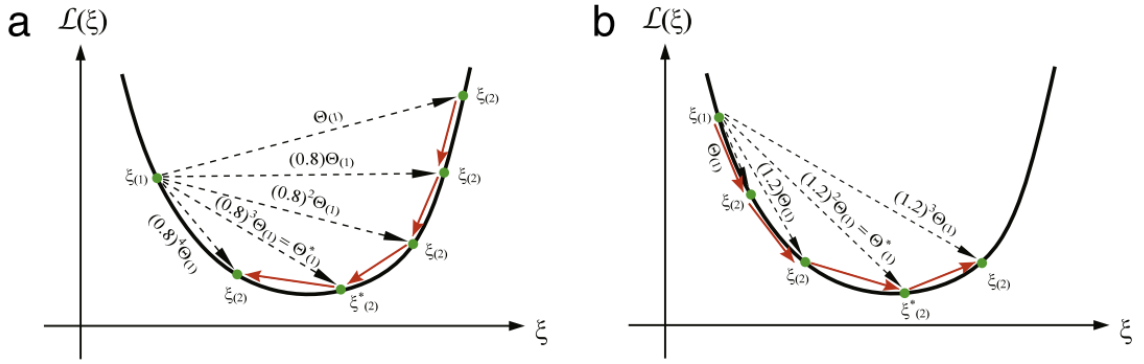

Figure 6.9 Backtracking line search for a parabolic function $\mathcal{L}(\xi)$. The search starts from $\xi_{(1)}$ and moves along the opposite direction of the local gradient to the next point $\xi_{(2)}$. The step length is decreased by a factor of 0.8 if $\mathcal{L}(\xi_{(1)}) \leq \mathcal{L}(\xi_{(2)})$ (a) or increased by a factor of 1.2 (b) if $\mathcal{L}(\xi_{(1)}) > \mathcal{L}(\xi_{(2)})$, until the optimal step length is found. (From Jung and Taciroglu, 2014)

As discussed in Chapter 4, the tool is less sensitive to fracture parameters such as angle and aspect ratio. We started from the simplest case, in which we only inverted for the radius r and conductance G of a single fracture. The fracture is placed on the positive electrode, 5 m away from the transmitter gap (excited by a voltage source of 20 V). The horizontal well under investigation is about 200 m long, and is composed of 22

standard 9 m (~ 30') long casing sections and 21 0.02 m long insulating gaps (Fig. 6.10). For the ease of interpretation, the conductance is converted to fracture width δ, assuming the fracture's conductivity is 3000 S/m. The model $\boldsymbol{m}$ is therefore a vector composed of two elements $\{\delta,\ r\}$. The cost function being optimized is defined in Eq. 6.5.

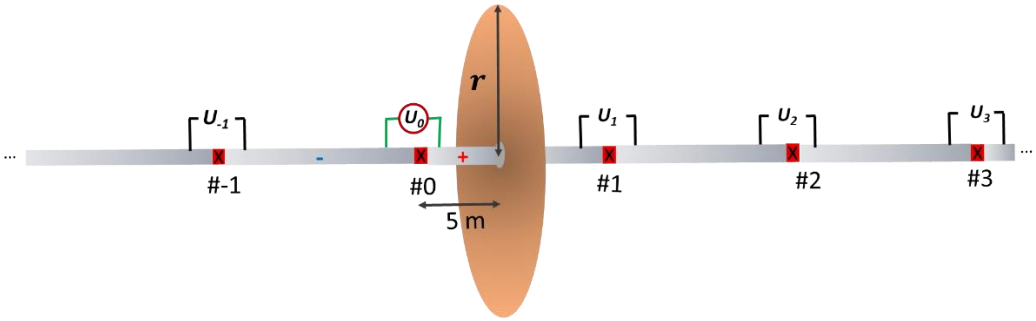

Figure 6.10 Illustration of the tool configuration that is used to invert for the radius and width of a single fracture.

The true model and the starting model for the fracture are {5 mm, 20 m} and {3.3 mm, 30 m}, respectively. We use the line search-based single-variable steepest descent method shown by Fig. 6.9 to solve the inverse problem iteratively. The first model parameter being searched is the fracture width δ, followed by the fracture radius r. The process is repeated until there is no change in the model parameters. In the first iteration, the fracture width converges at 5.3 mm and the radius settles at 26.5 m with this updated width. The change of the cost function with respect to the model parameters in the first iteration is shown by Fig. 6.11 and 6.12. After three iterations, the inverted model stops changing and the final solution is {5.3 mm, 25.6 m}, which is {6.0%, 28.0%} different from the true model.

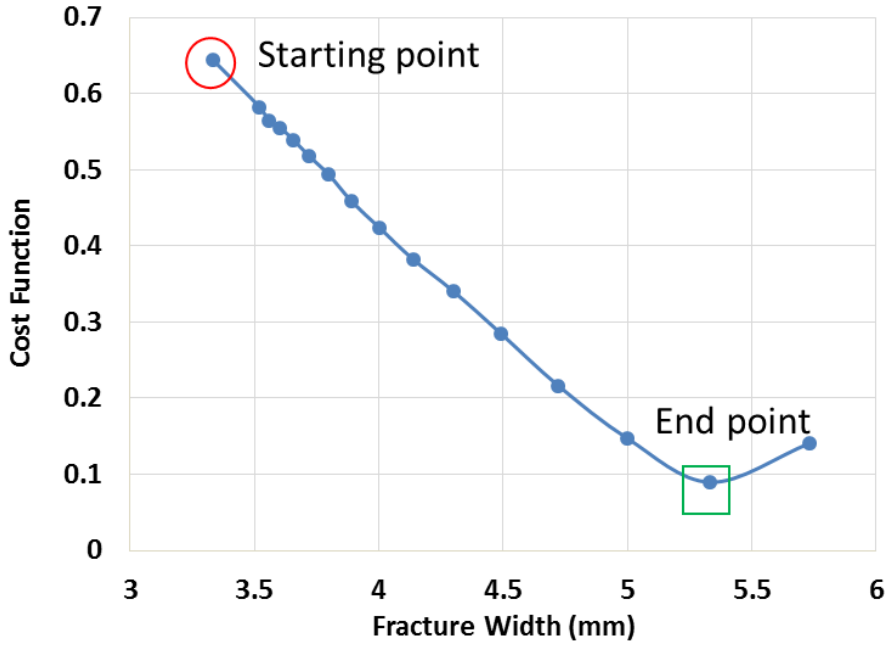

Figure 6.11 The change of the cost function with respect to the fracture width. The red circle and the green square mark the starting and end point in this iteration, respectively.

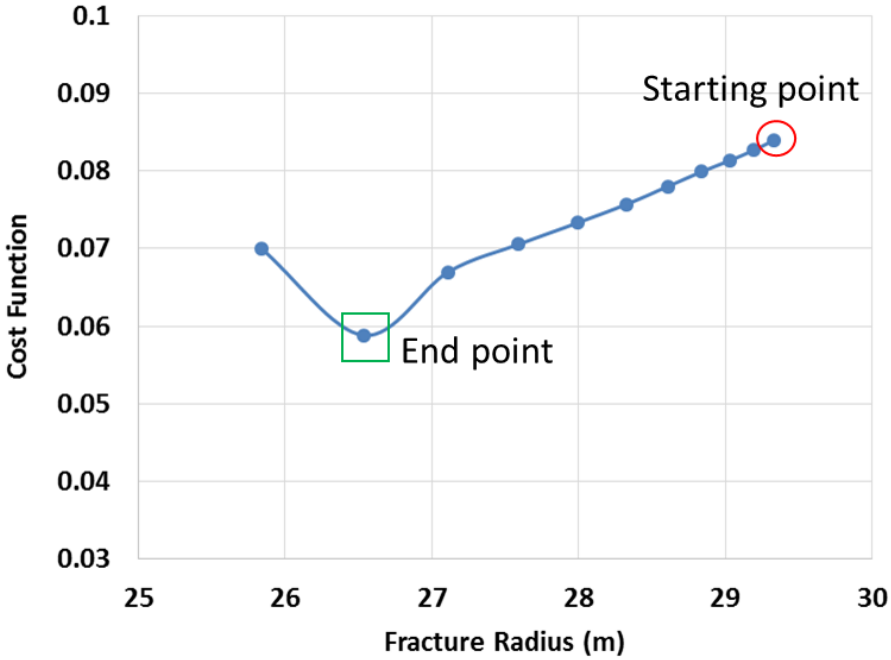

Figure 6.12 The change of the cost function with respect to the fracture radius.

In Chapter 5 we confirmed the necessity of exciting multiple gaps in a logging sequence, for extracting the geometries of multiple fractures. In order to test the steepest descent method for a multiple-fracture problem, we mimic the logging process using an idealized test case. Suppose conductive proppant is injected in only one fracture stage, and we run the tool to detect proppant distribution in three fractures. All three fractures are assumed to be in contact with different casing sections. As the tool moves in the wellbore, it excites the insulating gaps #0, #1 and #2, each at a time by a voltage source of 20 V, before and after hydraulic fracturing operations (Fig. 6.13). Six sets of synthetic data are obtained from the receiver gaps.

The radius r and conductance G of these three fractures will be extracted one by one using the synthetic data. Again for the ease of interpretation, the conductance is converted to fracture width, assuming the fracture's conductivity is 3000 S/m. The model vector $\boldsymbol{m}$ is therefore composed of six parameters $\{\delta_1, \delta_2, \delta_3, r_1, r_2, r_3\}$ and the overall objective (cost) function is the summation of the objective functions (Eq. 6.5) calculated at three excitation locations. The forward simulations involve all three fractures, since the size of this problem is relatively small (Fig. 6.13).

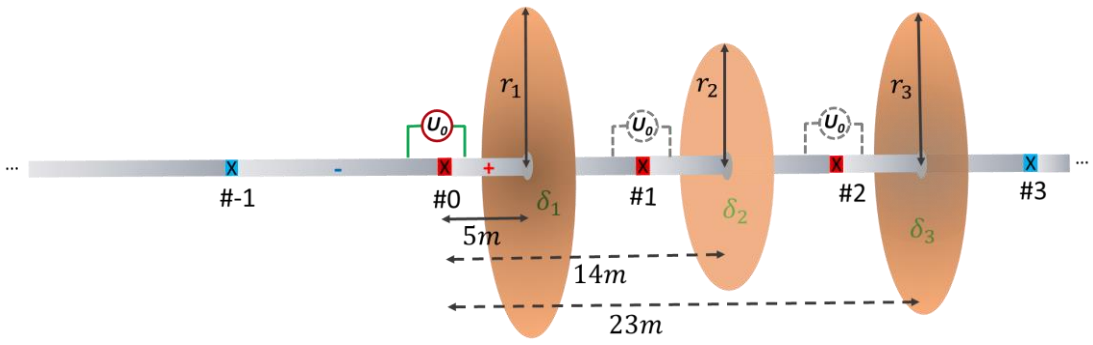

Figure 6.13 Illustration of the logging process for inversion analysis. Three fracture are present, each separated by an insulating gap.

The true model and the starting model for the fracture are {4.8 mm, 3.5 mm, 5 mm, 31 m, 22 m, 28 m} and {3.3 mm, 3.3 mm, 3.3 mm, 20 m, 20 m, 20 m}, respectively. The line search-based single-variable steepest descent method is used again to solve the inverse problem iteratively, which means the width δ_1 and radius r_1 of the first fracture are updated, followed by the widths and radii of the other fractures. The change of the cost function with respect to the parameters of the first fracture (located 5 m from the transmitter gap) in the first iteration is shown by Fig. 6.14 and 6.15. The inverted results stop changing after three iterations and the final model turns out to be {4.7 mm, 3.4 mm, 4.9 mm, 24.8 m, 29.0 m, 24.8 m}. Compared with the true model, the inverted widths of the three fractures are very accurate with an average error of 2.5%. But the inverted radii are fairly inaccurate with an average and maximum error of 21.1% and 31.8%, respectively.

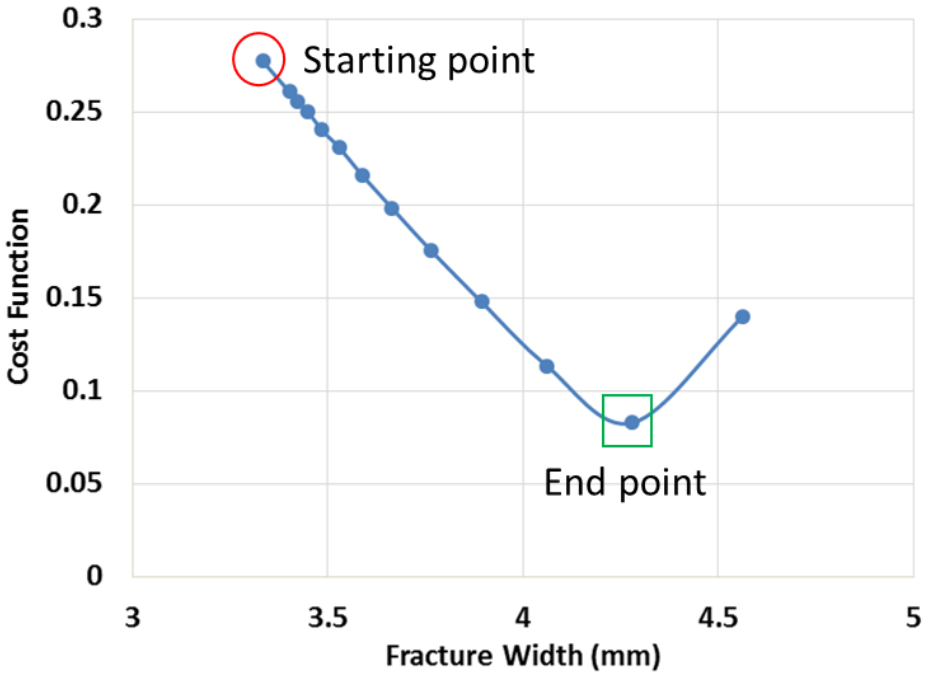

Figure 6.14 The change of the cost function with respect to the width of the first fracture (located 5 m from the transmitter gap). The red circle and the green square mark the starting and end point in this iteration, respectively.

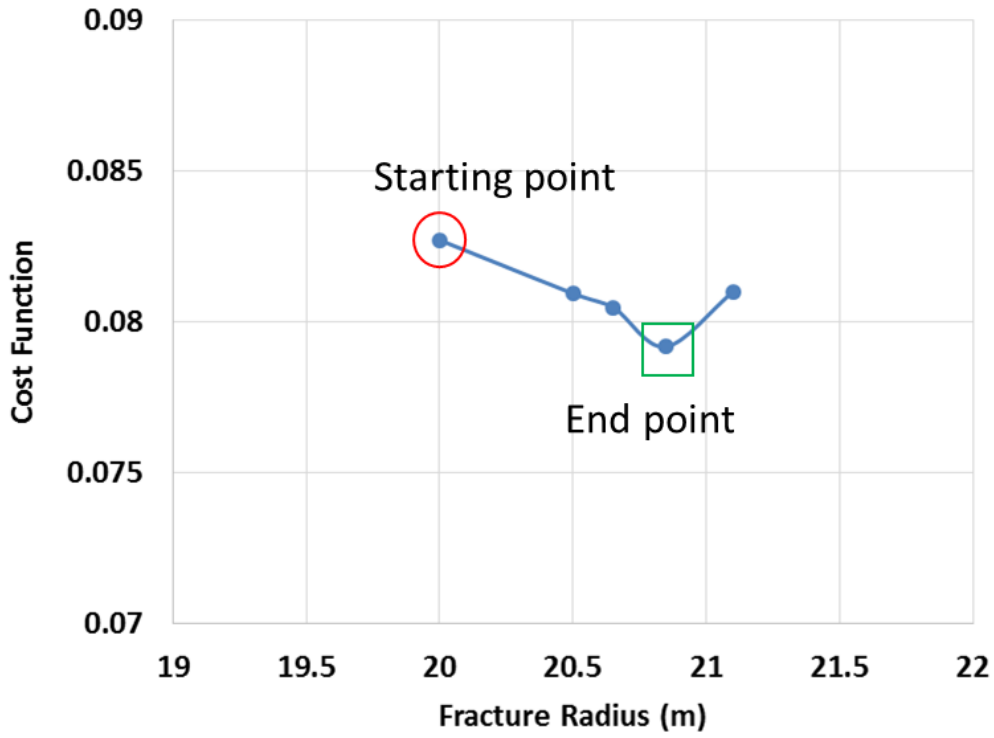

Figure 6.15 The change of the cost function with respect to the radius of the first fracture.

6.6 INVERSE SOLVER TEST - VERY FAST SIMULATED ANNEALING

To test the method of very fast simulated annealing (VFSA) and make a fair comparison with the method of steepest descent, the same scenarios shown in Fig. 6.10 and 6.13 are used to run the inverse simulations.

For the single-fracture case, the true model $\{\delta_1, r_1\}_{\text{true}}$ is set to {5 mm, 20 m}. The inversion starts randomly from predefined intervals for both fracture width [2 mm, 8 mm] and radius [10 m, 50 m]. Following a relatively fast cooling scheme ($T = 10 \cdot e^{-0.5 \cdot k}$, k is the iteration number), the results converge at {5.1 mm, 19.7 m} after 40 iterations. The relative errors from the method of steepest descent and VFSA are summarized in Table 6.1 for comparison. The fracture width and radius from VFSA are

apparently much more accurate with errors both within 2%, meaning that VFSA is a more decent method for this single-fracture case.

	Error in Fracture Width (%)	Error in Fracture Radius (%)
Steepest Descent	6.0	28.0
VFSA	2.0	1.5

Table 6.1 The relative errors for the single-fracture case from steepest descent and VFSA.

For the multiple-fracture scenario, the true model is kept the same. So the parameters of the three fractures $\{\delta_1, \delta_2, \delta_3, r_1, r_2, r_3\}_{\text{true}}$ are set to {4.8 mm, 3.5 mm, 5 mm, 31 m, 22 m, 28 m}. The inversion starts randomly from predefined intervals for both fracture width [2 mm, 8 mm] and radius [10 m, 50 m]. The results converge after 40 iterations, following a same cooling scheme ($T = 10 \cdot e^{-0.5 \cdot k}$, k is the iteration number) (Fig. 6.16(a), (b)). As a global search method, VFSA permits increase of the objective function occasionally, which allows it to jump out of local minima if there are any. In contrast, the possibility of accepting 'bad' solutions is zero for the method of steepest descent.

Fig. 6.16(c) and (d) show the comparison between the true model parameters and the inverted ones from clean synthetic data. The resolution for radius and width is 0.5 m and 0.1 mm, respectively. VFSA gives very accurate estimates of the fracture width and less accurate estimates of the fracture radius. The error ranges from 0% to 2.1% for the inverted width and from 4.6% to 15.8% for the inverted radius. The inverted data for three excitation locations (gap #0, #1 and #2) converge to the true data as well (Fig. 6.17). Theoretically the accuracy can be further improved by adopting a more gentle

temperature scheme and allowing more searches at each temperature, which will of course increase the computation cost (Sen and Stoffa, 2013).

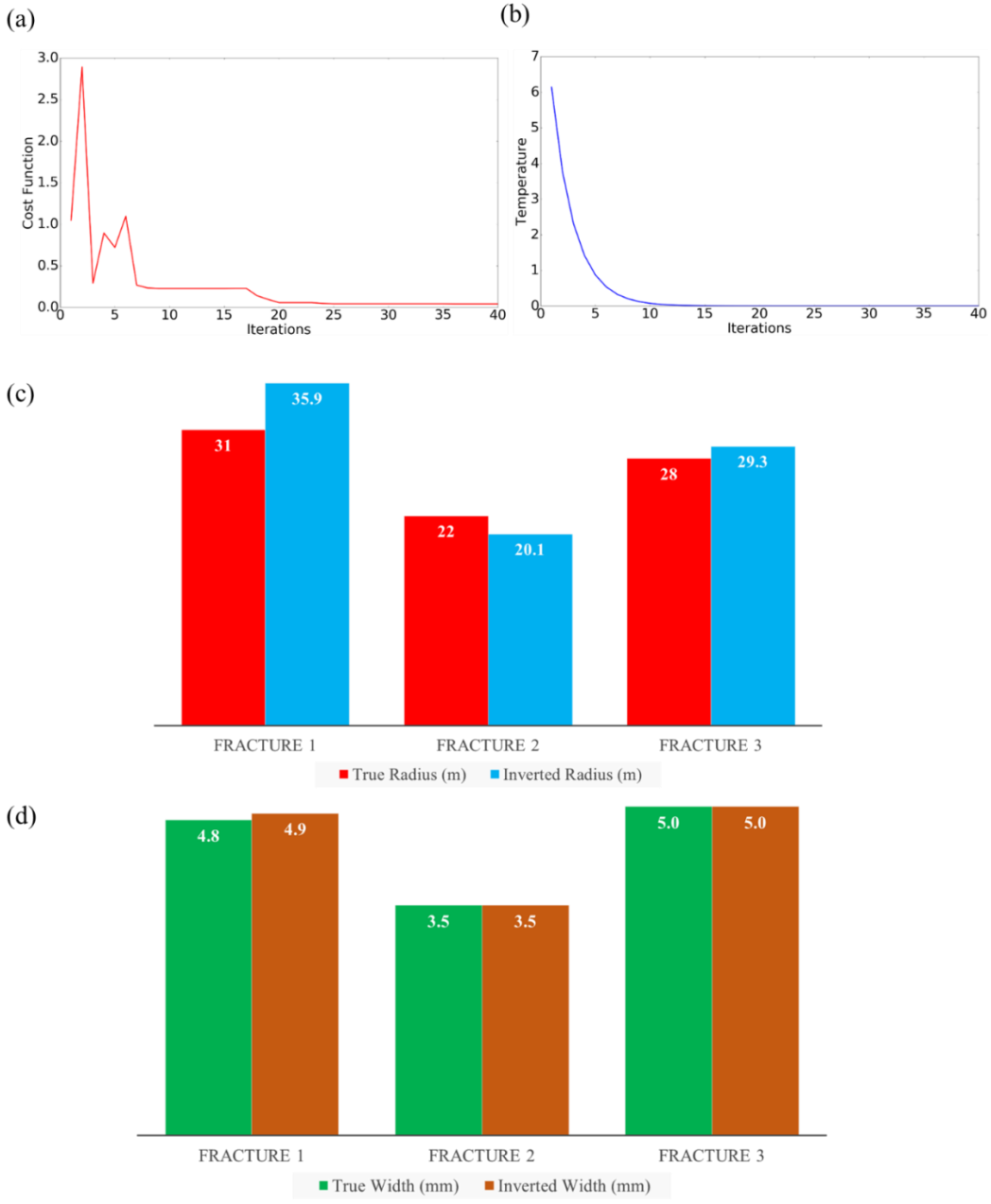

Figure 6.16 (a) Cost function in each iteration. (b) The temperature scheme used for the study. (c) Comparison between true radii and inverted radii of the three fractures. (d) Comparison between true widths and inverted widths of the three fractures.

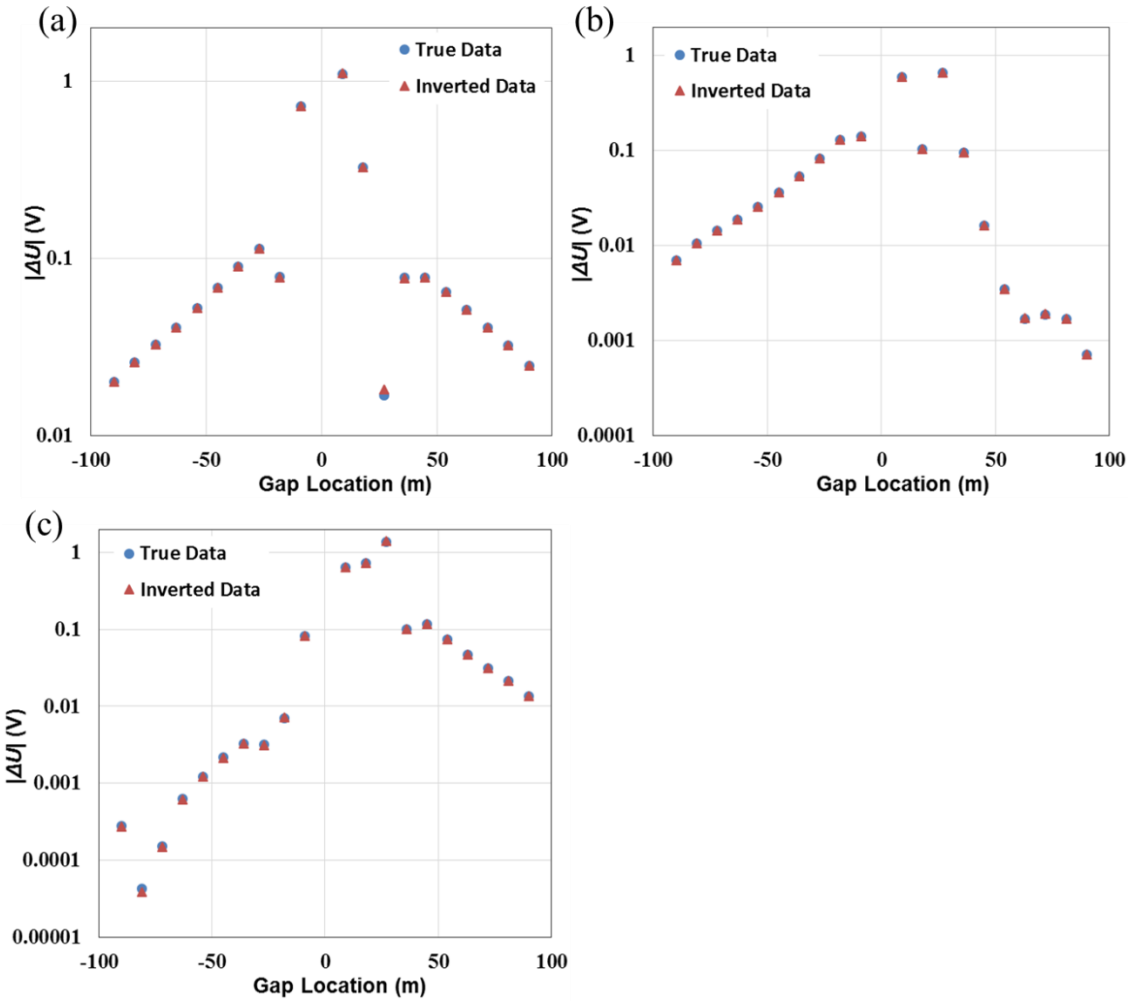

Figure 6.17—Comparison between true data and inverted data for three excitation locations. (a), (b) and (c) correspond to the data when gap #0, #1 and #2 (Fig. 6.13) are excited, respectively.

The relative errors for the multiple-fracture case from steepest descent and VFSA are summarized in Table 6.2 for comparison. Clearly VFSA offers much more accurate results, especially for fracture radius. The accuracy can be further improved by imposing more iterations and a slower cooling schedule. The method of steepest descent, on the other hand, gets trapped in a local minimum and is not able to jump out to reach the global optimal solution.

	Error in Fracture Width (%)		Error in Fracture Radius (%)	
	Average	Maximum	Average	Maximum
Steepest Descent	2.5	2.9	21.1	31.8
VFSA	0.7	2.1	9.7	15.8

Table 6.2 The relative errors for the multiple-fracture case from steepest descent and VFSA.

In actual field measurements noise is inevitable due to background noise and limited tool resolution. Reduction of noise by improving sensor resolution requires extra effort and cost, which can reduce the utility of a field deployable tool. The influence of noise, however, can be minimized by a robust inverse solver. We take one step further to investigate the robustness of VFSA by introducing random noise into the synthetic data. Assuming the voltage sensors have resolution of ~10 μV, the noise floor is within 1% of the calculated voltages for most of the receiver gaps (Fig. 6.17), when a source voltage of 20 V is applied. To properly demonstrate the robustness of the inverse solver, and also to account for other unknown noise sources, we introduce a pessimistic noise level of 2% to the data. The inversion process using VFSA is repeated.

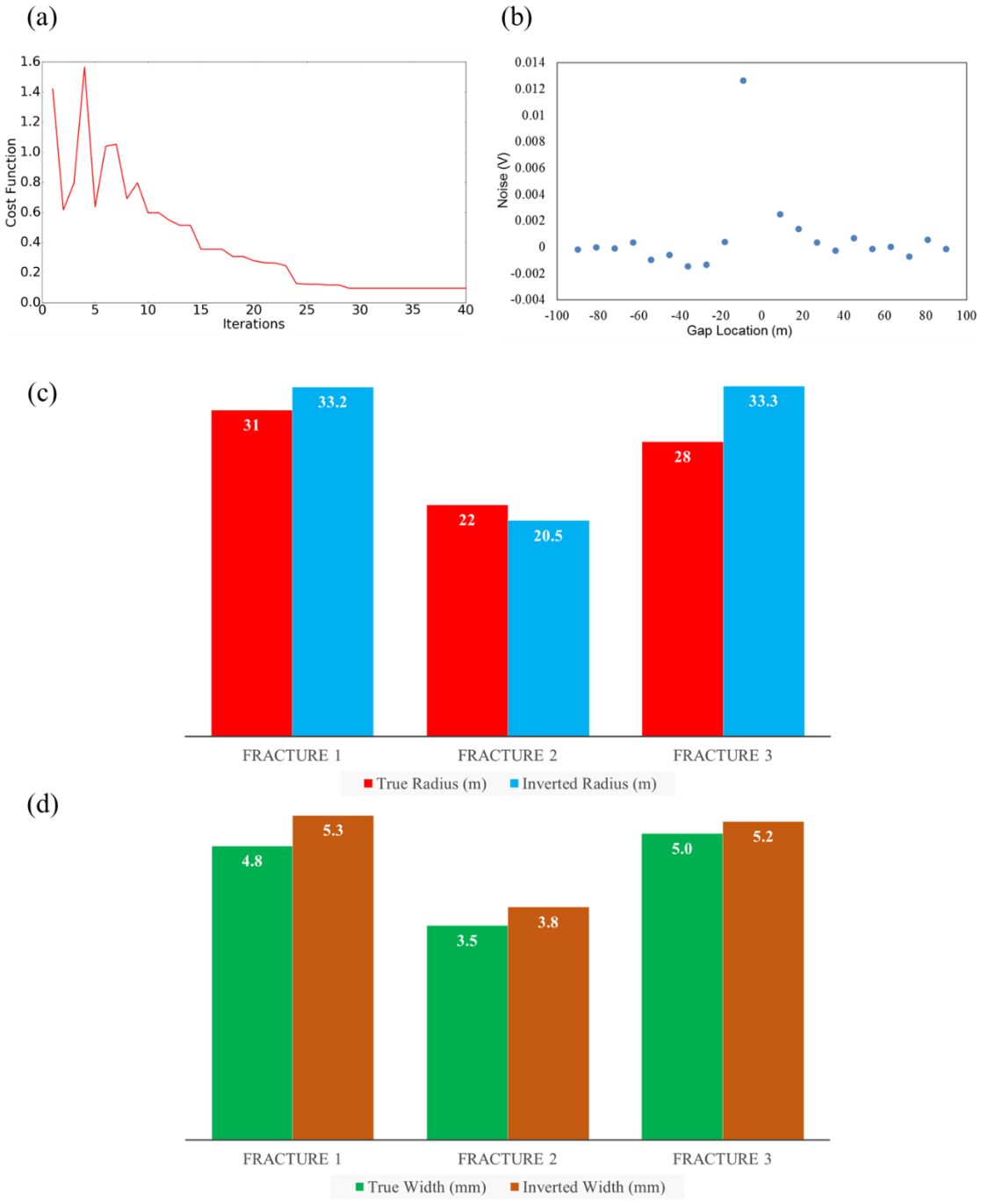

Figure 6.18—(a) Cost function in each iteration when inverting the noisy data. (b) 2% of random noise is added to the clean synthetic data. (c) Comparison between true radii and inverted radii of the three fractures. (d) Comparison between true widths and inverted widths of the three fractures.

Fig. 6.18(a) shows the cost function following the same temperature scheme (Fig. 6.16(b)) when $\pm$2% random noise is added to the same synthetic data (Fig. 6.18(b)). The results show that the errors for the inverted fracture radii range from 6.8% to 18.9%, and the errors for inverted widths range from 3.3% to 10.0% (Fig. 6.18(c), (d)). Compared to the results from clean synthetic data (Fig. 6.16(c), (d)), the inverted widths from noisy data are slightly less accurate, whereas the overall accuracy of the inverted radii remains similar. This shows the proposed VFSA is relatively insensitive to 2% random noise in the 'measured' data and is a robust inverse algorithm for our specific application.

6.7 SUMMARY

This chapter focused on building a model-based inversion framework. The framework incorporate the forward modeling methods introduced in Chapter 3 and an inversion kernel, which is able to extract the fracture parameters from the measured data in a fully automated process. Using this framework, the performance of steepest descent method and very fast simulated annealing are evaluated and compared.

The inversion results reveal that the method of steepest descent can be used to extract the parameters of both a single fracture and multiple fractures. But as a deterministic (greedy) algorithm, it can be easily trapped in a local minimum. VFSA, as a global optimization method, allows us to jump out of the local minima by accepting 'bad' solutions with a time-varying probability. Due to that reason, VFSA offers much more accurate inversion results for multiple fractures. Moreover, it is proved to be a robust inverse solver capable of inverting noisy data. These conclusions will help to develop an optimal methodology for inverse modeling of downhole electrical measurements using the tool, which will be presented in the following chapter.

NOMENCLATURE

U = voltage, V

ΔU = differential voltage before and after hydraulic fracturing, V

E = objective function

T = temperature for VFSA

d = distance from the excited gap, m

δ = fracture width, mm

G = fracture conductance, S

r = fracture radius, m

$\boldsymbol{m}$ = model parameter vector

Chapter 7: Inversion Results with Uncertainty Estimation

7.1 BACKGROUND

Many geophysical inverse problems suffer from the problem of non-uniqueness, which means that more than one model may fit the observed data very well (Sen and Stoffa, 1996; Sen and Stoffa, 2013). A major cause for this problem is the lack of adequate measurements (data), which leaves us with an under-determined system (Menke, 1984). Our resistivity tool relies on the measurements at the insulating gaps, which are placed far apart along the wellbore. Moreover, unlike induction methods which can make both co-polarized and cross-polarized measurements (Yang et al., 2015; Zhang et al., 2016), our tool makes one-dimensional voltage measurements. Therefore, limited data are collected for extracting the geometrical parameters of multiple fractures, which can easily lead to an underdetermined problem if not handled properly. The decreasing sensitivity to fracture size as the size grows, and the interactions between neighboring fractures can possibly be an additional cause for non-uniqueness. For these reasons, we need to conduct the inversion within a range of parameters and estimated uncertainty bounds, to give the interpreter enough information for making the right decisions.

Another challenge for our inverse problem is to properly account for the error or noise in the data. The source of noise can be errors in the measurements, which may be caused by instrument resolution, interference from the environment, or the use of inexact theory for predicting the data (Tarantola, 1987). Reduction of noise by improving sensor resolution requires extra effort and cost, which can reduce the utility of a field deployable tool. Alternatively, the influence of noise on the inversion results can be minimized by a robust inverse solver. Hence we need to test the robustness of our inversion methods to make sure a certain level of noise can be tolerated.

In the previous chapter a model-based inversion framework was built, which is able to incorporate the forward modeling methods and an inversion kernel. We have also proved that very fast simulated annealing (VFSA) is a more suitable optimization method that can provide much more accurate inversion results than the steepest descent method. Based on our framework and VFSA, this chapter presents a methodology for extracting the geometries of multiple fractures by inverting the measured data from a logging sequence. Likewise, the fractures are assumed to be circular disks with uniform thickness. Inversion results with different tool configurations and noise levels in the data are presented to prove the robustness of the method. Uncertainties in the estimated results are approximated using statistical methods. This chapter also presents inversion results when more realistic conditions are encountered, e.g., fracture deviation from the well, complex fractures, etc.

7.2 INVERSION METHODOLOGY – DIVIDE AND CONQUER

As stated in Chapter 5, we are faced with a problem of mapping proppant distribution in multiple fractures instead of one or a few. Horizontal wells with toe-up lengths of 2500 ft to over 5000 ft are quite common. These wells may have more than 100 fractures (Fig. 7.1). Including all the fractures results in an over complicated geometry for inverse modeling, due to the requirement of mesh refinement around these fractures with large aspect ratio. Therefore, we need a strategy to decrease the size of the problem, without sacrificing the integrity of the original geometry.

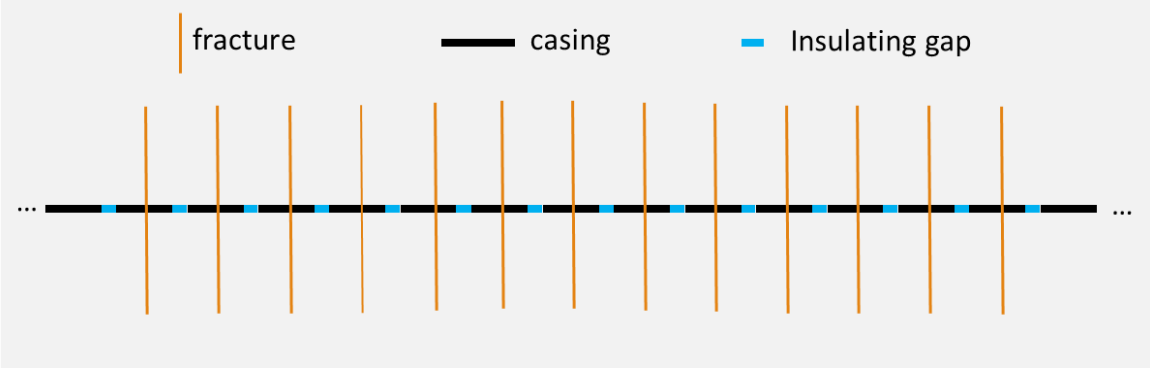

Figure 7.1 A schematic depicting a horizontal well with multiple fractures.

We have also learned that the influence from passive fractures (not in direct contact with the electrodes) is limited to a very short distance. Only fractures next to the receiver gaps need to be incorporated in the simulations. This means we can possibly solve the multiple-fracture inverse problem by using the so-called 'divide and conquer' strategy (Karp 1977). The original problem can be divided into sub-problems of manageable size, which are naturally disjoint. Then the sub-problems are solved separately and the inversion results for the sub-problems are patched back together (Kirkpatrick et al., 1983). Solving the sub-problems can easily be achieved in parallel by modern computers to save cost and time. So how should we divide the problem without sacrificing the integrity of the original geometry?

Following the work in Chapter 5, we mainly examine two strategies for each excitation location: (i) only the voltages at 8 receivers, 4 on each side of the transmitter, are used for inversion; (ii) only the voltages at 6 receivers, 3 on each side of the transmitter, are considered. All the measured voltages at other receiver gaps are computed but abandoned because they are relatively small.

Without loss of generality, we assume there is one fracture on each of the casing sections. If not specified otherwise, we assume the fractures are circular with uniform

thickness and they are symmetric about the wellbore. Hence, each fracture is associated with two model parameters (radius and width). For case (i), at least 10 fractures should be included in the geometry (Fig. 5.12), so this leads to 20 parameters in the model $\boldsymbol{m}$. Clearly it is an under-determined problem with only 8 elements in the data $\boldsymbol{d}$. Since the tool excites the gaps continuously, one at a time, the measurements at different excitation locations can be combined to make an even-determined or over-determined sub-system (out of the original one shown by Fig. 7.1) that can be solved with ease. For example, if measurements from four excitations (at gap 0, 1, 2 and 3 in Fig 7.2 (a)) are combined, we are faced with an inverse sub-problem with 26 model parameters (13 fractures in Fig. 7.2 (a)) and 32 data points (strategy 1). Likewise, if we combine the measurements from four excitation locations for case (ii), we are faced with an inverse problem with 22 model parameters (11 fractures in Fig. 7.2 (b)) and 24 data points (strategy 2). Both cases can be solved using our inversion framework and VFSA.

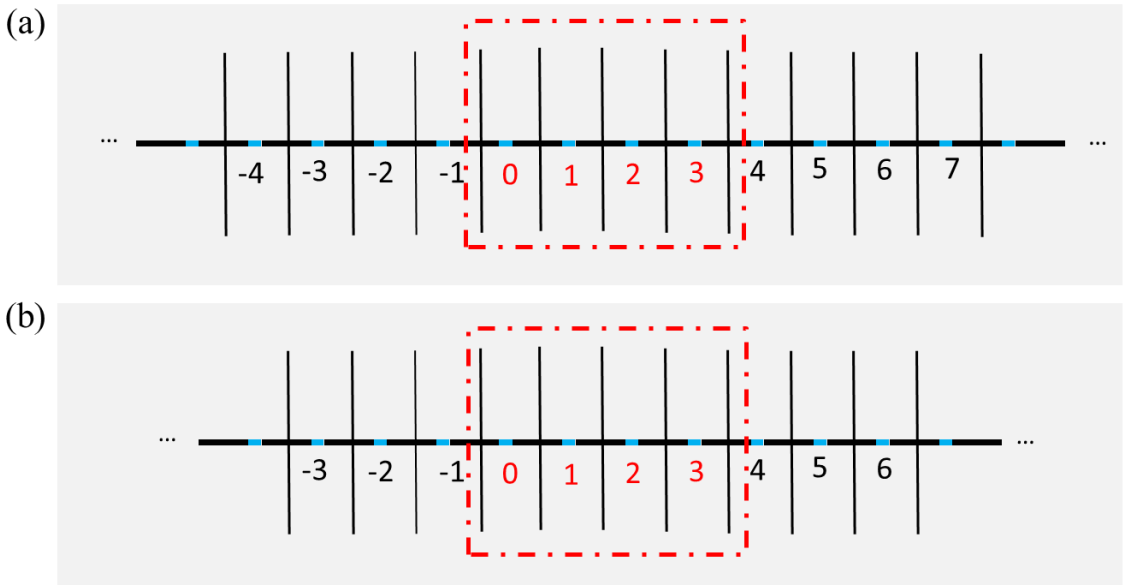

Figure 7.2 (a) 13 fractures are involved in a four-excitation (at gap 0, 1, 2 and 3) sub-problem, if voltages at 8 receivers from each excitation are used for inversion. (b) 11 fractures are involved in a four-excitation (0, 1, 2 and 3) sub-problem, if voltages at 6 receivers from each excitation are considered. The red dashed rectangles mark the fractures directly in contact with the casing sections that have been excited when the tool moves from gap 0 to 4.

Going back to the original problem with tens of hydraulic fractures on a horizontal well (Fig. 7.1), we can divide it into a few sub-problems using either of the proposed strategies above, solve these sub-problems and patch the solutions back. In the following sections of this chapter, we will focus on solving the sub inverse problems using both strategies and estimating the uncertainty bounds. When not specified otherwise, all the fractures are located in the middle of the casing sections. The electrical conductivity for all the fractures is set to 3000 S/m. As the tool moves in the wellbore, it excites the insulating gaps 0, 1, 2 and 3, one at a time by a voltage source of 20 V, before and after hydraulic fracturing operations.

The cost function to be minimized using VFSA is defined as:

$$E(\boldsymbol{m}_{inv}) = \sum_{j=1}^{4} \sum_{i=1}^{n} w_i \cdot [d_i(\boldsymbol{m}_{inv}) - d_i(\boldsymbol{m}_{true})]^2. \qquad (7.1)$$

Here i is the receiver gap index and n represents the number of receivers from each excitation, which is 8 and 6 for strategy 1 and 2, respectively. j is the excitation index, which ranges from 1 to 4. d_i is the data at receiver i, which is the differential voltage before and after hydraulic fracturing operations. w_i is the weight put on each receiver and it is defined as i^2 to compensate for the decay of signal with respect to distance from the transmitter. 2% and 5% Gaussian noise are introduced to the data in the following form:

$$d_i \leftarrow d_i(1+\alpha), \tag{7.2}$$

where α is a randomly generated number with a zero mean and 2% or 5% standard deviation.

7.3 INVERSION RESULTS FROM STRATEGY 1

We started testing our inversion framework by solving the sub-problem resulting from strategy 1, when 13 fractures are involved in a four-excitation logging sequence (Fig. 7.2(a)). The data are synthesized by running the forward simulations at four excitation locations in parallel. The widths and radii (26 model parameters) for the 13 fractures from left to right in Fig. 7.2(a) are randomly set as shown in Table 7.1 (true model).

Fracture	Width				Radius			
	True (mm)	Inverted (mm)	Uncertainty (%)	Error (%)	True (m)	Inverted (m)	Uncertainty (%)	Error (%)
1	4.8	4.7	33.5	3.8	25	19.6	30.2	21.8
2	5.5	4.7	36.2	14.7	32	22.5	41.1	29.7
3	4.7	5.5	26.7	18.5	31	24.7	30.3	20.4
4	5.2	5.3	22.7	1.9	29	27.2	25.0	6.2
5	5.3	5.1	8.3	3.7	27	29.6	17.3	9.6
6	4.8	4.8	5.8	1.2	33	31.8	16.9	3.7
7	4.7	4.6	11.0	0.8	29	30.9	13.1	6.5
8	5.2	5.0	11.4	3.0	32	32.2	11.5	0.6
9	5.0	4.9	9.8	1.6	30	29.2	15.3	2.7
10	4.5	5.1	25.7	14.0	28	26.6	29.6	5.0
11	4.2	4.6	43.5	9.3	29	25.2	36.5	13.1
12	5.7	4.7	43.2	16.3	27	24.2	44.7	10.4
13	5.2	4.5	39.1	12.9	31	22.1	33.6	28.6
Average (5 marked in red)			9.3	2.1			14.8	4.6

Table 7.1 The true model and inverted model when 2% Gaussian noise is added to the synthetic data. The values for the inverted model are the average from 15 inversion runs.

First 2% Gaussian noise is added to the synthetic data. Search intervals of [2 mm, 8 mm] and [10 m, 50 m] are defined for the widths and radii, respectively. Both the starting model and updated model using VFSA will be bounded within these intervals. A relatively fast cooling scheme, $T = 10 \cdot e^{-0.5 \cdot k}$ (k is the iteration number), is followed (Fig 7.3). At each temperature 8 searches are allowed and the results converge after 40

iterations, which takes 320 searches in total. Fig 7.3 also shows an example of how the cost function evolves as the iterations proceed. As a global search method, it is evident from the plot that VFSA permits increases in the objective function occasionally, which differs from gradient-based methods that only accept better solutions. This allows it to jump out of local minima and eventually reach the global minimum.

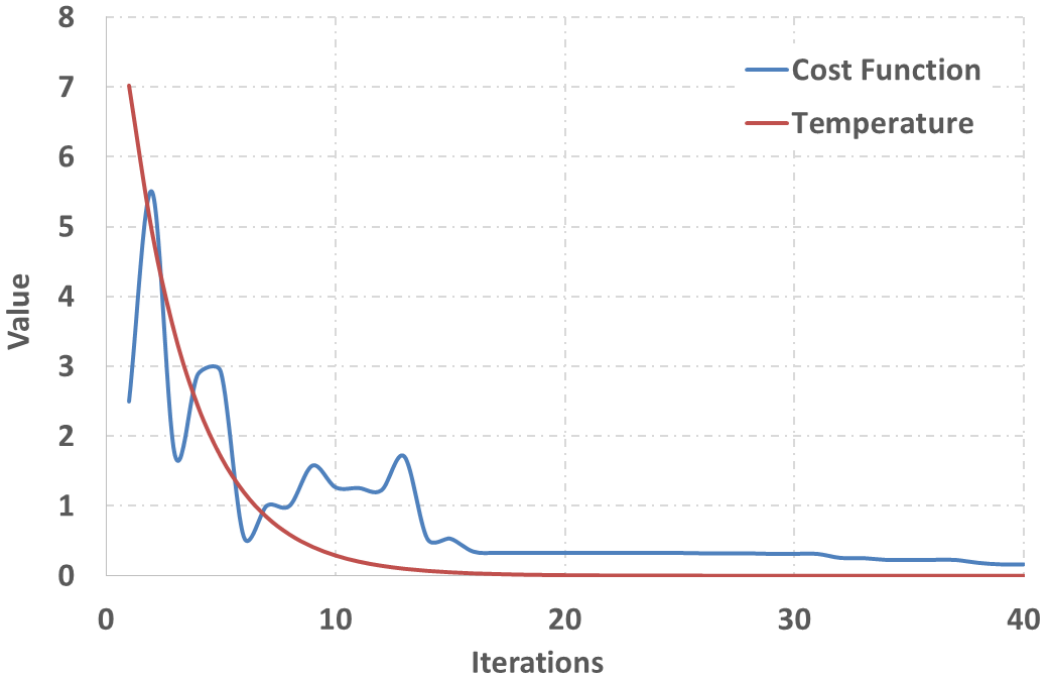

Figure 7.3 Cost function and temperature at each iteration during an inversion process.

The inversion procedure is repeated 15 times. Thereafter, the average and standard deviation of the model parameters are calculated. Table 7.1 compares the true and inverted model. The relative error with respect to the true model spans a very wide range for both the inverted widths and radii. In Fig. 7.2 (a) the 5 fractures directly in contact with the casing sections, that have been excited when the tool moves from gap 0 to 4, are marked by a red dashed rectangle. It is found that the inversion results for these 5 fractures are the most accurate (shown in red in Table 7.1). As we move towards both

ends, the relative error grows rapidly. In Chapter 5 we concluded that when multiple fractures are present, it is the ones that are in direct contact with the excited casing sections that dominate the measured voltages at the receivers. This conclusion conveniently explains the varying accuracy in the inversion results.

The true and inverted widths and radii for the 5 fractures highlighted in Table 7.1 are also plotted in Fig. 7.4. The error bars (uncertainties) represent one standard deviation associated with each parameter, meaning that the model parameters will fall within this range 68% of the time. The average relative errors for the inverted widths and radii are 2.1% and 4.6%, respectively. The average uncertainties for the inverted widths and radii turn out to be higher at 9.3% and 14.8%, respectively. Overall, VFSA offers very accurate solutions with reasonable uncertainties for the fractures directly in contact with the casing sections that have been excited, when 2% Gaussian noise is added to the synthetic data. It should be noted that although the 8 fractures on two sides of this sub-problem (fractures not marked in Fig. 7.2(a)) are not properly captured, they can be accurately solved using the data acquired when the tool excites the gaps right next to them.

Applying the ‘divide and conquer’ strategy proposed earlier, the data acquired in a multi-stage fractured well can be divided into multiple groups, each containing the measurements from four excitation locations. Five fractures directly in contact with the casing sections that have been excited are solved by inverting each group of data. The solutions are then patched back without sacrificing the integrity of the original geometry. This guarantees both accuracy and efficiency, since the sub-problems can be solved in parallel with ease.

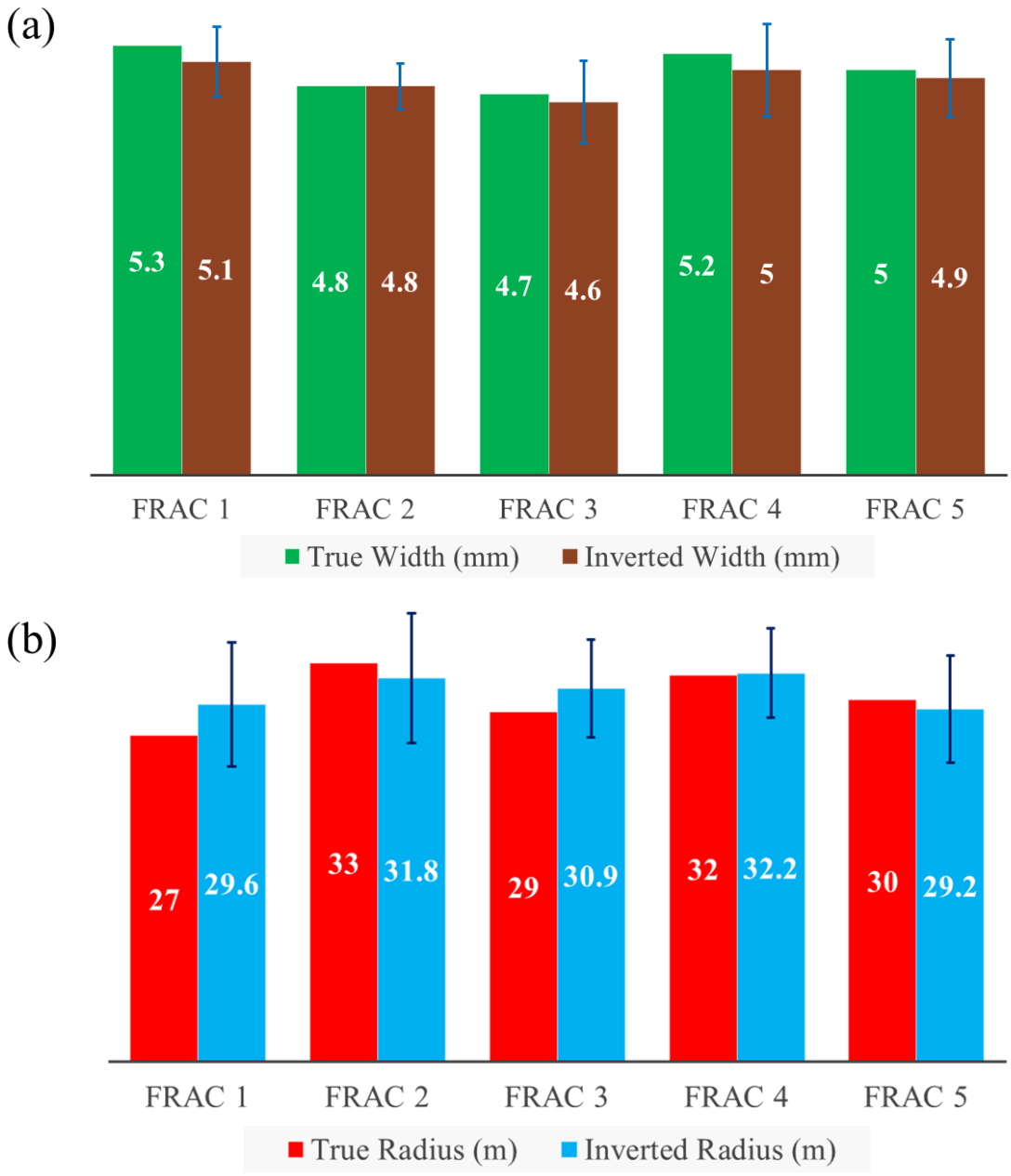

Figure 7.4 Comparison between the true and inverted model for the five fractures highlighted in Table 7.1. 2% Gaussian noise is added to the data. The error bars indicate the uncertainties associated with each parameter.

The covariance and correlation matrices are also calculated to investigate the correlation between different model parameters. In the covariance matrix (Table 7.2) the

element in the i, j position is the covariance between the i^{th} and j^{th} elements in the model vector. The correlation matrix (Table 7.3) can also help us interpret the interactions or correlations between different model parameters. Take the 6th column in Table 7.3 as an example, the coefficients show a clear correlation between the radius of fracture 1 and those of other fractures. As a fracture's distance from fracture 1 increases, the correlation decreases due to the vanishing interaction between them. Correlation leads to non-uniqueness of the inverted model, but it does not seem to be a big concern, since we only observed a slight uncertainty in the inverted model.

	δ_1	δ_2	δ_3	δ_4	δ_5	r_1	r_2	r_3	r_4	r_5
δ_1	**6.60**									
δ_2	1.45	**2.76**								
δ_3	-2.15	3.28	**9.34**							
δ_4	-3.24	2.94	9.67	**11.73**						
δ_5	-2.06	2.23	7.25	9.02	**8.41**					
r_1	1.91	-1.83	-6.77	-5.86	-3.18	**26.25**				
r_2	-4.59	1.64	2.13	1.62	-2.72	-9.88	**28.78**			
r_3	1.51	0.56	4.60	4.59	3.79	-3.79	-11.94	**16.39**		
r_4	-3.82	2.00	3.91	3.48	2.81	-4.40	7.80	-5.23	**13.76**	
r_5	-2.31	-1.37	4.28	4.91	2.60	1.74	-2.85	6.21	-7.08	**19.87**

Table 7.2 Covariance matrix for the inverted model. Each element on the diagonal is the variance of the corresponding model parameter.

	δ_1	δ_2	δ_3	δ_4	δ_5	r_1	r_2	r_3	r_4	r_5
δ_1	1									
δ_2	0.34	1								
δ_3	-0.27	0.65	1							
δ_4	-0.37	0.52	0.92	1						
δ_5	-0.28	0.46	0.82	0.91	1					
r_1	0.15	-0.21	-0.43	-0.33	-0.21	1				
r_2	-0.33	0.18	0.13	0.09	-0.17	-0.36	1			
r_3	0.15	0.08	0.37	0.33	0.32	-0.18	-0.55	1		
r_4	-0.40	0.32	0.34	0.27	0.26	-0.23	0.39	-0.35	1	
r_5	-0.20	-0.19	0.31	0.32	0.20	0.08	-0.12	0.34	-0.43	1

Table 7.3 Correlation matrix for the inverted model.

To investigate the robustness of the inverse solver, we introduce a higher level of noise, 5% Gaussian noise to the synthetic data. Again the inversion procedure is repeated for 15 times, each time from a different starting model. The inversion follows the same cooling scheme (Fig. 7.3) and converges after 320 searches in total. This time we only focus on the five fractures directly in contact with the casing sections that have been excited (marked by the red rectangle in Fig. 7.2(a)). These five fractures are numbered 1 to 5 from left to right. The comparison between the true and inverted model is shown in Table 7.4 and Fig. 7.5.

Fracture	Width				Radius			
	True (mm)	Inverted (mm)	Uncertainty (%)	Error (%)	True (m)	Inverted (m)	Uncertainty (%)	Error (%)
1	5.3	5.1	10.1	4.1	27	30.1	18.0	11.5
2	4.8	4.8	9.1	1.3	33	31.1	15.3	5.6
3	4.7	4.5	9.5	2.6	29	31.9	17.5	9.8
4	5.2	4.9	9.7	5.8	32	29.6	17.6	7.5
5	5.0	4.8	11.1	4.3	30	29.1	17.9	3.0
Average			9.9	3.6			17.3	7.5

Table 7.4 The true model and inverted model for the fiver fractures marked in Fig. 7.2(a), when 5% Gaussian noise is added to the synthetic data.

In this case, the average relative errors for the inverted widths and radii are 3.6% and 7.5%, respectively. The average uncertainties for the inverted widths and radii turn out to be higher at 9.9% and 17.3%, respectively. Compared to the results when 2% Gaussian noise is added, the relative errors and uncertainties increase slightly. However, this does not necessarily mean the results become less accurate due to the increased noise level. Since the inversion results and the associated uncertainties are estimated by running a small number of simulations, the slightly decreased accuracy might originate from the selection of samples. Nevertheless, we did not observe a considerable degradation of the inversion results when up to 5% Gaussian noise is introduced to the synthetic data, meaning VFSA is a robust solver that can tolerate noise in the data.

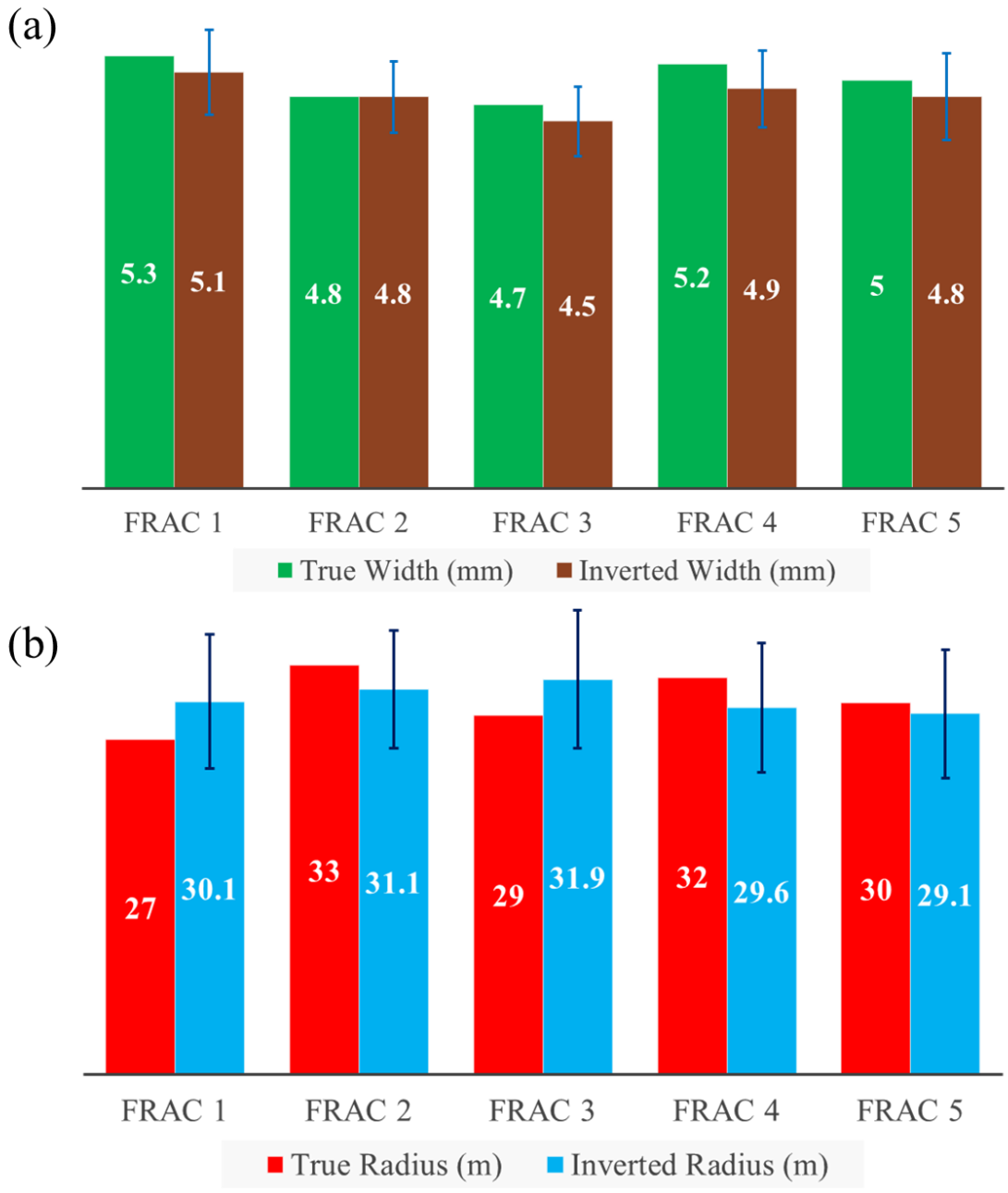

Figure 7.5 Comparison between the true and inverted model for the five fractures highlighted in Table 7.1. 5% Gaussian noise is added to the data. The error bars indicate the uncertainties associated with each parameter.

7.4 INVERSION RESULTS FROM STRATEGY 2

We also tested our inversion framework by solving the sub-problem resulting from strategy 2, when 11 fractures are involved in a four-excitation logging sequence (Fig. 7.2(b)). Likewise, the data are synthesized by running the forward simulations at four excitation locations in parallel. The widths and radii (22 model parameters) for the 11 fractures from left to right in Fig. 7.2(b) are randomly set , shown in Table 7.5 (true model).

	Width				Radius			
Fracture	True (mm)	Inverted (mm)	Uncertainty (%)	Error (%)	True (m)	Inverted (m)	Uncertainty (%)	Error (%)
1	4.8	5.1	30.5	4.9	25	23.9	37.1	4.2
2	5.5	5.5	22.0	0.4	32	25.6	26.0	19.9
3	4.7	4.7	25.1	0.7	31	29.6	22.7	4.5
4	5.2	5.1	12.1	0.9	29	29.7	15.7	2.6
5	5.3	5.5	8.3	3.2	27	31.2	13.5	15.7
6	4.8	5.0	6.6	3.5	33	32.3	19.7	2.0
7	4.7	4.6	3.6	2.0	29	30.3	16.2	4.4
8	5.2	4.9	4.7	5.6	32	31.1	18.4	2.9
9	5.0	5.4	21.7	7.3	30	26.1	26.2	12.8
10	4.5	4.3	33.3	5.2	28	23.9	38.2	14.7
11	4.2	4.9	34.4	18.6	29	25.5	37.7	12.0
Average (5 marked in red)			7.1	3.0			16.7	5.5

Table 7.5 The true model and inverted model when 2% Gaussian noise is added to the synthetic data. The values for the inverted model are the average from 15 inversion runs.

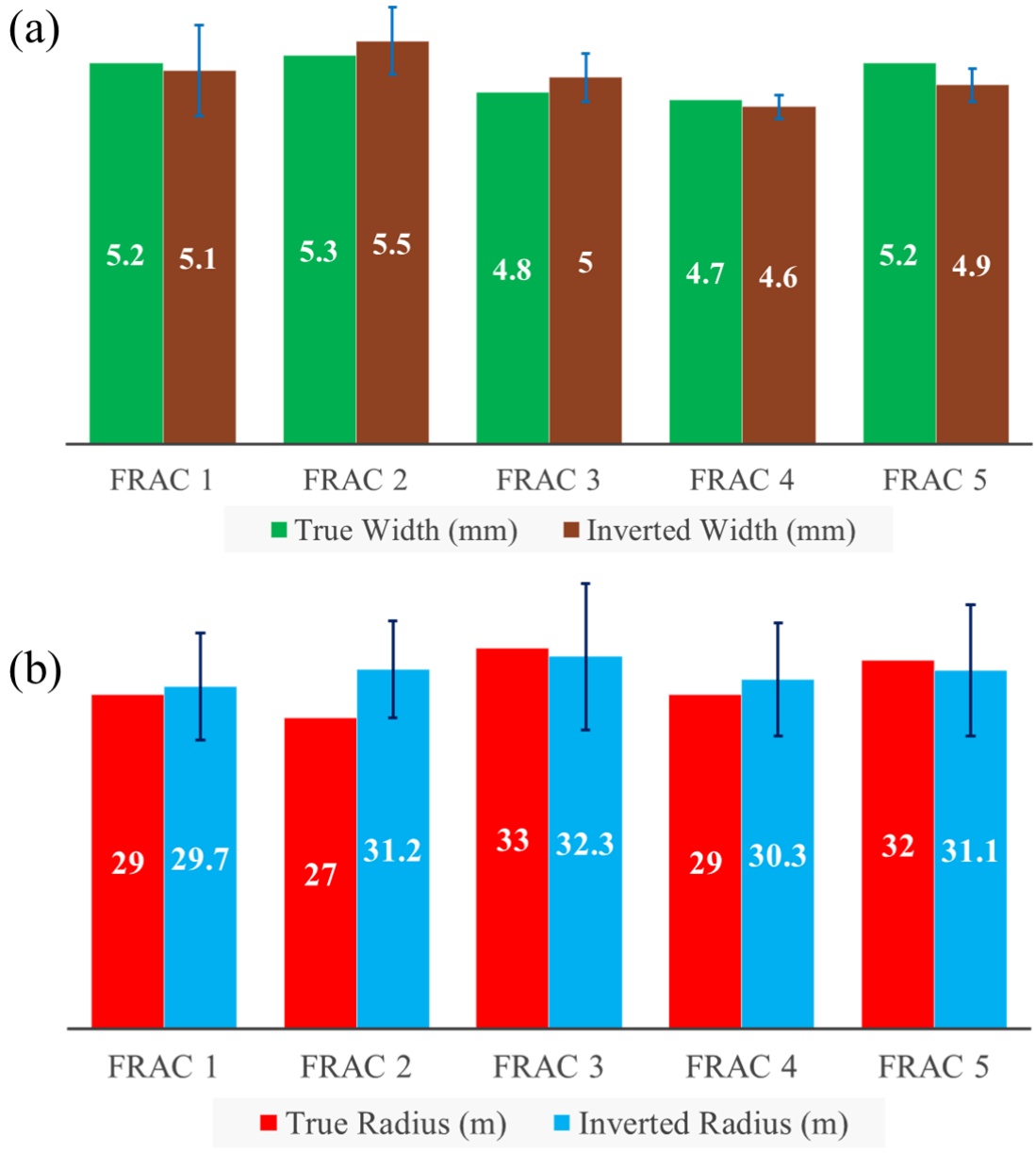

Figure 7.6 Comparison between the true and inverted model for the five fractures highlighted in Table 7.5. 2% Gaussian noise is added to the data. The error bars indicate the uncertainties associated with each parameter.

To make the results comparable with those from inversion strategy 1, we added 2% Gaussian noise to the synthetic data and ran the inversion simulations, following the

same temperature scheme. Table 7.5 compares the true and inverted model. In Fig. 7.2 (b) the 5 fractures directly in contact with the casing sections, that have been excited when the tool moves from gap 0 to 4, are marked by a red dashed rectangle. It is also found that the inversion results for these 5 fractures are the most accurate (shown in red in Table 7.5). As we move towards both ends, the relative error grows rapidly, which is consistent with what was observed when using inversion strategy 1.

The true and inverted widths and radii for the 5 fractures highlighted in Table 7.5 are also plotted in Fig. 7.6. The average relative errors for the inverted widths and radii are 3.0% and 5.5%, respectively. The average uncertainties corresponding to the inverted widths and radii are 7.1% and 16.7%, respectively. Again, when using a different inversion strategy, VFSA still provides very accurate solutions with reasonable uncertainties for the fractures directly in contact with the casing sections that have been excited, when 2% Gaussian noise is added to the synthetic data. Similarly, although the 6 fractures on two sides of this sub-problem (fractures not marked in Fig. 7.2(b)) are not properly captured, they can be accurately solved using different batches of data, acquired when the tool excites the gaps right next to these fractures.

To further verify the robustness of the inverse solver, we now introduce 5% Gaussian noise to the synthetic data and solve the fracture parameters using the same strategy. Again the inversion procedure is repeated for 15 times, each time from a different starting model. The inversion follows the same cooling scheme (Fig. 7.3) and converges after 320 searches in total. This time we only focus on the five fractures directly in contact with the casing sections that have been excited (marked by the red rectangle in Fig. 7.2(b)). These five fractures are numbered 1 to 5 from left to right. The comparison between the true and inverted model is shown in Table 7.6 and Fig. 7.7.

Fracture	Width				Radius			
	True (mm)	Inverted (mm)	Uncertainty (%)	Error (%)	True (m)	Inverted (m)	Uncertainty (%)	Error (%)
1	5.2	5.1	10.1	1.0	29	29.4	18.0	1.2
2	5.3	5.3	7.9	1.0	27	28.4	17.1	5.0
3	4.8	4.8	11.7	1.1	33	31.1	11.4	5.7
4	4.7	4.6	10.5	0.9	29	28.7	18.1	1.0
5	5.2	5.3	8.8	2.2	32	31.2	19.6	2.6
Average			9.8	1.2			16.8	3.1

Table 7.6 The true model and inverted model for the fiver fractures marked in Fig. 7.2(b), when 5% Gaussian noise is added to the synthetic data.

In this case, the average relative errors for the inverted widths and radii are 1.2% and 3.1%, respectively. The average uncertainties for the inverted widths and radii turn out to be higher at 9.8% and 16.8%, respectively. The estimated data for four excitation locations (gap #0, #1, #2 and #3) agree well with the true data (Fig. 7.8), and we also observe close match of the data for the previous cases. Compared to the results when 2% Gaussian noise is added, the relative errors decrease, but the uncertainties slightly increase. Overall, no remarkable changes are observed, meaning VFSA is a very robust solver that is not sensitive to up to 5% noise in the data. Since the inversion results and the associated uncertainties are estimated by running a small quantity of simulations, and no consistent increase of the errors is observed, the small discrepancies more likely originate from the selection of samples, instead of from the increased noise level.

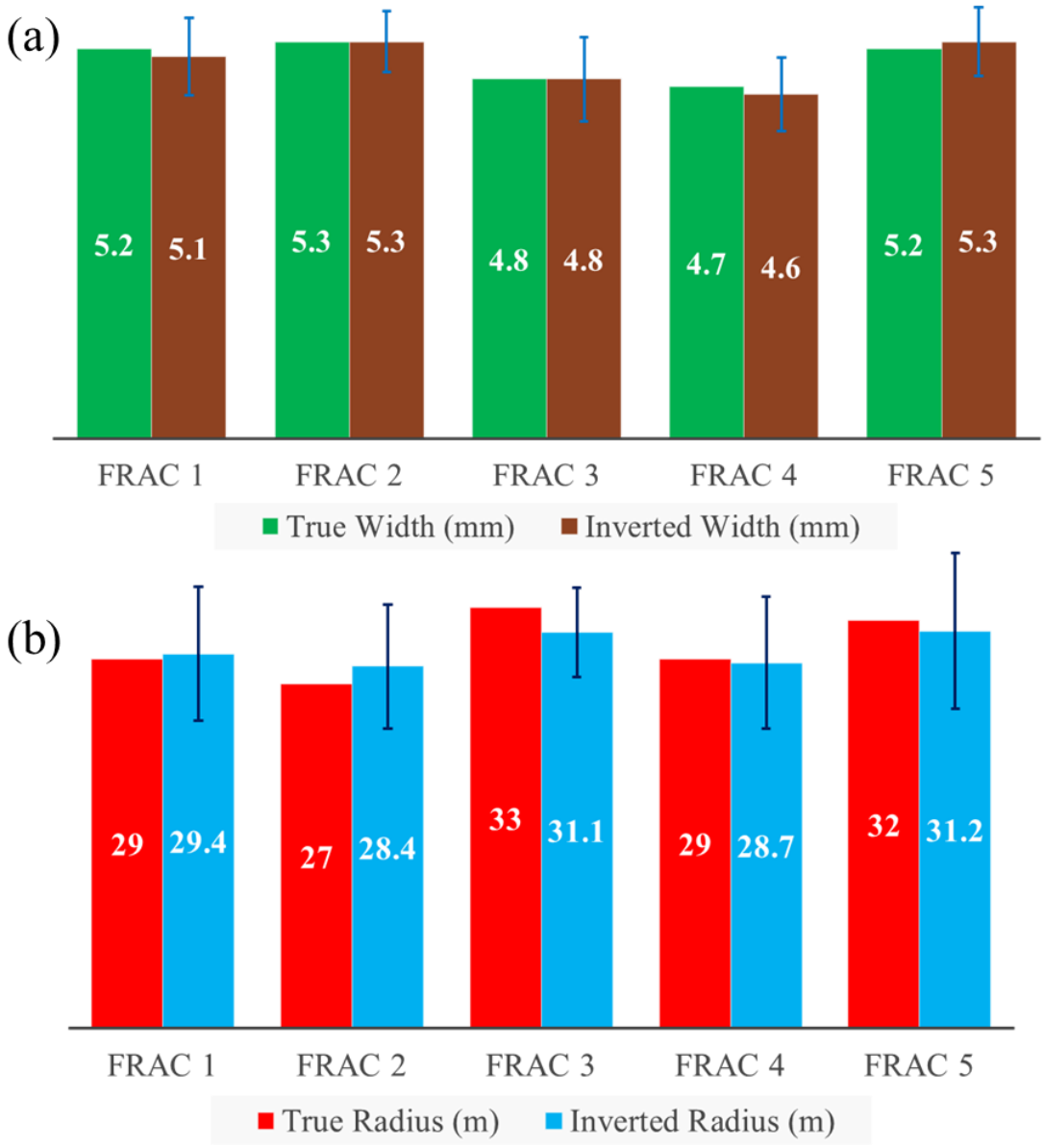

Figure 7.7 Comparison between the true and inverted model for the five fractures highlighted in Table 7.6. 5% Gaussian noise is added to the data. The error bars indicate the uncertainties associated with each parameter.

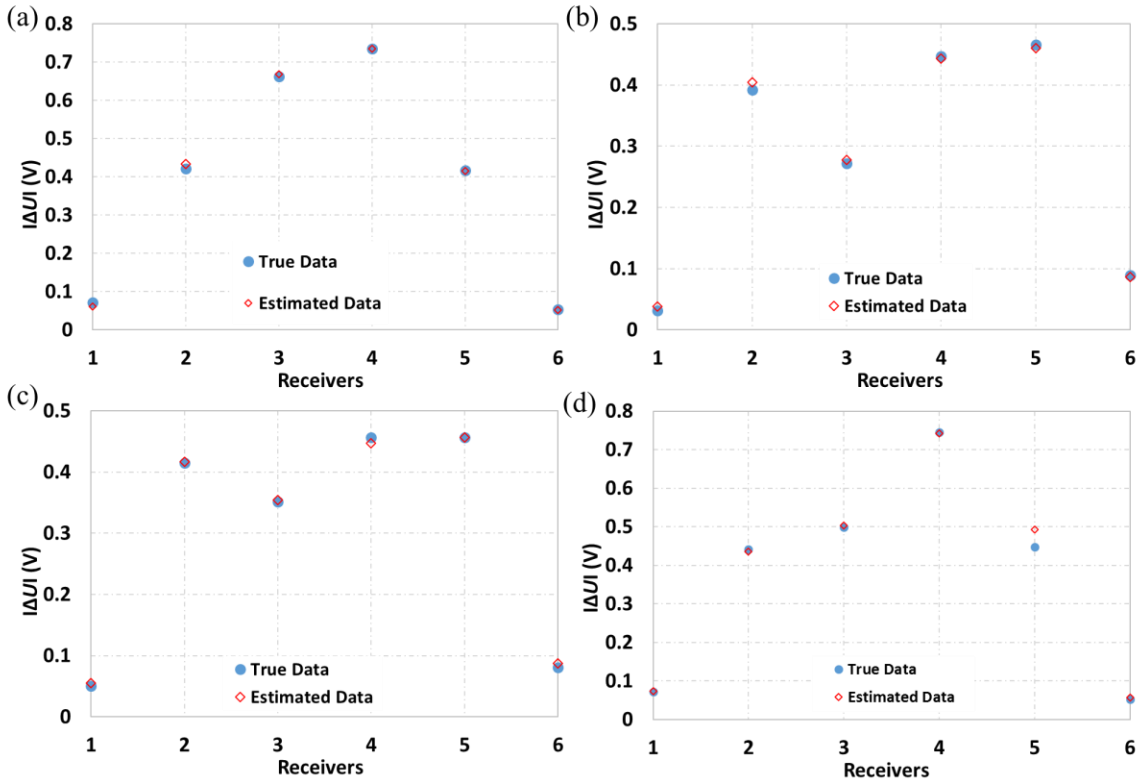

Figure 7.8 Comparison between true data and estimated data for four excitation locations. (a), (b), (c) and (d) correspond to the data when gap #0, #1, #2 and #3 are excited, respectively.

Once again, the covariance and correlation matrices are calculated to investigate the correlation between different model parameters. Take the 1st column in Table 7.8 as an example, the coefficients show clear correlation between the width of fracture 1 and those of other fractures. As a fracture's distance from fracture 1 increases, the correlation decreases due to the vanishing interaction between them. Similar to what we observed when using inversion strategy 1, non-uniqueness due to correlation does not seem to be a big concern, since we only observed moderate uncertainty in the inverted model.

	δ_1	δ_2	δ_3	δ_4	δ_5	r_1	r_2	r_3	r_4	r_5
δ_1	**9.68**									
δ_2	4.53	**6.19**								
δ_3	0.61	6.59	**11.23**							
δ_4	-2.14	3.58	8.01	**8.53**						
δ_5	-3.21	-0.14	1.84	4.94	**7.69**					
r_1	-4.17	0.21	-0.80	-1.03	-0.96	**27.85**				
r_2	0.47	3.04	6.97	3.47	-4.48	-2.62	**23.51**			
r_3	2.91	3.58	4.20	2.85	3.17	-4.52	-4.40	**12.50**		
r_4	1.72	4.75	7.29	0.90	-5.13	9.03	10.05	-0.71	**26.92**	
r_5	-0.62	4.61	8.76	10.21	5.02	5.42	5.50	9.56	1.15	**37.44**

Table 7.7 Covariance matrix for the inverted model. Each element on the diagonal is the variance of the corresponding model parameter.

	δ_1	δ_2	δ_3	δ_4	δ_5	r_1	r_2	r_3	r_4	r_5
δ_1	1									
δ_2	0.59	1								
δ_3	0.06	0.79	1							
δ_4	-0.24	0.49	0.82	1						
δ_5	-0.37	-0.02	0.20	0.61	1					
r_1	-0.25	0.02	-0.05	-0.07	-0.07	1				
r_2	0.03	0.25	0.43	0.25	-0.33	-0.10	1			
r_3	0.26	0.41	0.35	0.28	0.32	-0.24	-0.26	1		
r_4	0.11	0.37	0.42	0.06	-0.36	0.33	0.40	-0.04	1	
r_5	-0.03	0.30	0.43	0.57	0.30	0.17	0.19	0.44	0.04	1

Table 7.8 Correlation matrix for the inverted model.

7.5 REALISTIC FRACTURES – WHAT TO EXPECT

All the previous cases assume the fractures are circular with uniform thickness, and they are symmetric about the wellbore. So there are two model parameters (width and radius) associated with each fracture. These assumptions fail to capture some realistic conditions that are frequently encountered in the field. For example, the proppant settling due to gravity may lead to fractures that are asymmetric, i.e. mainly on the bottom side of the well. The fracture's width can be non-uniform, with less proppant on the fractures' edge. Moreover, tilted and complex fractures are not uncommon in reservoirs with low differential stresses.

Considering these factors in the inversion analysis will dramatically increase the number of model parameters, and ultimately lead to an underdetermined problem. As

mentioned earlier in this chapter, an underdetermined problem suffers from large uncertainties in the inversion results. We have seen about 15% average uncertainties in the inversion results when the fractures are assumed circular with uniform thickness. While we keep our inverse model simple, it is important to study the accuracy we may sacrifice when more complicated conditions are encountered. For this purpose, a single fracture that has more realistic properties is tested, in order to give us a good idea of how our inversion strategy may overestimate/underestimate the actual fracture geometry.

For all the following cases, a fracture with a conductivity of 3000 S/m is placed 5 m away from the transmitter gap (#0), in contact with the positive electrode (Fig. 7.9). A few realistic conditions are tested separately. We use a circular fracture with uniform thickness as the inverse model, which means an equivalent fracture will be extracted by inverting the synthetic data (Fig. 7.9). A circular fracture with radius r=25 m and width δ=4.8 mm is used as the base case for reference.

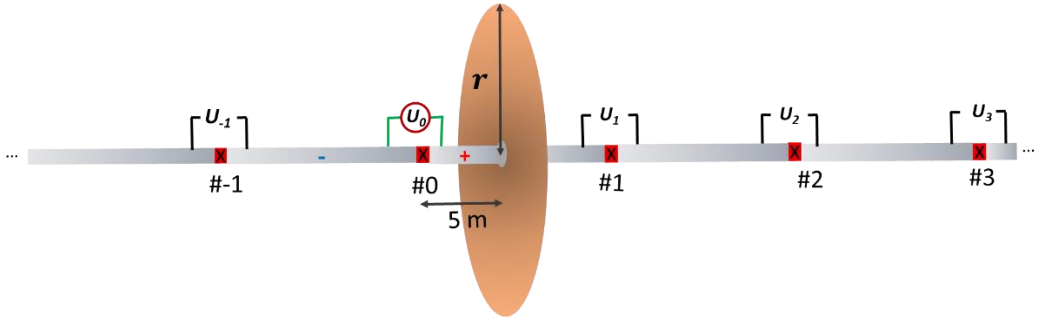

Figure 7.9 Illustration of the tool configuration that is used to invert for the radius and width of a single fracture.

7.5.1 Fracture deviation from the wellbore

Proppant settling due to gravity results in a fracture that deviates from the wellbore by distance d (Fig. 7.10). It should be noted that Fig. 7.10 is a simplified representation of a one-sided fracture and the actual propped fracture is very likely to be

of irregular shape. To investigate how our inversion strategy performs with an asymmetric proppant distribution, we simulate a few cases by varying d and use the computed voltages (synthetic data) for inversion analysis. The fracture's radius and width are kept as 25 m and 4.8 mm. Again our inverse model assumes the fracture is circular, uniform and symmetrical to the wellbore. Hence an equivalent fracture symmetrical to the wellbore, which induces similar signals at the receivers, is produced from the inversion.

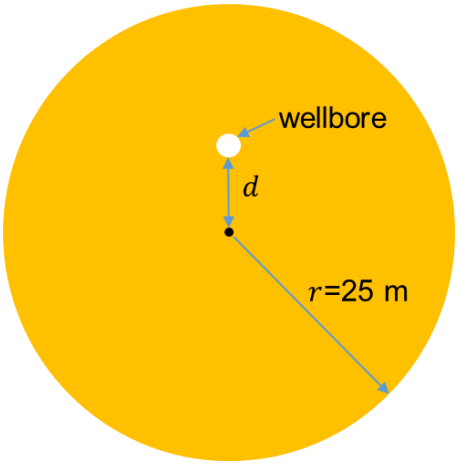

Figure 7.10 A circular fracture that deviates from the wellbore by distance d.

The estimated fracture width and radius from inversion as a function of the fracture's deviation from the wellbore are plotted in Fig. 7.11. When the fracture is symmetrical to the wellbore (the base case when d=0), the estimated and true fracture parameters agree well, with errors below 4%. As the deviation increases, the estimated fracture width has a tiny decrease, whereas the estimated radius drops 17% below the true fracture radius when d=15 m. Chapter 4 shows that when a fracture with radius of 30 m deviates from the wellbore for more than 10 m, the receivers are capable of recognizing the differences in the signals. The inversion results here are consistent with what has been

concluded earlier. Hence we should be aware that our inverse model underestimates the fracture size by providing an equivalent fracture symmetrical to the wellbore, when proppants settle primarily on one side the well. When this happens, the average distance between the proppant and the wellbore is larger than that when the fracture is symmetrical to the wellbore, therefore a smaller fracture is projected by the tool.

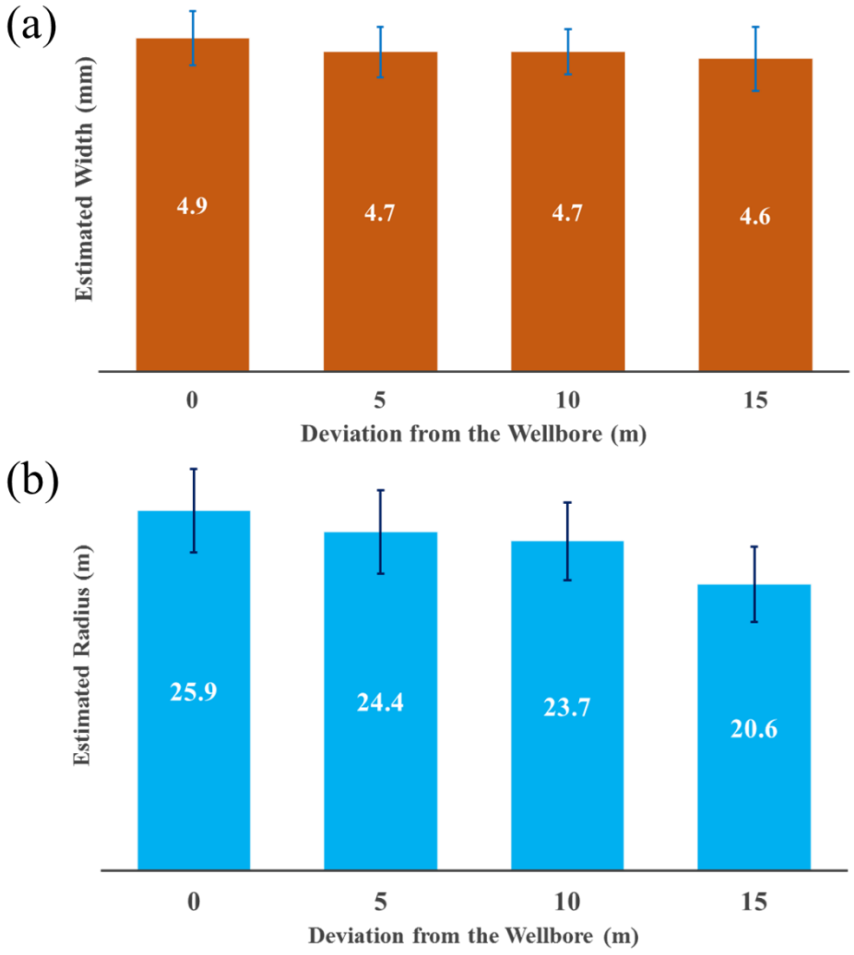

Figure 7.11 The estimated fracture width (a) and radius (b) as a function of the fracture's deviation from the wellbore. The error bars mark the uncertainties associated with the model parameters.

7.5.2 Non-uniform fracture width

Another scenario that happens often in a fracking job is that the fracture's width is not uniform. Moving towards the edge of the fracture, less proppant is transported there due to settling and bridging near the wellbore. We use a simplified model to represent this scenario (Fig 7.12). A fracture with a radius of 25 m is divided evenly into 5 layers and different width profiles are specified (Fig. 7.13(a)). The induced voltages at the receiver gaps for different cases are computed by running forward simulations and the synthesized data are used for inversion analysis. Four cases are compared: (A) The fracture has a constant width of 4.8 mm (base case); (B) The width drops linearly towards the edge; (C) The width drops faster following a second-order polynomial function; (D) The width drops even quicker following a power law. Our inverse model still assumes a circular fracture with uniform width. The goal is to investigate how our inversion strategy performs under these special circumstances.

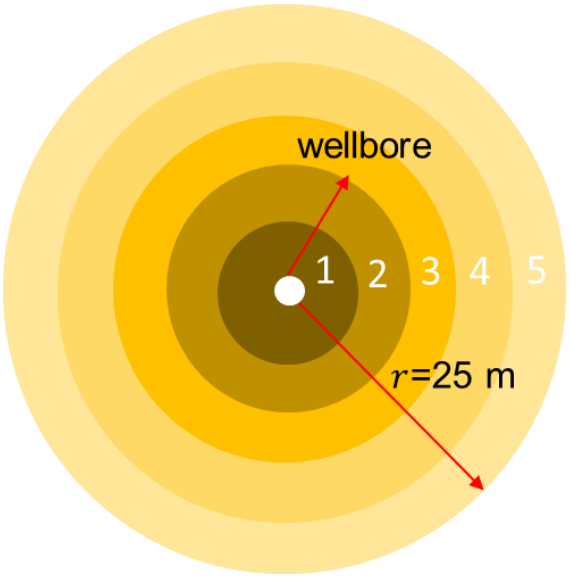

Figure 7.12 A simplified model for fractures with non-uniform width. The fracture has five layers and the width of each layer gets thinner towards the edge.

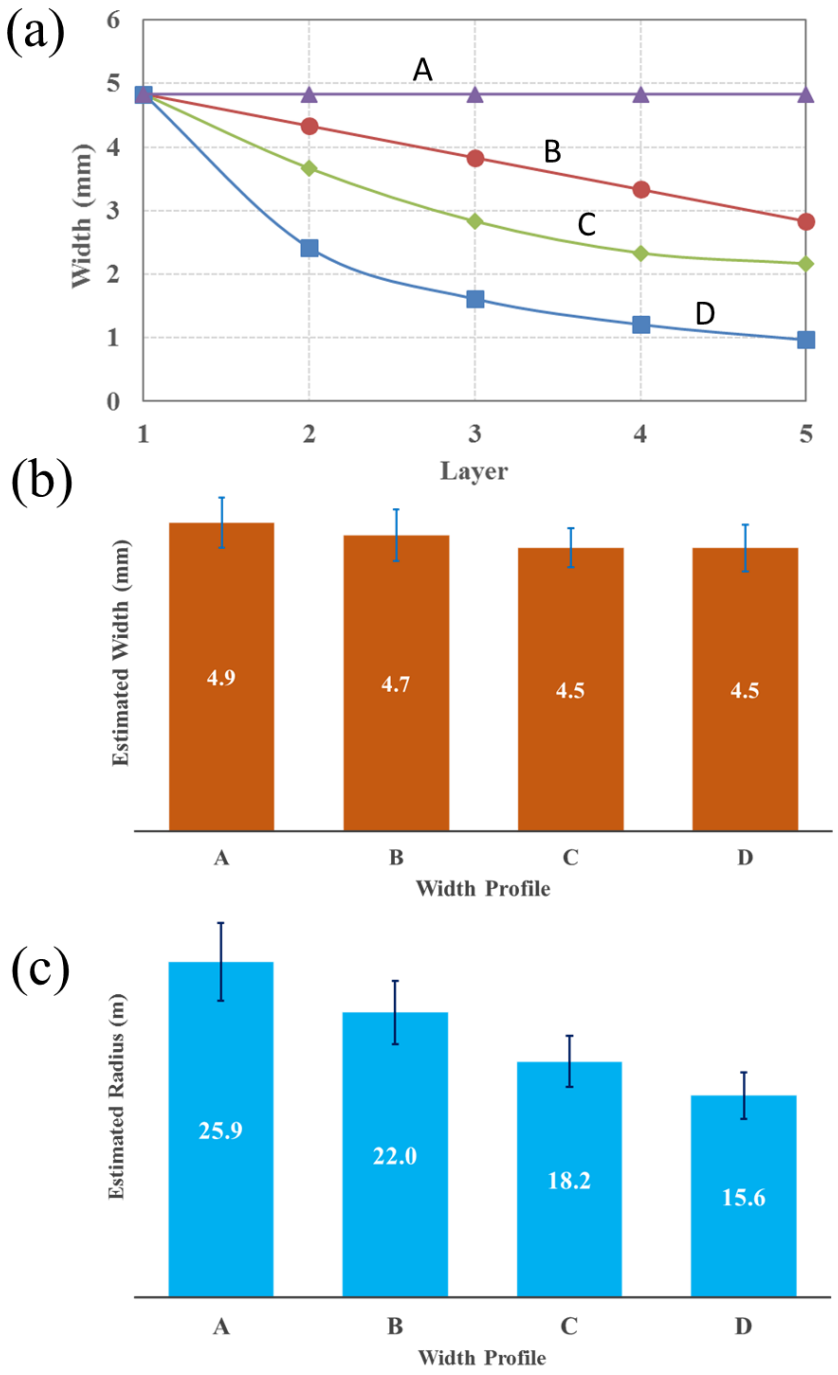

Figure 7.13 (a) Different width profiles used in the simulations. (b) The estimated fracture width corresponding to different scenarios. (c) The estimated fracture radius corresponding to different scenarios. The error bars mark the uncertainties associated with the model parameters.

The estimated fracture width and radius from inversion with respect to different width profiles are plotted in Fig. 7.13. The base case is when the fracture's width is uniform (4.8 mm) and is identical to the base case in Section 7.5.1. As the fracture width decreases faster towards the edge (case B, C and D), the estimated fracture width from inversion still follows the actual value near the wellbore. The estimated radius, however, drops 12.0%, 27.2% and 37.6% for case B, C and D, respectively. Hence data inversion provides equivalent fractures with uniform width (roughly equal to the actual width near the wellbore) but a smaller radius. The actual proppant volume and estimated volume from inversion are listed in Table 7.9.

	Actual Proppant Volume (m^3)	Estimated Proppant Volume (m^3)	Difference (%)
A	9.49	10.32	+6.0
B	6.74	7.14	-9.4
C	5.17	4.68	+16.4
D	2.93	3.41	+8.8

Table 7.9 Comparison between actual and estimated proppant volume.

By comparing the numbers for different cases, it can be found that the estimated fractures from inversion take similar amount of proppant to what the actual fractures do. Therefore it can be concluded that when a fracture's width drops towards the edge, our inverse model provides an equivalent fracture with uniform width (which is close to the actual fracture width near the wellbore) but smaller radius and it predicts about the same amount of proppant or volume of fracture.

7.5.3 Tilted fractures

Tilted fractures, i.e., fractures that are not perpendicular to the well axis, will be generated when the well is not aligned with the orientation of the minimum horizontal stress. We simulated fractures with different angles α (0° to 45°) that are placed 5 m away from the transmitter gap (Fig. 7.14). For all the cases, the fracture width and radius are kept as 4.8 mm and 25 m, respectively. The computed voltages at the receiver gaps for different cases are used for the inversion analysis. The inverse model still assumes a circular fracture with uniform width, perpendicular to the well axis.

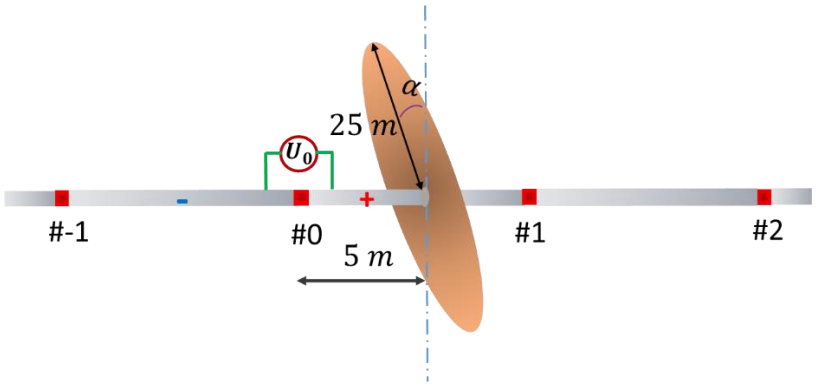

Figure 7.14 A tilted fracture of angle α is placed 5 m away from the transmitter gap.

The estimated fracture width and radius from inversion of data for different fracture angles are plotted in Fig. 7.15. The base case is when the fracture is perpendicular to the well axis (α=0°) and the errors for the estimated width and radius are both within 5%. As the fracture angle increases from 15° to 45°, the estimated fracture width is 6.3%, 22.9% and 33.3% larger than the actual width, respectively. The estimated radius is ~8.8% larger when the fracture angle is 15° and 30°, but is 6.4% smaller than the actual radius when the angle is 45°.

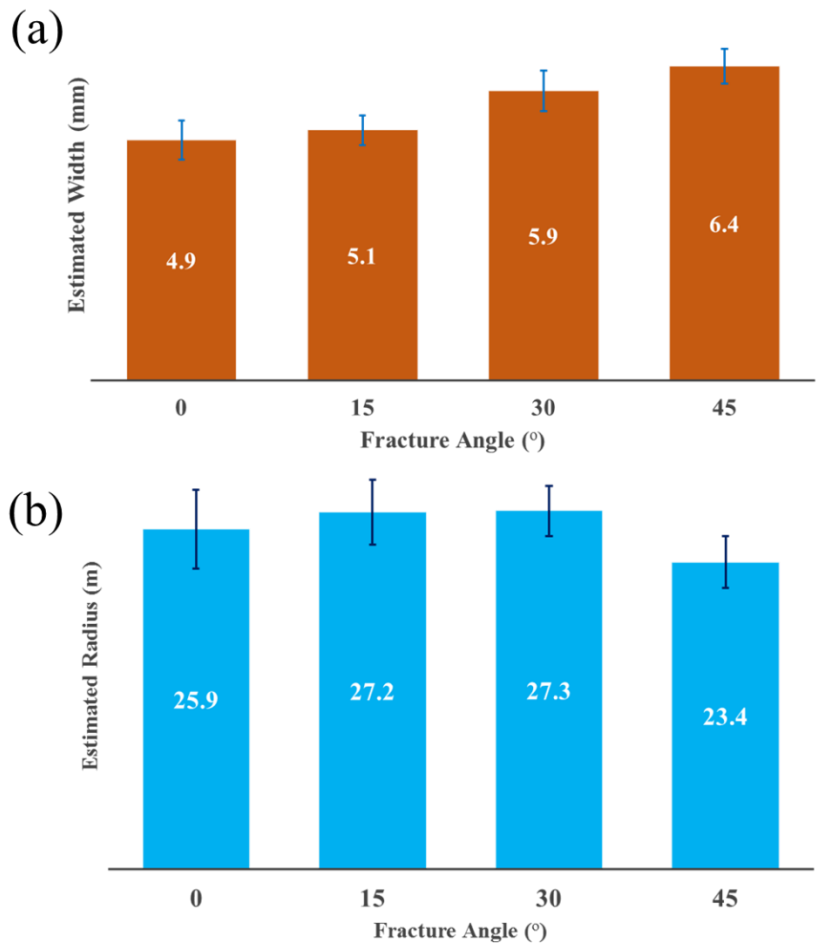

Figure 7.15 (a) The estimated fracture width corresponding to different scenarios. (b) The estimated fracture radius corresponding to different scenarios. The error bars mark the uncertainties associated with the model parameters.

When the fracture tilts from orthogonality with the wellbore, the average distance between the fracture and the well axis, where the receiver gaps are placed, becomes smaller. More current distributed over the fracture's surface will reach the receivers, especially the ones near the transmitter gap. They are interpreted as thicker and larger fractures from the synthetic data. However, when the angle becomes too big (e.g., 45°), the current is limited to a small region near the transmitter. A large portion of the current

from the fracture will flow to the two closest receivers next to the transmitter and die out. This is why it is interpreted as a smaller, but thicker fracture.

7.5.4 Complex fractures

We also simulated a complex fracture to test the inverse solver. For the sake of consistency, the complex fracture is made by adding a few branches to a planar fracture used in the previous sections (r=25 m, δ=4.8 mm). This same planar fracture is also used here as a reference case. The new fracture branches have a constant width (4.8 mm) and height (40 m) and their positions are specified in Fig. 7.16.

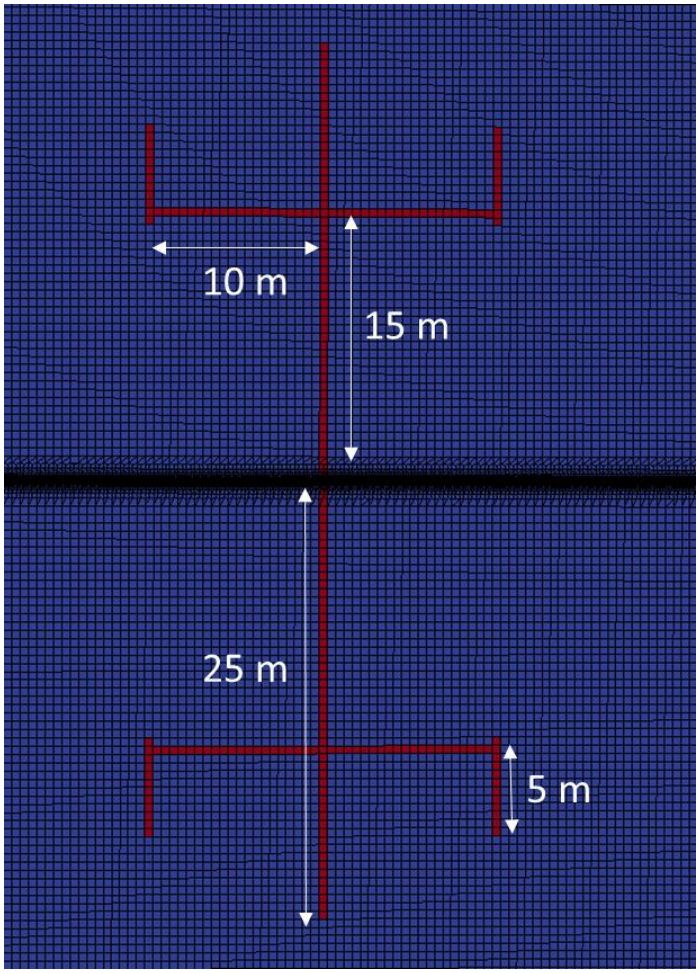

Figure 7.16 A complex fracture with a few fracture branches.

The estimated width and radius for the equivalent planar fracture obtained from the inversion (without branches) are plotted in Fig. 7.17. It can be seen that our inverse solver can estimate the geometry of a planar fracture well. However, when fracture branches are added, the inverse model estimates an equivalent fracture with larger width and radius to account for the newly added branches. The proppant volume of the actual complex fracture and the estimated one are calculated to be 20.9 m^3 and 16.3 m^3, respectively. This means that the influence of a complex fracture on the measured signals is not simply dominated by the proppant volume. Instead it is a synergy of multiple factors, such as proppant volume, and proppant distribution around the well.

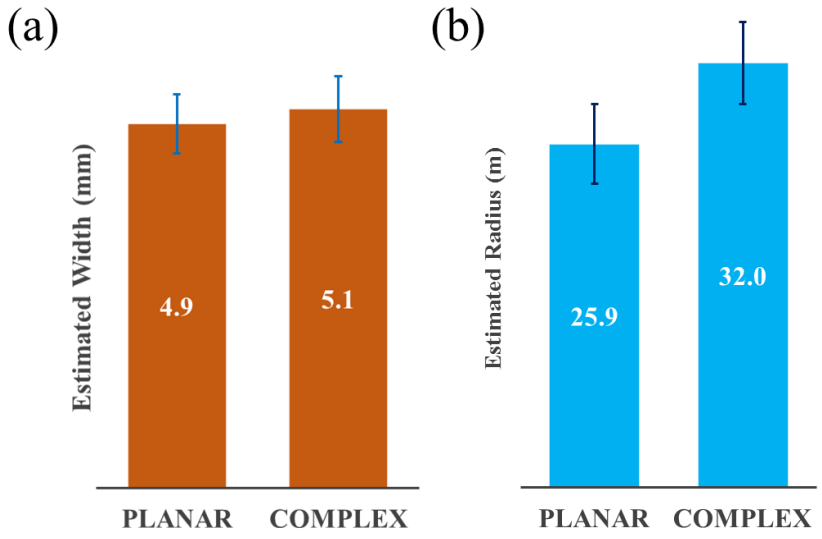

Figure 7.17 The estimated fracture width (a) and radius (b) corresponding to a planar and complex fracture.

7.6 ADDITIONAL OBSERVATIONS

Both Section 7.3 and 7.4 show inversion results obtained from synthetic data with different noise levels (2% and 5%). To draw a concrete conclusion on the solver's robustness, we ran an additional set of simulations using inversion strategy 2 (6 receivers

are involved for each excitation) with clean synthetic data. The errors and uncertainties for different cases are listed in Table 7.10.

	Width		Radius	
Noise (%)	Average Error (%)	Average Uncertainty (%)	Average Error (%)	Average Uncertainty (%)
0	2.5	4.3	7.1	15.7
2	3	5.5	7.1	16.7
5	1.2	3.1	9.8	16.8

Table 7.10 Error and uncertainty of the estimated fracture parameters corresponding to different noise levels in the synthetic data.

The results in Table 7.10 show that there is no pattern in the accuracy and uncertainty when noise level goes up, which means our inverse solver is not sensitive to up to 5% noise in the data. While the average error remains low, the consistent but higher uncertainty is accounted by the mutual interactions between fractures.

The randomly selected fracture geometry parameters in the previous cases have a relatively small variation. To further understand how a wider variation in the model parameters affects the solver's performance, we ran a case with three fractures and the true radii of the three fractures were 20 m, 5 m and 40 m, respectively. The data were synthesized using three excitation locations (#0, #1 and #2 in Fig. 7.18 (a)). The comparison between the true and inverted model is plotted in Fig. 7.18 (b) and (c).

The average errors for the estimated fracture width and radius are 1.2 % and 6.3 %, respectively. The accuracy is on the same level as observed in the previous cases, which implies that a wider variation in the model parameters doesn't affect the solver's performance. The true data and estimated data also match well for all three excitation locations (Fig. 7.19), which further validates the accuracy of the inversion results.

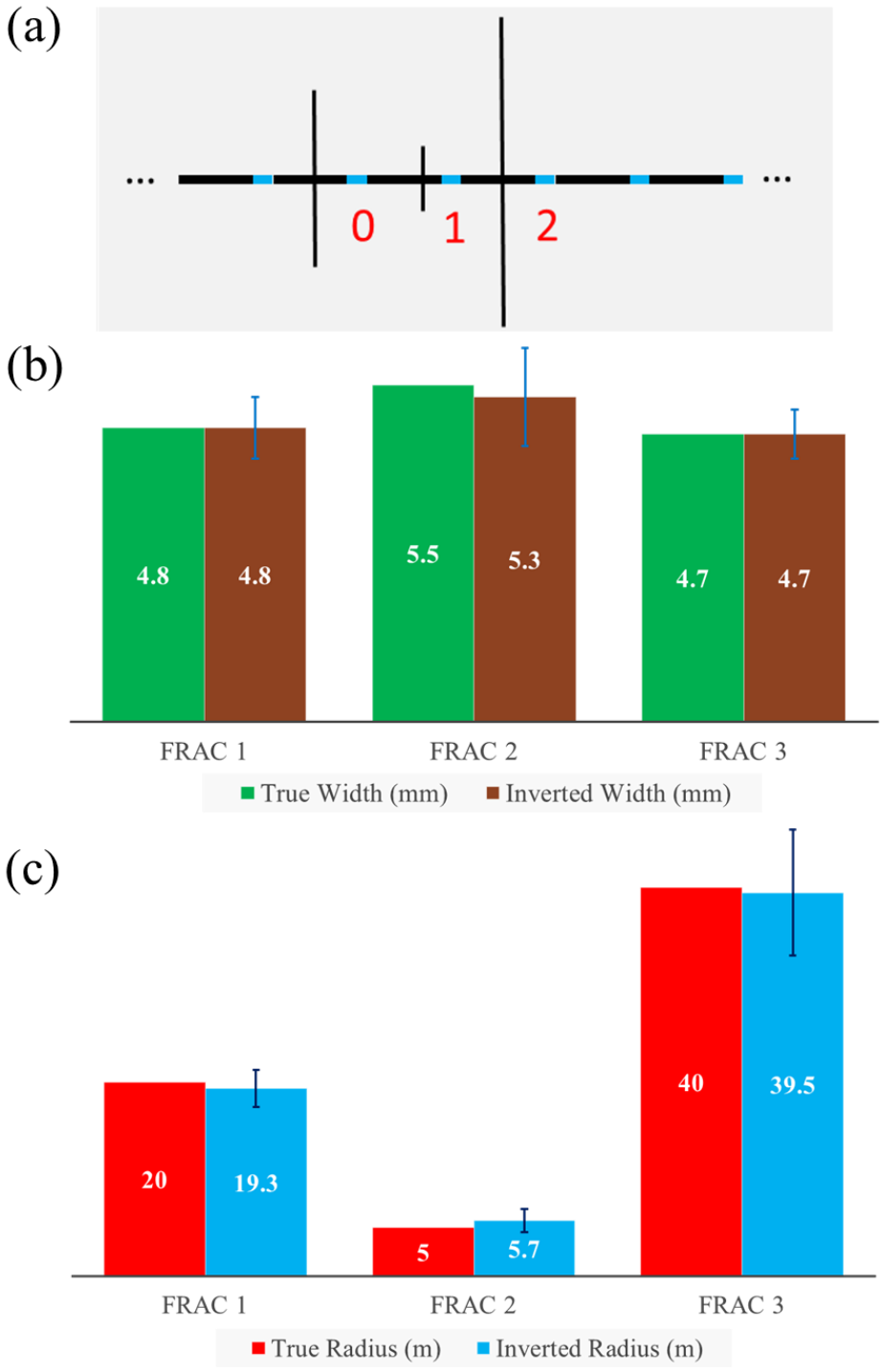

Figure 7.18 (a) The data are synthesized using three excitation locations (#0, #1 and #2). (b), (c). Comparison between the true and inverted model for three fractures with a wide variation in the radius. 5% Gaussian noise is added to the data.

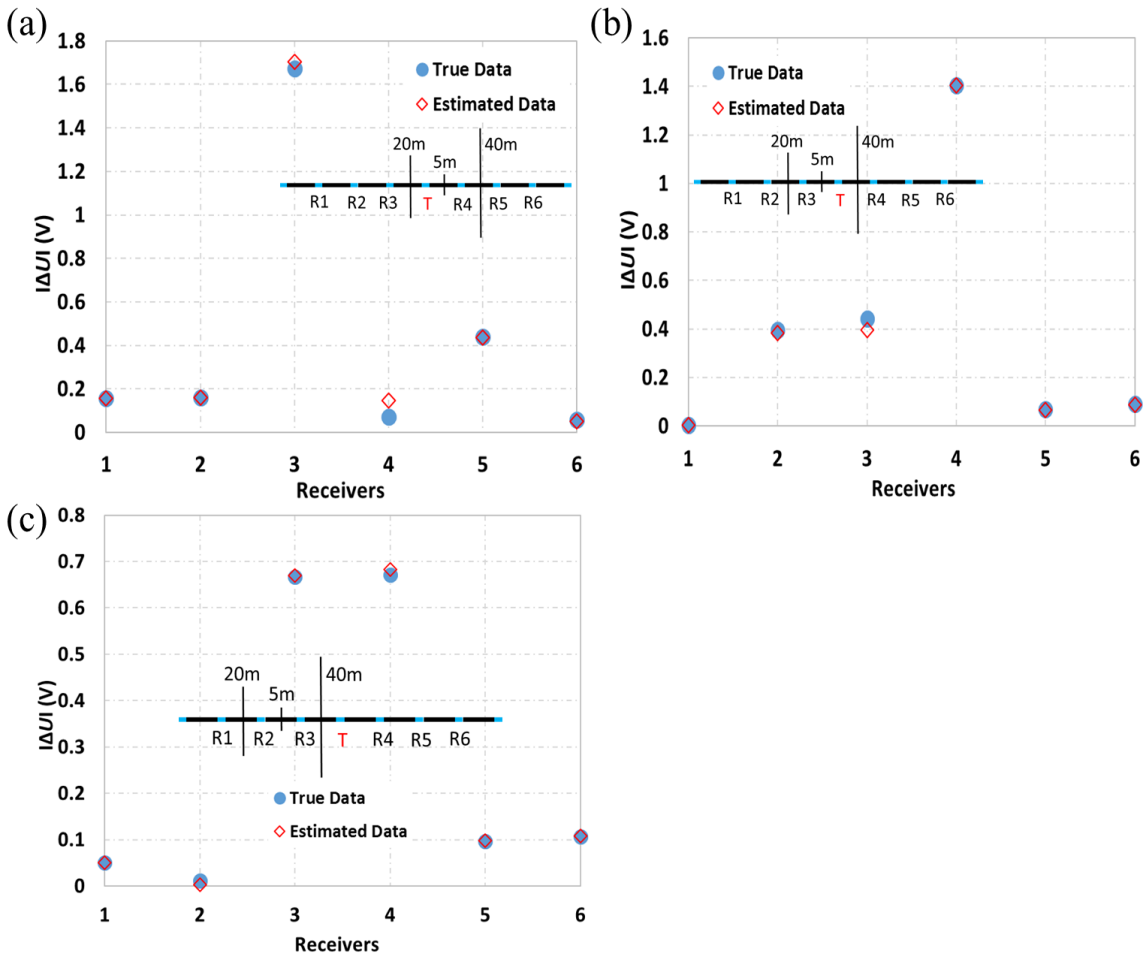

Figure 7.19 Comparison between true data and estimated data for three excitation locations. (a), (b) and (c) correspond to the data when gap #0, #1 and #2 (Fig. 7.18 (a)) are excited, respectively.

We also investigated how the search interval affects the convergence of VFSA. Two cases are compared: A) the search intervals for fracture width and radius are [2 mm, 8 mm] and [10 m, 50 m], respectively; B) the search intervals are narrowed down to [3 mm, 6 mm] and [15 m, 40m]. For both cases we used the same synthetic data from Section 7.4, with 5% noise added. Fig. 7.20 shows the change of the cost function with iterations when the same cooling scheme (Fig. 7.3) is followed. A narrower search interval keeps the cost function lower at the beginning, since the starting model is closer

to the true model. Eventually VFSA can lead the inverted model to converge at similar values, no matter where the starting point is. This means our inverse solver based on VFSA is able to find the fracture geometry parameters even when there is not enough prior knowledge to narrow down the search interval.

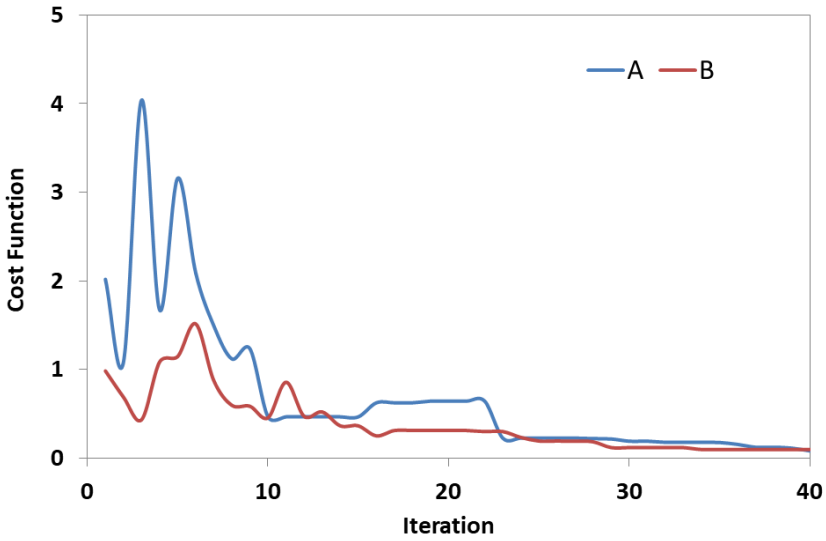

Figure 7.20 Cost function VS iteration during the inversion process. In case A the search intervals for fracture width and radius are [2 mm, 8 mm] and [10 m, 50 m], respectively. The search intervals for case B are set as [3 mm, 6 mm] and [15 m, 40 m].

7.7 SUMMARY

This chapter presents a methodology for extracting the geometries of multiple fractures by inverting the measured data from a logging sequence. Based on the inversion framework proposed in Chapter 6, it was found that the original problem can be divided into sub-problems with smaller size, solved separately, and the solutions can be patched back to address the original problem.

We examined two strategies for solving the original inverse problem using a 'divide and conquer' approach. For both cases, the original data are divided into batches, each with data from four excitations. (1) If for each excitation location, voltages at 8

receivers (4 on each side of the transmitter) are used for inversion, the widths and radii of 13 fractures involved can be solved using each batch of data. (2) If for each excitation location, voltages at 6 receivers (3 on each side of the transmitter) are used for inversion, the widths and radii of 11 fractures involved can be solved using each batch of data. It was found that using both strategies, the 5 fractures directly in contact with the casing sections that have been excited, can be accurately solved by inverting one batch of data. The other 8 fractures (for strategy 1) or 6 fractures (for strategy 2), although cannot be captured properly using this batch of data, will be solved accurately using different sets of data. Once all the sub-problems are solved, the solutions are then patched back without sacrificing the integrity of the original geometry. This strategy guarantees both accuracy and efficiency, since the sub-problems can be solved in parallel with ease.

The robustness of the inverse solver VFSA was also tested by adding noise to the synthetic data. Example cases show that when up to 5% Gaussian noise is introduced, VFSA still provides very accurate inversion results with moderate uncertainties. We also observed a clear correlation between the parameters of neighboring fractures, but it did not lead to considerable non-uniqueness in the inversion results.

Some more realistic conditions, e.g., fractures that are asymmetric to the wellbore, non-uniform fracture widths and complex fractures, are also investigated. The goal is to give the interpreter a good idea of how our inversion strategy projects these complicated conditions in the simplified inverse model (fractures that are circular, uniform and symmetrical to the well). The results show that when a fracture is asymmetric to the wellbore, the estimated fracture width remains close, but the predicted fracture radius turns out to be smaller. For a fracture with smaller width towards the edge, the inverse model provides a smaller fracture to account for the decrease in the width. A complex fracture (multiple strands of fractures) is interpreted as a single planar fracture with a

larger width and radius. For a tilted fracture, both the width and the radius are overestimated when the angle is small. But when the fracture angle is larger than 45^{o}, the fracture is interpreted as a thicker one with smaller size.

Chapter 8: Conclusions

An electrode-based resistivity tool for mapping proppant distribution in hydraulic fractures in cased-hole wells was studied by forward and inverse modeling. The tool makes downhole electrical measurements and relies on conductive proppant as a contrast agent. An array of specialized gap subs with electrically insulated internal connections is installed as a permanent part of the casing string. A coiled-tubing conveyed BHA is run into the lateral to straddle and impose a voltage across each insulating gap one at a time, before and after fracturing operations. The voltages across all other insulating gaps in the casing string are measured, stored in memory, and uploaded to the BHA. This novel method overcomes the problem of through-casing signal attenuation typical for induction tools, by direct excitation of the casing sections. It also mitigates the problem of signal attenuation in borehole-to-surface and borehole-to-borehole measurements, by taking measurements in the same well. The following conclusions can be drawn from the current study:

- A resistivity core holder was used to measure the electrical resistivity of a candidate proppant, petroleum coke (PC), with different particle sizes. The results show that the effective electrical resistivity of this proppant decreases as the confining stress increases, due to better contact between the PC particles under higher stress. A packing of 100% PC shows an electrical resistivity of around $2 \times 10^{-4}\ \Omega \cdot m$ when the confining stress is above 3000 psi (which is on the low end of the expected stress on the proppant in a typical fracture). Particle size does not play a noticeable role in the measured results. The conductivity of the saturation fluid (sea water VS air) also has little impact on the measured electrical

conductivity, since it is mainly determined by the contact between the particles and the intrinsic conductivity of PC. (Chapter 2)

- When sand is mixed with PC, the effective resistivity increases with an increasing weight percentage of sand. This is because sand, as a non-conductive material, prevents direct contact between PC particles and changes the current path. The electrical resistivity stays reasonably low (~$6 \times 10^{-4}\ \Omega \cdot m$) when up to 50% sand is added. (Chapter 2)

- Hydraulic conductivity measurements on PC show that when sand is added, the fracture's hydraulic conductivity increases, probably because of the higher mechanical strength of sand. Even using 100% PC, the measured fracture conductivity is above 4 $\mathrm{md \cdot ft}$ under a confining stress of 6000 psi, which means the fracture is infinitely conductive for a general field-scale fracture in a typical shale (F_{CD} = 160). Notice that more sand mixed with the PC leads to a trade-off between a higher electrical resistivity and a higher fracture conductivity. When applying this proppant in the field, the ratio of PC to sand should be tailored according to the field conditions to assure the mixture is both electrically and hydraulically conductive. (Chapter 2)

- A numerical forward model based on FVM has been built and benchmarked to simulate the tool's response to hydraulic fractures. Two important simplifications are made: (i) replacing the casing and mud system by a single solid volume with an equivalent volume-averaged conductivity; (ii) replacing the thin hydraulic fracture by a thicker one with lower conductivity, maintaining the product of their conductivity σ and thickness δ (conductance), i.e., $\sigma \cdot \delta$, constant. Both

simplifications are shown to significantly reduce the computation time, without sacrificing the accuracy of the solutions. (Chapter 3)

- The forward model was applied to investigate the tool's sensitivity to multiple variables for a single fracture. The results show that the fracture's presence modifies the path for current from the source into the formation and hence modifies the potential distribution along the insulator-separated casing string, compared to the no-fracture case. The tool is highly sensitive to fracture location. When the fracture is in direct contact with the transmitter electrode, a strong current leaks from the excited casing section into the fracture and then into the formation. When there is no direct contact between a transmitter electrode and the fracture, less leakage of current from the casing sections into the formation and then to the fracture occurs. This is why the measured voltages at the receiver gaps are much stronger when the fracture touches the excited casing section. (Chapter 4)
- The tool is also very sensitive to fracture conductance. More current is pulled from the electrode as the fracture becomes more conductive. An increase in formation resistivity leads to similar results. (Chapter 4)
- Depending on their distance from the fracture, the receiver gaps show varying sensitivities to fracture radii in the range of typical propped fracture sizes of 50 m – 100 m. If a threshold signal of $\pm 2\%$ is assumed to be the limitation for differentiation between fractures of different sizes, the results show that it is difficult to accurately determine the radius for fractures that are larger than 100 m in radius. This investigation depth is far larger than what an induction tool can achieve, even in an open-hole environment. (Chapter 4)

- The simulations also show that the tool is sensitive to fracture orientation (angle from the wellbore axis). Most of the single receiver gaps can easily detect fracture angles greater than 30^{o} from orthogonal if a threshold of $\pm 2\%$ is assumed to be the limitation for differentiation. The simulated signals are shown to be less sensitive to the fracture's asymmetry from the well axis, as well as the fracture's aspect ratio. This is because the dominant effect governing the signal level is the fracture's influence on the current pulled from the electrode into the formation – an effect which depends on the fracture's location with respect to the source, its conductance and size, more strongly than it does on its shape and position with respect to the well. (Chapter 4)
- We have also simulated the tool's response to multiple fractures on different casing sections. The results show that when multiple fractures are present, the one that is in contact with the excitation electrode dominates the signals received at the receiver gaps. A special scenario, when two fractures touch the same piece of casing, is also simulated using the forward model. In this case the two fractures induce very similar signals at the receiver gaps to those from one single fracture with double the width. These forward simulations provide important guidance for our inverse analysis, especially in multi-stage fractured horizontal wells.
- It was also found that the influence from passive fractures is limited in a very short distance. Only the fractures right next to the receiver gaps being considered need to be incorporated in the simulations. This means when simulating the tool's response in the presence of a large number of fractures, the geometry can be divided into several batches and solved separately, without sacrificing the integrity of the original geometry. (Chapter 5)

- A model-based inversion framework was built to extract the fracture geometries from the data in a fully automatic process. The framework incorporates the FVM-based forward modeling methods and an inversion kernel. Using this framework, the performance of a steepest descent method and very fast simulated annealing was evaluated and compared. The inversion results reveal that the method of steepest descent can be used to extract the parameters fractures, but as a deterministic (greedy) algorithm, it can be easily trapped at a local minimum. VFSA, as a global optimization method, allows us to jump out of the local minima by accepting 'bad' solutions with a time-varying probability. Due to this reason, VFSA offers much more accurate inversion results for multiple fractures. Moreover, it was shown to be a robust inverse solver capable of inverting noisy data. (Chapter 6)
- The inversion framework, together with VFSA, can be used to extract the parameters of multiple fractures by inverting the data acquired in a logging sequence. It was found that the original problem can be divided into sub-problems with smaller size, solved separately, and the solutions can be patched back to address the original problem. We examined two strategies for solving the original inverse problem using a 'divide and conquer' approach. For both cases, the 5 fractures directly in contact with the casing sections that have been excited, can be accurately solved by inverting one batch of data in a sub-problem. Once all the sub-problems are solved, the solutions are then patched back without sacrificing the integrity of the original geometry. The robustness of the inverse solver VFSA was also tested by adding noise to the synthetic data. Example cases show that when up to 5% Gaussian noise is introduced, VFSA still provides very accurate inversion results with moderate uncertainties (Chapter 7).

- Some more fracture geometries, such as fractures deviating from the well, non-uniform fracture width and complex fractures, are also investigated. The goal is to provide us a good idea of how our inversion strategy interprets these complicated conditions in the simplified inverse model (circular, uniform and symmetrical to the well). The results show that when a fracture deviates from the wellbore, the estimated fracture width is correctly inferred, but the fracture radius turns out to be smaller. For a fracture with smaller width towards the edge, the inverse model provides a smaller fracture radius to account for the change in width. The branches in a complex fracture are interpreted as a larger width and radius of a planar fracture. For a tilted fracture, both the width and the radius are overestimated when the angle is small. But when the fracture angle is larger than 45^{o}, the fracture is interpreted as a thicker one with smaller size. (Chapter 7)

The findings listed above show the tool's capability of robustly detecting conductive proppants in hydraulic fractures. A structure was built to study the tool's sensitivity to various parameters, and to extract fracture parameters effectively by inverting the measured data from the tool. We also suggest a candidate proppant PC that possesses high electrical and hydraulic conductivity, and therefore is suitable for this application.

Future Work

It should be recognized in the meantime that this work mostly focuses on numerical modeling of the tool. More work needs to be done before a downhole tool can be deployed in the field. Some of the recommended areas for future research include:

- Some parts of the numerical model need be further improved. For example, the speed of our forward simulations can be accelerated by solving the governing equation by functional or domain decomposition. The main factors that slow down the simulations are the complexity in the geometry and the large contrast in material properties. We are faced with features that have very large aspect ratios, e.g., the well and the fractures, and this implies that many levels of mesh refinement are needed around these features. The large contrast in the electrical conductivities of casing and insulating gap makes the matrices ill-conditioned and requires a large number of iterations for the solver to converge. Better matrix conditioners may be helpful in resolving this issue.
- The insulating gaps, the main body and the electronics for the tool need to be designed and built. They have to be able to withstand high pressure and temperature in the downhole environment. This requires a lot of expertise in electrical and mechanical engineering. Some technical challenges are likely to come up when building the tool. The electronics, e.g., voltage sensors, need to be tested in the lab to quantify the resolution and noise level of the instruments. This will allow the interpreter to recognize the quality of the measured data and the fracture parameters obtained from the inversion.
- While the simulations results are encouraging, tests of a field-deployable tool through experiments are needed to further prove this method for effective proppant mapping. Perhaps a prototype tool, which can be tested in a shallow well with ease, is a good starting point. A comparison between the preset (true) fracture geometries and the estimated ones from data inversion can provide direct evidence of the tool's performance. Some improvements may need to be made to

remedy the defects in the design and manufacturing that may come up during the tests.

Bibliography

Adachi, J., Siebrits, E., Peirce, A. and Desroches, J., 2007. Computer simulation of hydraulic fractures. International Journal of Rock Mechanics and Mining Sciences, 44(5), pp.739-757.

Aldridge, D.F. and Oldenburg, D.W., 1989. Direct Current Electric Potential Field Associated with Two Spherical Conductors in a Whole-Space. Geophysical prospecting, 37(3), pp.311-330.

Arora, K., Cazenave, A., Engdahl, E.R., Kind, R., Manglik, A., Roy, S., Sain, K. and Uyeda, S., 2011. Encyclopedia of solid earth Geophysics. Springer Science & Business Media.

Aster, R.C., Borchers, B. and Thurber, C.H., 2011. Parameter estimation and inverse problems (Vol. 90). Academic Press.

Basu, S. and Sharma, M.M., 2014, February. A new method for fracture diagnostics using low frequency electromagnetic induction. In SPE Hydraulic Fracturing Technology Conference. Society of Petroleum Engineers.

Berryman, J.G. and Hoversten, G.M., 2013. Modelling electrical conductivity for earth media with macroscopic fluid-filled fractures. Geophysical Prospecting, 61(2), pp.471-493.

Bhatnagar, A., 2016. Overcoming Challenges in Fracture Stimulation through Advanced Fracture Diagnostics. In SPE Asia Pacific Hydraulic Fracturing Conference. Society of Petroleum Engineers.

Blyton, C.A., Gala, D.P. and Sharma, M.M., 2015, September. A comprehensive study of proppant transport in a hydraulic fracture. In SPE Annual Technical Conference and Exhibition. Society of Petroleum Engineers.

Blyton, C.A.J., 2016. Proppant transport in complex fracture networks (Doctoral dissertation).

Bryant, E.C., Hwang, J. and Sharma, M.M., 2015, February. Arbitrary fracture propagation in heterogeneous poroelastic formations using a finite volume-based cohesive zone model. In SPE Hydraulic Fracturing Technology Conference. Society of Petroleum Engineers.

Bunger, A.P., Zhang, X. and Jeffrey, R.G., 2012. Parameters affecting the interaction among closely spaced hydraulic fractures. SPE Journal, 17(01), pp.292-306.

Cannan, C., Bartel L., Palisch T., and Aldridge D., 2015. Electrically conductive proppant and methods for detecting, locating and characterizing the electrically conductive proppant: U.S. Patent 8,931,553.

Carey, M.A., Mondal, S. and Sharma, M.M., 2015, October. Analysis of water hammer signatures for fracture diagnostics. In SPE Annual Technical Conference and Exhibition. Society of Petroleum Engineers.

Carey, M.A., Mondal, S., Sharma, M.M., and Hebert, D.B., 2016. Correlating Water Hammer Signatures with Production Log and Microseismic Data in Fractured Horizontal Wells. In SPE Hydraulic Fracturing Technology Conference. Society of Petroleum Engineers.

Casero, A., Pace, G., Malone, B.P., Cantaloube, F.Y., Tealdi, L., Malonga, H. and Seale, R.A., 2008, January. Continuous Pumping, Multistage, Hydraulic Fracturing in Kitina Field, Offshore Congo, West Africa. In SPE International Symposium and Exhibition on Formation Damage Control. Society of Petroleum Engineers.

Castaneda, J.C., Castro, L., Craig, S.H., Moore, C. and Myatt, J.H., 2010, January. Coiled-Tubing Fracturing: An Operational Review of a 43-Stage Barnett Shale Stimulation. In SPE/ICoTA Coiled Tubing and Well Intervention Conference and Exhibition. Society of Petroleum Engineers.

Catlett, R.D., Spencer, J.D., Lolon, E. and Bucior, D., 2013, February. Evaluation of two horizontal wells in the eagle ford using oil-based chemical tracer technology to optimize stimulation design. In SPE Hydraulic Fracturing Technology Conference. Society of Petroleum Engineers.

Cipolla, C.L. and Wright, C.A., 2000, January. State-of-the-art in hydraulic fracture diagnostics. In SPE Asia Pacific Oil and Gas Conference and Exhibition. Society of Petroleum Engineers.

Dahi-Taleghani, A. and Olson, J.E., 2011. Numerical modeling of multistranded-hydraulic-fracture propagation: Accounting for the interaction between induced and natural fractures. SPE journal, 16(03), pp.575-581.

Dawson, M. and Kampfer, G., 2016. Breakthrough in hydraulic fracture & proppant mapping: Achieving increased precision with lower cost. Unconventional Resources Technology Conference (URTEC).

Duenckel, R.J., Smith, H.D., Hao, S., Gao, D., Palisch, T.T. and Han, X., 2011. A New Method to Identify Proppant Location in Induced Fractures. In International Petroleum Technology Conference. International Petroleum Technology Conference.

Durst, D.G., Harris, J.T., Contreras, J.D. and Watson, D.R., 2008, January. Improved Single-Trip Multistage Completion Systems for Unconventional Gas Formations. In SPE Tight Gas Completions Conference. Society of Petroleum Engineers.

Dusseault, M. and McLennan, J., 2011. Massive multistage hydraulic fracturing: Where are we. American Rock Mechanics Association.

Eisner, L., Fischer, T. and Le Calvez, J.H., 2006. Detection of repeated hydraulic fracturing (out-of-zone growth) by microseismic monitoring. The Leading Edge, 25(5), pp.548-554.

Elahi, S.H. and Jafarpour, B., 2018. Dynamic Fracture Characterization From Tracer-Test and Flow-Rate Data With Ensemble Kalman Filter. SPE Journal.

Everett, M.E. and Schultz, A., 1996. Geomagnetic induction in a heterogenous sphere: Azimuthally symmetric test computations and the response of an undulating 660-km discontinuity. Journal of Geophysical Research: Solid Earth, 101(B2), pp.2765-2783.

Fang, Y., Dai, J., Yu, Z., Zhou, J. and Liu, Q.H., 2017. Through-casing hydraulic fracture evaluation by induction logging I: An efficient EM solver for fracture detection. IEEE Transactions on Geoscience and Remote Sensing, 55(2), pp.1179-1188.

Fisher, M.K., Wright, C.A., Davidson, B.M., Goodwin, A.K., Fielder, E.O., Buckler, W.S. and Steinsberger, N.P., 2002, January. Integrating fracture mapping technologies to optimize stimulations in the Barnett Shale. In SPE annual technical conference and exhibition. Society of Petroleum Engineers.

Friehauf, K.E., 2009. Simulation and design of energized hydraulic fractures. The University of Texas at Austin.

Gabelmann, J., M. Oerkfitz, T. Hosback, and M. M. Sharma, 2017, Modular Electrode Resistivity Tool for Improved Fracture Diagnostics: U.S. Patent 62/518,950.

Gadeken, L.L., Smith Jr, H.D. and Nguyen, C., 1986. Tracerscan–A Spectroscopy Technique for Determining the Distribution of Multiple Radioactive Tracers in Downhole Operations.

Gibson, W.C., 2014. The method of moments in electromagnetics. CRC press.

Gore, G.L. and Terry, L.L., 1956. Radioactive tracer techniques. Journal of Petroleum Technology, 8(09), pp.12-17.

Grae, A., Duenckel, R.J., Nelson, J.R., Smith, H.D., Han, X. and Palisch, T.T., 2012, January. Field Study Compares Hydraulic Fracture Diagnostic Technologies. In SPE Hydraulic Fracturing Technology Conference. Society of Petroleum Engineers.

Grieser, W.V., Shelley, R.F. and Soliman, M.Y., 2009, January. Predicting production outcome from multi-stage, horizontal Barnett completions. In SPE Production and Operations Symposium. Society of Petroleum Engineers.

Grieve, R.A. and Osinski, G.R., 2011. Impact craters on Earth. In Encyclopedia of Solid Earth Geophysics (pp. 593-599). Springer Netherlands.

Haber, E., Ascher, U.M., Aruliah, D.A. and Oldenburg, D.W., 2000. Fast simulation of 3D electromagnetic problems using potentials. Journal of Computational Physics, 163(1), pp.150-171.

Haber, E., Schwarzbach, C. and Shekhtman, R., 2016. Modeling electromagnetic fields in the presence of casing. In SEG Technical Program Expanded Abstracts 2016 (pp. 959-964). Society of Exploration Geophysicists.

Haustveit, Kyle, K. Dahlgren, H. Greenwood, T. Peryam, B. Kennedy, and M. Dawson. "New Age Fracture Mapping Diagnostic Tools-A STACK Case Study." In SPE Hydraulic Fracturing Technology Conference and Exhibition. Society of Petroleum Engineers, 2017.

Heagy, L.J., Oldenburg, D.W. and Chen, J., 2014. Where does the proppant go? Examining the application of electromagnetic methods for hydraulic fracture characterization. GeoConvention 2014, CSEG, Search and Discovery Article 90224.

Hoversten, G.M., Commer, M., Haber, E. and Schwarzbach, C., 2015. Hydro-frac monitoring using ground time-domain electromagnetics. Geophysical Prospecting, 63(6), pp.1508-1526.

Huang, S. and Torres-Verdín, C., 2016. Inversion-based interpretation of borehole sonic measurements using semianalytical spatial sensitivity functions. Geophysics, 81(2), pp.D111-D124.

Huang, S., Yang, Q., Matuszyk, P.J. and Torres-Verdín, C., 2013. High-resolution interpretation of sonic logging measurements using stochastic inversion with spatial slowness sensitivity functions. In SEG Technical Program Expanded Abstracts 2013 (pp. 524-528). Society of Exploration Geophysicists.

Ingber, L., 1989. Very fast simulated re-annealing. Mathematical and computer modelling, 12(8), pp.967-973.

Iriarte, J., Merritt, J. and Kreyche, B., 2017, March. Using Water Hammer Characteristics as a Fracture Treatment Diagnostic. In SPE Oklahoma City Oil and Gas Symposium. Society of Petroleum Engineers.

Jasak, H., 1996. Error Analysis and Estimation for the Finite Volume Method with Applications to Fluid Flows, 1996(Doctoral dissertation, Ph.D. Thesis, University of London Imperial College).

Jin, J.M., 2011. Theory and computation of electromagnetic fields. John Wiley & Sons.

Jin, J.M., 2015. The finite element method in electromagnetics. John Wiley & Sons.

Johnston, R.H., Trofimenkoff, F.N. and Haslett, J.W., 1987. Resistivity response of a homogeneous earth with a finite-length contained vertical conductor. IEEE Transactions on Geoscience and Remote Sensing, (4), pp.414-421.

Jung, J. and Taciroglu, E., 2014. Modeling and identification of an arbitrarily shaped scatterer using dynamic XFEM with cubic splines. Computer Methods in Applied Mechanics and Engineering, 278, pp.101-118.

Kampfer, G. and Dawson, M., 2016, June. A Novel Approach to Mapping Hydraulic Fractures Using Poromechanic Principles. In 50th US Rock Mechanics/Geomechanics Symposium. American Rock Mechanics Association.

Karp, R.M., 1977. Probabilistic analysis of partitioning algorithms for the traveling-salesman problem in the plane. Mathematics of operations research, 2(3), pp.209-224.

King, G.E., 2010, January. Thirty years of gas shale fracturing: What have we learned?. In SPE Annual Technical Conference and Exhibition. Society of Petroleum Engineers.

Kirkpatrick, S., Gelatt, C.D. and Vecchi, M.P., 1983. Optimization by simulated annealing. Science, 220(4598), pp.671-680.

LaBrecque, D., Brigham, R., Denison, J., Murdoch, L., Slack, W., Liu, Q.H., Fang, Y., Dai, J., Hu, Y., Yu, Z. and Kleinhammes, A., 2016, February. Remote imaging of proppants in hydraulic fracture networks using electromagnetic methods: Results of small-scale field experiments. In SPE Hydraulic Fracturing Technology Conference. Society of Petroleum Engineers.

Le Calvez, J.H., Craven, M.E., Klem, R.C., Baihly, J.D., Bennett, L.A. and Brook, K., 2007, January. Real-time microseismic monitoring of hydraulic fracture treatment: A tool to improve completion and reservoir management. In SPE Hydraulic Fracturing Technology Conference. Society of Petroleum Engineers.

Ley-Cooper, A.Y., Munday, T., Gilfedder, M., Ibrahimi, T., Annetts, D. and Cahill, K., 2015. Inversion of legacy airborne electromagnetic datasets to inform the hydrogeological understanding of the northern Eyre Peninsula, South Australia. Goyder Institute for Water Research Technical Report Series.

Lou, Z. and Jin, J.M., 2006. A novel dual-field time-domain finite-element domain-decomposition method for computational electromagnetics. IEEE transactions on antennas and propagation, 54(6), pp.1850-1862.

Mackie, R.L., Madden, T.R. and Wannamaker, P.E., 1993. Three-dimensional magnetotelluric modeling using difference equations—Theory and comparisons to integral equation solutions. Geophysics, 58(2), pp.215-226.

Manchanda, R., Bryant, E.C., Bhardwaj, P. and Sharma, M.M., 2016, February. Strategies for effective stimulation of multiple perforation clusters in horizontal wells. In SPE Hydraulic Fracturing Technology Conference. Society of Petroleum Engineers.

Manchanda, R., Sharma, M.M. and Holzhauser, S., 2014. Time-dependent fracture-interference effects in pad wells. SPE Production & Operations, 29(04), pp.274-287.

Mayerhofer, M.J., Lolon, E., Warpinski, N.R., Cipolla, C.L., Walser, D.W. and Rightmire, C.M., 2010. What is stimulated reservoir volume?. SPE Production & Operations, 25(01), pp.89-98.

Mayerhofer, M.J., Stegent, N.A., Barth, J.O. and Ryan, K.M., 2011, January. Integrating fracture diagnostics and engineering data in the marcellus shale. In SPE Annual Technical Conference and Exhibition. Society of Petroleum Engineers.

Menke, W., 1984. The resolving power of cross-borehole tomography. Geophysical Research Letters, 11(2), pp.105-108.

Newman, G.A. and Alumbaugh, D.L., 1995. Frequency-domain modelling of airborne electromagnetic responses using staggered finite differences. Geophysical Prospecting, 43(8), pp.1021-1042.

Nocedal, J., 2006. Numerical optimization. Springer.

Olson, J.E. and Taleghani, A.D., 2009, January. Modeling simultaneous growth of multiple hydraulic fractures and their interaction with natural fractures. In SPE hydraulic fracturing technology conference. Society of Petroleum Engineers.

Ouchi, H., Katiyar, A., York, J., Foster, J.T. and Sharma, M.M., 2015. A fully coupled porous flow and geomechanics model for fluid driven cracks: a peridynamics approach. Computational Mechanics, 55(3), pp.561-576.

Palisch, T., Al-Tailji, W., Bartel, L., Cannan, C., Czapski, M. and Lynch, K., 2016, February. Recent Advancements in Far-Field Proppant Detection. In SPE Hydraulic Fracturing Technology Conference. Society of Petroleum Engineers.

Potluri, N.K., Zhu, D. and Hill, A.D., 2005, January. The effect of natural fractures on hydraulic fracture propagation. In SPE European Formation Damage Conference. Society of Petroleum Engineers.

Prats, M., 1961. Effect of vertical fractures on reservoir behavior-incompressible fluid case. Society of Petroleum Engineers Journal, 1(02), pp.105-118.

Press, W.H., 1989. Numerical recipes in Pascal: the art of scientific computing (Vol. 1). Cambridge University Press.

Roussel, N.P. and Sharma, M.M., 2011. Optimizing fracture spacing and sequencing in horizontal-well fracturing. SPE Production & Operations, 26(02), pp.173-184.

Sahai, R., Miskimins, J.L. and Olson, K.E., 2014, February. Laboratory results of proppant transport in complex fracture systems. In SPE Hydraulic Fracturing Technology Conference. Society of Petroleum Engineers.

Saldungaray, P., Palisch, T. and Duenckel, R., 2012. Novel traceable proppant enables propped frac height measurement while reducing the environmental impact. In SPE/EAGE European Unconventional Resources Conference & Exhibition-From Potential to Production.

Scott, M.P., Johnson, R.L., Datey, A., Vandenborn, C.B., and Woodroof, R.A., 2010. Evaluating hydraulic fracture geometry from sonic anisotropy and radioactive tracer logs. In SPE Asia Pacific Oil and Gas Conference and Exhibition. Society of Petroleum Engineers.

Seale, R.A., Donaldson, J. and Athans, J., 2006, January. Multistage fracturing system: Improving operational efficiency and production. In SPE Eastern Regional Meeting. Society of Petroleum Engineers.

Sen, M.K. and Stoffa, P.L., 1996. Bayesian inference, Gibbs' sampler and uncertainty estimation in geophysical inversion. Geophysical Prospecting, 44(2), pp.313-350.

Sen, M.K. and Stoffa, P.L., 2013. Global optimization methods in geophysical inversion. Cambridge University Press.

Settari, A. and Mourits, F.M., 1998. A coupled reservoir and geomechanical simulation system. Spe Journal, 3(03), pp.219-226.

Sharma, M.M. and Manchanda, R., 2015, September. The role of induced un-propped (IU) fractures in unconventional oil and gas wells. In SPE Annual Technical Conference and Exhibition. Society of Petroleum Engineers.

Shewchuk, J.R., 1994. An introduction to the conjugate gradient method without the agonizing pain.

Shrivastava, K. and Sharma, M.M., 2018, January. Proppant Transport in Complex Fracture Networks. In SPE Hydraulic Fracturing Technology Conference and Exhibition. Society of Petroleum Engineers.

Sierra, J.R., Kaura, J.D., Gualtieri, D., Glasbergen, G., Sarker, D., and Johnson, D., 2008. DTS monitoring of hydraulic fracturing: experiences and lessons learned. In SPE Annual Technical Conference and Exhibition. Society of Petroleum Engineers.

Sookprasong, P.A., Gill, C.C., and Hurt, R.S., 2014. Lessons Learned from DAS and DTS in Multicluster, Multistage Horizontal Well Fracturing: Interpretation of Hydraulic Fracture Initiation and Propagation through Diagnostics. In IADC/SPE Asia Pacific Drilling Technology Conference. Society of Petroleum Engineers.

Symington, W.A., Kaminsky, R.D., Meurer, W.P., Otten, G.A., Thomas, M.M. and Yeakel, J.D., 2010. ExxonMobil's Electrofrac™ Process for In Situ Oil Shale Conversion. In Oil Shale: A Solution to the Liquid Fuel Dilemma (pp. 185-216). American Chemical Society.

Tarantola, A., 1987. Inversion of travel times and seismic waveforms. In Seismic tomography (pp. 135-157). Springer, Dordrecht.

Tong, S. and Mohanty, K.K., 2016. Proppant transport study in fractures with intersections. Fuel, 181, pp.463-477.

Um, E.S., Commer, M., Newman, G.A. and Hoversten, G.M., 2015. Finite element modelling of transient electromagnetic fields near steel-cased wells. Geophysical Journal International, 202(2), pp.901-913.

Versteeg, H.K. and Malalasekera, W., 2007. An introduction to computational fluid dynamics: the finite volume method. Pearson Education.

Wang, T., Tang, X., Yu, L., Kriegsh, B., Fanini, O. and Ugueto, G., 2005. Characterizing fractures with multicomponent induction measurements. Petrophysics, 46(01).

Warpinski, N.R. and Du, J., 2010, January. Source-mechanism studies on microseismicity induced by hydraulic fracturing. In SPE Annual Technical Conference and Exhibition. Society of Petroleum Engineers.

Warpinski, N.R., 1996. Hydraulic fracture diagnostics. Journal of Petroleum Technology, 48(10), pp.907-910.

Watson, D.R., Durst, D.G., Harris, J.T. and Contreras, J.D., 2008, January. One-trip multistage completion technology for unconventional gas formations. In CIPC/SPE Gas Technology Symposium 2008 Joint Conference. Society of Petroleum Engineers.

Webster, P., Cox, B. and Molenaar, M., 2013. Developments in diagnostic tools for hydraulic fracture geometry analysis. Unconventional Resources Technology Conference (URTEC).

Weiss, C.J., Aldridge, D.F., Knox, H.A., Schramm, K.A. and Bartel, L.C., 2016. The direct-current response of electrically conducting fractures excited by a grounded current source. Geophysics, 81(3), pp.E201-E210.

Wright, C.A., Davis, E.J., Golich, G.M., Ward, J.F., Demetrius, S.L., Minner, W.A. and Weijers, L., 1998b, January. Downhole tiltmeter fracture mapping: finally measuring hydraulic fracture dimensions. In SPE Western Regional Meeting. Society of Petroleum Engineers.

Wright, C.A., Davis, E.J., Weijers, L., Golich, G.M., Ward, J.F., Demetrius, S.L. and Minner, W.A., 1998a, January. Downhole tiltmeter fracture mapping: a new tool for directly measuring hydraulic fracture dimensions. In SPE Annual Technical Conference and Exhibition. Society of Petroleum Engineers.

Wu, C.H., Yi, S. and Sharma, M.M., 2017. Proppant Distribution among Multiple Perforation Clusters in a Horizontal Wellbore. In SPE Hydraulic Fracturing Technology Conference and Exhibition. Society of Petroleum Engineers.

Wu, K. and Olson, J.E., 2013. Investigation of the impact of fracture spacing and fluid properties for interfering simultaneously or sequentially generated hydraulic fractures. SPE Production & Operations, 28(04), pp.427-436.

Wu, W., Russell, R. and Sharma, M.M., 2017, September. An Experimental Method to Study the Impact of Fracturing Fluids on Fracture Conductivity in Heterogeneous Shales. In Unconventional Resources Technology Conference, Austin, Texas, 24-26 July 2017 (pp. 808-821). Society of Exploration Geophysicists, American Association of Petroleum Geologists, Society of Petroleum Engineers.

Yamamoto, K., Shimamoto, T. and Sukemura, S., 2004. Multiple fracture propagation model for a three-dimensional hydraulic fracturing simulator. International Journal of Geomechanics, 4(1), pp.46-57.

Yang, D. and Oldenburg, D., 2017. 3D EM modeling of steel casings using an equivalent RL circuit network. In 6th International Symposium on Three-Dimensional Electromagnetics.

Yang, D., Oldenburg, D. and Heagy, L., 2016. 3D DC resistivity modeling of steel casing for reservoir monitoring using equivalent resistor network. In SEG Technical Program Expanded Abstracts 2016 (pp. 932-936). Society of Exploration Geophysicists.

Yang, K., Celik, E., Torres-Verdin, C. and Yilmaz, A.E., 2013, January. Detection and quantification of 3D hydraulic fractures with multi-component low-frequency borehole resistivity measurements. In 2013 SEG Annual Meeting. Society of Exploration Geophysicists.

Yang, K., Torres-Verdín, C. and Yılmaz, A.E., 2015. Detection and quantification of three-dimensional hydraulic fractures with horizontal borehole resistivity measurements. IEEE Transactions on Geoscience and Remote Sensing, 53(8), pp.4605-4615.

Yu, Z., Zhou, J., Fang, Y., Hu, Y. and Liu, Q.H., 2017. Through-casing hydraulic fracture evaluation by induction logging II: The inversion algorithm and experimental validations. IEEE Transactions on Geoscience and Remote Sensing, 55(2), pp.1189-1198.

Zhang, P., Brick, Y. and Sharma, M.M., 2018 a. Numerical study of an electrode-based resistivity tool for fracture diagnostics in steel-cased wellbores. Geophysics, 83(2), pp.D41-D48.

Zhang, P., Sen, M.K., Sharma, M.M., Gabelmann, J. and Glowka, D., 2018 b. Mapping Proppant Distribution in Hydraulic Fractures in Cased Wellbores Using Low Frequency Downhole Electrical Measurements. In SPE Hydraulic Fracturing Technology Conference and Exhibition. Society of Petroleum Engineers.

Zhang, P., Shiriyev J., Torres-Verdín C., Sharma M.M., Brick Y., Massey J., and Yilmaz A.E., 2016. Fracture Diagnostics Using a Low-Frequency Electromagnetic Induction Method. In 50th US Rock Mechanics/Geomechanics Symposium. American Rock Mechanics Association.

Zhang, S. and Zhu, D., 2017. Inversion of Downhole Temperature Measurements in Multistage Fracture Stimulation in Horizontal Wells. In SPE Annual Technical Conference and Exhibition. Society of Petroleum Engineers.

Zhou, J. and Xue, C., 2011, January. Experimental investigation of fracture interaction between natural fractures and hydraulic fracture in naturally fractured reservoirs. In SPE Europec/Eage Annual Conference and Exhibition. Society of Petroleum Engineers.